EXPERIMENTAL AND NUMERICAL INVESTIGATIONS OF THE EFFECTS OF INCIDENT TURBULENCE ON THE FLOW OVER A SURFACE-MOUNTED PRISM

by

Yasser Mohamed El-Okda

Dissertation Submitted to the Faculty of the Virginia Polytechnic Institute and State University in partial fulfillment of the requirements for the degree of

Doctor of Philosophy
in
Engineering Mechanics

Muhammad R. Hajj, Co-Chair
Saad A. Ragab, Co-chair
William J. Devenport
Ziyad N. Masoud
Don H. Morris

Febraury 11, 2005
Blacksburg, Virginia

Keywords: Surface-Mounted Prism, Low-Rise Structures, Particle Image Velocimetry, Large Eddy Simulation, Compact Upwind Schemes

EXPERIMENTAL AND NUMERICAL INVESTIGATIONS OF THE EFFECTS OF INCIDENT TURBULENCE ON THE FLOW OVER A SURFACE-MOUNTED PRISM

by

Yasser Mohamed El-Okda

Abstract

The issue of the effects of free stream turbulence on the flow field over a surface-mounted prism is examined through experimental and numerical investigations. In the experimental studies, particle image velocimetry measurements are conducted in the ESM water tunnel at Reynolds number of $9,600$ and under two cases of turbulent inflow conditions. The results show that the mean flow separation, reattachment and parameters such as mean velocity, root mean square, Reynolds stresses and turbulent kinetic energy are affected by the turbulence characteristics of the incident flow. The instantaneous dynamics of the interactions between the separating shear layer and the solid wall and between the shear layer and the turbulence in the incident flow are detailed.

In the numerical studies, large eddy simulations of the flow over a surface-mounted prism under two inflow conditions, namely, smooth inflow and isotropic homogeneous turbulence inflow, are performed. The use of a fifth-order scheme (CUD-II-5), which is a member of a family of Compact Upwind Difference schemes, in large eddy simulations of this flow is assessed. The performance of this scheme is validated by comparing the rate of temporal decay of isotropic turbulence with available experimental measurements for grid-generated turbulence. The results show that the spectra are sensitive to the method of flux vector splitting needed for the implementation of the upwind scheme. With van Leer splitting, the CUD-II-5 scheme is found to be too dissipative. On the other hand, using the Lax-Friedrichs vector splitting yields good agreement with experiments by controlling the level of artificial dissipation. This led us to recommend a new procedure, we denote by C6CUD5 scheme, that

combines a compact sixth-order scheme with the CUD-II-5 scheme for large eddy simulation of complex flows. The simulation results, including flow patterns, pressure fields and turbulence statistics show that the CUD-II-5 scheme, with Lax-Friedricks flux vector splitting, provides high resolution of local flow structures. The results present new physical aspects of the flow topology over surface-mounted prisms. The effects of the incident homogeneous turbulence on the size of the separation region and suction pressures are determined by pointing out differences in the flow topologies between the two incident flow cases.

Dedication

I would like to dedicate this dissertation to my parents. I would like also to dedicate this dissertation to my wife *Mai* and my son *Abdul-Rahman*.

Acknowledgments

I would like to express my deep gratitude to my advisors Dr. Muhammad Hajj and Dr. Saad Ragab. They have been of great help, patience, understanding and of indefinite support. I'd like to also thank Dr. Don Morris, the Assistant Department Head, for his support through my graduate studies in the Department of Engineering Science and Mechanics.

I would like to thank Dr. William Devenport, and Dr. Ziyad Masoud for serving on my committee.

Contents

List of Figures

List of Tables

Chapter 1

Introduction and Literature Review

1.1 Background

The flow over a surface-mounted prism is a generic flow that has been used to simulate wind flows around low-rise structures, ship superstructure airwakes, flame stabilizers and other flows around bluff bodies. Besides being a model flow of these applications, there has been a great interest in the complex aspects of this flow. Studies of the flow over surface-mounted prisms have dealt with a wide range of characteristics covering overall quantities such as drag and lift forces, mean velocity field as well as local details such as pressure coefficients at different locations, unsteady features, and stability of the separating layers.

Becker, Lienhart and Durst [4] and Martinuzzi and Tropea [37] described the flow field around surface-mounted obstacles. A detailed review of junction flows including flows around surface-mounted blunt and streamlined bodies is provided by Simpson [56]. In cases where the flow is normal to one face of the surface-mounted prism, five different flow regions can be identified. These are

1. The incident flow which is mainly characterized by the mean velocity profile and its turbulence content.

2. The region on the upwind face where stagnation occurs and the horseshoe vortex

develops.

3. The flow around the sides of the prism where the flow separates and may reattach.

4. The recirculation region over the roof formed as a result of the flow separation at the leading edge of the prism. The flow on the roof may reattach before shedding vorticity in the wake of the prism.

5. The wake of the prism where a large vortex, called the portal vortex, develops and shed vortices are convected downstream.

As pointed by Murakami and Ilzuka [38] and Lübcke et al [52], several complex flow phenomena are associated with the different regions of the flow field as described above. These flow phenomena include streamline curvatures, the separating shear layer at the windward edge of the body, flow recirculation and formation of large unsteady vortical structures which shed in the wake of the body. Such a combination of complex and three-dimensional flow structures presents many difficulties when analyzing the flow around surface-mounted structures by either numerical or experimental investigations. Moreover, unsteady large-scale vortices, formed by the roll-up of separating free shear layers, are the dominant characteristics of turbulent flows over surface-mounted prisms. These vortical structures interact with each other and with the body surface resulting in secondary separations and excessive pressure fluctuations. The interaction of the large-scale vortices with the different turbulence scales in the incoming flow exacerbates their unsteady motion.

1.2 Effects of Incident Flow Characteristics

It is well known that boundary layers undergo transition to turbulence earlier due to enhanced turbulence in the free stream. Bearman and Morel [3], and Castro and Haque [7] showed that free stream turbulence enhances the shear-layer entrainment rates, reduces the distance to reattachment and modifies the relatively low-frequency "flapping" motion of the shear layer. Thus, one would expect the separating shear layer on the roof of a surface-

mounted prism to be significantly affected by the free stream turbulence. The separation zone on the upwind face forms due to flow stagnation at a point on this face and the redirection of the flow in a horizontal plane that contains this point. The flow above this plane moves over the roof of the prism and the flow below this plane moves around the edges forming a horseshoe vortex. The significance of the free stream turbulence on the separation zone on the upwind face needs to be examined from different perspectives. In one perspective, the boundary layer in the approaching flow and its role in the formation of the horseshoe vortex are affected by the free stream turbulence. In another perspective, the unsteady and turbulent characteristics of the free stream may affect the division of the incoming flow into the part that goes over the prism and the other that goes around it. Nozawa and Tamura [40] state that the incoming turbulence stimulates the separated shear layer and usually reduces the drag force on a square cylinder. On the other hand, and in the case of a surface-mounted prism, large suction peaks on the roof of the prism have been associated with the enhanced turbulence in the free stream. Kareem, Surry and Djakovich (1995), cited in Saathoff and Melbourne [50], showed that high turbulence intensity causes early reattachment of separated shear layers and high frequency pressure fluctuations on the side surfaces. Consequently, it is important to properly characterize the effects of free stream turbulence on the flow characteristics over surface-mounted prisms.

Hillier and Cherry [17] state that the mechanisms of the interaction between free stream turbulence and separating shear layers are unclear. This statement has its own significance. For instance, in predicting extreme wind loads on structures, building codes usually relate the load to a mean wind speed without specific details about turbulence characteristics of the free stream. This question becomes more challenging when realizing that turbulence parameters in the mean flow cannot be varied independently. For instance, increasing the level of turbulence in the small scales is usually associated with a decrease in the integral length scale. Moreover, two turbulent flows could have the same turbulence intensities but significantly different integral length scales. These difficulties make it extremely hard to perform numerical or wind tunnel simulations of turbulent flows over surface-mounted prism.

Rao [46] made a rather comprehensive discussion of issues concerning the extrapolation of wind tunnel model results of non-aerospace structures to full scale. Wind tunnel flow characteristics, model dissimilarities, scaling laws and effects of amplitude of oscillation on aerodynamic forces were the main aspects considered. He emphasized that while some corrections, by proper scaling, can be made for some effects like Reynolds number, it is not possible to correct for all factors involved in this problem. Lübcke et al [52] state that the challenge to the numerical simulation is the accurate presentation of the interaction between the mean transient motion and the residual turbulence. These challenges are more specifically faced when using wind tunnel or numerical simulations to predict wind loads on low-rise structures. In full scale flows, the wind speed and wind gusts, the non-uniform topology of the earth around buildings and its neighboring buildings, and the roughness of the ground due to small scale and large scale objects around low-rise structures, affect the turbulence intensity and the type of turbulent structures convected with the flow upon reaching the structure. Besides, Richards, Fong and Hoxey [48] emphasized that the incident flow turbulence within the atmospheric surface layer is highly anisotropic.

The differing effects of different turbulence characteristics in the incident flow on peak pressure coefficients on surface-mounted prisms have been the subject of many investigations. Tieleman, Reinhold and Hajj [61] showed that there are two approaches for the simulation of wind loads on low-rise structures. The first approach adopts the mean velocity profile and the integral length scale as the inflow simulation parameters. The second approach concentrates on the simulation of the turbulence intensity profile. They emphasized that the simulation of the horizontal turbulence intensities and the small-scale turbulence at roof height proved more effective in predicting the peak suction pressures than the simulation of mean wind profile and the integral length scale. In addition, they indicated that simulating the inflow based on the mean velocity profile and the integral length scales is not essential for the prediction of peak wind loads on low-rise buildings. Hajj, Tieleman and Tian [15] stated that reproduction of the full-scale Reynolds number of the atmospheric flow over and around low-rise structures is impossible due to geometric limitations, power requirements and compressibility effect. This difficulty hinders the simulation of the range and levels of turbulence

scales contained in atmospheric surface layer which consequently affects the prediction of extreme wind loads on low-rise structures. By applying orthonormal wavelet analysis to velocity records from three different wind tunnel simulations, they pointed out that when the energy levels of small scales, specifically the intermittent events, are enhanced compared to those of large scales, the mean and peak pressure values are significantly affected on the roof of wall mounted obstacles. Tieleman, Hajj and Reinhold [63] reported that agreement between model and field measurements of pressure coefficients on the roof of low-rise structures are possibly attained by duplicating the two horizontal turbulence intensities and their small-scale turbulence content, and by making sure that the model turbulence integral scale exceeds the magnitude of the scaled-down field value. These results clearly show that free stream turbulence in the incident flow significantly affects the near region of the flow field as determined from pressure measurements.

1.3 Numerical Investigations

There are two common approaches to include turbulence in the incident flow when conducting numerical simulations to determine the effects of free stream turbulence on the flow over surface-mounted prisms. In the first approach, the interest is in the generation of a flow environment that is close to that of an approaching surface boundary layer to a low-rise structure. To this end, both boundary layer mean and turbulence characteristics are given attention. In the second approach, turbulence of known characteristics is superimposed on the mean flow at the inflow boundary of the domain. In this case only turbulence characteristics are given attention. The boundary layer profile is either approximated with a known model, such as the law of the wall, or is let to be developed by itself over the domain floor over a short distance upstream of the prism. Lund, Wu, and Squires [34] provide a detailed review of the methods used to generate inflow turbulence for numerical simulations.

Kim and Boysan [22] discussed some of challenging issues when performing CFD simulations of environmental flows including flows over structures. First, the computation of these flows requires knowledge of the characteristics of the atmospheric boundary layer. Both mean wind

velocity profile and atmospheric turbulence characteristics are needed. Second, the complex topologies involved in such problems make the discretization of the computational domain very challenging. Third, the wide range of turbulence scales and the three-dimensional aspects have their own requirements in terms of computational needs. Finally, choosing the right turbulence model is not straightforward.

Murakami [39] gives an extensive review of the different turbulence simulations techniques used in wind engineering, namely direct numerical simulation (DNS), large eddy simulation (LES), and Reynolds-averaged Navier Stokes (RANS) simulation. He points out to the following difficulties when performing these simulations

1. The large Reynolds number
2. The impinging of the flow on the front wall
3. The sharp edge of the bluff body
4. The remaining effect of the obstacle at the outflow boundary
5. The turbulent inflow simulation

Murakami and Ilzuka [38] emphasized that LES is the most suitable tool for analyzing bluff body aerodynamic problems. They compared LES results to RSM, k-epsilon predictions and experimental data for the flow over a square cylinder. LES was found to produce better results than other computational models, even when the standard Smagorinsky model is used to model the sub-grid scales. Furthermore, in their review, they indicated that the use of the dynamic sub-grid scale model (DS model) improves the accuracy of the numerical solution. In addition to that, they suggested employing a technique for stabilizing the computations with the DS model as it becomes unstable when applied in the flow region past the bluff body.

Nozawa and Tamura [40] used large eddy simulation to predict the flow around a surface-mounted prism. They employed turbulent inflow in the simulation on both smooth and rough mounting surfaces. A self-similar boundary layer of zero pressure gradient was assumed at the

inflow. The turbulence was generated by marching the numerical simulation over a smooth or rough mounting surfaces. They solved the incompressible Navier-Stokes equations using a second-order central difference scheme for the convective terms everywhere except near the windward edge of the prism where they used a third-order upwind scheme to avoid instability. The Crank-Nicolson method was employed to difference the diffusion terms. They used the dynamic Smagronisky procedure to model the sub-grid scales. They simulated flows at Re numbers, based on the momentum thickness and the free stream velocity, of 7×10^3, 3×10^4, and 4.2×10^6. Although they were able to predict the mean pressure coefficients on the surface of the prism, the solution underestimated the peak pressure near the windward edge. Using three different inflow with varying turbulence intensities, namely 8%,14%, and 26%, they were able to emphasize the effect of the turbulence intensities on the size of the separation region on the roof of the prism.

Tutar and Oguz [67] conducted large eddy simulation of flows over a single building and parallel buildings. They used the finite volume method to solve the non-linear conservation equations. A point implicit, Gauss-Sidel, linear equation solver together with multigrid method and a second-order implicit time integration scheme were employed in their simulation. The RNG, Renormalization Group theory, model for the sub-grid scale eddy viscosity was used in their investigation. For the single building model, a grid of $63 \times 49 \times 54$ points was used and Reynolds number based on the model height was 7×10^4. In their computations, they used the wall functions to model the inner wall region of the building walls. Although they emphasized that the RNG sub-grid scale model resulted in better agreement with experiments for a single building than other models they tested, it did not succeed well to predict the flow over two parallel buildings specially at the entrance of the passage between them.

1.4 Experimental Investigations

Becker et al [4] carried out an experiment to study the structure of the flow field around three-dimensional obstacles of different aspect ratios and at different angles of attack to one

side of the model. Wind tunnel flow visualizations and two component LDA measurements were performed. In these experiments, the incident flow simulated a neutral atmospheric boundary layer of a typical suburban site up to a height of about 100m in full scale. They used obstacles with different width/height ratios $(2.8 - 4.0)$. The flow visualizations were performed at a Re number of 2×10^6, while the LDA measurements were obtained at Re numbers that varied between 2×10^4 and 7×10^4. Based on these experiments, they noted that the horseshoe vortex that develops around the sides of the obstacle is not observed downstream the building. Instead, separation of the flow along the obstacle sides occurs and alternating vortices are shed from each side of the obstacle. Furthermore, the dominant frequency measured at the top of the obstacle is twice that measured on the sides. this implied that a vortex from the top of the obstacle shed with each one of the alternating vortices that shed from the sides. The non-dimensional shedding frequency, St number, is reported to be 0.155. It was found to be constant for Re numbers above 2×10^5.

Saathoff and Melbourne [50] conducted wind tunnel experiments to investigate the effects of free stream turbulence on the flow around a square cylinder. To generate inflow turbulence, they used three bi-planar wooden grids. The grids were made of bars with diameters of 70, 37, and 16 mm and with the ratio of mesh size to bar diameter set to be equal to 4. The mean flow Re number based on the model height was 4×10^4 . They ran experiments at low and moderate free stream turbulence intensity (up to 12%) as well as high turbulence intensity ($> 20\%$). For the low turbulence intensity inflow, they showed that the pressure fluctuations were attributed to the periodic vortex shedding. At the high inflow turbulence intensities, the pressure fluctuations occur over a broader range of frequencies; although the vortex shedding frequency is still significant. This was attributed to the intermittent reattachment of the separated shear layer.

Kim, Ji and Seong [27] used particle image velocimetry (PIV) to investigate the flow around a rectangular prism. They were able to generate a thick boundary layer in a long enough wind tunnel. To enhance the boundary layer turbulence, they used both spires and fetch of roughness chain upstream of their model. They obtained detailed velocity measurements at three vertical planes parallel to the mean flow over the model. The Reynolds number in

their study was 7900 based on the prism height.

Tamura and Miyagi [60] investigated the effect of turbulence on aerodynamic forces on a square cylinder with various corner shapes, namely sharp, chamfered and round. They carried out wind tunnel measurements of averaged and fluctuating statistics of lift and drag forces on a squared section cylinders with the above mentioned corner shapes. They found that the reattachment of the separated flow over the leading edge of the cylinder is promoted with the use of chamfered and rounded edges. They also observed that the fluctuations in the lift coefficient on the cylinder are higher in the turbulent inflow than in uniform inflow.

Hoxey et al [19] made both full scale and model scale measurements of surface pressure on low-rise pitched-roof building. They investigated the effects of Reynolds number on the development of the separating shear layer on the roof of low-rise structures. They also provided an explanation to such development by discussing the vortex dynamics in the separating shear layer on the building roof. They found that the separated flow at the windward edge of the building is Reynolds number dependent for the case of sharp eaves. On the other hand, it is not Reynolds number dependent for curved eaves since it essentially reattaches on the roof.

1.5 Objectives

This thesis aims at providing physical explanations of the effects of the free stream turbulence on the flow characteristics over a surface-mounted prism. Experimental and numerical investigations are conducted to achieve this objective. In the experimental studies, particle image velocimetry is performed in the ESM water tunnel to obtain detailed aspects of the flow over surface-mounted prism under two different free stream turbulence conditions. In one condition, the free stream turbulence is generated by a surface-roughness element that yields predominantly spanwise vorticity. In the second condition, the free stream turbulence is generated by a set of vertical cylinders placed upstream of the surface-mounted prism. These cylinders generate cross-stream vortices that would be turned to form streamwise vortices

as the surface-mounted prism is encountered. The effects of these two different conditions on the mean flow parameters as well as on the instantaneous flow field are detailed.

In the numerical studies, large eddy simulation of the flow field over the surface-mounted prism under smooth and turbulent incident flows are performed. In the smooth case, no turbulence is present in the incident flow. In the turbulent case, homogeneous turbulence is introduced at the inflow boundary. The validation of the numerical code and implemented schemes is presented in this thesis. The mean flow parameters under the two inflow conditions are compared. It is to be noted here that smooth flow conditions could not be obtained in the ESM water tunnel. On the other hand, accurate simulation of the experimental conditions numerically is not possible because of the lack of detailed inflow conditions. Thus, a direct quantitative comparison between the numerical and experimental results is not performed. Rather, the effects of free stream turbulence, as determined from the numerical and experimental results are compared on a physical basis.

Chapter 2

Experimental Setup

2.1 Water Tunnel and Configurations Geometry

The experiments are conducted in the water tunnel facility of the Department of Engineering Science and Mechanics at Virginia Tech. The tunnel operates in a closed loop with up to 2500 gallons of water. Downstream of the settling chamber, a three-way convergence leads to the 0.6m × 0.6 m × 1.8 m test section. A 4500 GPM axial flow pump drives the flow at speeds up to 1 m/s with turbulence levels of less than 1%.

In this work, the effects of the turbulence level in the incident flow on the characteristics of the flow field around a surface mounted prism are investigated. Velocity measurements are obtained for the flow around a prism of dimensions 87 $mm(L) \times 57.8\ mm(W) \times 25.4\ mm(H)$ mounted to the floor of the water tunnel. The long side of the prism is set parallel to the mean flow. The prism is cut from a 0.025 m thick clear plexiglass sheet and the sides were machined to assure smooth surfaces as well as sharp model edges. A mounting plate made of clear plexiglass is used to hold the model to the tunnel floor. The plate is 1.22 m long and 0.61 m wide and 6.35 mm thick. Two counter-sunk screws are used to fix the prism to the mounting plate. The leading edge of the mounting plate, placed at the entrance of the test section, is chamfered to reduce boundary layer separation. The model is mounted at about 0.91 m downstream from the leading edge of the ground plate.

Two cases of different incident flow characteristics are considered. In the first case, turbulence is enhanced by installing a floor roughness element at the leading edge of the ground plate. This element consists of a wedge-like strip with a right triangular cross-section. The long side of the right angle of the triangular cross section is 0.1 m long and is placed facing the ground plate. The other side of the right angle is about 0.01 m long and is positioned facing the tunnel stream. This configuration allows us to achieve high-turbulence incident flow with dominant spanwise vorticity. In the second case, the flow is disturbed by installing rows of vertical cylinders upstream of the ground plate. The cylinders are cut from wooden rods. Seven cylinders with a 12.7 mm diameter are mounted evenly near the leading edge of the mounting plate. These cylinders are staggered in two rows; the first row is placed 0.05 m after the leading edge, while the second is placed behind the first one by 0.075 m. The lateral distance between two of the 12.7 mm cylinders is 150 mm. Sixteen other smaller size cylinders that are 8 mm in diameter are mounted evenly 0.04 m downstream of the second row of the large size cylinders. The configurations of both cases I and II are presented in figures 2.1 and 2.2, respectively.

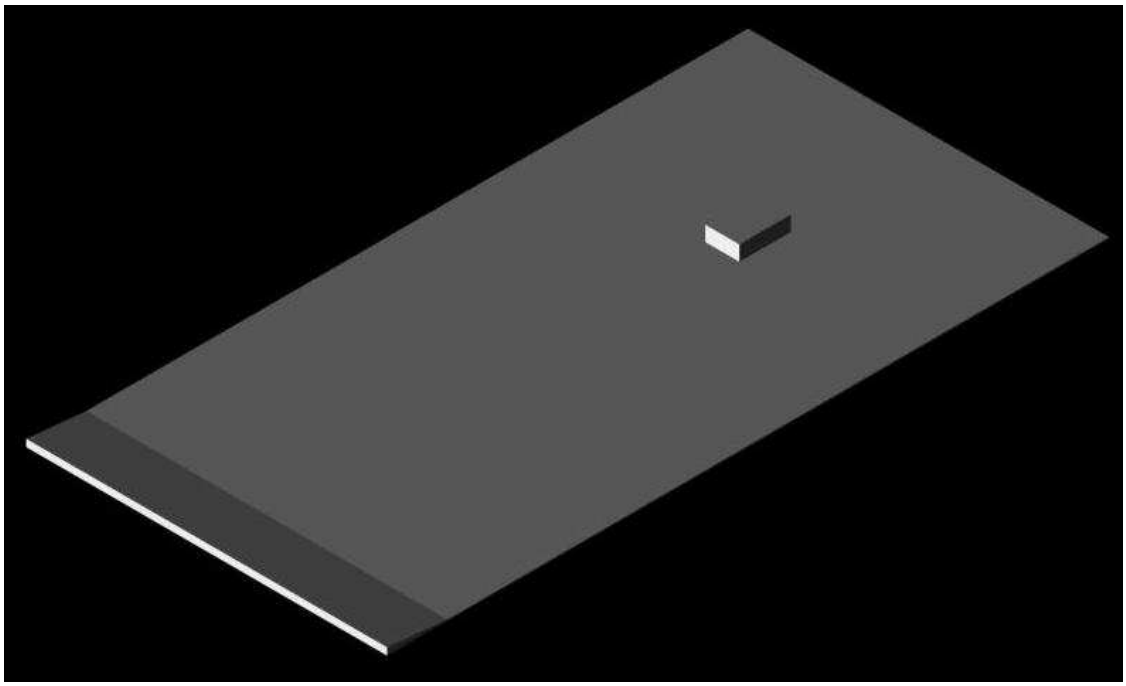

Figure 2.1: Schematic of the model mounted to the ground plate in case I configuration

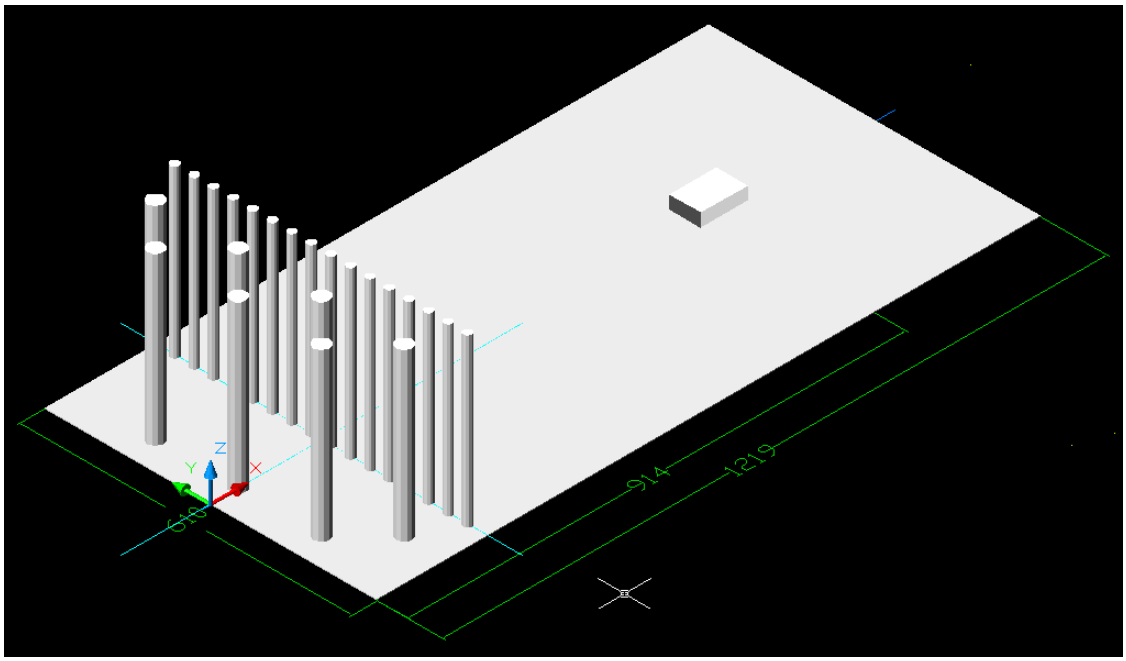

Figure 2.2: Schematic of the model mounted to the ground plate in case II configuration

2.2 PIV System

The digital particle image velocimetry (DPIV) techinque is used to measure mean and instantaneous flow field characteristics over the prism. The particle image velocimetry system included a $46 - Watt$ copper vapor pulsing laser used to illuminate the interrogation plane of the flow field. During the course of the experiments performed in this work, the peak power of the laser is found to be around 31 Watts at $10,000$ pulses per second. Using a set of sheet-forming optics, a laser sheet that is 0.003 m thick and up to 0.08 m wide is delivered to the test section. The laser sheet is delivered from below the test section in the vertical plane. A cylindrical lens is used to fold up the circular cross-section laser light beam into a sheet of laser light. Since the light sheet is folded from a circular cross-section beam, the light intensity is very low near the edges of the laser sheet. The formed laser light sheet is oriented parallel to the mean flow by adjusting the azimuthal angle of cylindrical lens with respect to the laser beam axis.

Images were acquired with a digital CMOS camera (Phantom 4.0) placed such that its optical axis is normal to the plane of interest. The camera is capable of recording 8-bit gray scale images up to 2040 frames at frame resolution of 512×512 pixels. This is the frame resolution mostly used during the experiment. The camera's sampling rate is as high as $10,000$ frames per second. The camera is capable of acquiring and storing up to a half gegabyte of data. A computer-controlled traversing system was employed. This traversing system has a main traversing scale that provides for the necessary movement parallel to the test section. In the current experiment, three scales were primarily used. In addition to the main scale, two more scales are used to move the camera normal to the field of view and another scale is used to move the camera vertically. There are two main timing modes of PIV measurements: the double-pulsed frame mode, and the continuous mode. In the double pulsed frame mode, pairs of images with very short time separations yet at low time resolution are acquired. In the continuous mode, continuous acquisition of images takes place at a fixed time separation between each two frames. This time separation is the reciprocal of the frame rate. In our experiment, the continuous mode was employed. To be able to take images of the flow field,

the flow has to be seeded with tracer particles. Particles of average size of 50 microns were used in these experiments.

Standard double frame cross correlation was performed to obtain the velocity field from a pair of consecutive images. A multi-pass, multi-grid with image shifting processing algorithm on a 61×61 final grid was employed. The pixel sizes of the acquired images ranged from 150 to 166 micron per pixel.

2.3 Mean Flow Characteristics at the Measuring Location Without the Model

In both cases I and II, the mean tunnel velocity was calibrated versus the tunnel pump drive-motor frequency. This allowed us to run the tunnel at almost the same mean freestream velocity. In the first case, the mean freestream velocity in the tunnel is 0.46 m/s, and in the second case, the mean freestream velocity is 0.44 m/s. Profiles of the mean and turbulence flow characteristics were measured at the model location without the model in place. Frames of 128×512 pixels were acquired over a period of eight seconds at a rate of 1000 fps.

Figure 2.3 shows the boundary layer velocity profiles for the x and z velocity components, U and W. The velocities are normalized with the mean velocity measured at the prism height, U_o. The Reynolds number calculated based on the prism height and the freestream velocity at the prism height is approximately 9600 in both cases I and II. A comparison of the normalized velocity profiles shows that the $U-$component in case II has the characteristics of a turbulent boundary layer with a thickness that is about 1.5 times the prism height. In case I, the $U-$ component is smaller over the range z/L between 0.0 and 1.0 and larger for z/L values above 1.6. This yields a higher displacement thickness for the profile of case I. The boundary layer displacement thicknesses are estimated to be 0.26 and 0.155 of the prism height in cases I and II, respectively. The Reynolds numbers based on the boundary layer displacment thisckness and the free stream velocity at the prism height are $2,585$ and $1,535$ for both cases I and II, respectively.

Figure 2.4 shows the distribution of the normalized U_{rms} and W_{rms} in the boundary layer at the model location without the model. The velocity fluctuations U_{rms} at the prism height reaches a maximum value of $0.1U_o$ in case I near $z/L = 0.85$. Additionally, the flow field around the prism height in case I is characterized by high-level of turbulence fluctuations that spread almost uniformly between $z/L = 0.6$ to $z/L = 1.15$. On the other hand, in case II, the highest level of velocity fluctuations reaches a sharp peak of $0.11U_o$ near $z/L = 0.4$. These fluctuations fall down to $0.06U_o$ at the prism height and keep decreasing. Span-wise normalized mean vorticity distributions in the boundary layer at the model location without the model are shown in figure 2.5. Obviously, the incident flow in case I has a higher level of span-wise vorticity between $z/L = 0.4$ and 1.0 and a smaller level between $z/L = 0.2$ and 0.4.

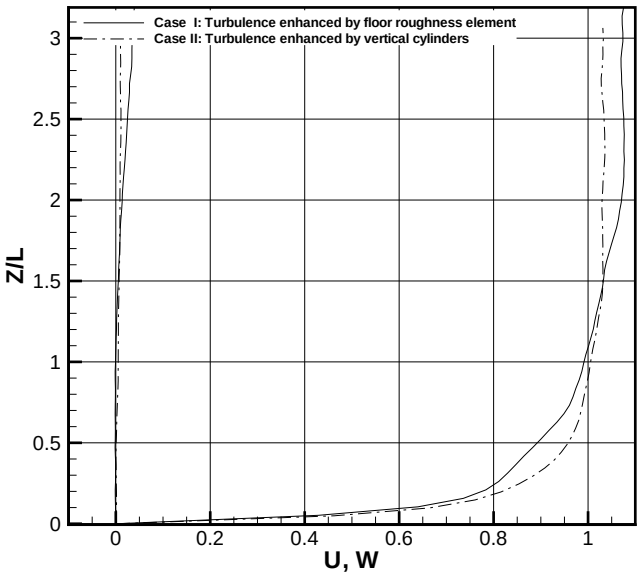

Figure 2.3: Normalized mean velocity profiles U/U_o and W/Uo for case I and case II

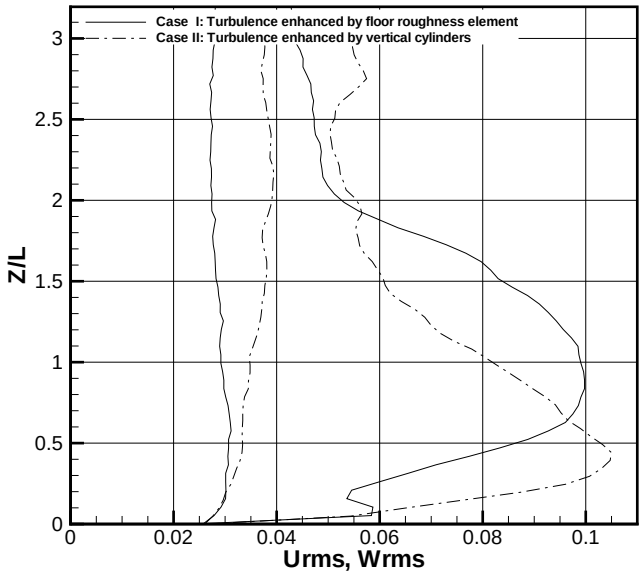

Figure 2.4: Normalized mean velocity fluctuations U_{rms} and W_{rms} for case I and case II

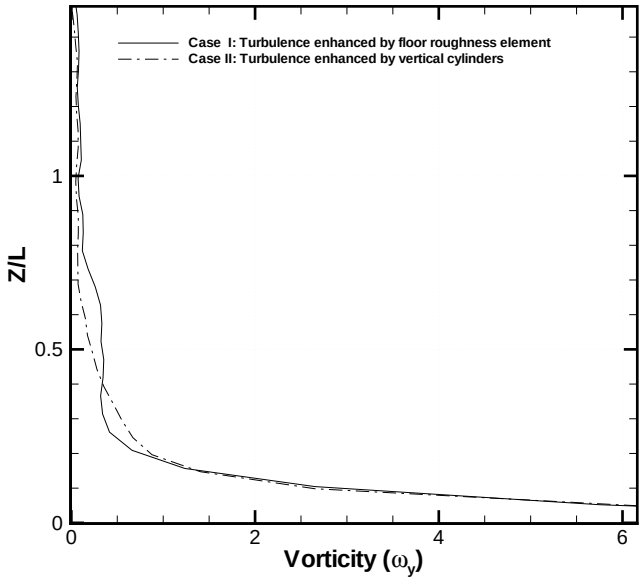

Figure 2.5: Normalized mean vorticity profiles Ω_y for case I and case II

Chapter 3

Experimental Results

In this chapter, the results of particle image velocimetry (PIV) measurements of the flow over a surface-mounted prism under two different incident flow conditions are presented. These results include mean flow characteristics such as the streamline patterns, mean velocity components, mean vorticity, as well as mean turbulence quantities, i.e. the Reynolds normal and shear stresses and turbulence kinetic energy. These parameters are compared for both flow conditions. The results also include a description of the interaction between the flow structures in the near field and the solid surface of the prism as observed in a sequence of events. Three measurement planes are used to investigate the flow field over the three-dimensional prism. The planes are parallel to the flow direction and are located at the center plane, quarter plane and near the edge of the prism. In all plots presented in this chapter, the coordinates are non-dimensionalized with the height of the prism. All measured quantities are normalized by using the height of the prism as the length scale and the free stream velocity as the velocity scale. Figure 3.1 shows a top view schematic of the prism showing projections of the three planes of interrogation on the ground and the free stream direction.

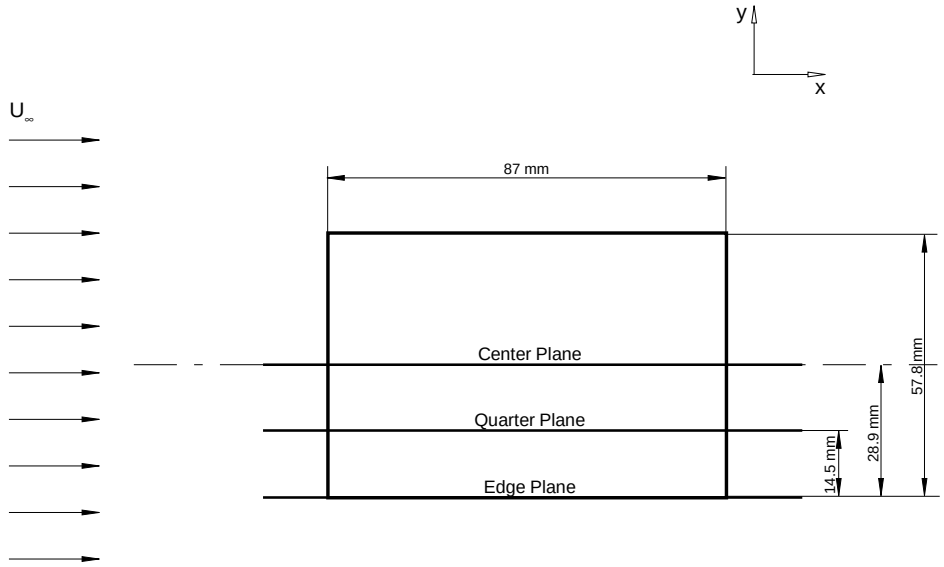

Figure 3.1: Top view of the prism with long side parallel to the mean flow showing projections of the three planes of interrogation on the ground

3.1 Mean Flow Field

The mean flow results of the flow over a surface-mounted prism are presented in this section. Two sets of averaged data are presented in the following discussion for each of cases I and II. The difference between the two sets is the size of the interrogation plane and the record duration. Both of these parameters were constrained by the storage capacity of the digital camera. In the first set, data were obtained over eight-seconds. The interrogation plane is a rectangular strip of dimensions 0.75×3.2 prism height. In the second set, data were obtained over a two-second period with the frame domain covering an area that is about three times as large as the area covered in the first set. It should be noted that the eight-second data sets of the flow just above the roof of the prism are only limited to the center plane. The

two-second scheme is followed to acquire data at the center plane, the quarter plane and and the edge plane for both cases I and II.

As an example of the physical quantites derived in this chapter, we present in figure 3.2 the mean vorticity distribution above the roof surface in the center plane averaged over eight seconds. Along with this distribution, we present lines of zero-U velocity component, maximum vorticity, and where the rate of strain is $0.5U/L$, where U is the freestream velocity at the prism height and L is the prism height. The maximm vorticity ($\Omega_y = \frac{\partial U}{\partial z} - \frac{\partial W}{\partial x}$) line is used to identify the core of the shear layer that separates from the leading edge. It matches with the line of maximum strain ($\gamma_{xz} = \frac{\partial U}{\partial z} + \frac{\partial W}{\partial x}$). It is expected that the line of maximum root mean square (RMS) fluctuations to match with these lines. Along the line where $\gamma_{xz} = 0.5U/L$, the mean vorticity has a very small values. Consequently, it is used to define the outer edge of the shear layer. The line of zero-U velocity represents the sepration line that emobdies the region of the flow reversal. Outside this region, the time-averaged flow moves in the same direction as the mean flow. Consequently, the zero-U line defines the flow reversal line. The point of intersection of the zero-U line and the solid wall will be referred to as the reattachment point.

It should be noted that the flow over the roof of the prism is characterized by two separation regions. The primary separation region starts with the main flow separation at the leading edge and reattaches further downstream. The secondary separation region is embodied within the primary region near the leading edge. As such, one should expect two lines where the $U-$velocity components has a zero value. It is important to note that the velocity magnitudes under the shear layer near the leading edge are very small. The resolution of the interrogation window is relatively large in comparison with the size of the secondary separation. Consequently, this separation region cannot be resolved. While the region of secondary separation may not be clearly identified, a point where the secondary separation starts might be identifiable from the zero-U velocity component. This point is identified by the intersection of the zero-U line and the solid surface right downstream of the leading edge.

Figures 3.3.a and 3.3.b show a comparison of the streamline patterns at the center plane on top of the surface-mounted prism under the two cases of incident turbulence averaged

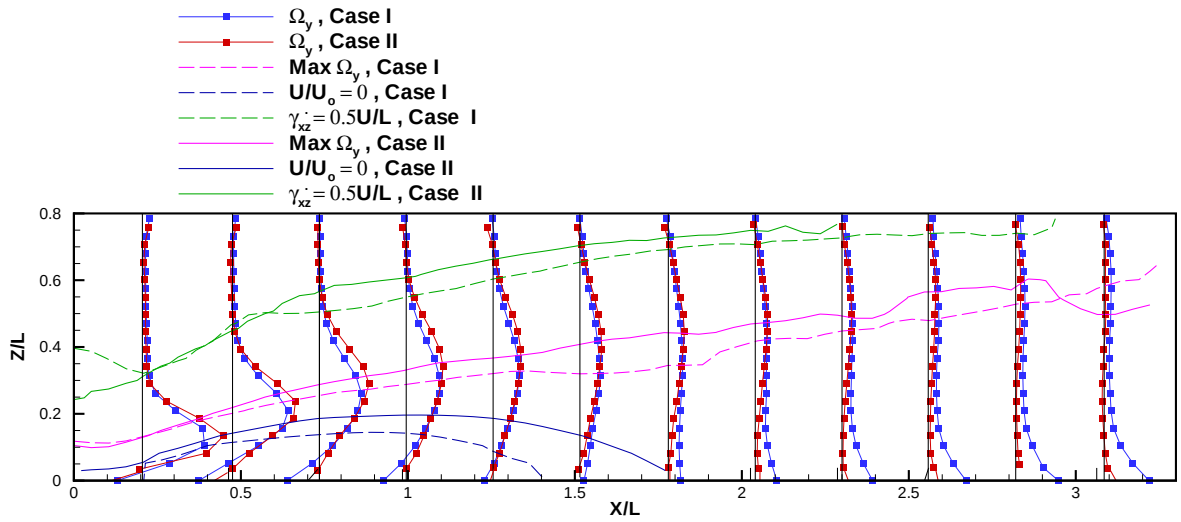

Figure 3.2: Distribution of normalized vorticity, Ω_y, for both case I and case II on the roof at the center plane averaged over 8 seconds

over eight seconds or eight thousand frames. In both cases, the separating flow over the top reattaches to the roof and forms a recirculation zone. In case I, where the turbulence was introduced with a floor roughness element, the mean flow reattachment point of the primary separation is near $x/L = 1.35$. The location of the reattachment point in case II, where turbulence was introduced by the vertically placed cylinders is near $x/L = 1.75$. Moreover, the location of the core of the recirculation zone in case I is given by the coordinates $x/L = 0.6$ and $z/L = 0.1$. In case II, this location is moved further downstream to $x/L = 0.8$ and slightly higher to $z/L = 0.15$.

Figures 3.4.a and 3.4.b show a wider region of the mean streamline patterns at the center plane over the surface-mounted prism in both cases I and II averaged over 2000 frames of the flow field. The wider region shows the recirculation zone near the upwind face in addition to the one on the roof of the prism. Both figures show the separation of the approaching flow into two parts divided by the stagnation streamline. The flow below the stagnation streamline forms a recirculation zone on the upwind face. This zone includes the horseshoe vortex that forms in front of the prism. The center of this vortex in both cases is given by the coordinates $x/L = -0.35$ and $z/L = 0.2$. The flow above the stagnation streamline is separated at the leading edge of the roof and reattaches to the roof further downstream. The red line in

both figures is the line of zero$-U$. Based on these lines, the location of the reattachment and the center of the recirculation zone are very close to the locations determined from the average over 8000 frames presented in figures 3.3.a and 3.3.b. Additionally, the location of the zero$-U$ line and the solid surface near the leading edge marks the location of the secondary separation. In both figures 3.4.a and 3.4.b, the stagnation streamline ends near $z/L = 0.7$.

Figures 3.4.c and 3.4.d show the mean streamline patterns at the quarter plane over the surface-mounted prism in both cases I and II. In comparison with figures 3.4.a and 3.4.b, the reattachment locations on the roof in case I moved slightly downstream to near $x/L = 1.55$. In case II, the reattachment location moved upstream to $x/L = 1.3$. The center of the recirculation zone in case I also moved further downstream to $x/L = 0.85$. In case II, this center moved from $x/L = 0.8$ to $x/L = 0.65$. On the other hand, the vertical location of the centers is nearly the same as the one observed in figures 3.4.a and 3.4.c. As for the recirculation zone near the bottom part of the upwind face of the prism, a comparison of figures 3.4.a and 3.4.c and figures 3.4.b and 3.4.d shows that the location of the centers are nearly the same at both the center and the quarter planes. The intersections of the zero$-U$ lines also mark the approximate location of the secondary separation near the leading edge and the reattachment further downstream. The stagnation streamline ends also near $z/L = 0.7$ in both the center and the quarter planes and for both cases. In summary, a comparison of the reattachment and stagnation points and of the locations of the centers of the recirculation zones on the roof and upwind surfaces of the prism do not show appreciable differences in their locations except for the reattachment points on the roof of the prism.

Figures 3.4.e and 3.4.f show a comparison of the mean streamline patterns near the side edge of the prism. The results show that, in both cases, the size of the recirculation region in the $x - z$ plane decreases significantly. On the other hand, the recirculation zone in both cases on the upwind face remains strong. The stagnation line ends near $z/L = 0.7$ on the upwind face in both cases, which is close to the locations observed at the other planes. The center of the recirculation zone on the upwind faces move closer to the floor surface and to the upwind face. In case I, the coordinates of the center of the recirculation zone on the upwind

face is near $x/L = -0.28.$ and $z/L = 0.12$. In case II, this location is near $x/L = -0.25$ and $z/L = 0.1$. Of interest to note also is the zero$-W$ line in case II that is closer to the solid surface. This line implies that the flow moves over the prism over this region.

Figures 3.5.a and 3.5.b show three-dimensional views of the mean streamline patterns in both flow cases I and II. The plots show the stagnation and reattachment points as well as the recirculation zones on the upwind face and on the roof of the prism. The results clearly show the horseshoe vortex that forms in front of the prism and the separation vortex on the roof. It is clear that the separation vortex on the roof changes direction and weakens near the edge of the prism. Thus, it is not observable in the $xz-$ plane of measurement near the edge. On the other hand, the horseshoe vortex maintains its form near the edge.

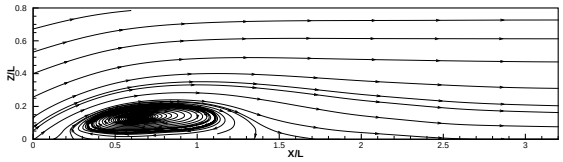

Figure 3.3.a: Streamlines pattern on the roof at the center plane averaged over 8 seconds. Case I

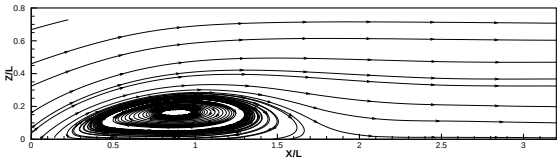

Figure 3.3.b: Streamlines pattern on the roof at the center plane averaged over 8 seconds. Case II

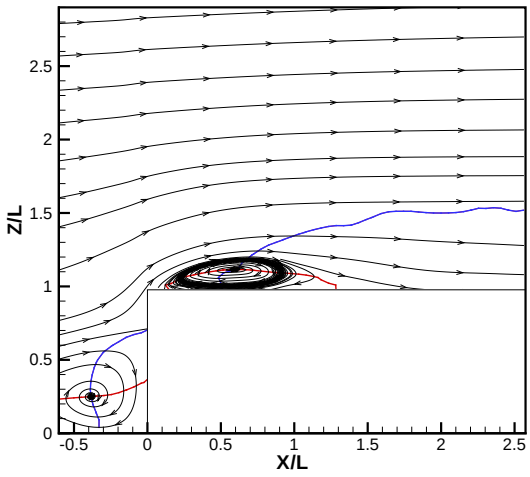

Figure 3.4.a: Streamlines pattern at the center plane averaged over 2 seconds. The red and blue lines mark the zero$-U$ amd zero$-W$ lines respectively. Case I

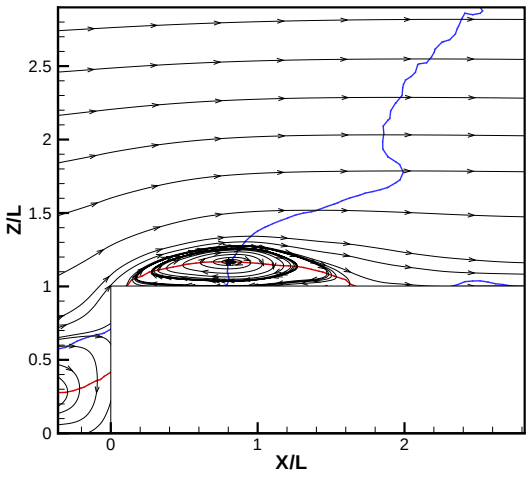

Figure 3.4.b: Streamlines pattern the center plane averaged over 2 seconds. The red and blue lines mark the zero$-U$ amd zero$-W$ lines respectively. Case II

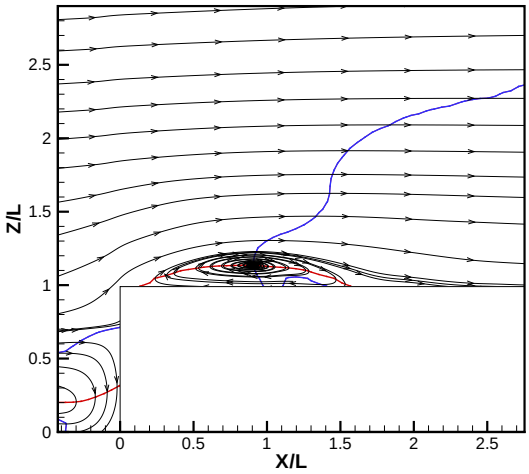

Figure 3.4.c: Streamlines pattern at the quarter plane averaged over 2 seconds. The red and blue lines mark the zero$-U$ amd zero$-W$ lines respectively. Case I

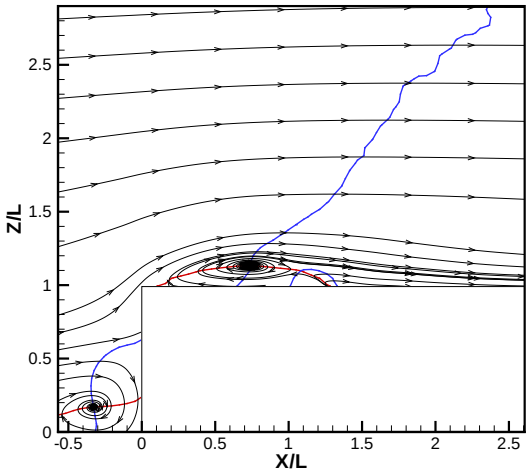

Figure 3.4.d: Streamlines pattern at the quarter plane averaged over 2 seconds. The red and blue lines mark the zero$-U$ amd zero$-W$ lines respectively. Case II

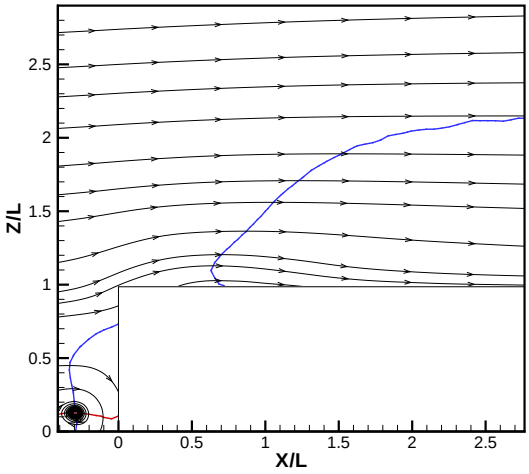

Figure 3.4.e: Streamlines pattern at the edge averaged over 2 seconds. The red and blue lines mark the zero$-U$ amd zero$-W$ lines respectively. Case I

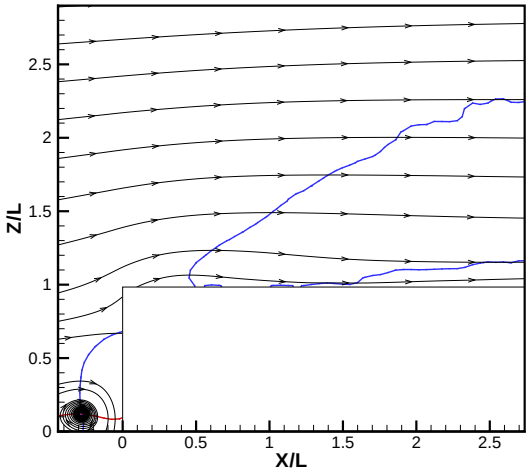

Figure 3.4.f: Streamlines pattern at the edge plane averaged over 2 seconds. The red and blue lines mark the zero$-U$ amd zero$-W$ lines respectively. Case II

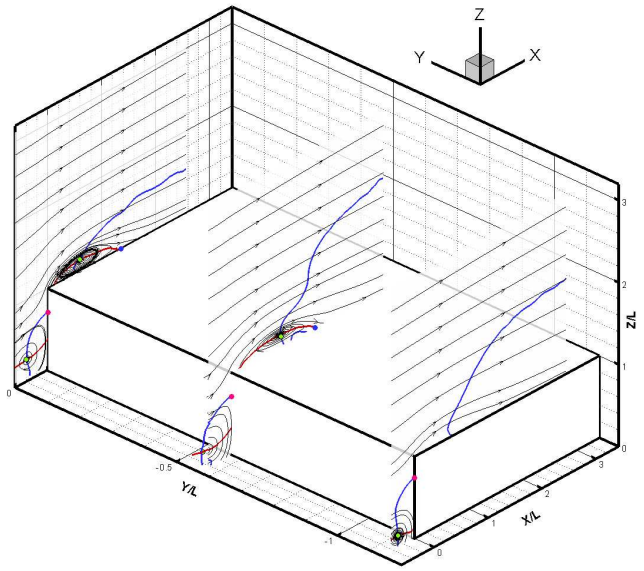

Figure 3.5.a: Streamlines pattern at the center, quarter and edge planes averaged over 2 seconds. Case I

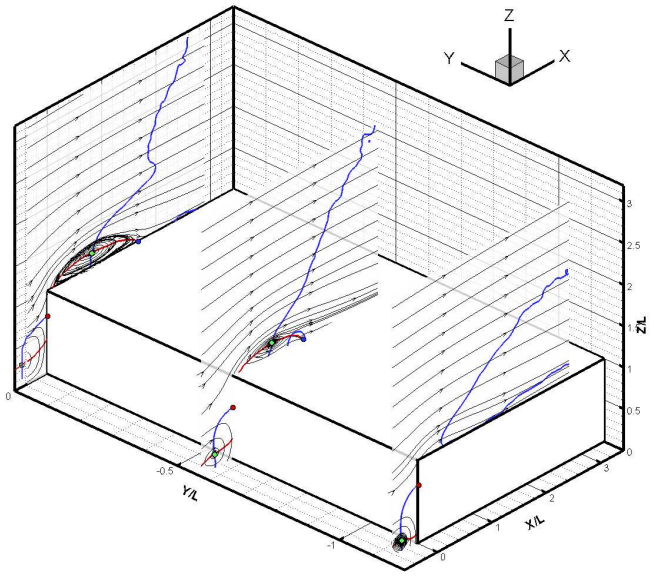

Figure 3.5.b: Streamlines pattern at the center, quarter and edge planes averaged over 2 seconds. Case II

The mean streamline patterns and discussions presented above give a qualitative description of the flow field. In the next set of figures, measurements of the mean velocity components U and W, the span-wise vorticity Ω_y, the turbulence kinetic energy and the $\overline{u'w'}$ component of the Reynolds stresses near the center plane, the quarter plane and the edge are presented to give quantitative values and comparisons of the two incident flow cases.

Figures 3.6.a and 3.6.b show a comparison of the normalized streamwise mean velocity component U. The secondary separation location is approximated by the intersection of the zero$-U$ line and the solid surface near the leaading edge. The reattachment point, further downstream, is determined as the point on the roof where U is zero. Obviously, the results show that turbulence generated by the floor roughness element (case I) causes earlier reattachment than turbulence generated by vertical cylinders (case II). The results also show that the mean reverse flow in case I has a maximum level of $-0.2U_o$ where U_o is the mean velocity of the free stream. In comparison, this value is $-0.3U_o$ in case II. A more detailed comparison is presented in figure 3.6.c which shows the vertical variations in the $U-$velocity component at the center plane in cases I and II. The blue dashed and solid lines show the zero-value contours for the $U-$ component and the reattachment locations on the roof. A comparison of the two lines shows the earlier reattachment of the flow in case I. A comparison of the distributions over x/L between 0.5 and 1.0 shows that the negative velocity component in the separation region is weaker in case I than in case II. In both cases, the location of the location of the secondary separation is approximated to be near $x/L = 0.25$.

Figures 3.7.a to 3.7.f show comparisons of the $U-$velocity component in cases I and II at the center plane, the quarter plane and near the edge of the prism. The results show that the reattachment point in the quarter plane is pushed further downstream in case I from the point observed at the center plane. It is pushed further upstream in case II. Moreover, the levels of the $U-$component at both planes in the circulation zones on the upwind face and the roof are about the same as observed at the center plane. On the other hand, figures 3.7.e and 3.7.f show that the negative velocity regime on the roof does not exist near the edge in comparison with the other planes. Additionally, the region of negative velocity on the

upwind face is reduced to a small area near the floor in comparison with the regions observed at the center and quarter planes.

A three-dimensional comparison of the $U-$component at the three planes is presented in figures 3.8.a and 3.8.b. The plots show the separation regions, reattachment and stagnation points as well as lines of zero U and W velocity components. The lines of zero $U-$ and $W-$velocity components are also plotted in the planes of measurements. The results clearly show the separation zones on the roof and the upwind face of the prism. In both cases, the separation zone on the roof weakens significantly near the edge. On the other hand, the horseshoe vortex on the upwind face remains strong. The significance of the contour line of zero $W-$component will be discussed next.

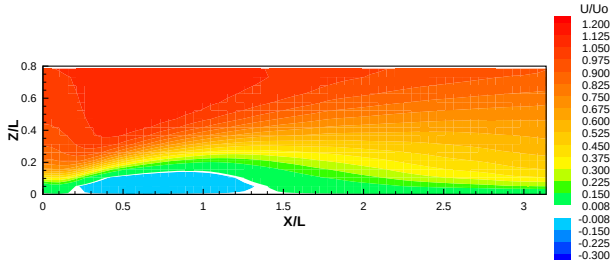

Figure 3.6.a: Contours of normalized streamwise velocity component, U/U_o, on the roof at the center plane averaged over 8 seconds. Case I

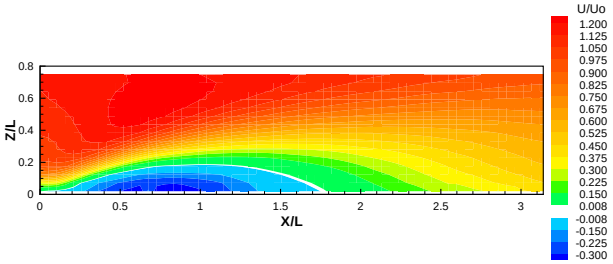

Figure 3.6.b: Contours of normalized streamwise velocity component, U/U_o, on the roof at the center plane averaged over 8 seconds. Case II

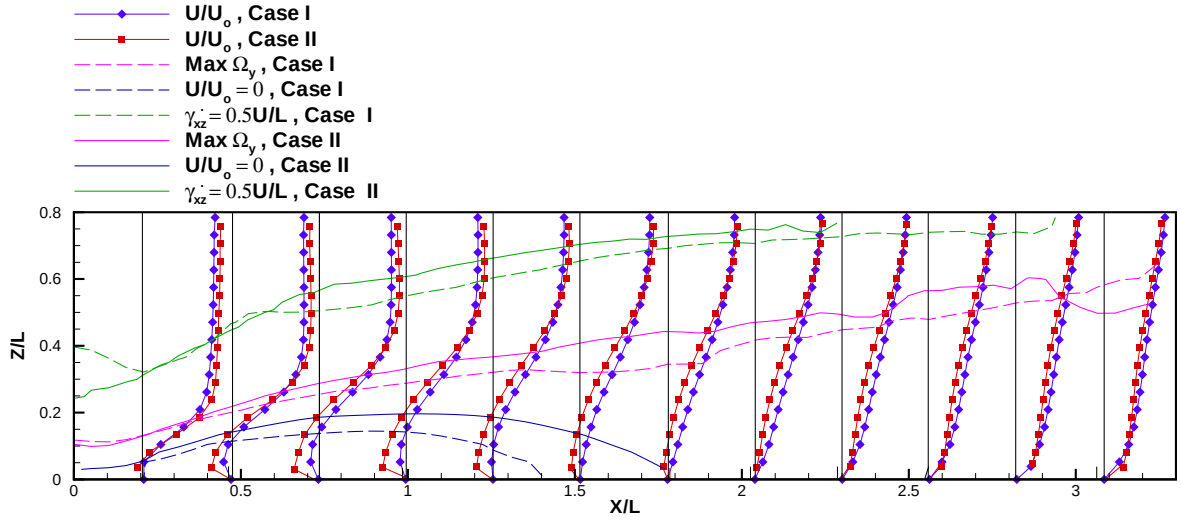

Figure 3.6.c: Distribution of normalized streamwise velocity component, U/U_o, for both case I and case II on the roof at the center plane averaged over 8 seconds

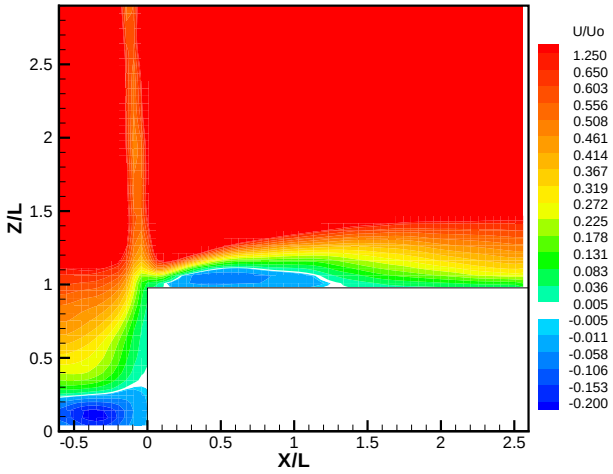

Figure 3.7.a: Contours of normalized streamwise velocity component, U/U_o, at the center plane averaged over 2 seconds. Case I

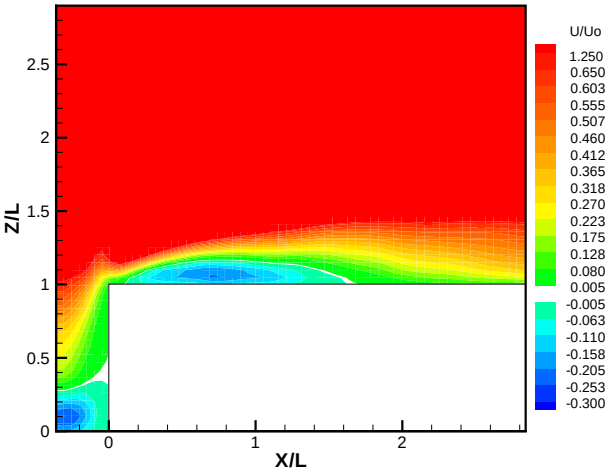

Figure 3.7.b: Contours of normalized streamwise velocity component, U/U_o, at the center plane averaged over 2 seconds. Case II

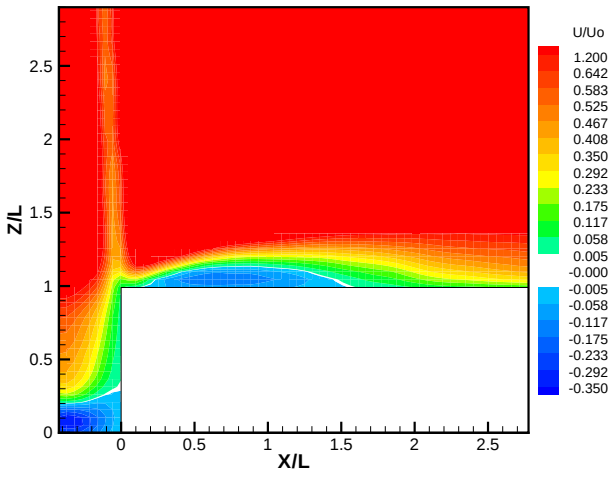

Figure 3.7.c: Contours of normalized streamwise velocity component, U/U_o, at the quarter plane averaged over 2 seconds. Case I

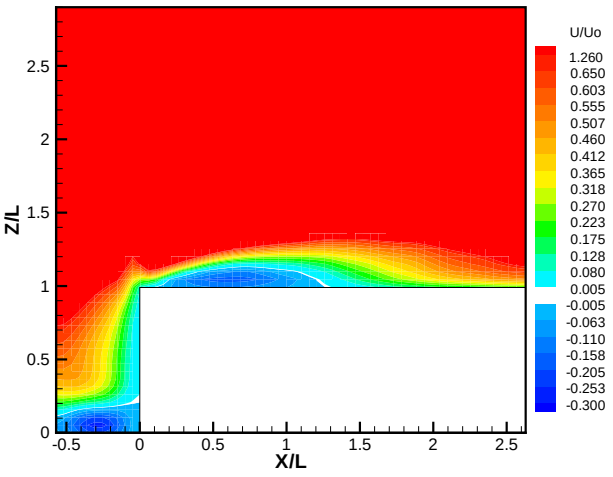

Figure 3.7.d: Contours of normalized streamwise velocity component, U/U_o, at the quarter plane averaged over 2 seconds. Case II

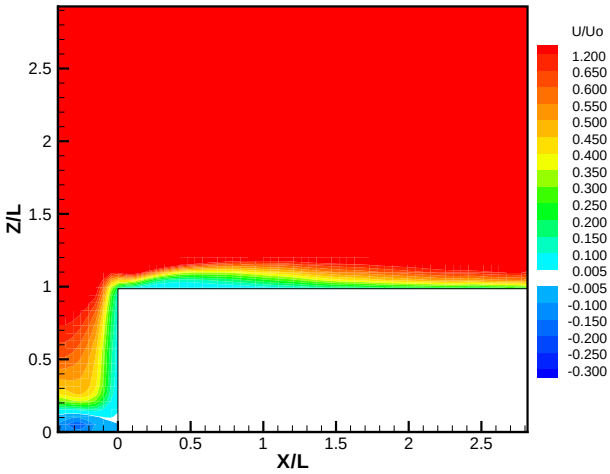

Figure 3.7.e: Contours of normalized streamwise velocity component, U/U_o, at the edge averaged over 2 seconds. Case I

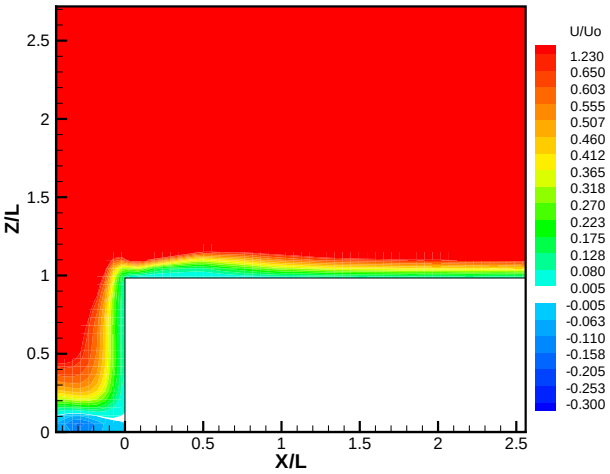

Figure 3.7.f: Contours of normalized streamwise velocity component, U/U_o, at the edge averaged over 2 seconds. Case II

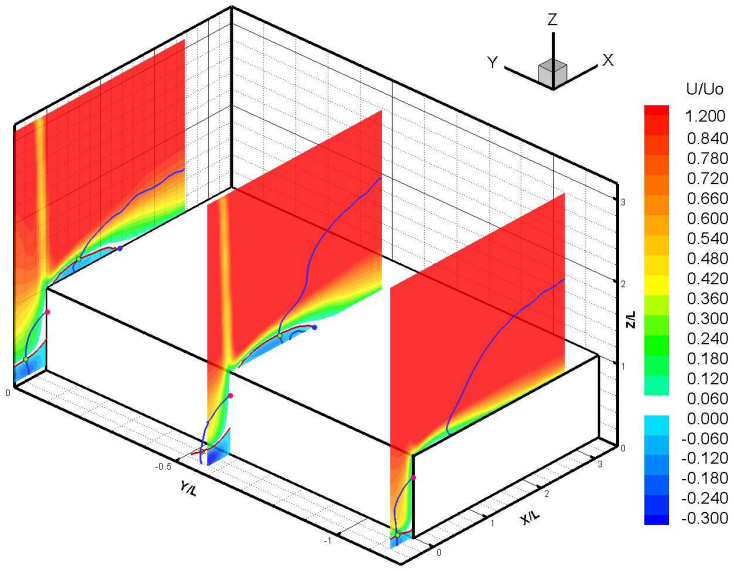

Figure 3.8.a: Contours of normalized streamwise velocity component, U/U_o, at the center, quarter and edge planes averaged over 2 seconds. Case I

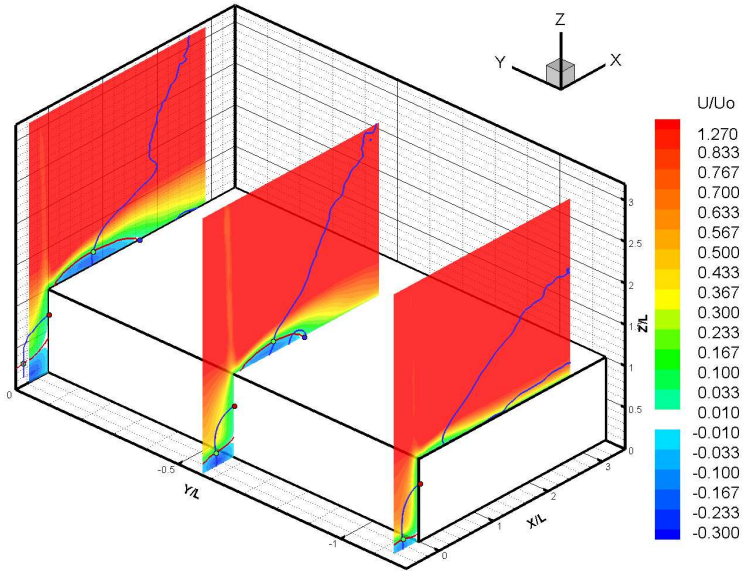

Figure 3.8.b: Contours of normalized streamwise velocity component, U/U_o, at the center, quarter and edge planes averaged over 2 seconds. Case II

Figures 3.9.a and 3.9.b show contour maps of the $W-$component of the mean velocity field averaged over eight seconds. Small values, in absolute sense, of this component are colored in white to separate the positive and negative components. Obviously, in terms of the $W-$component, the flow is separated into two regions. A region near the leading edge where the flow is pushed in the positive $z-$direction and another region further downstream where the flow curves towards the roof. The basic difference between the two cases in the fact that the zero$-W$ contour line starts near $x/L = 0.5$ on the roof and ends near $x/L = 1.5$ at the height z/L near 0.6 in case I. Additionally, the region bounded by $1.5 < x/L < 3.2$ and $z/L > 0.6$ has very low values of the $W-$ component. In comparison, the zero$-W$ contour line in case II starts near $x/L = 0.8$ which is further downstream when compared to case I. It extends up to $x/L = 2$ at the height $z/L = 0.75$. Moreover, the region of very low values is bounded by $x/L > 2.7$ and $z/L > 0.2$. These results show that the flow in case II is pushed further up in the $z-$direction than in case I as it encounters the prism and curves down at a slightly higher rate than in case I towards the roof. This conclusion is further strengthened by the comparison of the distribution of $W-$component over the roof of the prism in both cases I and II which is presented in figure 3.9.c. The results clearly show that up to $x/L = 1.0$, the flow in case II has a larger $W-$component in the region above $z/L = 0.2$. This is consistent with the larger region of flow separation observed in case II as determined from the zero$-U$ contour lines that are presented in figure 3.9.c. A comparison of the two distributions in the region $x/L > 2$ shows that while the $W-$ component is almost zero for $z/L = 0.35$ in case I, it maintains a negative value in case II. Again, this comparison is consistent with the fact that the reattachment point is further downstream in case II than in case I.

Figures 3.10.a-3.10.f show comparisons of the $W-$velocity component in cases I and II averaged over two seconds at the center plane, the quarter plane and near the edge of the prism. The plots in figures 3.10.a and 3.10.f are consistent with the plots presented in figures 3.9.a and 3.9.b in terms of the location of the zero $W-$component and the separation of positive and negative regions. At the quarter plane, figure 3.10.c shows that the zero $W-$component location on the roof is further downstream in comparison with figure 3.10.a (at the center plane). On the other hand, this location at the quarter plane is further upstream at the quar-

ter plane (figure 3.10.d) in comparison with the location at the center plane (figure 3.10.b). On the other hand, figures 3.10.c and 3.10.d show that the flow is pushed further upward near the upwind face of and has a higher negative $W-$component beyond the reattachment point. This is consistent with the conclusions made at the center plane. Figures 3.10.e and 3.10.f show contour maps of the $W-$component near the edge of the prism. The results show that the location of the zero$-W$ component on the roof is about the same in both cases and that the line of separation between the two regions is also about the same. The major observed difference is in case II which shows a second line of zero$-W$ value between $x/L = 1.5$ and the end of the measuring frame near $x/L = 2.5$. This line shows that the flow on the side of the prism has a slight positive W component in case II; a notion that is not clearly identified in case I.

Figures 3.11.a and 3.11.b show contour maps of the mean $w-$component with the three planes of measurements set in a three-dimensional domain of the flow field. Superimposed on the maps are the lines of zero U and W components. The results clearly show that the recirculation zones on the upwind face in both cases (horseshoe vortex) have similar characteristics. The stagnation point is located near $z/L = 0.7$ on all planes. The location of the center of the zone curves towards the upwind face near the edge of the prism. On the other hand, the separation zone on the roof shows different characteristics. In case I, it occupies a smaller region than in case II. The location of the center is closer to the roof at both the center and quarter planes. In both cases, the separation zone is not observed near the edge. Yet in case II, the flow has a positive cross-stream component in the reattachment region.

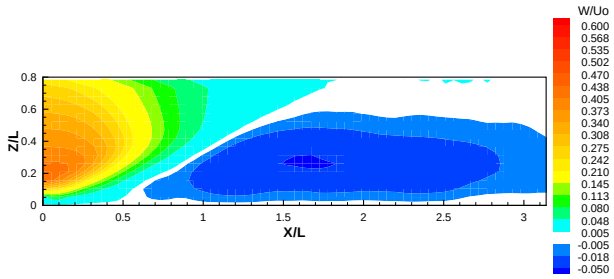

Figure 3.9.a: Contours of normalized cross-stream velocity component, W/U_o, on the roof at the center plane averaged over 8 seconds. Case I

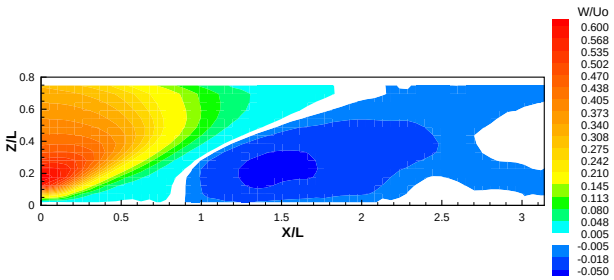

Figure 3.9.b: Contours of normalized cross-stream velocity component, W/U_o, on the roof at the center plane averaged over 8 seconds. Case II

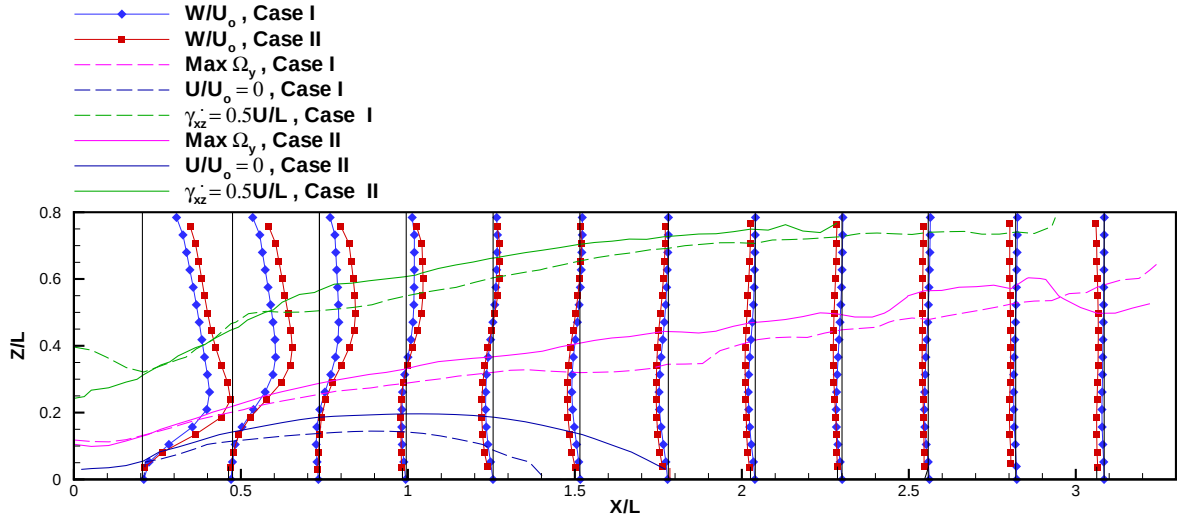

Figure 3.9.c: Distribution of normalized cross-stream velocity component, W/U_o, for both case I and case II on the roof at the center plane averaged over 8 seconds

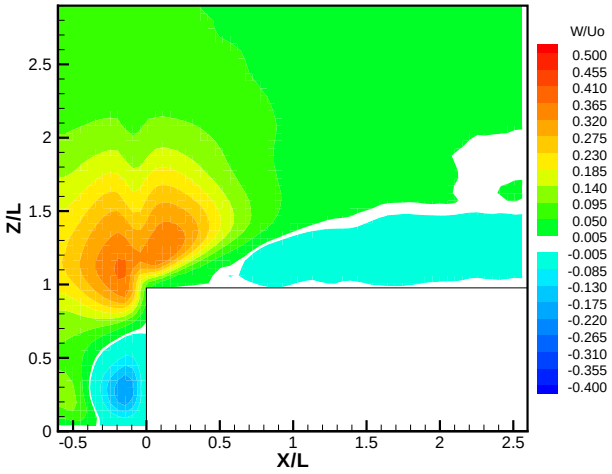

Figure 3.10.a: Contours of normalized cross-stream velocity component, W/U_o, at the center plane averaged over 2 seconds. Case I

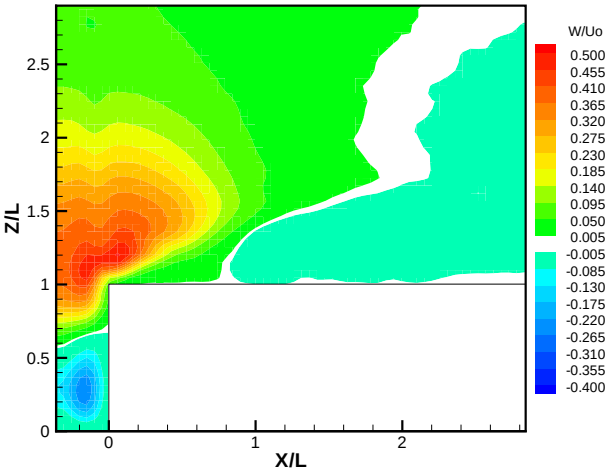

Figure 3.10.b: Contours of normalized cross-stream velocity component, W/U_o, at the center plane averaged over 2 seconds. Case II

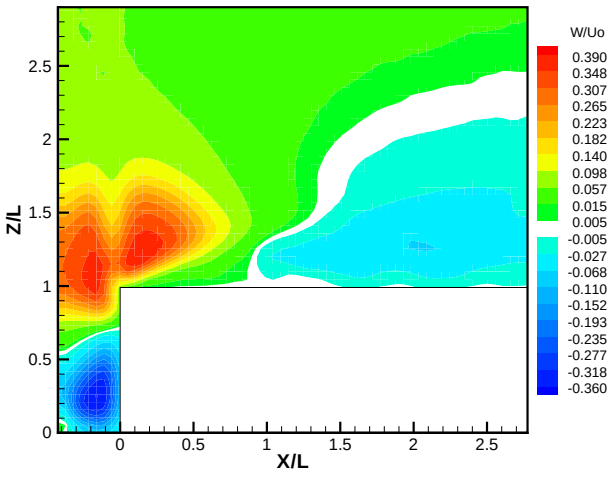

Figure 3.10.c: Contours of normalized cross-stream velocity component, W/U_o, at the quarter plane averaged over 2 seconds. Case I

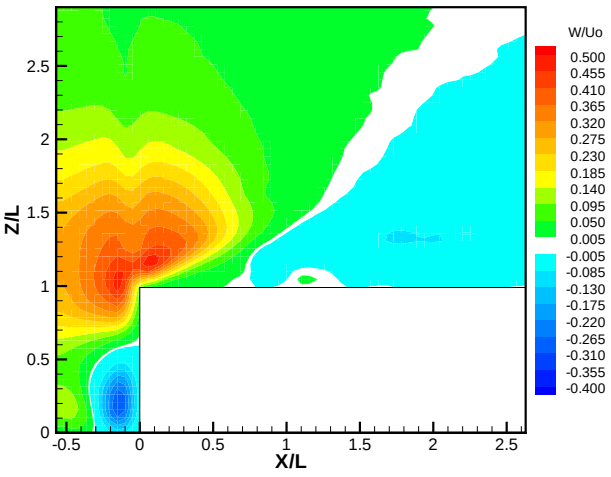

Figure 3.10.d: Contours of normalized cross-stream velocity component, W/U_o, at the quarter plane averaged over 2 seconds. Case II

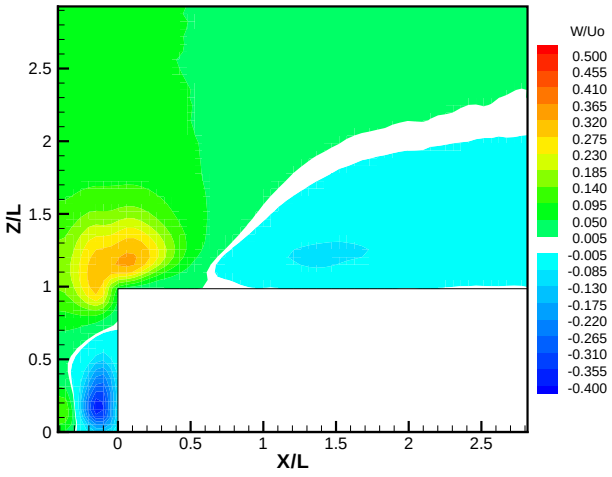

Figure 3.10.e: Contours of normalized cross-stream velocity component, W/U_o, at the edge averaged over 2 seconds. Case I

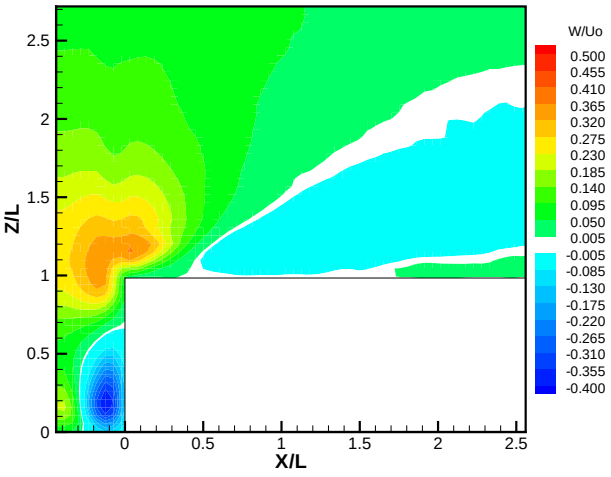

Figure 3.10.f: Contours of normalized cross-stream velocity component, W/U_o, at the edge averaged over 2 seconds. Case II

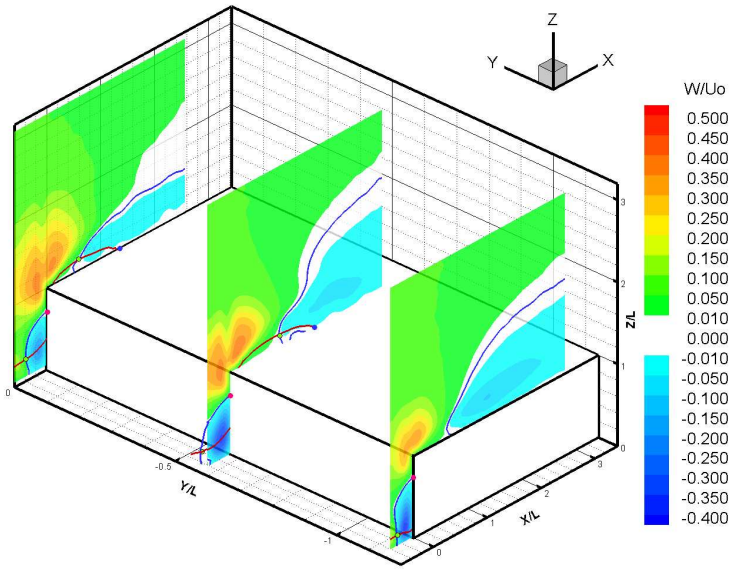

Figure 3.11.a: Contours of normalized cross-stream velocity component, W/U_o, at the center, quarter and edge planes averaged over 2 seconds. Case I

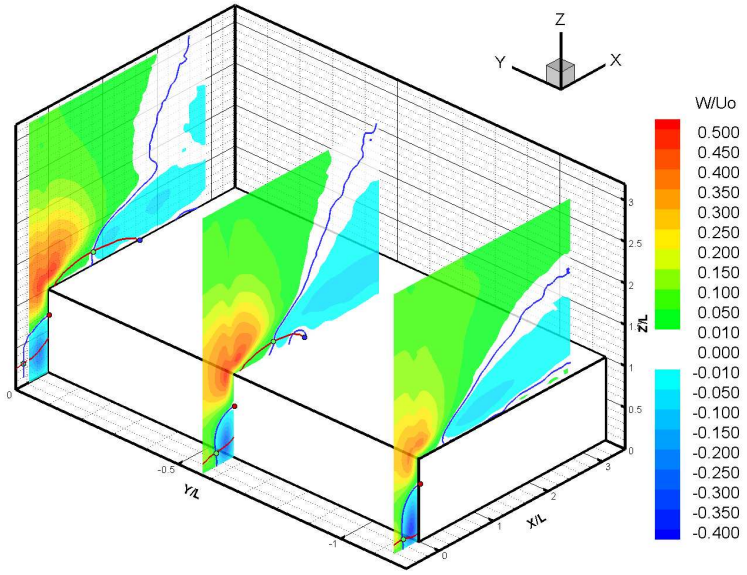

Figure 3.11.b: Contours of normalized cross-stream velocity component, W/U_o, at the center, quarter and edge planes averaged over 2 seconds. Case II

Figures 3.12.a and 3.12.b show contour maps of the normalized vorticity component Ω_y averaged over eight seconds. The maximum vorticity near the leading edge has the same magnitude in both flow cases. One major difference between the two cases is the angle of the shear layer near the edge as represented by the line of maximum vorticity. The line of development of the shear layer in case I makes a smaller angle with the roof than the line of the shear layer development in case II. This causes the vorticity to be confined to a smaller region near the roof in case I than in case II. Figure 3.12.c shows the distribution of the normalized vorticity component Ω_y in the region above the roof. The results show that the level of the maximum vorticity is about the same in both cases. On the other hand, the contour line of maximum vorticity in case II is higher than the corresponding line in case I. This difference increases from small values about 1% near $x/L = 0.5$ to about 8% near $x/L = 2.5$. Finally, it is noted that the separation region in case I shows slightly higher levels of negative vorticity than case II near the wall. In the region beyond reattachment, case I shows appreciably higher levels of positive vorticity near the wall. This higher level of vorticity near the wall is due to the fact that the shear layer is closer to the wall in case I than in case II.

Figures 3.13.a to 3.13.f show contour maps of the normalized vorticity components Ω_y in three planes, namely, the center plane, the quarter plane and the edge averaged over two seconds. The similarities and differences noted in figures 3.12.a and 3.12.b are observed when comparing figures 3.13.a and 3.13.b. In addition, the vorticity associated with the horseshoe vortex on the upwind face and the opposite sign vorticity generated on the wall have similar levels in both cases. A comparison of the vorticity maps in the recirculation zones at the quarter planes and near the edge shows that both maximum positive and negative vorticity have almost the same levels and that the maps cover the same region over the roof. The three-dimensional view of the normalized vorticity component on the prism constructed with the three planes of measurements are presented in figures 3.14.a for case I and 3.14.b for case II. The results show that, except for the center plane, the observed variations in the mean U and W components do not have a big effect on the maximum vorticity level near the leading edge or on the region where appreciable levels of normalized vorticity are measured.

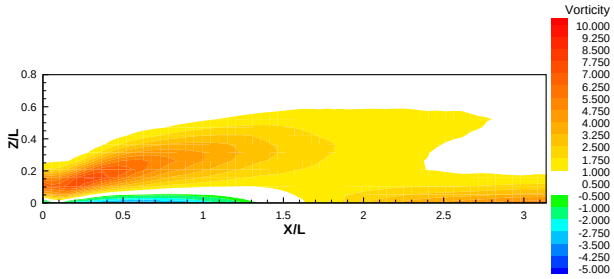

Figure 3.12.a: Contours of normalized vorticity, Ω_y, on the roof at the center plane averaged over 8 seconds. Case I

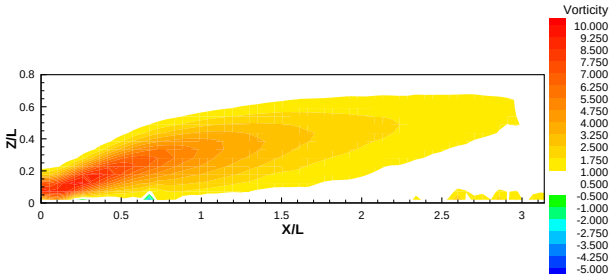

Figure 3.12.b: Contours of normalized vorticity, Ω_y, on the roof at the center plane averaged over 8 seconds. Case II

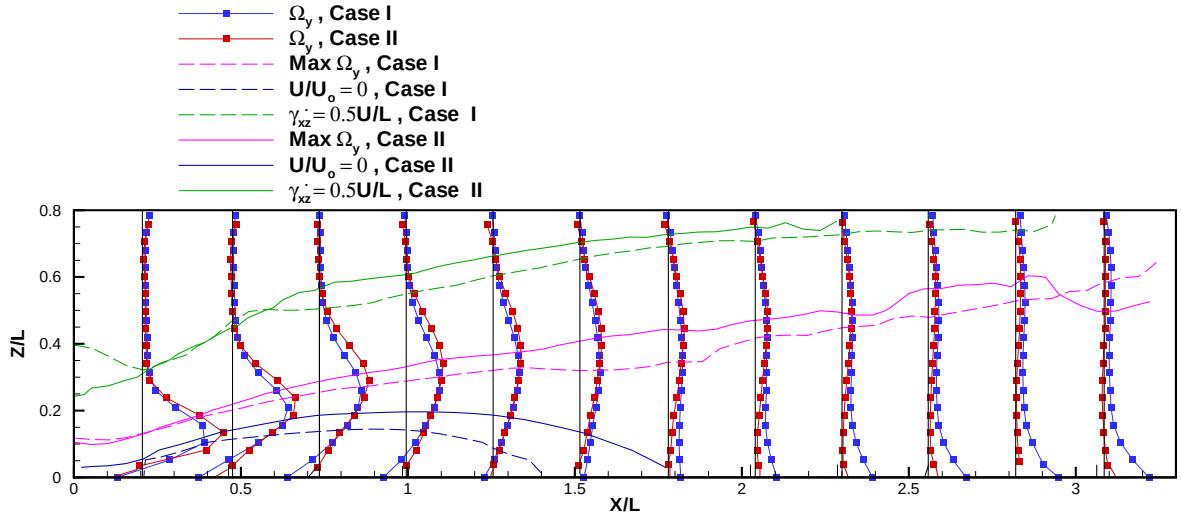

Figure 3.12.c: Distribution of normalized vorticity, Ω_y, for both case I and case II on the roof at the center plane averaged over 8 seconds

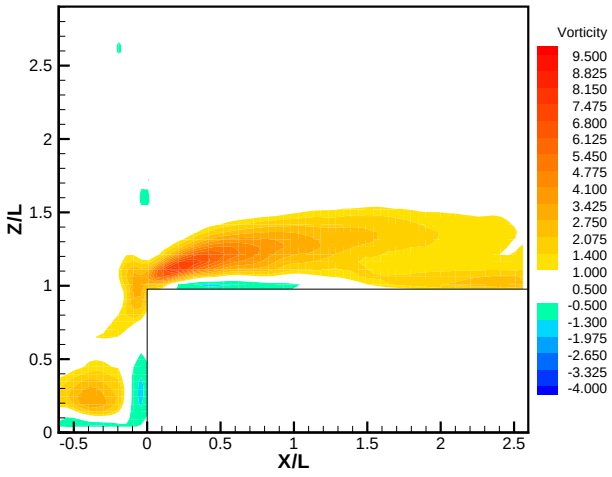

Figure 3.13.a: Contours of normalized vorticity, Ω_y, at the center plane averaged over 2 seconds. Case I

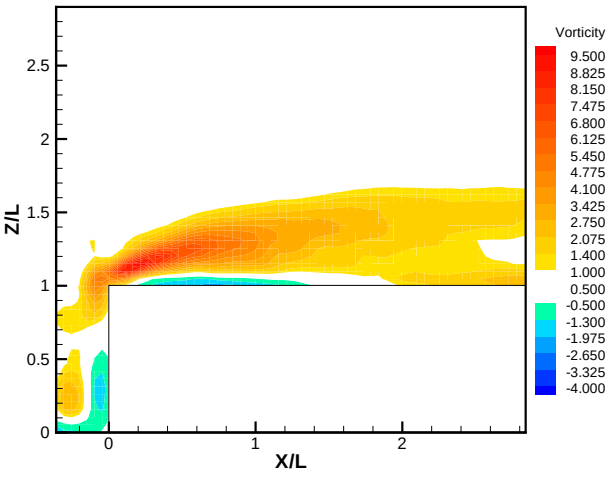

Figure 3.13.b: Contours of normalized vorticity, Ω_y, at the center plane averaged over 2 seconds. Case II

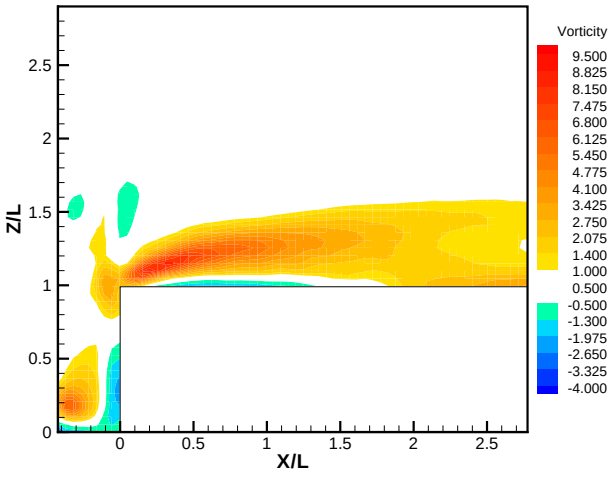

Figure 3.13.c: Contours of normalized vorticity, Ω_y, at the quarter plane averaged over 2 seconds. Case I

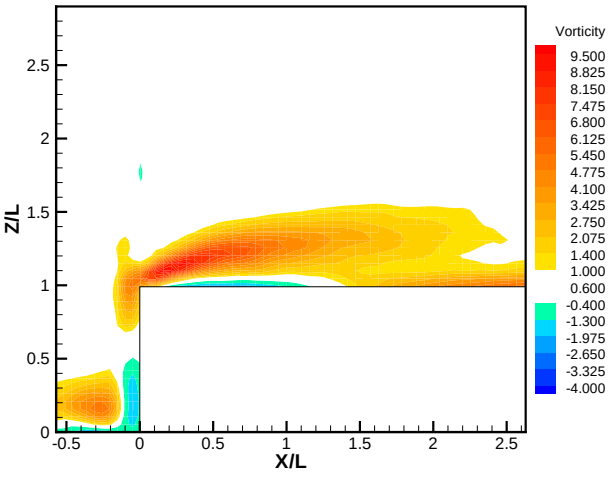

Figure 3.13.d: Contours of normalized vorticity, Ω_y, at the quarter plane averaged over 2 seconds. Case II

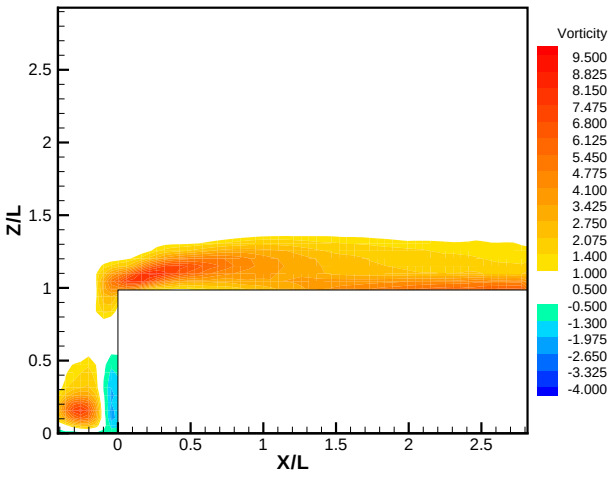

Figure 3.13.e: Contours of normalized vorticity, Ω_y, at the edge averaged over 2 seconds. Case I

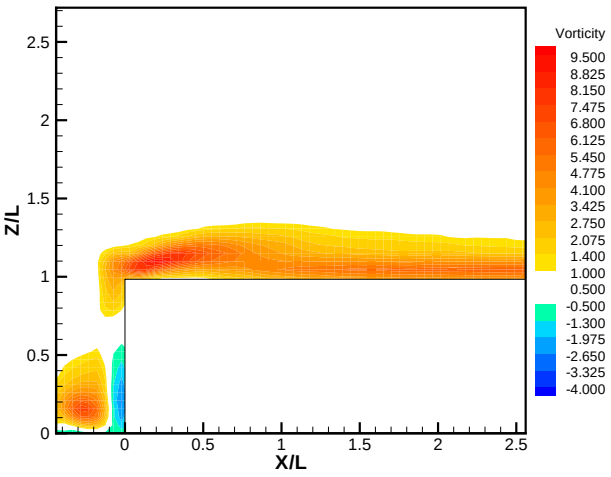

Figure 3.13.f: Contours of normalized vorticity, Ω_y, at the edge averaged over 2 seconds. Case II

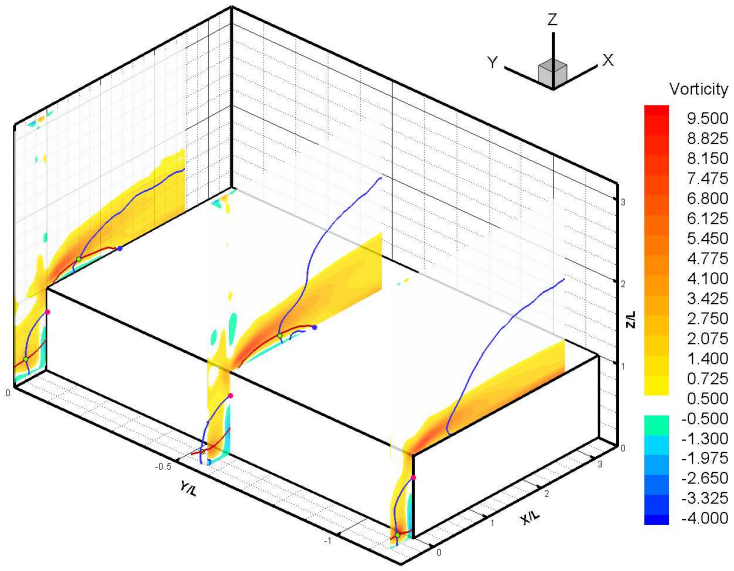

Figure 3.14.a: Contours of normalized vorticity, Ω_y, at the center, quarter and edge planes averaged over 2 seconds. Case I

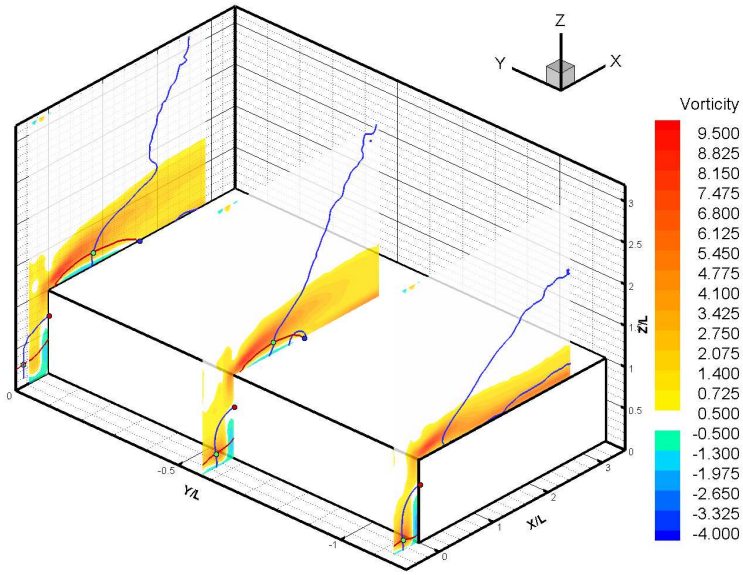

Figure 3.14.b: Contours of normalized vorticity, Ω_y, at the center, quarter and edge planes averaged over 2 seconds. Case II

In the next set of plots, levels of mean quantities related to turbulent fluctuations in the flow field for cases I and II are compared. Figures 3.15.a and 3.15.b show a comparison of the contour maps of the normalized value of the mean square fluctuation component $\overline{u'^2}$. The results clearly show that the maximum level of fluctuations is much larger in case II than in case I. Moreover, the most intense turbulence fluctuations in case I cover the region given by $0.5 < x/L < 3.0$ and $0.15 < z/L < 0.6$. In comparison, the most intense $\overline{u'^2}$ fluctuations in case I covers a much smaller region $0.5 < x/L < 1.5$ and $0.15 < z/L < 0.4$. The difference presented above is also noted in the distribution of the normalized $\overline{u'^2}$ presented in figure 3.15.c. The results clearly show that the line of maximum vorticity component Ω_y matches with the line of maximum $\overline{u'^2}$ in both cases. Moreover, the line where $\dot{\gamma}_{xz}$ is equal to $0.5U/L$ matches well with the line where $\overline{u'^2}$ is almost zero.

Figures 3.16.a to 3.16.f show contour maps of the mean square fluctuations component $\overline{u'^2}$ averaged over two seconds. The same differences in terms of magnitude and location of maximum $\overline{u'^2}$ observed in figures 3.15.a and 3.15.b are noted when comparing figures 3.15.a and 3.15.b. These differences extend to the quarter plane which shows that the maximum $\overline{u'^2}$ are larger in case II than in case I and cover a wider region of the flow over the roof. On the other hand, the level of $\overline{u'^2}$ in the horseshoe vortex is about the same in both flow cases. Near the edge, figures 3.16.e and 3.16.f show that the flow in case II has a higher level of $\overline{u'^2}$ than in case I although the difference is smaller than what is noted at the center and quarter planes. The three-dimensional perspectives presented in figures 3.17.a and 3.17.b show that the region of high $\overline{u'^2}$ is smaller in size and magnitude at the quarter plane than at the center plane. Moreover, these regions are above the line of zero $U-$ component and extend to cover the area downstream of the reattachment point.

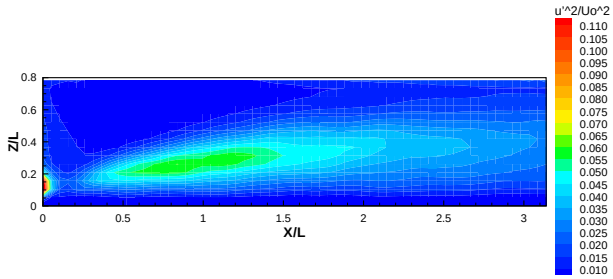

Figure 3.15.a: Contours of normalized $\overline{u'^2}$ on the roof at the center plane averaged over 8 seconds. Case I

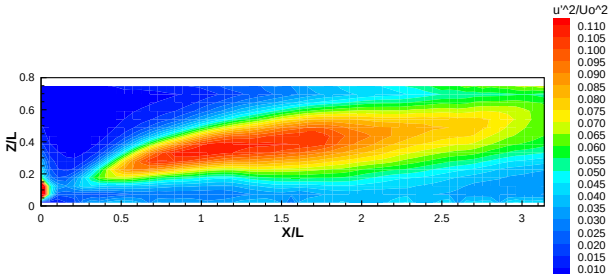

Figure 3.15.b: Contours of normalized $\overline{u'^2}$ on the roof at the center plane averaged over 8 seconds. Case II

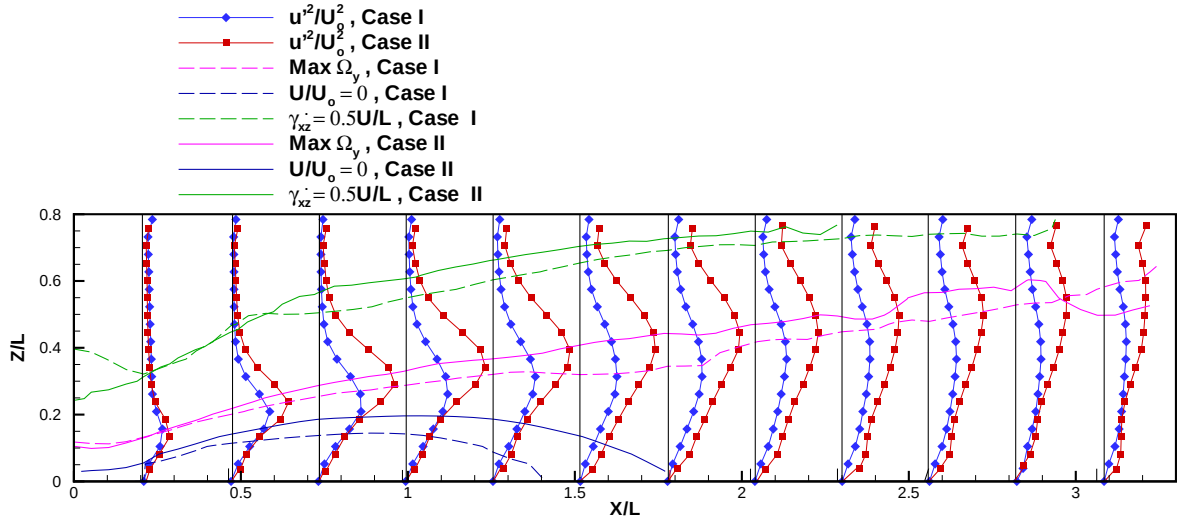

Figure 3.15.c: Distribution of normalized $\overline{u'^2}$ for both case I and case II on the roof at the center plane averaged over 8 seconds

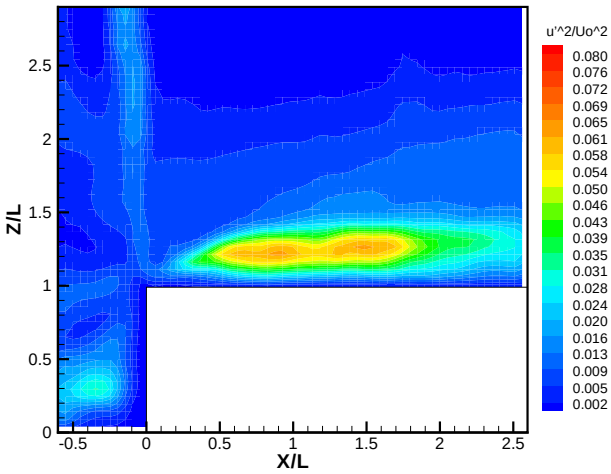

Figure 3.16.a: Contours of normalized $\overline{u'^2}$ at the center plane averaged over 2 seconds. Case I

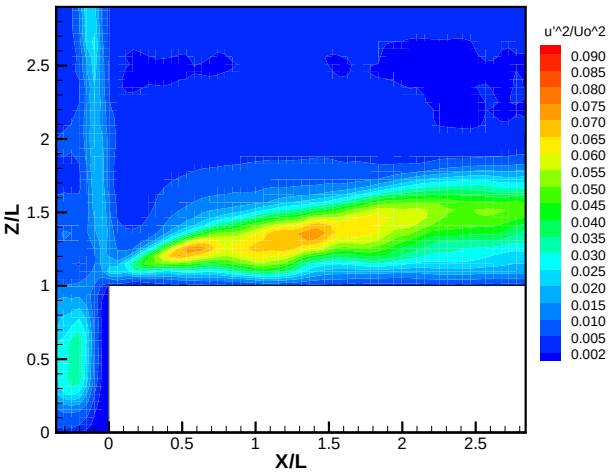

Figure 3.16.b: Contours of normalized $\overline{u'^2}$ at the center plane averaged over 2 seconds. Case II

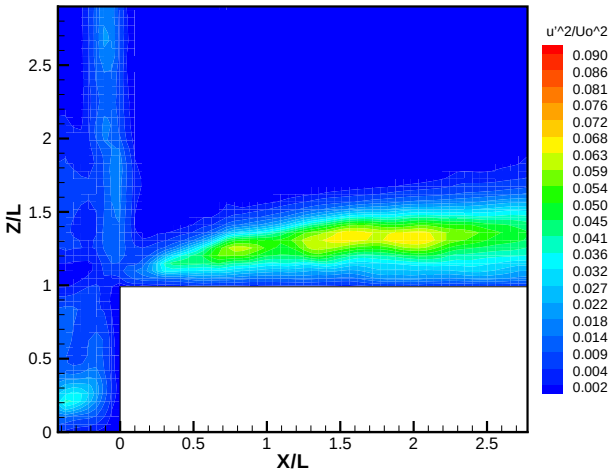

Figure 3.16.c: Contours of normalized $\overline{u'^2}$ at the quarter plane averaged over 2 seconds. Case I

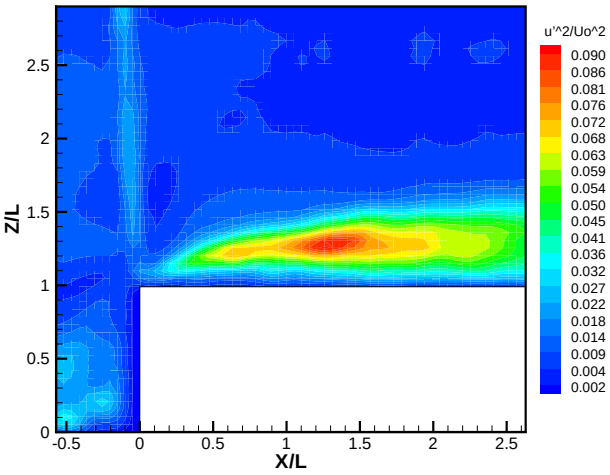

Figure 3.16.d: Contours of normalized $\overline{u'^2}$ at the quarter plane averaged over 2 seconds. Case II

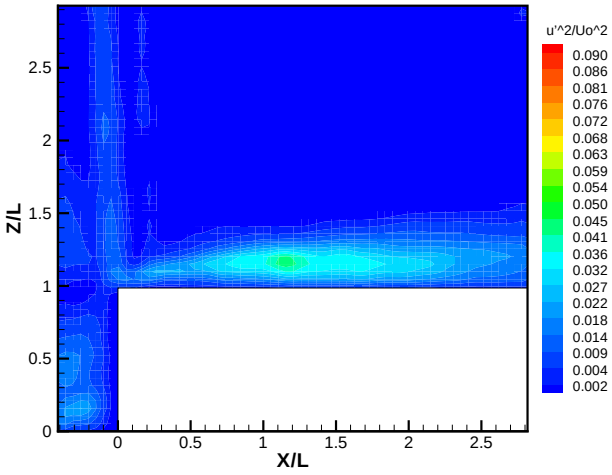

Figure 3.16.e: Contours of normalized $\overline{u'^2}$ at the edge averaged over 2 seconds. Case I

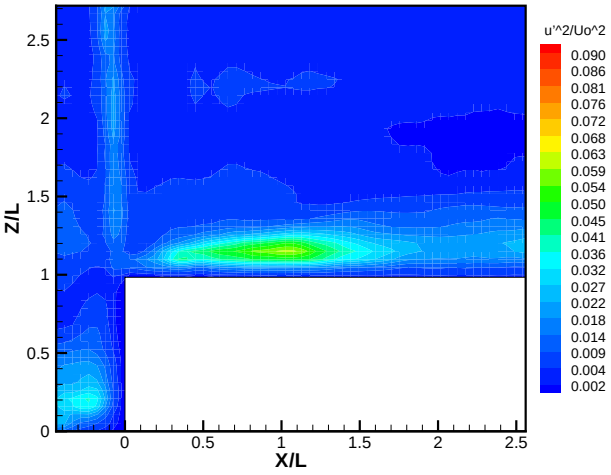

Figure 3.16.f: Contours of normalized $\overline{u'^2}$ at the edge averaged over 2 seconds. Case II

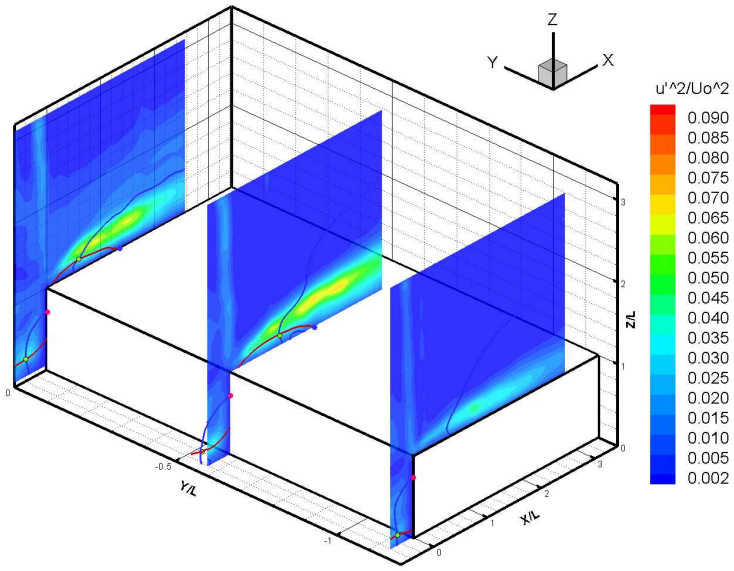

Figure 3.17.a: Contours of normalized $\overline{u'^2}$ at the center, quarter and edge planes averaged over 2 seconds. Case I

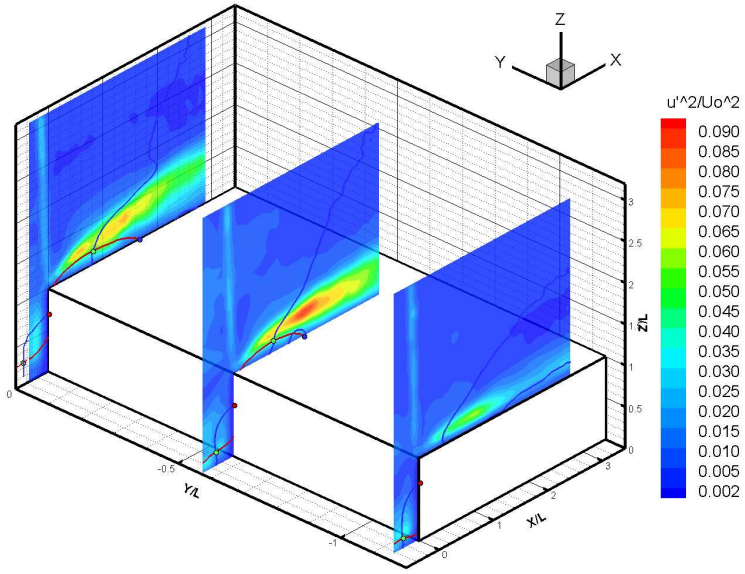

Figure 3.17.b: Contours of normalized $\overline{u'^2}$ at the center, quarter and edge planes averaged over 2 seconds. Case II

Figures 3.18.a and 3.18.b show contour maps of the normalized mean square fluctuations component $\overline{w'^2}$ averaged over eight seconds. Figure 3.18.c shows the distribution of the normalized values of $\overline{w'^2}$. The results show that the flow in case II has higher values of $\overline{w'^2}$ than in case I. In comparison with the maximum $\overline{u'^2}$, the locations of maximum $\overline{w'^2}$ are further downstream in both flow cases. A comparison of the levels of $\overline{u'^2}$ and $\overline{w'^2}$ shows that the maximum values of $\overline{w'^2}$ are about one third the maximum values of $\overline{u'^2}$ in both cases. The distributions of the normalized values of $\overline{w'^2}$ above the prism in both flow cases show that $\overline{w'^2}$ is much larger in case II than in case I. Moreover, the locations of maximum $\overline{w'^2}$ are slightly lower than those of maximum vorticity at the different x/L coordinates.

Figures 3.19.a to 3.19.f show contour maps of the normalized values of $\overline{w'^2}$ at the center plane, quarter plane and near the edge for both flow cases. The plots clearly show that the flow in case II yields significantly higher levels of $\overline{w'^2}$ than the flow in case I at the center and the quarter planes. On the other hand, the levels of $\overline{w'^2}$ in both flows are comparable near the edge. The three-dimensional perspective of $\overline{w'^2}$ obtained from the three planes for both flow cases are presented in figures 3.20.a and 3.20.b. The plots show the same differences discussed above. Moreover, they show that the region of maximum $\overline{w'^2}$ is associated with the flow area downstream of the reattachment point in both cases.

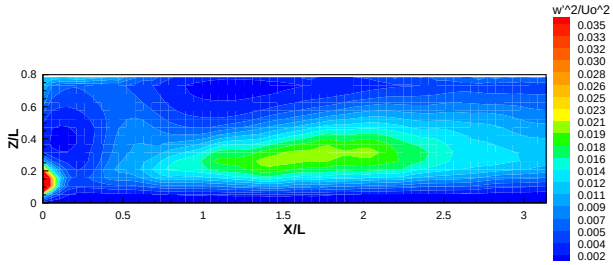

Figure 3.18.a: Contours of normalized $\overline{w'^2}$ on the roof at the center plane averaged over 8 seconds. Case I

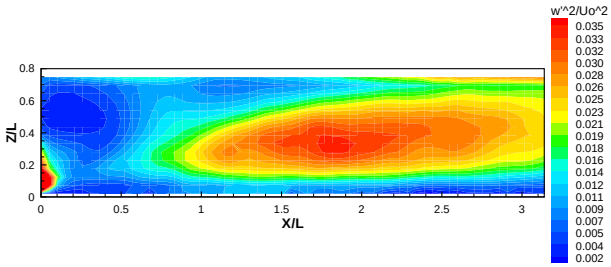

Figure 3.18.b: Contours of normalized $\overline{w'^2}$ on the roof at the center plane averaged over 8 seconds. Case II

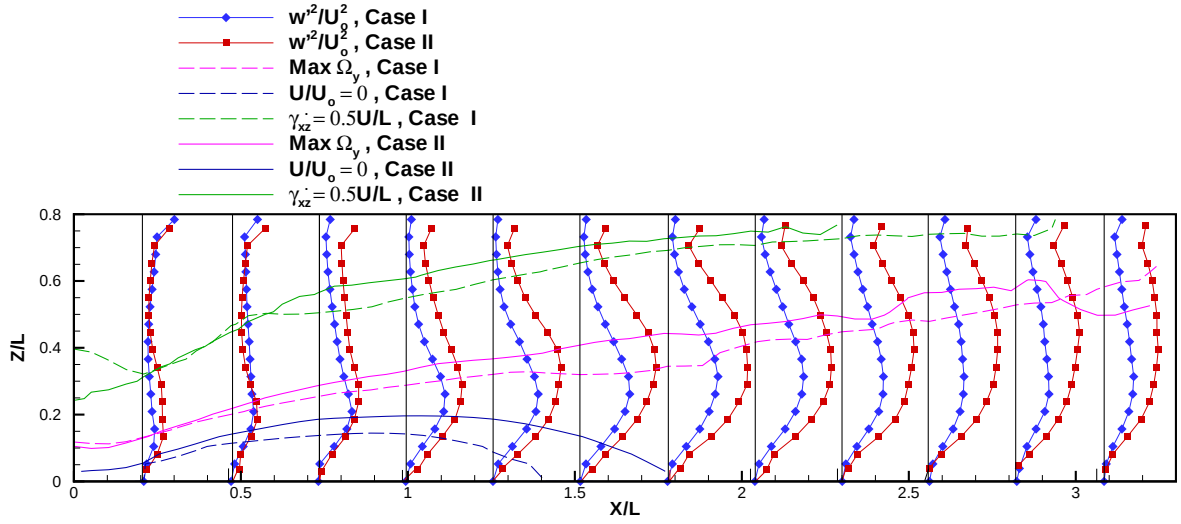

Figure 3.18.c: Distribution of normalized $\overline{w'^2}$ for both case I and case II on the roof at the center plane averaged over 8 seconds

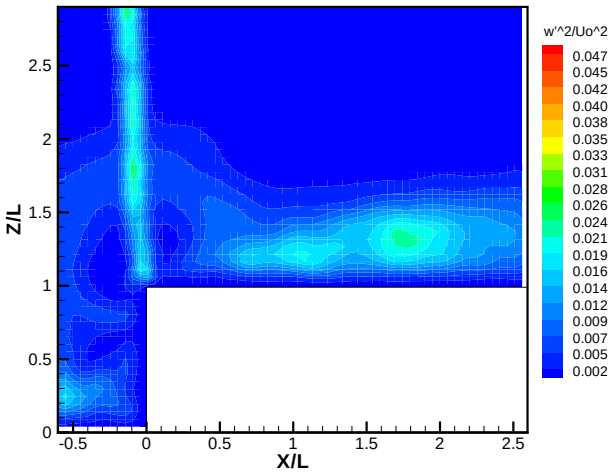

Figure 3.19.a: Contours of normalized $\overline{w'^2}$ at the center plane averaged over 2 seconds. Case I

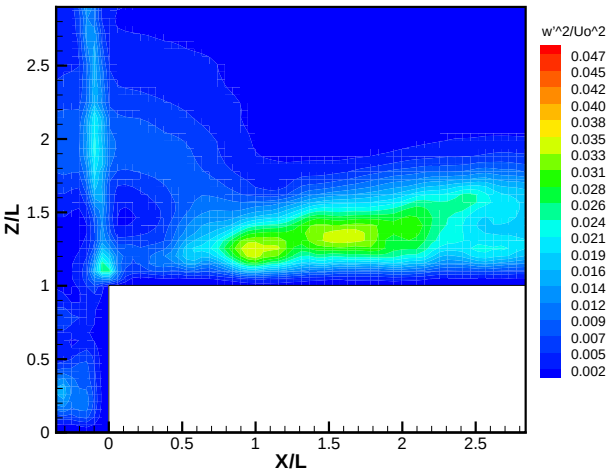

Figure 3.19.b: Contours of normalized $\overline{w'^2}$ at the center plane averaged over 2 seconds. Case II

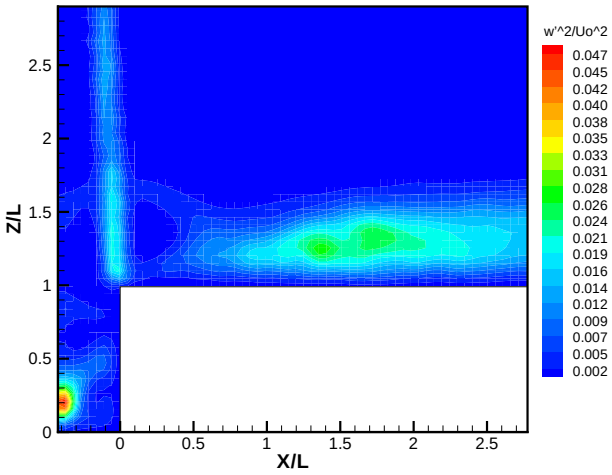

Figure 3.19.c: Contours of normalized $\overline{w'^2}$ at the quarter plane averaged over 2 seconds. Case I

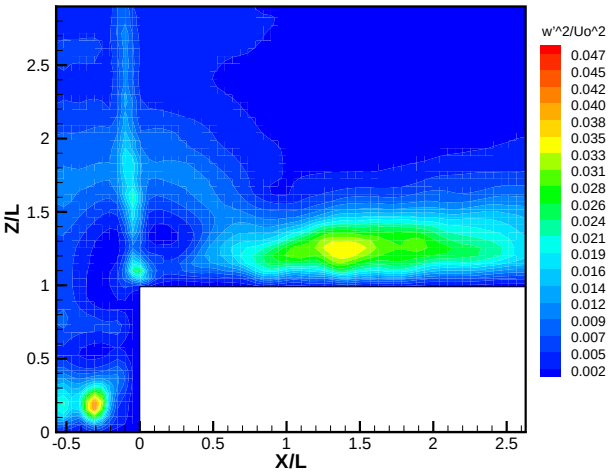

Figure 3.19.d: Contours of normalized $\overline{w'^2}$ at the quarter plane averaged over 2 seconds. Case II

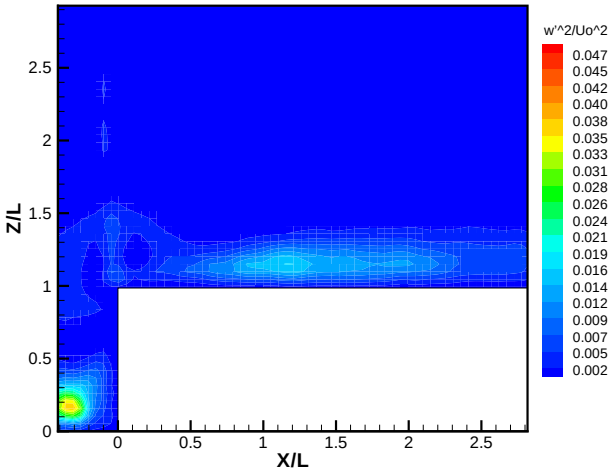

Figure 3.19.e: Contours of normalized $\overline{w'^2}$ at the edge averaged over 2 seconds. Case I

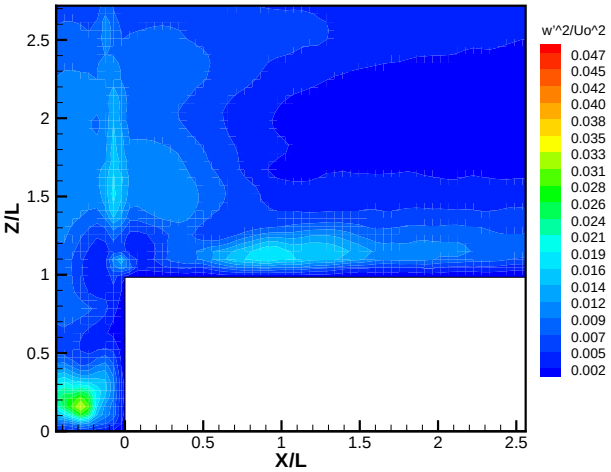

Figure 3.19.f: Contours of normalized $\overline{w'^2}$ at the edge averaged over 2 seconds. Case II

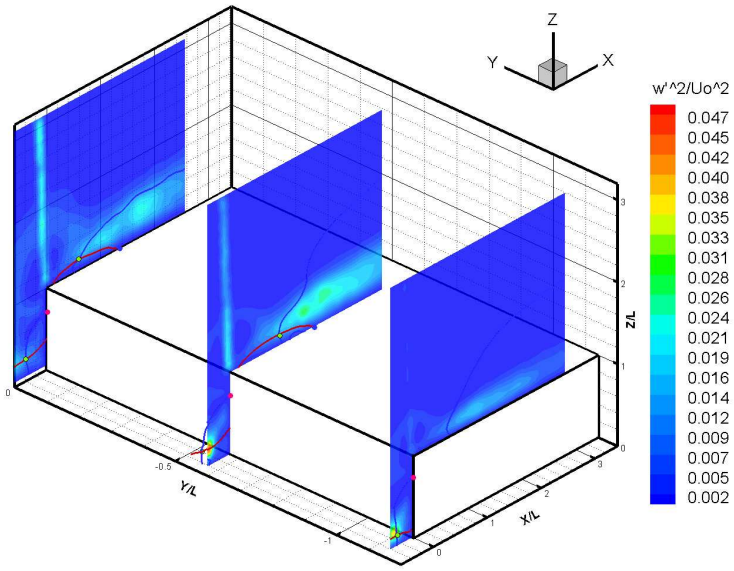

Figure 3.20.a: Contours of normalized $\overline{w'^2}$ at the center, quarter and edge planes averaged over 2 seconds. Case I

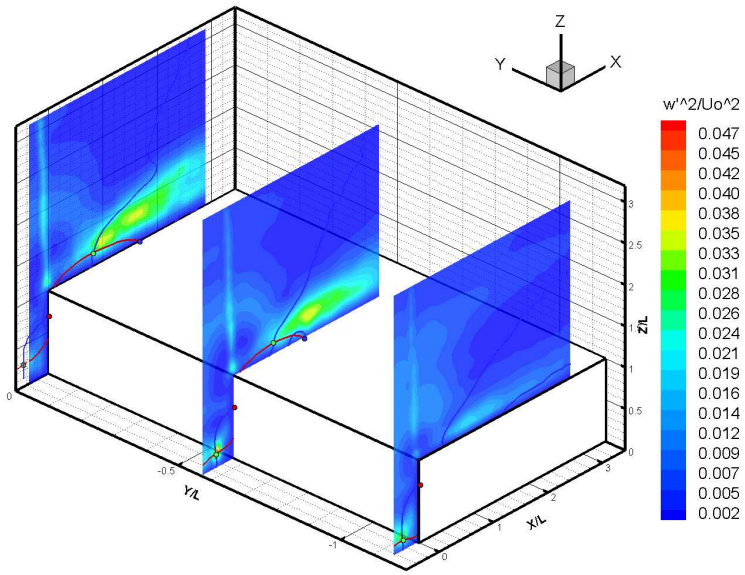

Figure 3.20.b: Contours of normalized $\overline{w'^2}$ at the center, quarter and edge planes averaged over 2 seconds. Case II

Figures 3.21.a and 3.21.b show the Reynolds stress component $\overline{u'w'}$ for both flow cases. A comparison of the two plots shows that the levels of this component is much higher (50%) in case II than in case I. Figure 3.21.c shows the distributions of the Reynolds stress componenet $\overline{u'w'}$ for both flow cases in the region above the roof of the prism. These distributions show that up to $x/L = 2$, the cross-stream locations of maximum $\overline{u'w'}$ match with those of maximum vorticity. Beyond $x/L = 2$, the maximum vorticity location is slightly higher than the maximum $\overline{u'w'}$ at the different x/L measuring locations.

Figures 3.22.a to 3.22.f show contour maps of the Reynolds stress component $\overline{u'w'}$ at the center plane, quarter plane and near the edge. The maps presented in figures 3.22.a to 3.22.d show that this component is much larger in case II than in case I. On the other hand, these values are comparable in the plane near the edge as shown in figures 3.22.e and 3.22.f. These notions are further stressed by the three-dimensional perspectives of $\overline{u'w'}$ over the three planes of measurements presented in figures 3.23.a and 3.23.b.

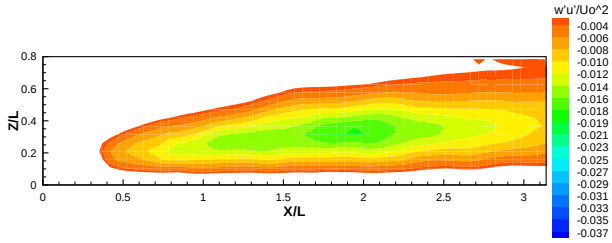

Figure 3.21.a: Contours of normalized $\overline{u'w'}$ on the roof at the center plane averaged over 8 seconds. Case I

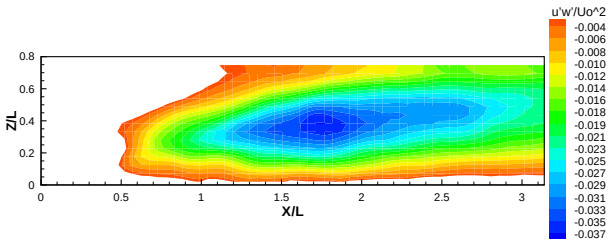

Figure 3.21.b: Contours of normalized $\overline{u'w'}$ on the roof at the center plane averaged over 8 seconds. Case II

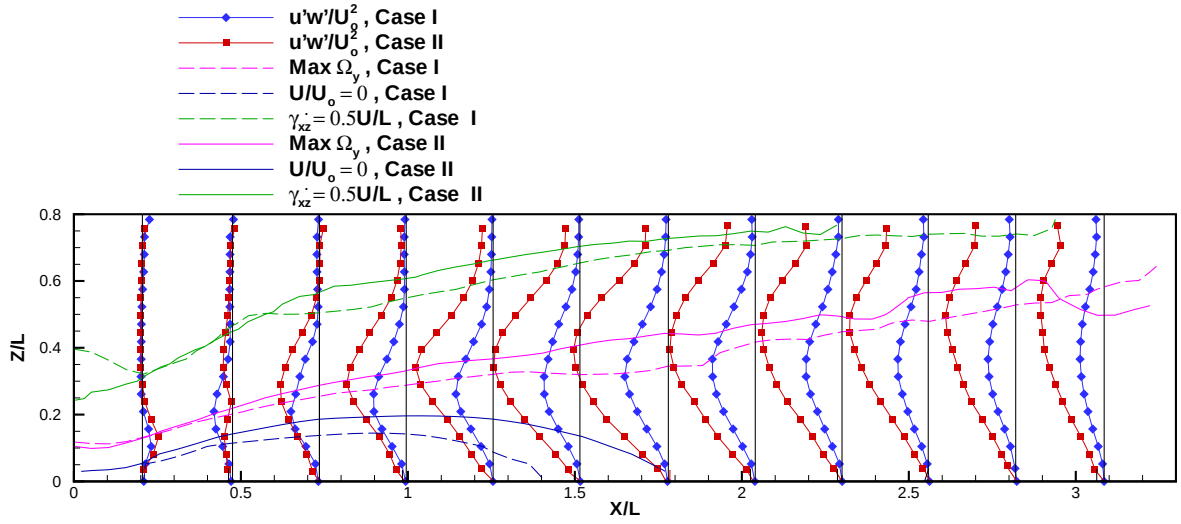

Figure 3.21.c: Distribution of normalized $\overline{u'w'}$ for both case I and case II on the roof at the center plane averaged over 8 seconds

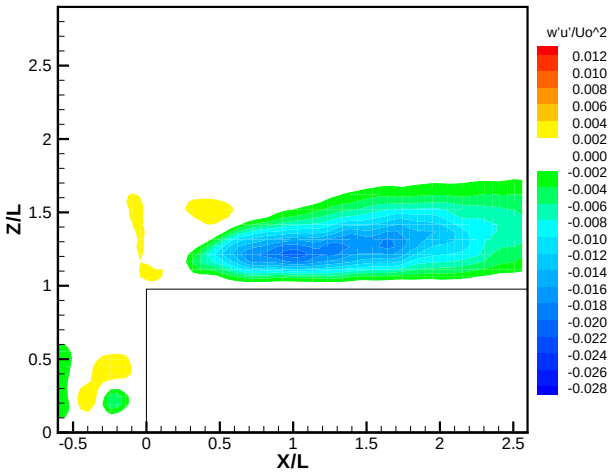

Figure 3.22.a: Contours of normalized $\overline{u'w'}$ at the center plane averaged over 2 seconds. Case I

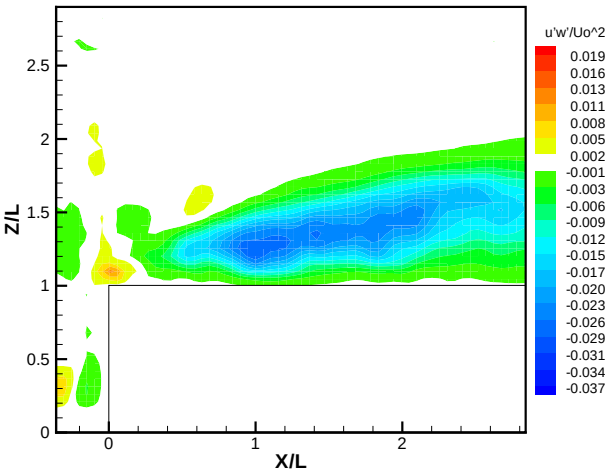

Figure 3.22.b: Contours of normalized $\overline{u'w'}$ at the center plane averaged over 2 seconds. Case II

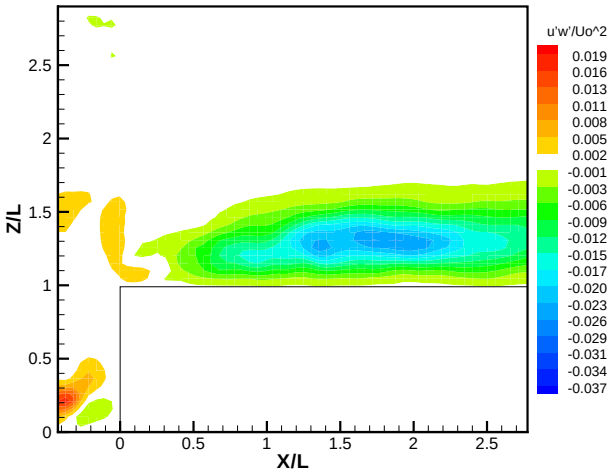

Figure 3.22.c: Contours of normalized $\overline{u'w'}$ at the quarter plane averaged over 2 seconds. Case I

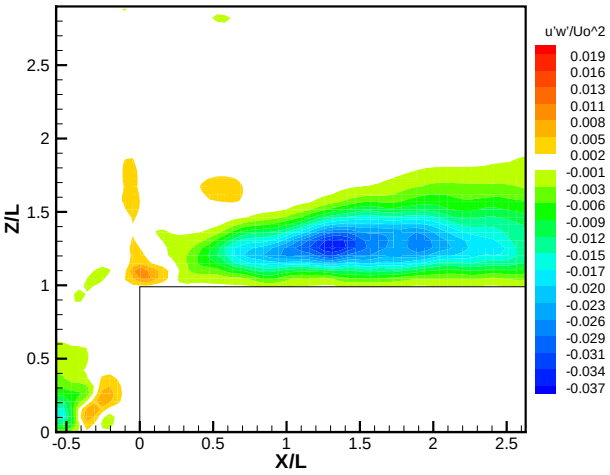

Figure 3.22.d: Contours of normalized $\overline{u'w'}$ at the quarter plane averaged over 2 seconds. Case II

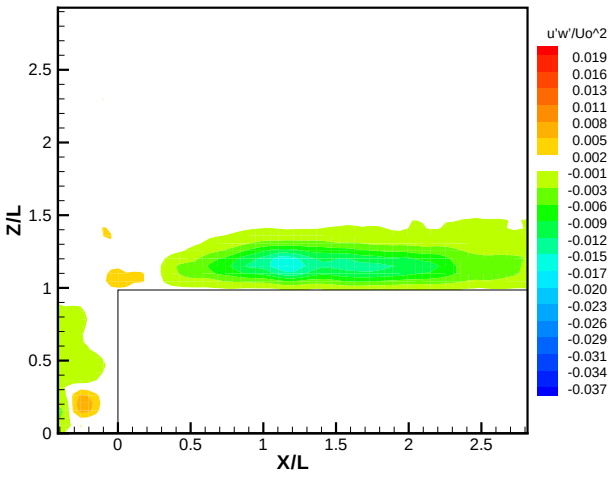

Figure 3.22.e: Contours of normalized $\overline{u'w'}$ at the edge averaged over 2 seconds. Case I

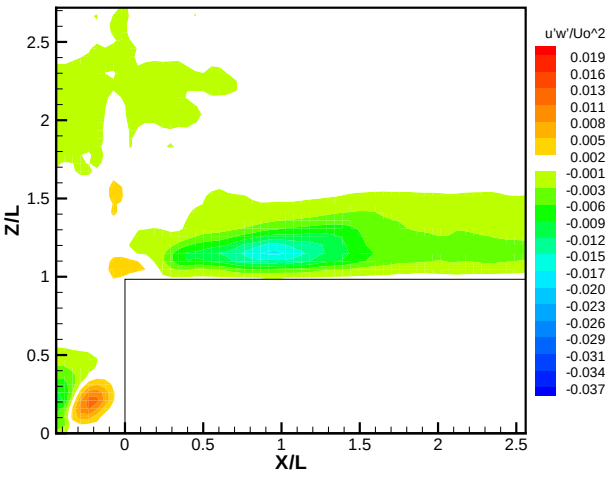

Figure 3.22.f: Contours of normalized $\overline{u'w'}$ at the edge averaged over 2 seconds. Case II

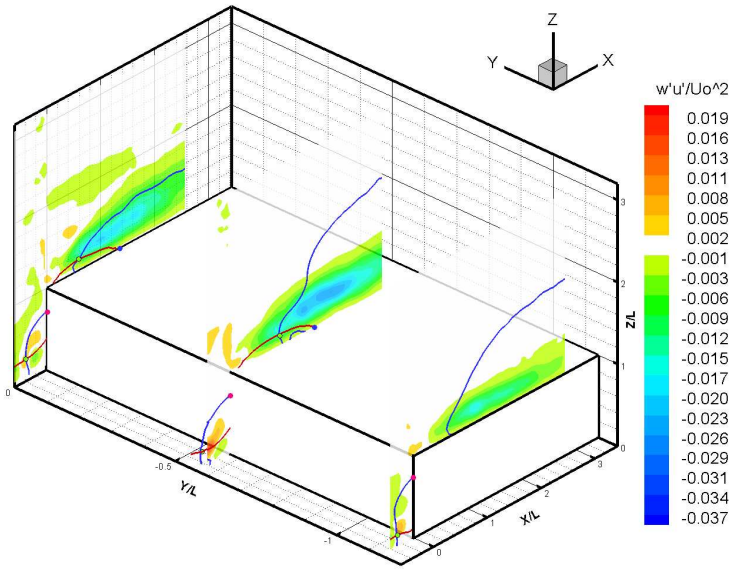

Figure 3.23.a: Contours of normalized $\overline{u'w'}$ at the center, quarter and edge planes averaged over 2 seconds. Case I

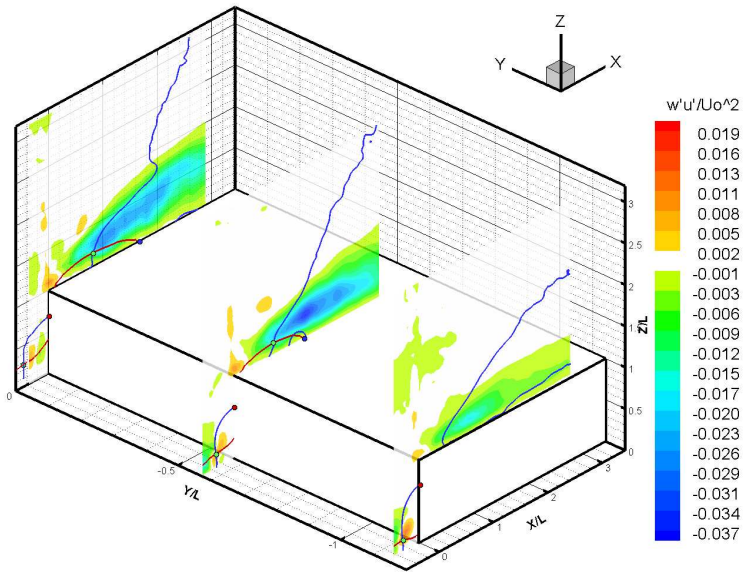

Figure 3.23.b: Contours of normalized $\overline{u'w'}$ at the center, quarter and edge planes averaged over 2 seconds. Case II

3.2 Instantaneous Flow Field

Figures 3.24 through 3.28 show representative sequences of the development of the instantaneous flow field over the surface mounted prism in cases I and II. All the plots presented in these figures show contour maps of the vorticity on the left side of the page and specified contour lines on the right side. In the contour maps, small vorticity values are colored in white to differentiate the positive and negative vorticity regions. In the plots of the contour lines, the positive contours are drawn with solid lines. The negative contours are drawn with dashed lines.

The sequence presented in figure 3.24 shows the development and interactions of vorticity regions with the solid surface on the roof of the prism in case II over a duration of 0.23 seconds. At the relative time $t = 0$, a shear layer forms on the roof of the prism. This layer consists of a vortex sheet with positive vorticity that is separated from the roof. The origin of this sheet is in the boundary layer on the upwind face that separates the at the prism leading edge. At time $t = 0.008$ seconds, the positive vorticity starts to accumulate and strengthens over certain parts of the sheet. The interaction of the accumulated vorticity with the solid surface leads to the enhancement of the negative vorticity at the roof near $x/L = 1.5$ as observed at $t = 0.016$ seconds. At time $t = 0.024$ seconds, the negative vorticity region near $x/L = 1.5$ is lifted-up by the positive vorticity in the shear layer. This negative vorticity penetrates the positive vorticity region and causes the detachment of a part of the shear layer as observed at $t = 0.04$ seconds. The same mechanism described above is repeated near $x/L = 0.5$ between $t = 0.024$ seconds, when negative vorticity is generated near the wall, and 0.052 seconds, when the negative vorticity cuts the shear layer. Basically, the accumulation and strengthening of positive vorticity, observed at $t = 0.024$ over $0.5 \leq x/L \leq 1.0$ leads to the generation of negative vorticity on the wall. The interaction of the positive and negative vorticity regions causes the lifting of the negative vorticity into the flow to cut-off the positive vorticity. It is important to note here that the characteristic size of the detached region of positive vorticity is about one half the height of the prism. Between $t = 0.064$ seconds and 0.23 seconds it is noted that the detached region of positive vorticity

is convected downstream at a speed of about $35 cm/sec$ which is about 80% of the mean flow velocity. Another important observation is the difference in the flow characteristics over the different time periods. Between $t = 0$ and 0.016 seconds, the shear layer is well separated and its thickness is about 1/5 the height of the prism. Between $t = 0$ and 0.064 seconds, the detached positive vorticity gets closer to the wall. This closeness of the vortex to the wall leads to enhanced drop in surface pressure fluctuations. At other times, such as between $t = 0.176$ and 0.23 seconds, when the region of negative vorticity at the wall is lifted up, the separated positive vorticity near the leading edge is pressed nearer to the roof in comparison with the observation made over times between $t = 0.0$ seconds and $t = 0.016$ seconds.

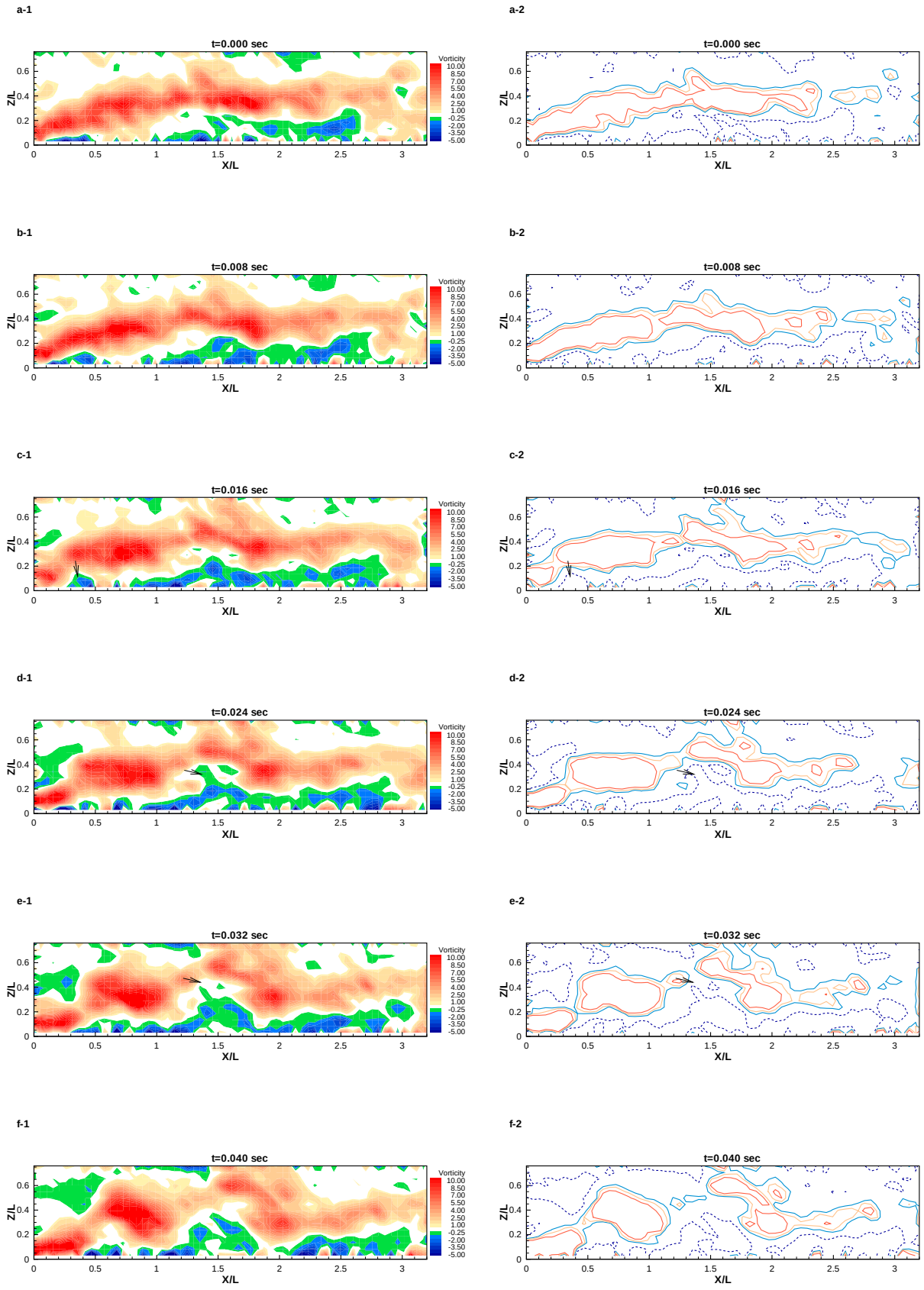

Figure 3.24: Sequence of instantaneous vorticity, ω_y,maps on the roof in the center plane showing vorticity cut-off via negative vorticity from the roof. Case II

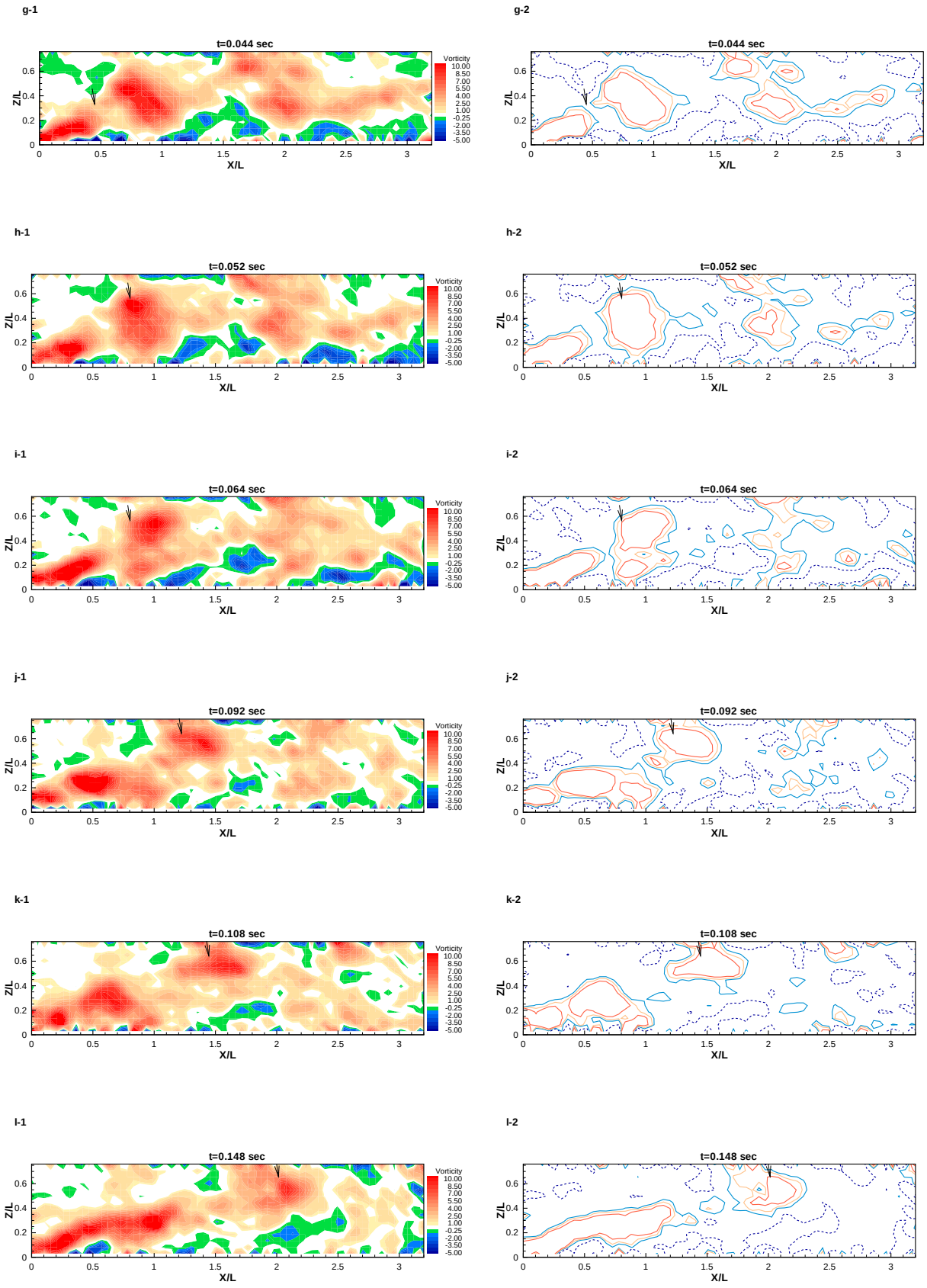

Figure 3.24: Continued, sequence of instantaneous vorticity, ω_y, maps on the roof in the center plane showing vorticity cut-off off via negative vorticity from the roof. Case II

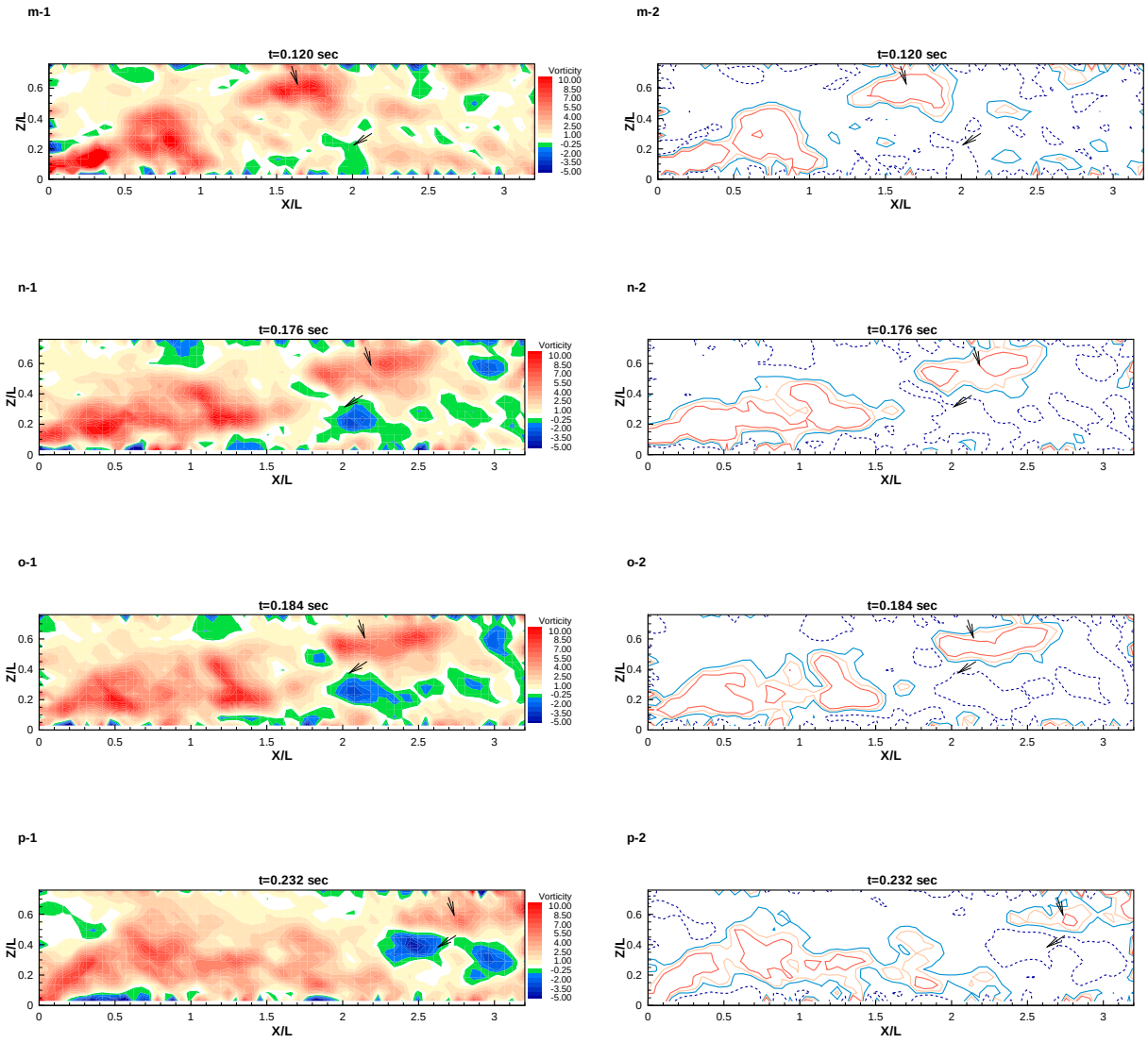

Figure 3.24: Continued, sequence of instantaneous vorticity, ω_y, maps on the roof in the center plane showing vorticity cut-off via negative vorticity from the roof. Case II

The same sequence of events observed in case II has been identified in case I as shown in figures 3.25 and 3.26. In figure 3.25, the results show an initial separating shear layer with positive vorticity between the relative times $t = 0.0$ and 0.032 seconds. Below this positive vorticity, there is a smaller region of negative vorticity near the wall. As the positive vorticity starts to accumulate within the shear layer, the opposite vorticity, generated near the wall becomes stronger and is lifted up as shown at $t = 0.052$ seconds. The lifted negative vorticity penetrates the shear layer and cuts off part of the positive vorticity which is then shed downstream. As this phenomenon takes place, another region of negative vorticity generated at the wall near $x/L = 1$ is lifted into the flow to cut-off the remaining part of the shear layer as shown at times $t = 0.088$ seconds and $t = 0.096$ seconds.

Figure 3.26 shows a similar sequence of interactions between the different vorticity regions as observed in figure 3.25. Basically, negative vorticity is generated near the wall at x/L near 1.3 between the relative times $t = 0.0$ and $t = 0.008$ seconds. This vorticity is lifted up into the flow to cut-off the positive vorticity and cause the shedding of a part of the original shear layer as shown between times 0.016 and 0.044 seconds. While figures 3.25 and 3.26 show similarities in the vortex interaction, they show a difference in the orientation in the region of negative vorticity. In figure 3.25, the region of negative vorticity is lifted up and is oriented in the direction of the flow. In figure 3.26, the orientation of the negative vorticity region is against the flow. The important issue here is that when the negative vorticity is lifted up by the strong positive vorticity on its right, it actually causes the positive vorticity on its left to get closer to the wall. Consequently, when the negative region has an orientation opposite to the mean flow, it brings down the part of the positive vorticity that is closer to the leading edge (up to $x/L = 1.0$) as shown in figures 3.26.e and 3.26.f. In comparison, The cut-off happens after $x/L = 1.5$ when the negative vorticity is oriented in the direction of the flow.

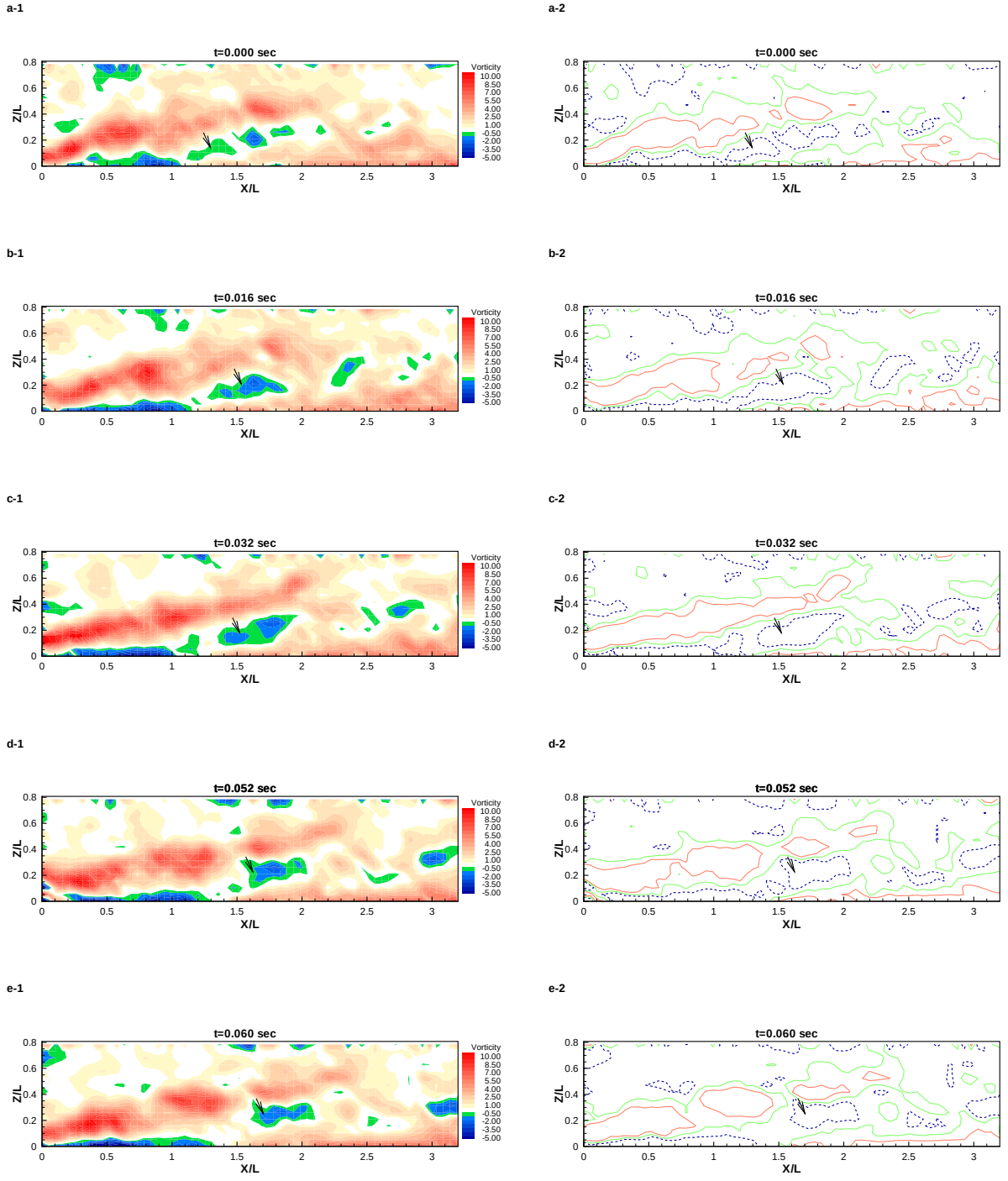

Figure 3.25: Sequence of instantaneous vorticity, ω_y, maps on the roof in the center plane showing vorticity cutt-off via negative vorticity from the roof with negative vorticity shed after the mean reattachment point. Case I

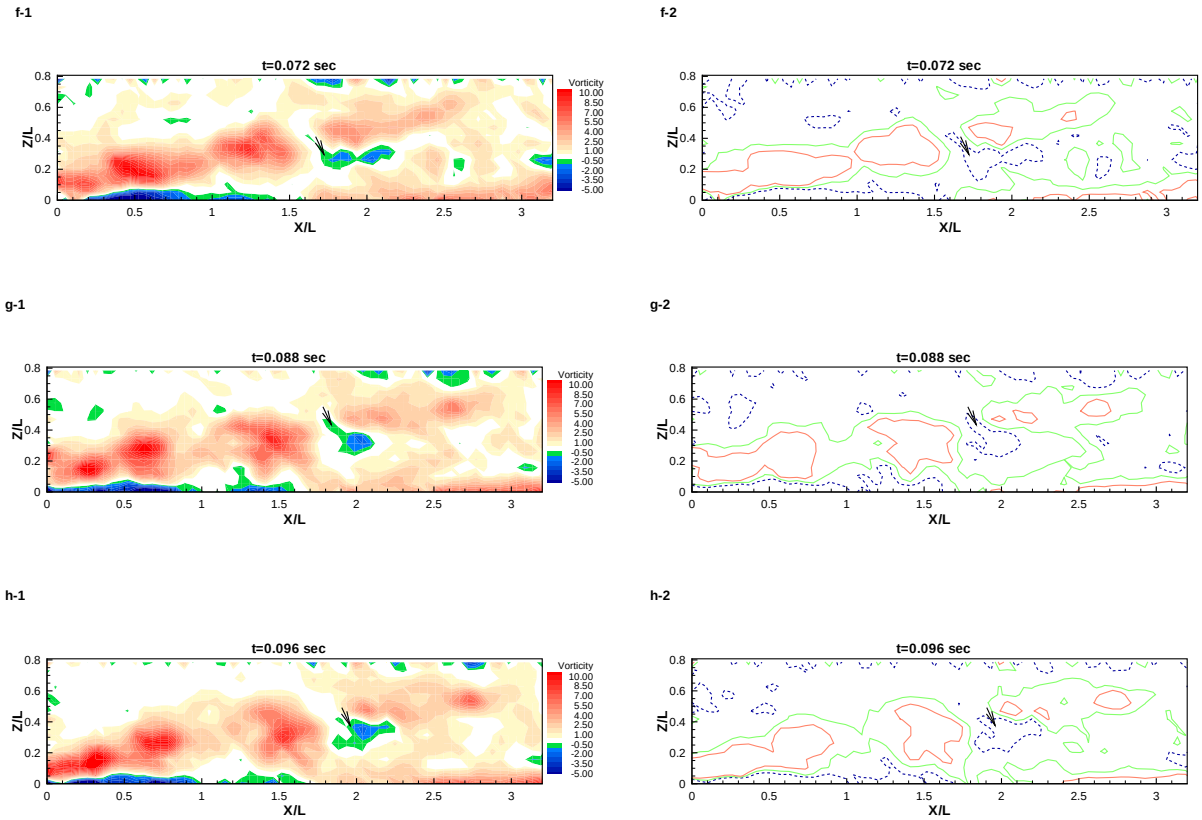

Figure 3.25: Continued, sequence of instantaneous vorticity, ω_y, maps on the roof in the center plane showing vorticity cut-off via negative vorticity from the roof with negative vorticity shed after the mean reattachment point. Case I

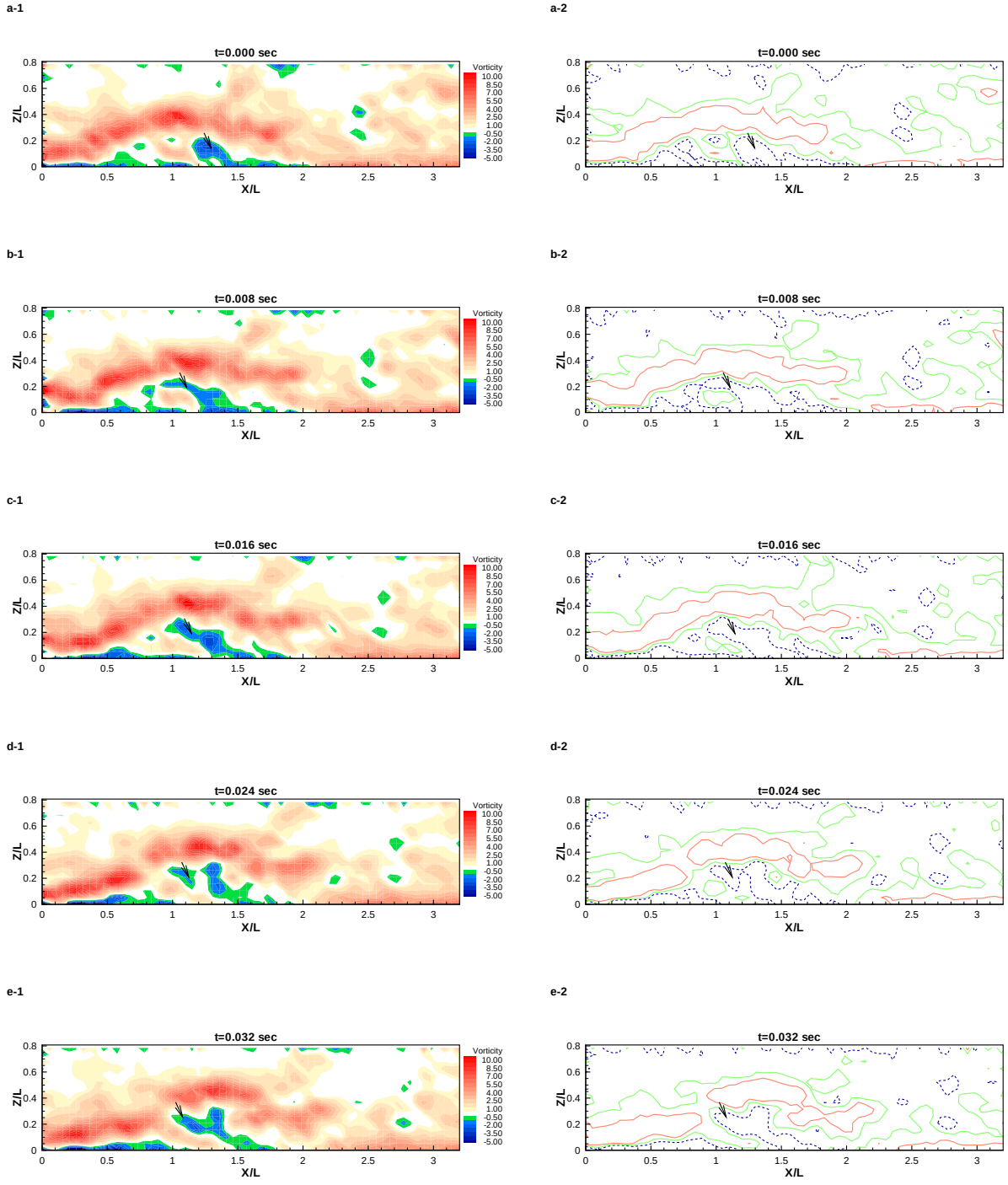

Figure 3.26: Sequence of instantaneous vorticity, ω_y maps on the roof in the center plane showing vorticity cut-off via negative vorticity from the roof with negative vorticity shed before the mean reattachment point. Case I

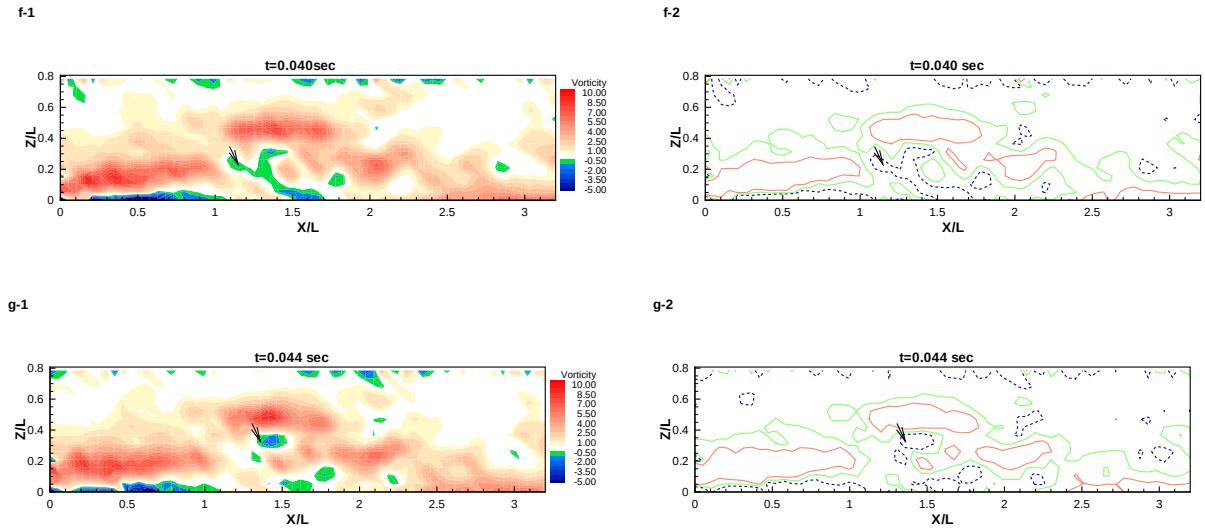

Figure 3.26: Continued, sequence of instantaneous vorticity, ω_y maps on the roof in the center plane showing vorticity cut-off via negative vorticity from the roof with negative vorticity shed before the mean reattachment point. Case I

The results presented above show how the positive vorticity, that has its source in the boundary layer on the upwind face, separates on the roof of the prism and interacts with the solid surface. The same mechanisms are observed in both cases I and II. Next, the interaction between the separating positive vorticity and the opposite-sign vorticity in the incident flow is examined.

Figures 3.27 and 3.28 show two representative sequences of the instantaneous flow field in case I over durations of 0.06 and 0.052 seconds, respectively. The two sequences show the interaction between the negative vorticity in the incident flow and the shear layer of positive vorticity. In figure 3.27, at relative time $t = 0.0$ seconds, a parcel of fluid with negative vorticity approaches the shear layer. The negative vorticity parcel moves along the boundary of the shear layer. At time $t = 0.016$, the negative vorticity parcel is pulled down by the induced velocity of the positive vorticity in the shear layer. The negative vorticity fluid then penetrates the shear layer near $x/L = 1.0$. The negative vorticity flow continues to penetrate the shear layer and finally cuts it off. It can be seen in figure 3.27, at times between $t = 0.044$, to 0.060 seconds, that as the shear layer is being cut-off by the negative vorticity, it is also pushed down towards the roof. It can be seen that the shear layer becomes perfectly parallel to the roof between $t = 0.052$ and $t = 0.060$ seconds. The same sequence of events observed in figure 3.27 is noted in figure 3.28.

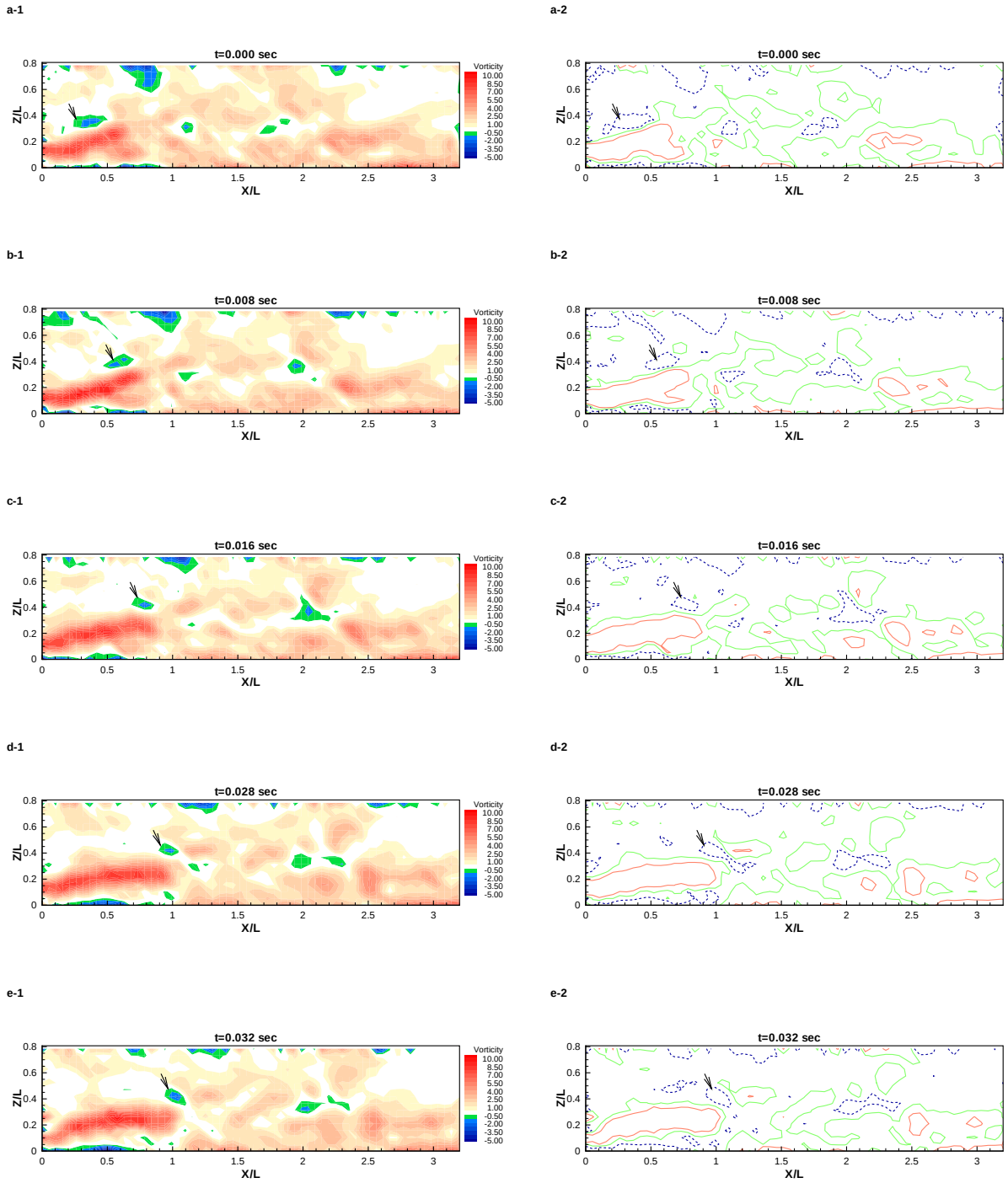

Figure 3.27: Sequence of instantaneous vorticity, ω_y on the roof in the center plane showing the effect of inflow vorticity. Case I

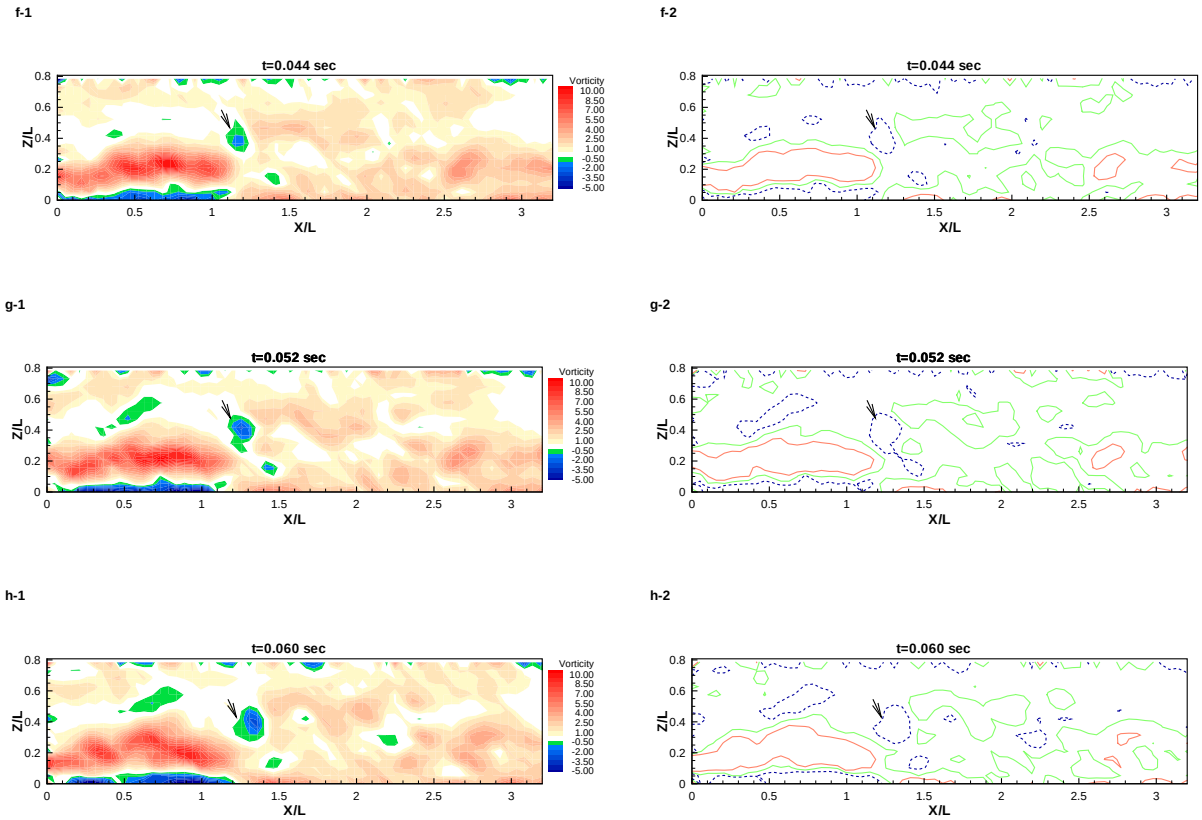

Figure 3.27: Continued, sequence of instantaneous vorticity, ω_y, on the roof in the center plane showing the effect of inflow vorticity. Case I

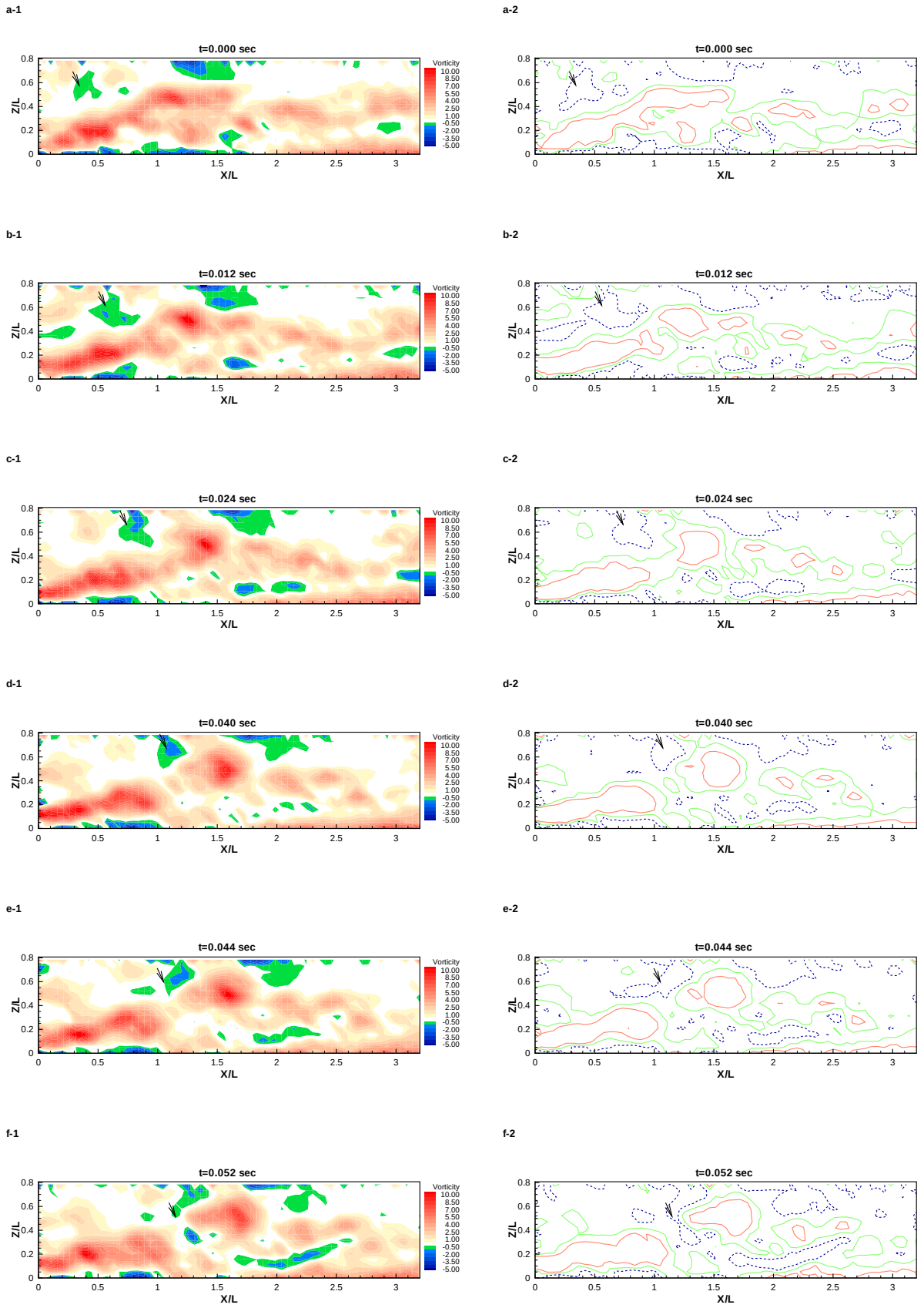

Figure 3.28: Another sequence of instantaneous vorticity, ω_y, on the roof in the center plane showing the effect of inflow vorticity. Case I

Chapter 4

Mathematical Formulation and Numerical Methods

4.1 Mathematical Formulation

4.1.1 Governing Equations

The compressible Navier-Stokes equations, the total energy equation and the equation of state consitiute the governing equations for the the current simulation and are given by:

Continuity Equation:

$$\frac{\partial \rho^*}{\partial t^*} + \frac{\partial (\rho^* u_j^*)}{\partial x_j^*} = 0, \tag{4.1}$$

Momentum Equation:

$$\frac{\partial (\rho^* u_i^*)}{\partial t^*} + \frac{\partial (\rho^* u_i^* u_j^* + p^* \delta_{ij})}{\partial x_j^*} = \frac{\partial \sigma_{ij}^*}{\partial x_j^*}, \tag{4.2}$$

Energy Equation:

$$\frac{\partial (\rho^* E^*)}{\partial t^*} + \frac{\partial [(\rho^* E^* + p^*) u_j^*]}{\partial x_j^*} = \frac{\partial}{\partial x_j^*} \left(\sigma_{ij}^* u_i^* - q_j^* \right), \tag{4.3}$$

Equation of State:

$$p^* = \rho^* R^* T^*, \tag{4.4}$$

Where

$$E^* = \frac{p^*}{(\gamma - 1)\rho^*} + \frac{1}{2} u_i^* u_i^*, \tag{4.5}$$

$$\sigma^*{}_{ij} = \mu^* \left(\frac{\partial u_i^*}{\partial x_j^*} + \frac{\partial u_j^*}{\partial x_i^*} - \frac{2}{3} \frac{\partial u_k^*}{\partial x_k^*} \delta_{ij} \right), \tag{4.6}$$

$$q_j^* = -\kappa^* \frac{\partial T^*}{\partial x_j^*}, \tag{4.7}$$

and where t^* is time and x_i^*, $i = 1, 2, 3$ are Cartesian coordiantes. The corresponding fluid velocity, pressure, density, temperature, stress tensor, total specific energy and heat flux are repectively denoted by u_i^*, p^*, ρ^*, T^*, σ_{ij}^*, E^* and q_j^*. The gas constant R^* and the ratio of specific heats γ^* for air are taken as $287.06\, Jkg^{-1}K^{-1}$ and 1.4, respectively.

Using reference length L_r^*, velocity U_r^*, density ρ_r^*, temperature T_r^*, specific heat at constant pressure $c_{p_r}^*$, dynamic viscosity μ_r^* and thermal conductivity κ_r^*, we define non-dimensional flow variables by:

$$t = \frac{t^* U_r^*}{L_r^*}, \quad x_i = \frac{x_i^*}{L_r^*}, \quad u_i = \frac{u_i^*}{U_r^*}, \quad \rho = \frac{\rho^*}{\rho_r^*}, \quad ,$$

$$T = \frac{T^*}{T_r^*}, \quad E = \frac{E^*}{U_r^{*2}}, \quad \mu = \frac{\mu^*}{\mu_r^*}, \quad \kappa = \frac{\kappa^*}{\kappa_r^*},$$

$$p = \frac{p^*}{\rho_r^* U_r^{*2}}, \quad c_p = \frac{c_p^*}{c_{p_r}^*} = 1 \tag{4.8}$$

The dimensionless variables t, x_i, u_i, T, E, μ, κ, p and c_p are, respectively, time, Cartisian cordinates, velocity, temperature, kinematic viscosity and thermal conductivity. Equations 4.1

through 4.7 can be be written in terms of the above dimensionless variables as follows:

Continuity Equation:

$$\frac{\partial \rho}{\partial t} + \frac{\partial (\rho u_j)}{\partial x_j} = 0, \tag{4.9}$$

Momentum Equation:

$$\frac{\partial (\rho u_i)}{\partial t} + \frac{\partial (\rho u_i u_j + p\delta_{ij})}{\partial x_j} = \frac{1}{Re}\frac{\partial \sigma_{ij}}{\partial x_j}, \tag{4.10}$$

Energy Equation:

$$\frac{\partial (\rho E)}{\partial t} + \frac{\partial [(\rho E + p)u_j]}{\partial x_j} = \frac{1}{Re}\frac{\partial}{\partial x_j}\left[\sigma_{ij}u_i - \frac{1}{Pr(\gamma-1)M^2}q_j\right], \tag{4.11}$$

Equation of State:

$$p = \rho\, R\, T, \tag{4.12}$$

$$E = \frac{p}{(\gamma-1)\rho} + \frac{1}{2}u_i u_i, \tag{4.13}$$

$$\sigma_{ij} = \mu\left(\frac{\partial u_i}{\partial x_j} + \frac{\partial u_j}{\partial x_i} - \frac{2}{3}\frac{\partial u_k}{\partial x_k}\delta_{ij}\right), \tag{4.14}$$

$$q_j = -\kappa\,\frac{\partial T}{\partial x_j}, \tag{4.15}$$

Three dimensionless parameters appear in the equations above, namely the Reynolds number (Re), the Prandtl number (Pr), and the Mach number(M). They are defined as follows:

$$Re = \frac{\rho_r^* U_r^* L_r^*}{\mu_r^*}, \tag{4.16}$$

$$Pr = \frac{\mu_r^* C_{p_r}}{\kappa_r^*}, \tag{4.17}$$

$$M = \frac{U_r^*}{\sqrt{\gamma R^* T_r^*}}, \tag{4.18}$$

and the nondimensional gas constant R is given by

$$R = \frac{1}{\gamma M^2}, \tag{4.19}$$

4.1.2 Large Eddy Simulation

In LES, the large scale motion is resolved directly, whereas the small-scale components of motion are modeled [44, 45, 36, 51]. The governing equations in terms of Favre-averaged variables are given by:

Continuity Equation:

$$\frac{\partial \bar{\rho}}{\partial t} + \frac{\partial (\bar{\rho} \widetilde{u}_j)}{\partial x_j} = 0, \tag{4.20}$$

Momentum Equation:

$$\frac{\partial (\bar{\rho} \widetilde{u}_i)}{\partial t} + \frac{\partial (\bar{\rho} \widetilde{u}_i \widetilde{u}_j + \bar{p} \delta_{ij})}{\partial x_j} = \frac{1}{Re} \frac{\partial \widetilde{\sigma}_{ij}}{\partial x_j} - \frac{\partial \tau_{ij}}{\partial x_j}, \tag{4.21}$$

Energy Equation:

$$\begin{aligned} &\frac{\partial (\bar{\rho} \widetilde{E})}{\partial t} + \frac{\partial [(\bar{\rho} \widetilde{E} + \bar{p}) \widetilde{u}_j]}{\partial x_j} \\ &= \frac{1}{Re} \frac{\partial}{\partial x_j} \left[\widetilde{\sigma}_{ij} \widetilde{u}_i - \frac{\widetilde{q}_j}{Pr(\gamma - 1) M^2} \right] - \frac{\partial (c_p \mathcal{Q}_j)}{\partial x_j}, \end{aligned} \tag{4.22}$$

Equation of State:

$$\bar{p} = \bar{\rho} \, R \, \widetilde{T}, \tag{4.23}$$

where

$$\widetilde{E} = \frac{\bar{p}}{(\gamma-1)\bar{\rho}} + \frac{1}{2}\widetilde{u}_i\widetilde{u}_i, \tag{4.24}$$

$$\widetilde{\sigma}_{ij} = \widetilde{\mu}\left(\frac{\partial\widetilde{u}_i}{\partial x_j} + \frac{\partial\widetilde{u}_j}{\partial x_i} - \frac{2}{3}\frac{\partial\widetilde{u}_k}{\partial x_k}\delta_{ij}\right), \tag{4.25}$$

$$\widetilde{q}_j = -\widetilde{\kappa}\frac{\partial\widetilde{T}}{\partial x_j}, \tag{4.26}$$

$$\tau_{ij} = \bar{\rho}\left(\widetilde{u_i u_j} - \widetilde{u}_i\widetilde{u}_j\right) \tag{4.27}$$

$$\mathcal{Q}_j = \bar{\rho}\left(\widetilde{u_j T} - \widetilde{u}_j\widetilde{T}\right) \tag{4.28}$$

Here τ_{ij} and $\mathcal{Q}_j$ are the sub-grid scale (SGS) stress tensor and the SGS heat flux, respectively, that need to be modeled in order to close the system of equations.

4.1.3 Sub-grid Scale Modelling

The dynamic version of the Smagorinsky's eddy-viscosity model [57] introduced by Germano *et al.* [14] is used to model the SGS stresses.

$$\tau_{ij} = -2C\bar{\rho}\bar{\Delta}^2\left|\widetilde{S}\right|\left(\widetilde{S}_{ij} - \frac{1}{3}\widetilde{S}_{kk}\delta_{ij}\right) + \frac{1}{3}\tau_{kk}\delta_{ij}, \tag{4.29}$$

$$\tau_{kk} = 2C_I\,\bar{\rho}\,\bar{\Delta}^2\left|\widetilde{S}\right|^2 \tag{4.30}$$

where

$$\widetilde{S}_{ij} = \frac{1}{2}\left(\frac{\partial\widetilde{u}_i}{\partial x_j} + \frac{\partial\widetilde{u}_j}{\partial x_i}\right), \tag{4.31}$$

$$\left|\widetilde{S}\right| = \left(2\widetilde{S}_{ij}\widetilde{S}_{ij}\right)^{\frac{1}{2}}, \tag{4.32}$$

$$\bar{\Delta} = (\Delta_1\,\Delta_2\,\Delta_3)^{\frac{1}{3}}, \tag{4.33}$$

$$\widehat{\Delta} = (\widehat{\Delta}_1\,\widehat{\Delta}_2\,\widehat{\Delta}_3)^{\frac{1}{3}}. \tag{4.34}$$

Here C, Δ_i and $\widehat{\Delta}_i$ are the Smagorinsky coefficient, the grid filter width and the test filter width, respectively. In the present study, $\widehat{\Delta}_i = 2\bar{\Delta}_i$ is used.

As in the work of Toh and Ragab, the coefficients, C and C_I are determined by extending Zhang and Chen's new filtered dynamic subgrid-scale model [72] as follows:

$$C = \frac{\widehat{\overline{\mathcal{L}_{ij}^d}\,\overline{\mathcal{M}_{ij}}}}{\widehat{\overline{\mathcal{M}_{ij}}\,\overline{\mathcal{M}_{ij}}}}, \quad C_I = \frac{\widehat{\bar{\mathcal{L}}}_{kk}}{\widehat{2\,\bar{\Delta}^2\bar{\rho}\,|\bar{\widetilde{S}}|^2} - \widehat{2\,\bar{\Delta}^2\bar{\rho}|\widetilde{S}|^2}} \tag{4.35}$$

where

$$\mathcal{L}_{ij} = \widehat{\bar{\rho}\widetilde{u}_i\widetilde{u}_j} - \frac{\widehat{\bar{\rho}\widetilde{u}_i}\,\widehat{\bar{\rho}\widetilde{u}_j}}{\widehat{\bar{\rho}}}, \quad \mathcal{L}_{ij}^d = \mathcal{L}_{ij} - \frac{1}{3}\mathcal{L}_{kk}\delta_{ij} \tag{4.36}$$

and

$$\mathcal{M}_{ij} = -2\widehat{\Delta}^2\widehat{\bar{\rho}}|\bar{\widetilde{S}}|\widehat{\bar{\widetilde{S}}_{ij}^d} + 2\bar{\Delta}^2\widehat{\bar{\rho}|\widetilde{S}|\widetilde{S}_{ij}^d}\ , \tag{4.37}$$

The symbol $\widehat{\ }$ represents double filtering, i.e., a grid filter ($^-$) is applied first followed by a test filter ($\widehat{\ }$).

The SGS heat flux is modeled using Smagorinsky's eddy-diffusivity model as follows:

$$\mathcal{Q}_j = -C\frac{\bar{\Delta}^2\bar{\rho}\,|\widetilde{S}|}{Pr_T}\frac{\partial\widetilde{T}}{\partial x_j} \tag{4.38}$$

where

$$Pr_T = \frac{C\widehat{\overline{\mathcal{N}_j}\,\overline{\mathcal{N}_j}}}{\widehat{\overline{\mathcal{K}_k}\,\overline{\mathcal{N}_k}}} \tag{4.39}$$

$$\mathcal{N}_j = -\widehat{\Delta}^2\,\widehat{\bar{\rho}}\,|\bar{\widetilde{S}}|\frac{\partial\bar{\widetilde{T}}}{\partial x_j} + \bar{\Delta}^2\widehat{\bar{\rho}|\widetilde{S}|}\frac{\partial\widetilde{T}}{\partial x_j} \tag{4.40}$$

$$\mathcal{K}_j \ = \ \widehat{\bar{\rho}\widetilde{u}_j\bar{\widetilde{T}}} - \frac{\widehat{\bar{\rho}\widetilde{u}_j}\,\widehat{\bar{\rho}\bar{\widetilde{T}}}}{\widehat{\bar{\rho}}} \tag{4.41}$$

Compressibility effects are not significant in the current simulations, therefore, we neglect

the terms involving C_I, and also we assume $Pr_T = 0.7$. The coefficient C is also averaged over homogeneous directions when they exist.

4.2 Numerical Methods

In this work, the simulation is advanced in time using a low-storage Runge-Kutta fourth-order scheme. In LES, it is important to minimize artificial dissipation that is inherent to most numerical schemes [43]. It is well known that explicit fifth-order upwind schemes introduce unacceptable dissipation. Tolstykh [65] developed a fifth-order non-centered compact scheme in which the artificial dissipation is controllable. This scheme is implemented in this work to evaluate the convective terms. The viscous and turbulent stresses terms are evaluated using a fourth-order central difference scheme.

4.2.1 Fifth-Order Compact Upwind Scheme *CUD-II-5*

The fifth-order compact upwind scheme *CUD-II-5* for conservative flux is given by Tolstykh [65]. For a grid variable f, the first derivative, $\partial f/\partial x$, evaluated by the *CUD-II-5* can be written in terms of the difference operator L_h as,

$$L_h(f_i) \;=\; \frac{1}{2h}\left(\Delta(s) + s\,R_h^{-1}\,Q_h\,(I + \frac{\Delta_2}{12})^{-1}\Delta_2\right)\,f_i \tag{4.42}$$

Where $\Delta(s)$ is the first-order upwind operator which is given by,

$$\begin{aligned} \Delta(s)f_i &= (\Delta_o - s\Delta_2)\,f_i \\ \Delta_o f_i &= f_{i+1} - f_{i-1} \\ \Delta_2 f_i &= f_{i+1} - 2f_i + f_{i-1} \end{aligned} \tag{4.43}$$

The operators Q_h and R_h are given by,

$$Q_h = I + \left(\frac{a}{2} - \frac{s_1}{4}\right) \Delta_o + \left(\frac{1}{6} - \frac{a}{2} s_1\right) \Delta_2 \tag{4.44}$$

$$Q_h = I + \left(\frac{b}{2} - \frac{s_1}{4}\right) \Delta_o + \left(\frac{1}{6} - \frac{b}{2} s_1\right) \Delta_2 \tag{4.45}$$

where I is the identity operator and,

$$a = -\frac{2}{15s} \ , \qquad b = \frac{1}{5s} \tag{4.46}$$

To obtain the above difference operator, L_h, s^2 has to be set to $\frac{4}{5}$ in the definition of a family of fifth-order compact upwind schemes given by Tolstykh [65] to reduce the stencile of the operators Q_h and R_h from five point to three points, confining the system to be solved to a tri-diagonal system. It should be noted that Q_h and R_h are always positive definite for $s > 0$ and are always negative definite for $s < 0$ if and only if sign s_1 is the same as sign s and $|s_1| > \frac{5}{24}$. This control on the positivity and negativity of the scheme is an important property for emplying flux vector splitting for upwind schemes. In addition, Tolstykh [66] showed that the value of s_1 controls the phase error and dissipation for waves in the range of $2h$ to $6h$, where h is the grid step as shown in figure 4.1. This figure shows also the dispersion error of the compact six-order central difference scheme.

The following algorithem is followed to compute the first derivative approximated by equation 4.42:

1. Solve tri-diagonal system for $f^{(1)}$

$$\left(I + \frac{\Delta_2}{12}\right) f^{(1)} = \Delta_2 f \tag{4.47}$$

2. Solve tri-diagonal system for $f^{(2)}$

$$R_h \, f^{(2)} = Q_h \, f^{(1)} \tag{4.48}$$

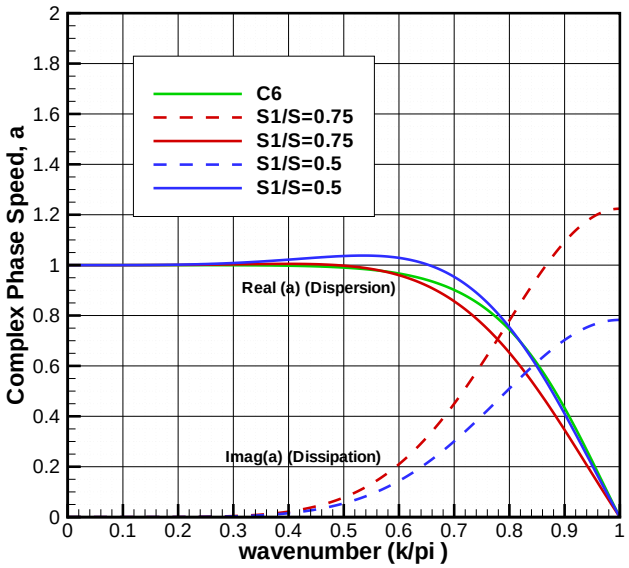

Figure 4.1: Effect of the parameter s_1 on the phase error and the numerical dissipation of the CUD-II-5 scheme

3. Evaluate

$$L_h(f) \;=\; \frac{1}{2h}\left(\Delta(s)f + s\, f^{(2)}\right) \tag{4.49}$$

Since the operators Q_h and R_h depend only on the parameter s_1, then their three-point inversion of the tri-diagonal matrices can be done at the begining of the computation and invoked when needed.

Chapter 5

Code Verification

The numerical schemes used in our Navier-Stokes code are a fourth-order Runge-Kutta scheme for time advancement and a fifth-order compact upwind scheme for space discretization of the convective terms. It is important to show that this combination of schemes does not excessively dissipate vortical flows when a relatively coarse grid is used or integration is performed over a long period of time. To this end, we consider three test cases:

1. A finite-core vortex flow that exactly satisfies the compressible Euler equations (Shu 2001).

2. Compressible laminar boundary layer flow over a flat plate.

3. Linear stability of compressible Blasius boundary.

We compare numerical results of our code with the exact analytic solution in case (1), finite-difference solution to the boundary-layer equations in case (2), and finite-difference solution to the linear stability eigenvalue problem in case (3). These cases verify the convective and viscous componenets of the code for smooth flows. To verify the code for turbulent flow, we simulate the temporal decay of isotropic homogeneous turbulence and compare the results with experimental data for grid-generated turbulence.

5.1 A Finite-Core Two-Dimensional Inviscid Vortex Flow

Shu (2001) [55] has given a finite-core vortex flow that exactly satisfies the steady two-dimensional compressible Euler equations. In dimensionless variable, the core diameter is 2, the maximum azimothal velocity is about 0.8 and the entropy is constant throughout the flow field. To simulate this flow, we use Cartesian computational domain [0,10]x[0,10] and place the vortex center at (5,5) at time $t = 0$. We apply periodic boundary conditions in two directions. The vortex should remain stationary and undamped. We can also add a uniform velocity (1,1) to the velocity field of the stationary vortex, and that causes it to convect along the diagonal and returns to its initial position in 10 units of time. In dimensionless form, the analytic solution to the velocity field of the stationary vortex is given by

$$(u(x,z), w(x,z)) = \frac{\epsilon}{2\pi} e^{0.5(1-r^2)}(-\overline{z}, \overline{x}) \tag{5.1}$$

where,
$(\overline{x}, \overline{z}) = (x-5, z-5)$, and $r^2 = \overline{x}^2 + \overline{z}^2$.

The vortex strength is given by ϵ which is assumed to be 5. The temperature and entropy are give by

$$T = 1 - \frac{(\gamma-1)\epsilon^2}{8\gamma\pi^2} e^{1-r^2} \tag{5.2}$$

$$S(x,z) = 1 \tag{5.3}$$

The temperature and entropy are related to the density ρ and the pressure p by

$$T = \frac{p}{\rho} \tag{5.4}$$

$$S(x,z) = \frac{p}{\rho^\gamma} \tag{5.5}$$

5.1.1 Grid Sensitivity Study

A uniform velocity field $(1, 1)$ is added to the above solution and used to initialize the simulation. The simulation is conducted for 10 units of time. As a result of applying periodic boundary conditions, the vortex is convected along the diagonal of the square computational domain and returns to its initial location. Three uniform Cartesian grids are used: a coarse grid of 21×21, a medium grid of 41×41, and a fine grid of 81×81 points. The number of points on the vortex diameter in the three grids is 5, 9 and 17, respectively. Figures 5.1 and 5.2 show the velocity u and the vorticity ω_y distributions along a cut through the vortex core. The results show that the vortex suffers little decay as compared to the exact solution even with a very coarse resolution of five points on the core diameter.

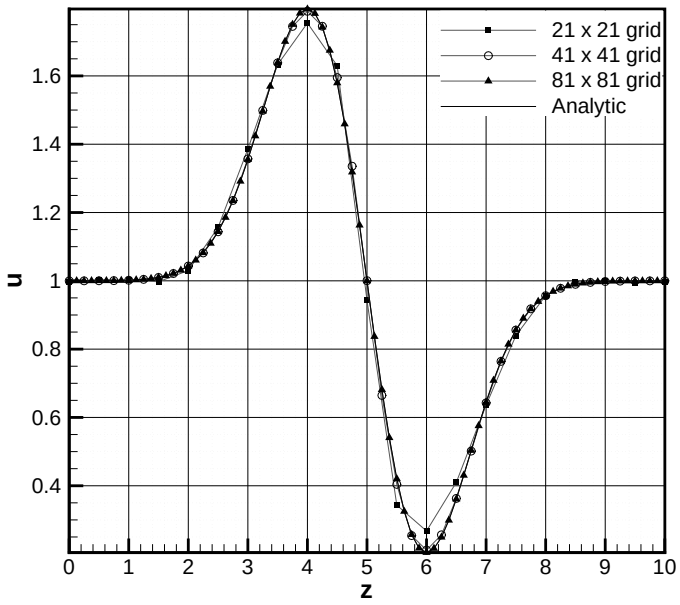

Figure 5.1: Velocity profile along the vortex core at $t = 10$

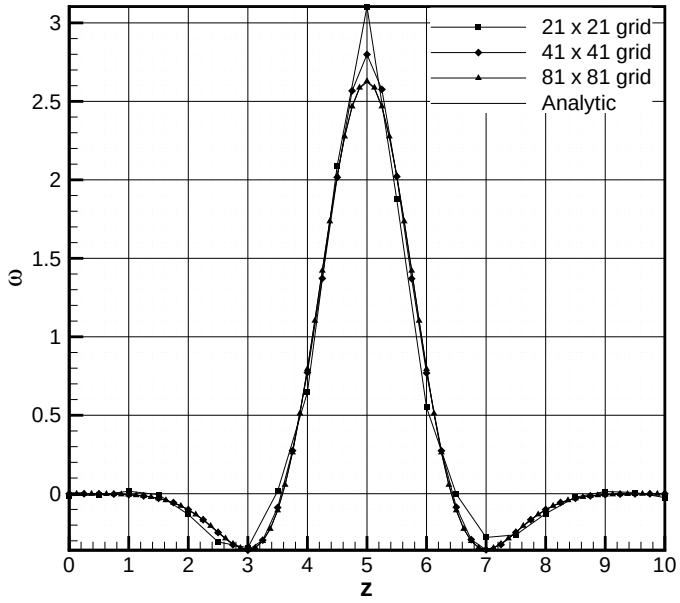

Figure 5.2: Vorticity profile along the vortex core at $t = 10$

5.1.2 Effects of Artificial Damping Coefficient

The artificial damping in the fifth-order scheme is controlled by one parameter C_5 (denoted in this chapter by C) that we have to choose. Here we investigate the effects of the coefficient C on the quality of the vortex solution. Four values of C (0.0,0.25,0.5 and 1.0) are selected and the convected vortex simulation is run for 10 units of time. Figure 5.3 shows the distribution of the u velocity component along the core of the vortex on the fine grid. The peak velocity error is about 7×10^{-5} for $C = 0.25$. This error increases by one order of magnitude in the case of $C = 1.0$.

5.1.3 Long-Time Integration

It is also important to demonstrate that the combination of the fifth-order scheme in space and the fourth-order Runge-Kutta in time can preserve the vortex over a long-time integration. The damping coefficient C is taken to be 0.25 and the fine grid is used. Comparison

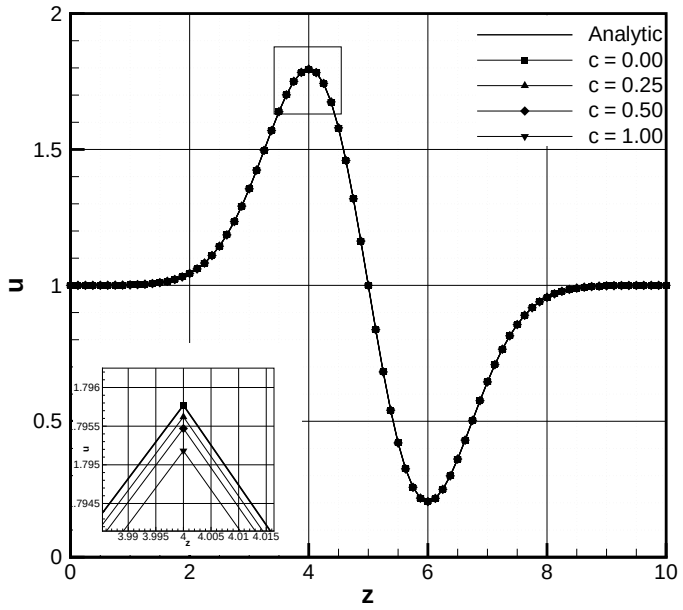

Figure 5.3: Velocity profile along the vortex core at $t = 10$ for different values of C

between the numerical results and exact analytic solution at times $t = 10$ and $t = 100$ is shown in Figures 5.4 and 5.5 for the velocity and vorticity distributions, respectively. We find a small decrease in the peak velocity of about 0.1% after $t = 10$, and a 2% increase in the peak vorticity, which may be attributed to numerical dispersion. Nevertheless, the vortex is preserved over a long integration time. This implies that the proposed combination of space and time discretization is suitable for long-time integration which is essential for turbulence simulations. Shu [7] has compared results obtained by a fifth-order WENO scheme to those of a second-order (TVD) scheme, and concluded that the later scheme is too dissipative for long-time integration.

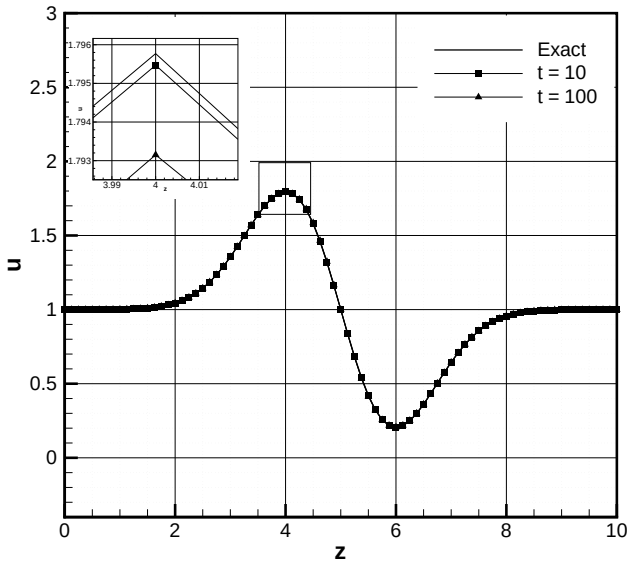

Figure 5.4: Velocity profile along the vortex core at $t = 10$ and $t = 100$

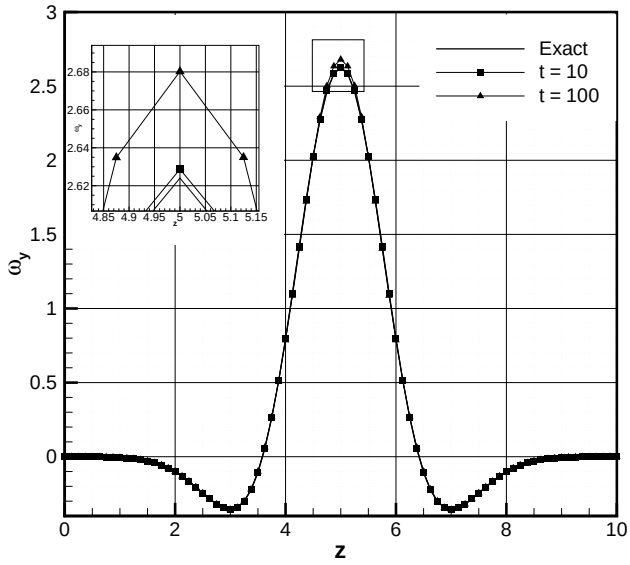

Figure 5.5: Vorticity profile along the vortex core at $t = 10$ and $t = 100$

5.2 Compressible Laminar Boundary-Layer Flow

The second test case is a compressible laminar boundary layer developing over a flat plate at zero incidence. This is a spatially developing flow that needs inflow and out flow boundary conditions. We solve the unsteady compressible Navier-Stokes equations over a rectangular domain in the $x-z$ plane, where $z = 0$ is the plate surface and $z = z_{max}$ is the top free stream boundary. The plate leading edge is at $x = 0$, and the inflow and outflow boundaries are set at x_1 and x_2, respectively, where $0 < x_1 < x_2$. The Reynolds number based on the free stream velocity U_∞ and the distance from the leading edge of the plate, x, is denoted by Re_x. At the inflow boundary, x_1, the velocity profiles $u(x_1, z)$ and $w(x_1, z)$ and the temperature profile $T(x_1, z)$ are specified by the solutions to the compressible boundary-layer equations. By employing such an inflow boundary condition we are able to avoid the leading edge region that would require a very fine grid to resolve. However, the boundary layer solution is not valid for low Re_x, or near the leading edge of the plate. In particular, the boundary-layer theory predicts a vertical velocity profile $w(x, z)$ that is singular at the leading edge, $x = 0$. In the Navier-Stokes computation both of the velocity profiles u and w need to be specified at the inflow boundary. Therefore, if the w profile at the inflow boundary is given by the boundary-layer theory, the Navier-Stokes computation will require an adjustment region. The length of the adjustment region depends on the Re_x at the inflow. We will investigate the effects of this parameter on the quality of the comparison between boundary-layer theory and Navier-Stokes computations.

5.2.1 Effects of Reynolds Number at Inflow

It was important for us to establish a minimum inflow Reynolds number Re_x above which boundary-layer profiles can be used at the inflow boundary. To this end we solve the Navier-Stokes equations in time until a steady state is obtained. A gird $nx \times nz$ of 61×31 is used. Three values of the inflow Reynolds number are considered: Re_x of 1000, 2000 and 6000. In the three cases, the computational domain in the x direction is $(x_1, x_2) = (0.1, 1.9), (0.2, 2.0), (0.6, 2.4)$, respectively. The Reynolds number based on x at any station

along the plate is the value of the non-dimensional x multiplied by $10,000$ (the dimensionless x is obtained by scaling the dimensional x^* by a viscous length scale $x = \frac{{U_\infty}^* \times x^*}{\nu^* \times 10^4}$ and similarly $z = \frac{{U_\infty}^* \times z^*}{\nu^* \times 10^4}$). Comparisons between boundary layer theory and Navier-Stokes computations are made at the middle of the computational domain, namely at $x = 1.0$, $x = 1.1$, and $x = 1.5$, for the three inflow Reynolds numbers, respectively. These stations corresponds to $Re_x = 10,000$, $Re_x = 11,000$ and $Re_x = 15,000$, respectively.

Figures $5.6 - 5.11$ show the velocity profiles u and w and temperature profile T of the developed boundary layer for inflow Re_x of 1000, to the left and 2000, to the right. The corresponding Blasius boundary layer profile is plotted on top of the numerical solution. The figures show very good agreement of the simulation with Blasius solution. However, the convergence time for the inflow Reynolds number of 1000 was about 17 time units and it was 9 time units for the case of 2000 inflow Reynolds number. Figure 5.12 shows the pressure coefficient at mid section versus time for both cases of inflow Re_x of 1000 and 2000. The figure shows that the solution oscillates several orders of magnitudes for the case of inflow Re_x of 1000 as much as that of the case of inflow Re_x of 2000. Such large oscillations can be attributed to the fact that the Blasius solution is not valid at low Reynolds number. Clearly this is expected since the Blasius solution is an asymptotic solution.

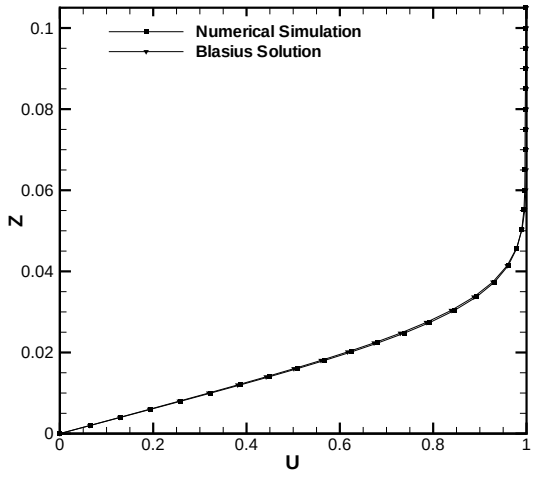

Figure 5.6: u profile from Navier-Stokes at $x = 1$ and the corresponding Blasius solution for inflow $Re_x = 1000$

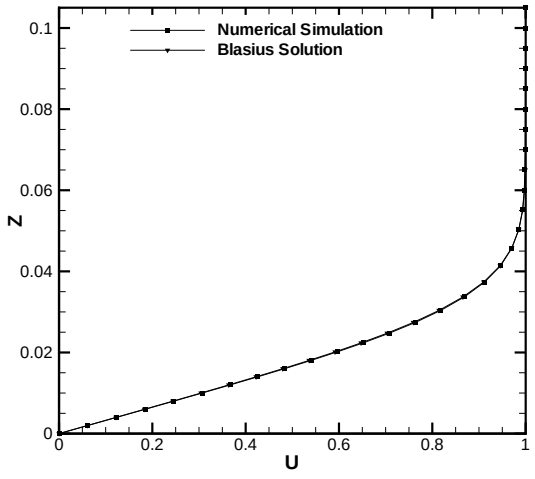

Figure 5.7: u profile from Navier-Stokes at $x = 1.1$ and the corresponding Blasius solution for inflow $Re_x = 2000$

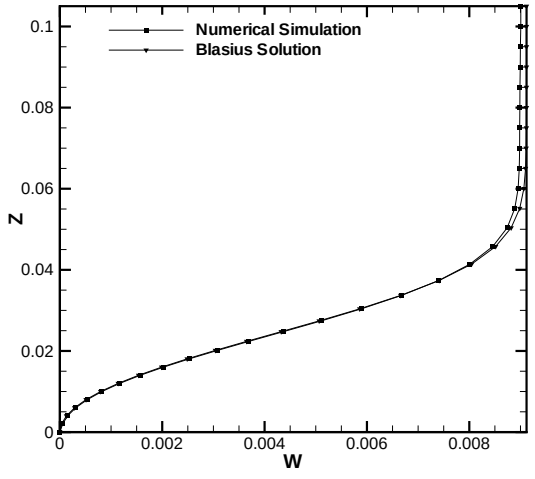

Figure 5.8: w profile from Navier-Stokes at $x = 1$ and the corresponding Blasius solution for inflow $Re_x = 1000$

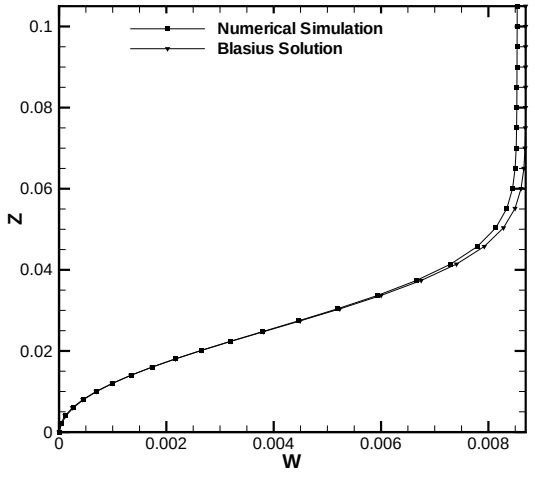

Figure 5.9: w profile from Navier-Stokes at $x = 1.1$ and the corresponding Blasius solution for inflow $Re_x = 2000$

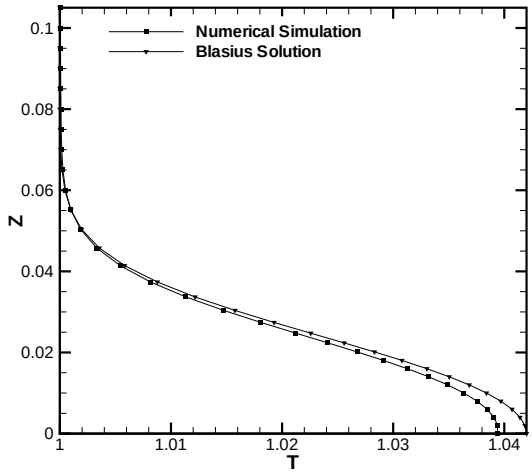

Figure 5.10: Temperature profile from Navier-Stokes at $x = 1$ and the corresponding Blasius solution for inflow $Re_x = 1000$

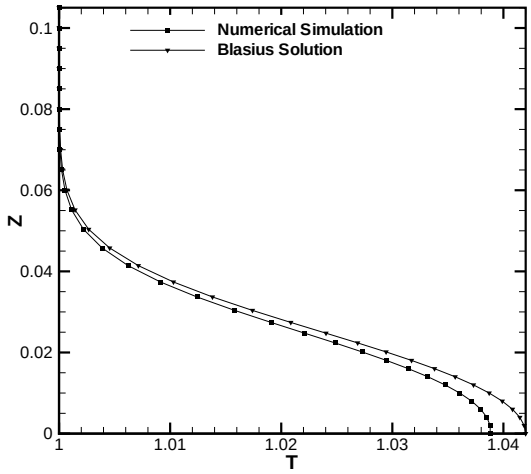

Figure 5.11: Temperature profile from Navier-Stokes at $x = 1.1$ and the corresponding Blasius solution for inflow $Re_x = 2000$

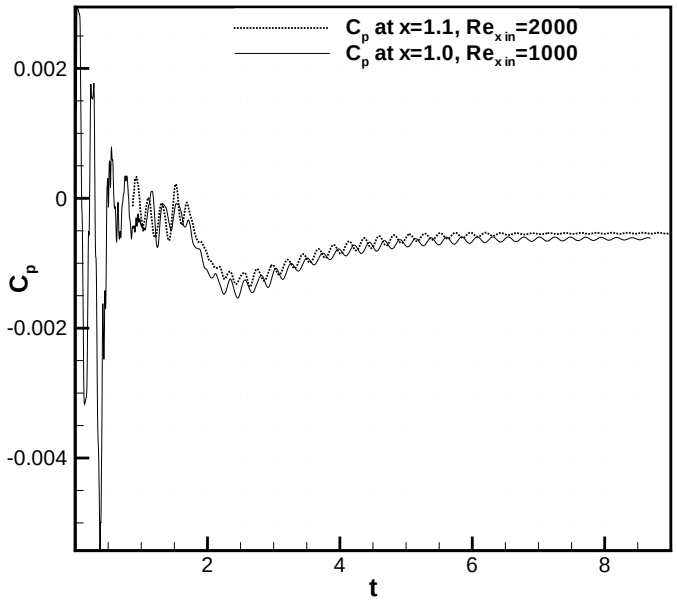

Figure 5.12: Time history of pressure coefficient at a point in plan crossing the mid x-station

5.2.2 Effects of a Sponge Layer at the Outflow Boundary

To damp the reflections of pressure waves at the domain boundary, it may be necessary to apply a sponge layer near the boundary. The sponge is mainly an artificial damping coefficient that increases towards the boundary. In this section we apply a sponge only at the outflow boundary in the x-direction to test its effect on the solution. Two x-distribution of damping coefficients have been tested. The Navier-Stokes solver is based on the fifth-order non-centered compact scheme in which flux splitting is performed by Lax-Friedrichs method. $F^{\pm} = \frac{1}{2}(F \pm C_5 \lambda q$. The flux splitting coefficient is taken to be the maximum eigenvalue of the flux Jacobian in a certain direction. This coefficient is then multiplied again by a constant which is usually chosen to be as close to zero as possible. The flux splitting adds an advantage to the compact upwind scheme. For an accurate scheme of odd order, it generates a differential term with an even order; order of the scheme plus one. This term acts as an artificial viscosity which damps numerical oscillations. It should be noted that a zero flux splitting coefficient reduces the spatial approximation to a sixth-order scheme, in which dispersion errors cause the solution to oscillate. On the other hand, a high flux splitting coefficient increases the artificial damping in the system, in other words, it increases the inherent artificial viscosity. It is important to minimize this artificial damping to avoid over dissipation. In our code, the flux-splitting coefficient, C_5, is taken to be 0.25. The sponge further modifies this constant by increasing its value near the boundary. This process dissipates reflected waves on the boundary during the numerical simulation. In this test case, we gradually modified this coefficient starting by a factor of 1 at the inlet boundary and ending by a factor of 2 at the exit boundary in the x-direction, which means that we highly damp any oscillations close to the exit boundary. Therefore, the flux splitting coefficients obtained from the eigenvalues are multiplied by a factor of 0.25 at the inflow boundary which increases to 0.5 at the outflow boundary. A grid of $nx \times nz$ of 61×31 is employed in this study. Figure 5.13 shows the values assumed by the damping coefficient along x-direction after modification. A boundary layer flow with inflow $Re_x = 6000$ and the domain extends in x-direction from 0.6 to 2.4. Figures 5.14 and 5.15 show the pressure coefficient development by both distributions at a point near the inflow boundary (at $x = 1.2$), and

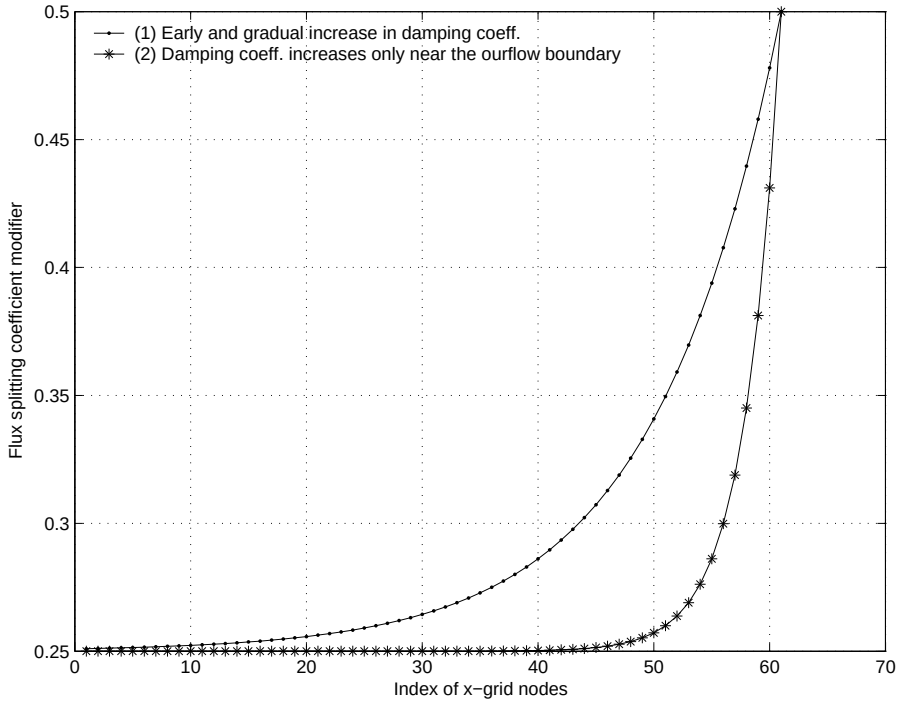

Figure 5.13: Profiles of split coefficient modifier (damping factor)

at a point near the exit flow boundary (at $x = 1.8$). At the first point (figure 5.14), one of the solutions is slightly damped while the other is not damped. It can be seen that they continue to oscillate in similar manner for a longer time than it can be seen from figure 5.15. The pressure oscillations at the point in figure 5.15 is damped early in the simulation with distribution (1), while the other one still has a larger magnitude. Although the steady state is approached quickly with larger damping, however, it might hinder capturing the proper turbulent flow field. In conclusion, the sponge layer, implemented by locally controlling the damping coefficient near the domain boundaries, seems to be working well locally and can be applied to reduce wave reflections inside the domain.

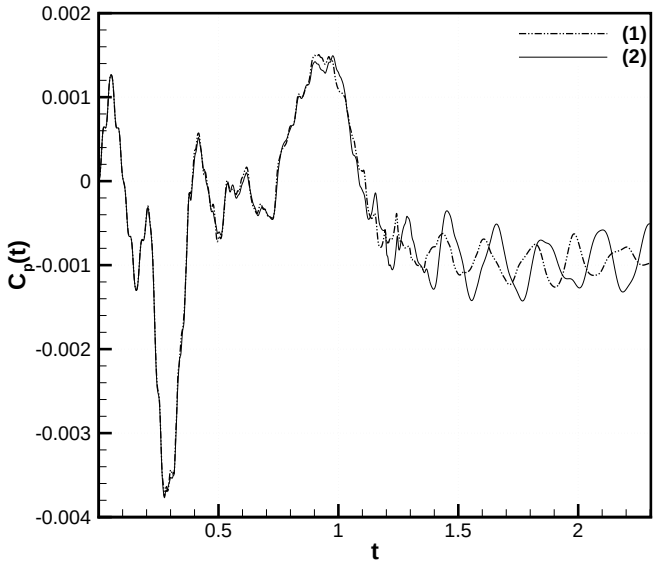

Figure 5.14: Pressure coefficient obtained upon using split coefficient modifier distributions 1 and 2 at $x = 1.2$

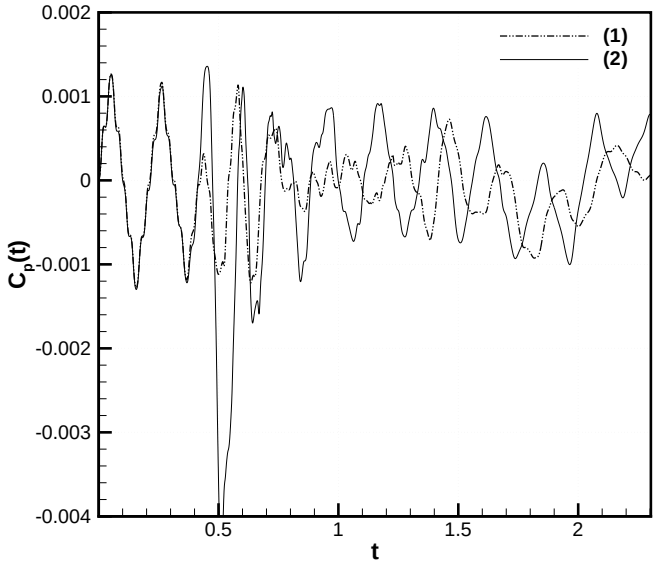

Figure 5.15: Pressure coefficient obtained upon using split coefficient modifier distributions 1 and 2 at $x = 1.8$

5.3 Comparison with Linear Stability Analysis

Comparison between direct numerical simulations and boundary-layer stability analysis provides a good test case for unsteady Navier-Stokes codes because of the complex structure of the eigenfunctions and the sensitivity of the eigenvalues (growth rates) to viscous effects near the wall, especially for viscous instabilities. The growth rate of a Tollmien-Schlichting wave is determined by the balance between viscous dissipation and production of disturbance kinetic energy. Therefore, the growth rate is a good indicator of the ability of a finite-difference scheme in resolving near wall regions, where viscous dissipation dominates, and critical layers where production of disturbance is significant.

Here, we outline the general procedure of linear stability theory. In the linear stability theory, a flow field variable is the sum of a basic state and a disturbance. In a compressible boundary layer flow, the basic state is obtained as the solution to Prandtl boundary-layer equations. The disturbance equations are obtained by subtracting the basic state equations from the resulting system of equations of the total flow. The system is further reduced by dropping the non-linear disturbance quantities. The resulting system of equations is a linear one with coefficients that depend on the basic state; the disturbance quantities are the unknowns. Parallel flow approximations are then invoked by assuming that the basic state depends only on the coordinate normal the wall. A normal mode solution is assumed for the disturbances and substituted into the linear system of equations. For the semi-infinite domain of a boundary-layer flow, the disturbances vanish at the wall and are bounded in the far field. Finally, we have a linear system of ordinary differential equations with homogenous boundary conditions, which is an eigenvalue problem. In the present analysis we assume the

disturbance to be a three-dimensional wave. The total flow quantities are given by

$$u(x,y,z,t) = U_o(z) + \hat{u}(z)e^{i(\alpha x+\beta y-\omega t)} \tag{5.6}$$

$$v(x,y,z,t) = \hat{v}(z)e^{i(\alpha x+\beta y-\omega t)} \tag{5.7}$$

$$w(x,y,z,t) = \hat{w}(z)e^{i(\alpha x+\beta y-\omega t)} \tag{5.8}$$

$$p(x,y,z,t) = \hat{p}(z)e^{i(\alpha x+\beta y-\omega t)} \tag{5.9}$$

$$T(x,y,z,t) = T_o(z) + \hat{T}(z)e^{i(\alpha x+\beta y-\omega t)} \tag{5.10}$$

Where $U_o(z)$ and $T_o(z)$ define the basic state obtained from the solution of compressible boundary-layer equations. The exponential terms represent the disturbance. α and β are the non-dimensional wavenumbers in the x and y directions. For temporal stability analysis, α and β are assumed to be real numbers and ω to be complex. $\hat{u}(z)$, $\hat{v}(z)$, $\hat{w}(z)$, $\hat{p}(z)$ and $\hat{T}(z)$ are the complex eigenfunctions corresponding to the complex frequency, $\omega(\omega = \omega_r + i\omega_i)$, and ω_i is the temporal growth rate. If $\omega_i > 0$, the disturbance is unstable and it grows with time and the disturbance decays when $\omega_i < 0$. The eigenvalue problem is solved numerically using a compact fourth-order finite difference scheme.

In this section, we use $\delta = \sqrt{\nu^* x^* / {U^*}_\infty}$ as a reference length. Navier-Stokes computations are initialized using the linear stability eigenfunctions. Two wave numbers in the $x-$direction are selected to be studied at Re_δ: $\alpha = 0.14$ and 0.21. At such a Reynolds number, the first wave number is a growing disturbance, while the other is a decaying disturbance. The numerical solution is marched one time step. A value of ω_i is extracted at z where the disturbance kinetic energy is maximum. The effects of grid resolution and the aforementioned damping coefficient on the linear stability of two and three-dimensional waves are also investigated.

Table 5.1 presents the basic state parameters for which the stability analysis is performed. Table 5.2 shows the disturbance parameters of the six cases understudy and the numerical damping coefficent C employed with each case. The growth rates of the waves under consideration are found from the linear stability theory and are presented in table 5.3, they are denoted by $(w_i)_{LS}$. Table 5.4 lists the growth rates obtained from the numerical simulation

$(w_i)_{NS}$ of the compressible boundary layer. Table 5.5 and 5.6 show the effects of the damping coefficient at the coarse grid used in the study on the disturbance growth rate. Table 5.5 data show the results at a weakly amplified disturbance (at the given Reynolds number and wave numbers) while table 5.6 shows the results of a weakly damped wave (at the given Reynolds number and wave numbers). It can be seen that the Navier-Stokes results match well the linear stability solution. The development of the solution for the two wave numbers considered are well resolved even with coarse grid.

Table 5.1: Basic State Parameters of the Linear Stability Analysis

Mach No.	:	0.5
Reynolds No.	:	860
Prantl No.	:	0.7075
T_∞	:	$273K$

Table 5.2: Disturbance Parameters for Linear Stability Analysis

Case No.	1	2	3	4	5	6
wave no in x-direction (α)	0.14	0.21	0.14	0.21	0.14	0.21
wave no in y-direction (β)	0	0	0.1	0.1	0.1	0.1
C(damping factor)	0.5	0.5	0	0	$0.0, 0.25, 0.5, 0.75$	$0.0, 0.25, 0.5, 0.75$

Table 5.3: Growth Rates Obtained From Linear Stability Theory

Case No.	$(w_r)_{LS}$	$(w_i)_{LS}$
1	0.04895	0.00201
2	0.07818	-0.00581
3	0.05176	0.00083
4	0.07877	-0.00889
5	0.05176	0.00083
6	0.07877	-0.00889

Table 5.4: Disturbance Growth Rate Obtained From Direct Numerical Simulation of Flat Plate Boundary Layer

Case No.	C	$GridSize$	$(w_i)_{NS}$	$(w_i)_{NS}/(w_i)_{LS}$
1	0.25	$09 \times 171 \times 09$	0.00182	0.86075
		$17 \times 171 \times 09$	0.00200	0.99562
		$33 \times 171 \times 09$	0.00201	0.99985
		$65 \times 171 \times 09$	0.00201	0.99999
2	0.25	$09 \times 171 \times 09$	−0.00621	1.06910
		$17 \times 171 \times 09$	−0.00583	1.00210
		$33 \times 171 \times 09$	−0.00581	0.99998
		$65 \times 171 \times 09$	−0.00581	0.99991
3a	0.25	$09 \times 171 \times 64$	0.00084	1.00650
		$17 \times 171 \times 64$	0.00083	1.00010
		$33 \times 171 \times 64$	0.00083	1.00000
		$65 \times 171 \times 64$	0.00083	1.00000
3b	0.25	$09 \times 171 \times 09$	0.00084	1.00350
		$17 \times 171 \times 17$	0.00083	1.00000
		$33 \times 171 \times 33$	0.00083	1.00000
		$65 \times 171 \times 65$	0.00083	1.00000
4a	0.25	$09 \times 171 \times 64$	−0.00888	0.99891
		$17 \times 171 \times 64$	−0.00889	0.99997
		$33 \times 171 \times 64$	−0.00889	0.99998
		$65 \times 171 \times 64$	−0.00889	0.99998
4b	0.25	$09 \times 171 \times 09$	−0.00889	0.99929
		$17 \times 171 \times 17$	−0.00889	0.99998
		$33 \times 171 \times 33$	−0.00889	0.99998
		$65 \times 171 \times 65$	−0.00889	0.99998
5	0	$09 \times 171 \times 09$	0.00084	1.00350
		$17 \times 171 \times 17$	0.00083	1.00000
		$33 \times 171 \times 33$	0.00083	1.00000
		$65 \times 171 \times 65$	0.00083	1.00000
	0.25	$09 \times 171 \times 09$	0.00055	0.66244
		$17 \times 171 \times 17$	0.00082	0.99002
		$33 \times 171 \times 33$	0.00083	0.99964
		$65 \times 171 \times 65$	0.00083	0.99992
	0.5	$09 \times 171 \times 09$	0.00027	0.32137
		$17 \times 171 \times 17$	0.00082	0.98000
		$33 \times 171 \times 33$	0.00083	0.99926
		$65 \times 171 \times 65$	0.00083	0.99982
	0.75	$09 \times 171 \times 09$	−0.00002	−0.01970
		$17 \times 171 \times 17$	0.00081	0.96998
		$33 \times 171 \times 33$	0.00083	0.99888
		$65 \times 171 \times 65$	0.00083	0.99982
6	0	$09 \times 171 \times 09$	−0.00889	0.99929
		$17 \times 171 \times 17$	−0.00889	0.99998
		$33 \times 171 \times 33$	−0.00889	0.99998
		$65 \times 171 \times 65$	−0.00889	0.99998
	0.25	$09 \times 171 \times 09$	−0.00924	1.03900
		$17 \times 171 \times 17$	−0.00890	1.00120
		$33 \times 171 \times 33$	−0.00889	1.00010
		$65 \times 171 \times 65$	−0.00889	1.00010
	0.5	$09 \times 171 \times 09$	−0.00959	1.07880
		$17 \times 171 \times 17$	−0.00891	1.00250
		$33 \times 171 \times 33$	−0.00889	1.00020
		$65 \times 171 \times 65$	−0.00889	1.00020
	0.75	$09 \times 171 \times 09$	−0.00995	1.11850
		$17 \times 171 \times 17$	−0.00893	1.00380
		$33 \times 171 \times 33$	−0.00890	1.00040
		$65 \times 171 \times 65$	−0.00889	1.00020

Table 5.5: Summary of the DNS Results Using A Coarse Grid ($09 \times 171 \times 09$) While Employing A Weakly Amplified Disturbance, Case 5

Numerical Damping Coef.	$(w_i)_{NS}$	$(w_i)_{NS}/(w_i)_{LS}$
$c = 0.0$	0.00084	1.00350
$c = 0.05$	0.00078	0.93514
$c = 0.1$	0.00072	0.86694
$c = 0.2$	0.00061	0.73055
$c = 0.25$	0.00055	0.66244
$c = 0.5$	0.00027	0.32137
$c = 0.75$	−0.00002	−0.01970

Table 5.6: Summary of the DNS Results Using A Coarse Grid ($09 \times 171 \times 09$) While Employing A Weakly Damped Disturbance, Case 6

Numerical Damping Coef.	$(w_i)_N S$	$(w_i)_N S/(w_i)_L S$
$c = 0.0$	−0.00889	0.99929
$c = 0.05$	−0.00896	1.00720
$c = 0.1$	−0.00903	1.01520
$c = 0.2$	−0.00917	1.03110
$c = 0.25$	−0.00924	1.03900
$c = 0.5$	−0.00959	1.07880
$c = 0.75$	−0.00995	1.11850

5.4 Temporal Decay of Isotropic Turbulence

Because of its simplicity and universality, temporal decay of isotropic homogenous turbulence has been used often as a test case for evaluation of sub-grid scale (SGS) models and numerical schemes for large eddy simulation (LES). In this study, simulations are obtained for grid generated turbulence as in the experiments of Comte-Bellot and Corrsin [9] (referenced to as CBC in this chapter). Case 'a' with grid size $M = 5.08$ cm is considered. The reference length is $L_r^* = M = 5.08$ cm, and reference velocity is $U_r^* = U = 10$ m/s. The Reynolds number is $Re = 34000$. The computational domain is a cube of side $10.8M$ moving with velocity U downstream of the grid. An initial velocity field which is divergence free and matches the 3D energy spectrum at station $Ut/M = 42$ is generated by a method described by Durbin and Reif [10] (page 241). The speed of sound at the reference temperature is adjusted so that the fluctuation Mach number is approximately 0.2. The initial density

and pressure fluctuations are zero. Periodic boundary conditions are applied in the three Cartesian coordinates.

For 32^3 grid, the 3D energy spectrum function $E(k)$ is shown in Figure 5.16 through 5.19. The symbols in these figures are the experimental data listed in table 3 of CBC. Lax-Friedrichs flux vector splitting (FVS) with ($C_5 = 0.1$) is used in Figure 5.16 while van Leer FVS is used in Figure 5.17. It is clear that the CUD5 is too dissipative if van Leer FVS is used. The results in Figure 5.16 were found to be sensitive to the value of C_5. Also shown in Figure 5.16 are results without the dynamic sub-grid scale model; there is a build-up of energy at high wave-numbers and computation is terminated at $Ut/M = 91$.

Instead of using CUD5 scheme at every time step, we have investigated its use in combination with the non-dissipative sixth-order compact (C6) scheme by Lele [32]. The CUD5 scheme is used to advance the solution one time step for every few time steps of the C6 scheme, that number is denoted by $IC6$. We refer to this combination as the C6CUD5 scheme. With Lax-Friedrichs FVS there is a trade off between C_5, which controls the level of artificial dissipation in the CUD5 scheme, and IC6. For IC6=7 and $C_5 = 0.8$, the 3D energy spectrum function is shown in Figure 5.18. Good agreement with experiments is evident at $Ut/M = 98$, but farther downstream at $Ut/M = 171$ there is significant decay at high wave-numbers and intermediate scales are overestimated. With van Leer FVS we found an upper limit of 6 on IC6 for which no energy build-up at high wave-numbers occurs. The results in Figure 5.19 show good agreement with the experimental data at $Ut/M = 98$, but significant decay at high wave-numbers at $Ut/M = 171$ is found. The intermediate scales are better predicted with van Leer than with Lax-Friedrichs FVS.

The decay of the resolved turbulent kinetic energy, computed as a volume average in the physical space

$$\frac{1}{2}q^2 = \frac{1}{2}\langle \widetilde{u}_i \widetilde{u}_i \rangle \tag{5.11}$$

is depicted in Figure 5.20 for the same conditions as Figures 5.18 and 5.19. After a short transient period, the decay follows the anticipated theoretical power law, $t^{-1.4}$, Hinze [18],

Eq 3.188, page 267. The transient period is because the initial field does not represent real turbulence. An iterative procedure for generating initial velocity field as given by Carati et al. [5] should be used. The dynamic model coefficient C is shown in Figure 5.21.

Next, we presents results for the C6CUD5 scheme on a 64^3 grid. The three-dimensional energy spectrum function is shown in Figure 5.22 for Lax-Friedrichs FVS ($IC6 = 10, C_5 = 1.0$) and in Figure 5.23 for van Leer FVS ($IC6 = 9$). Although the low and intermediate wave-numbers are well predicted by both FVS methods, van Leer FVS provides better resolution of the intermediate scales than Lax-Friedrichs FVS. Both FVS methods still damp the high wave-numbers relative to the unfiltered experimental data. Spectra from simulations without a SGS model are also shown, the build up of energy at high wave-numbers terminates the simulations at time $Ut/M = 59$ and $Ut/M = 56$ for the two methods of FVS. The decay of the resolved turbulent kinetic energy is shown in Figure 5.24, and the dynamic model coefficients C is shown in Figure 5.25. They have the same characteristics as with the 32^3 grid.

We note that the high wave-numbers in Figures 5.18 and 5.22 suffer higher damping at the later stage of decay (e.g. at $Ut/M = 171$) than at the early stage (e.g. $Ut/M = 98$). This is due the composition of the parameter $\lambda = |\widetilde{u}| + \widetilde{a}$ in the Lax-Friedrichs FVS. Initially $\widetilde{a}$ is about five times $|\widetilde{u}|$, but that ratio increases to about 12 as the turbulence decays. Because mass and energy fluxes are proportional to $\widetilde{u}$, damping provided by splitting the flux increases with time. If we take $\lambda = |\widetilde{u}|$ instead of $|\widetilde{u}| + \widetilde{a}$, then the damping effect of splitting the flux also decays with time. The energy spectrum function on a 32^3 grid with this form of λ is shown in Figure 5.26, consistent decay of the high wave-number range is evident. The decay of the resolved turbulent kinetic energy and the dynamic model coefficient C for this simulation are shown in Figures 5.27 and 5.28, respectively.

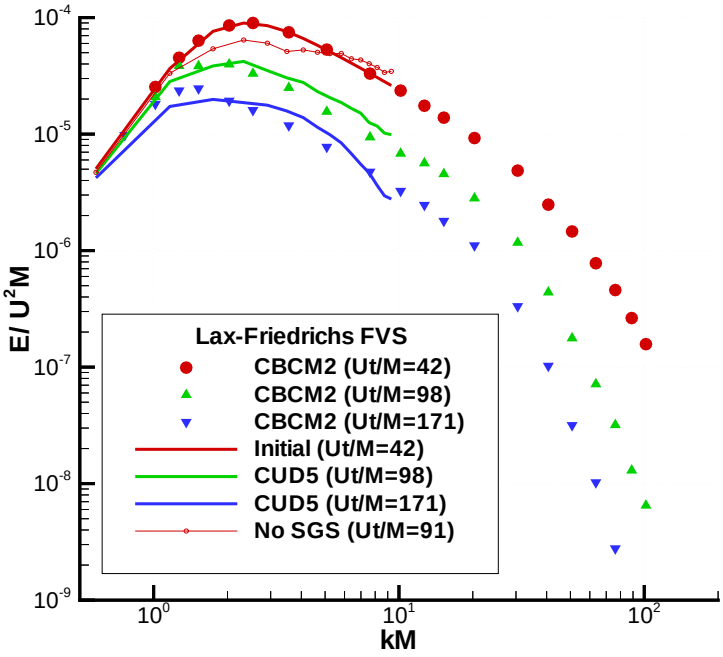

Figure 5.16: Energy Spectrum, 32^3 grid, $C_5 = 0.1$.

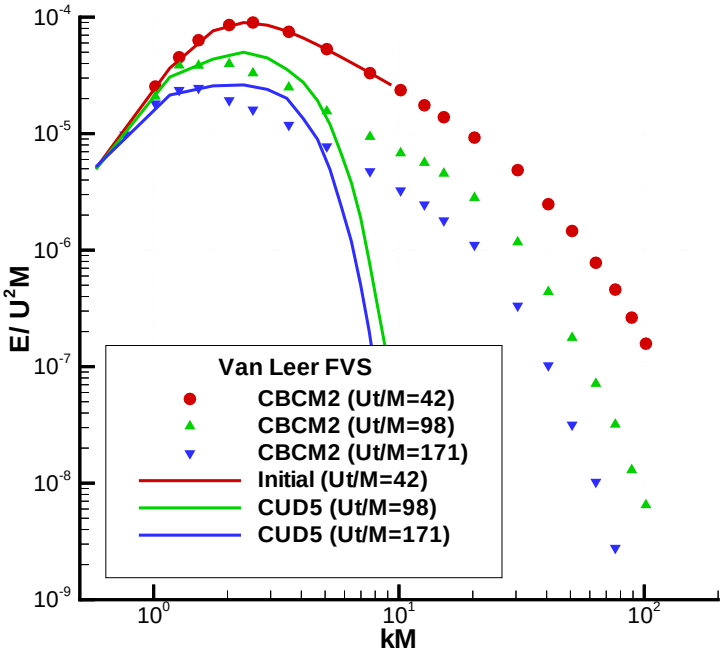

Figure 5.17: Energy Spectrum, 32^3 grid.

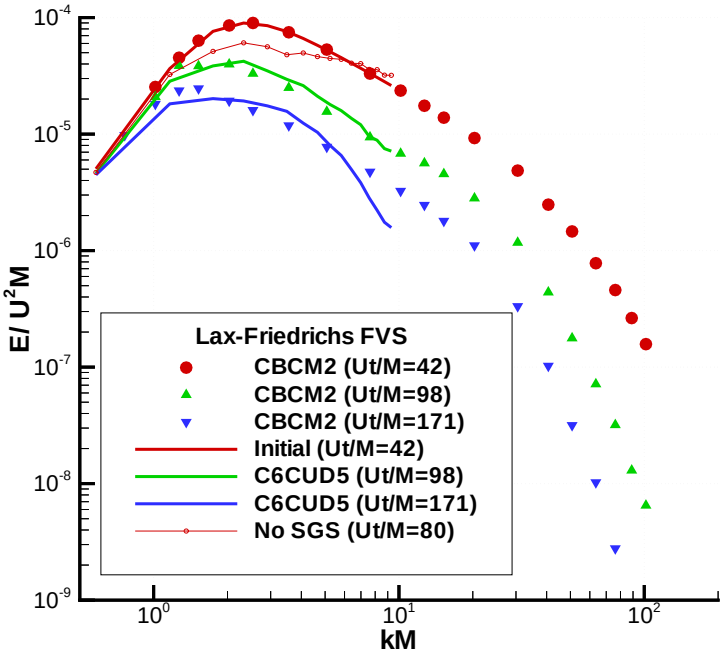

Figure 5.18: Energy Spectrum, 32^3 grid, $IC6 = 7, C_5 = 0.8$.

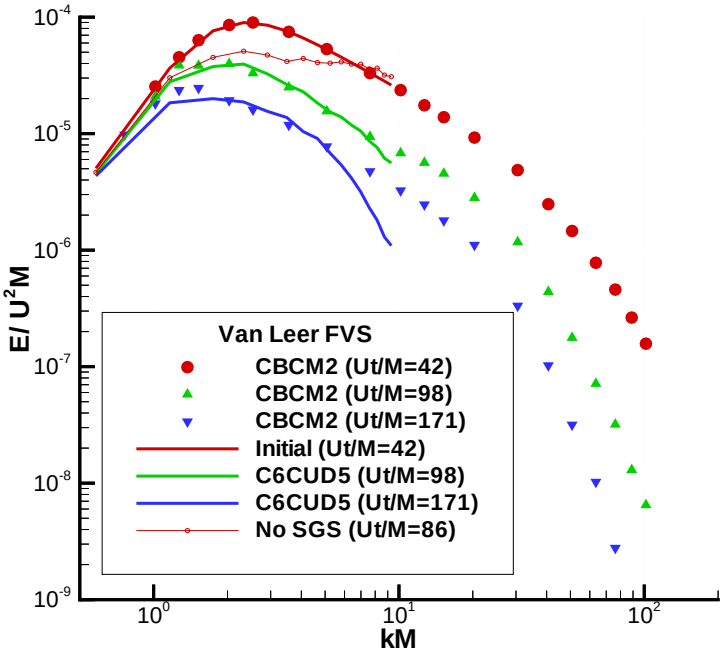

Figure 5.19: Energy Spectrum, 32^3 grid, $IC6 = 6$.

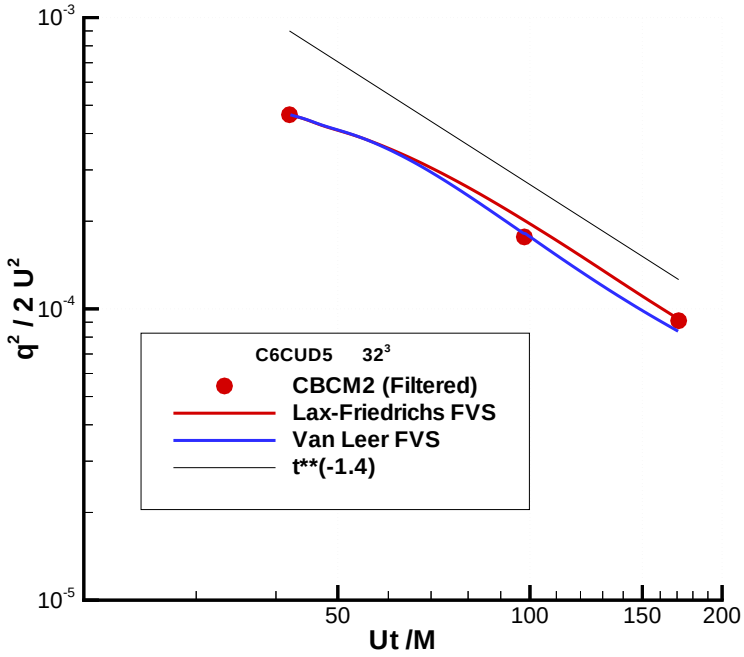

Figure 5.20: Decay of Turbulent Kinetic Energy.

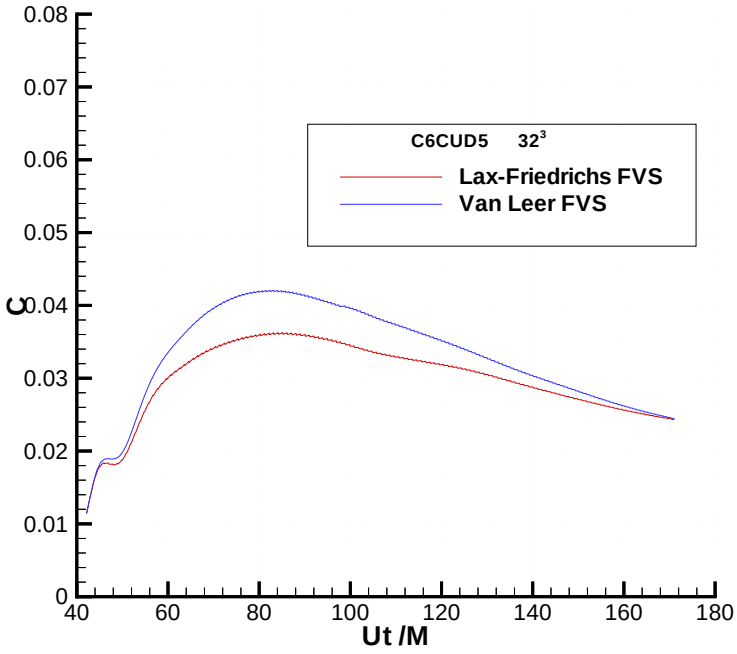

Figure 5.21: Dynamic Model Coefficient.

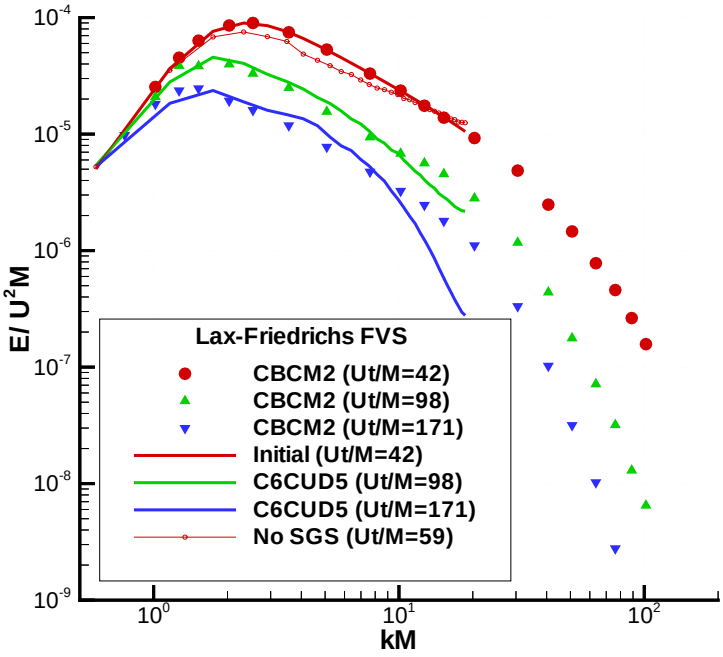

Figure 5.22: Energy Spectrum, 64^3 grid, $IC6 = 10, C_5 = 1.0$.

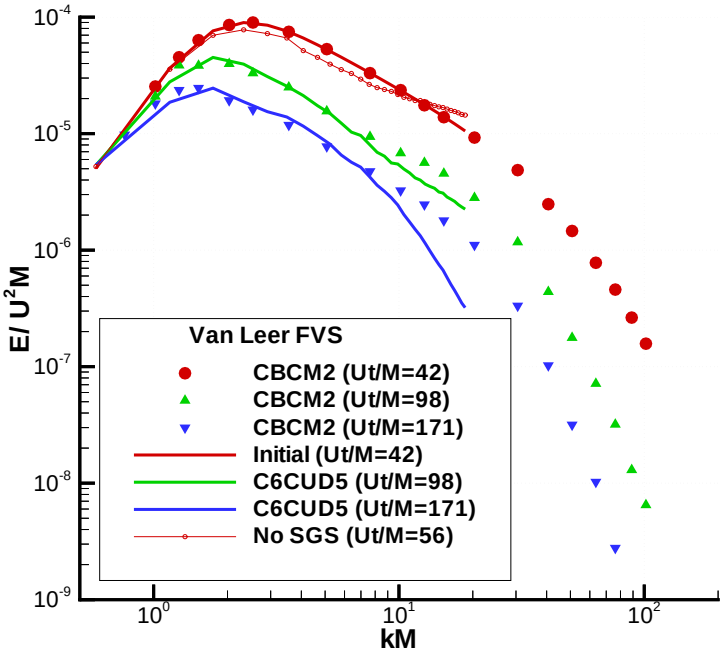

Figure 5.23: Energy Spectrum, 64^3 grid, $IC6 = 9$.

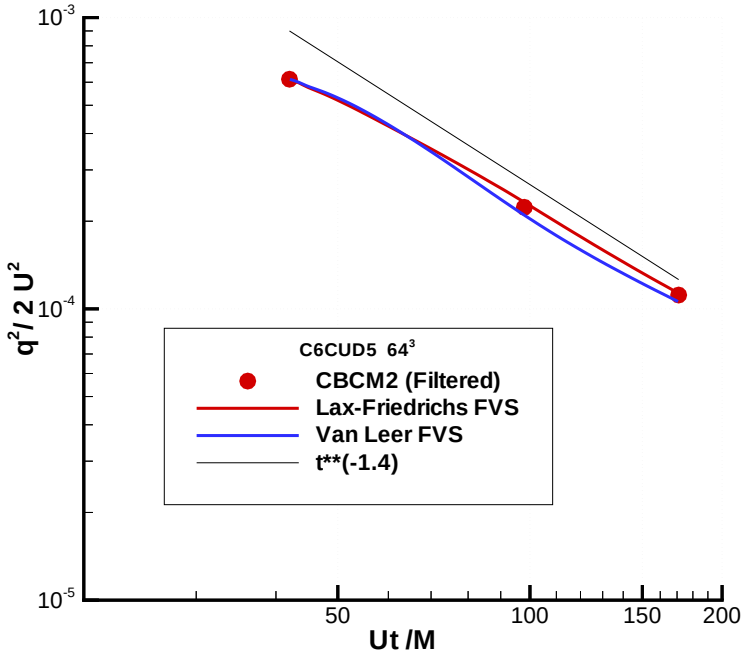

Figure 5.24: Decay of Turbulent Kinetic Energy.

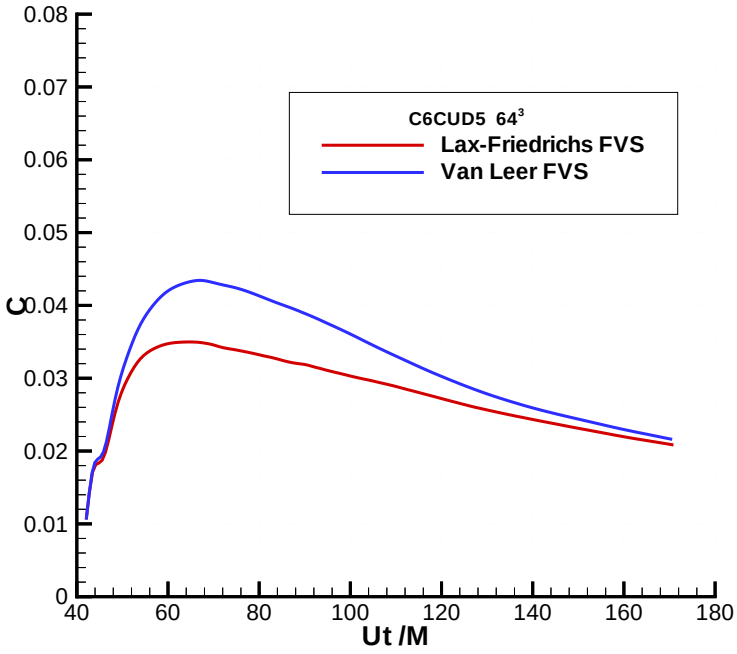

Figure 5.25: Dynamic Model Coefficient.

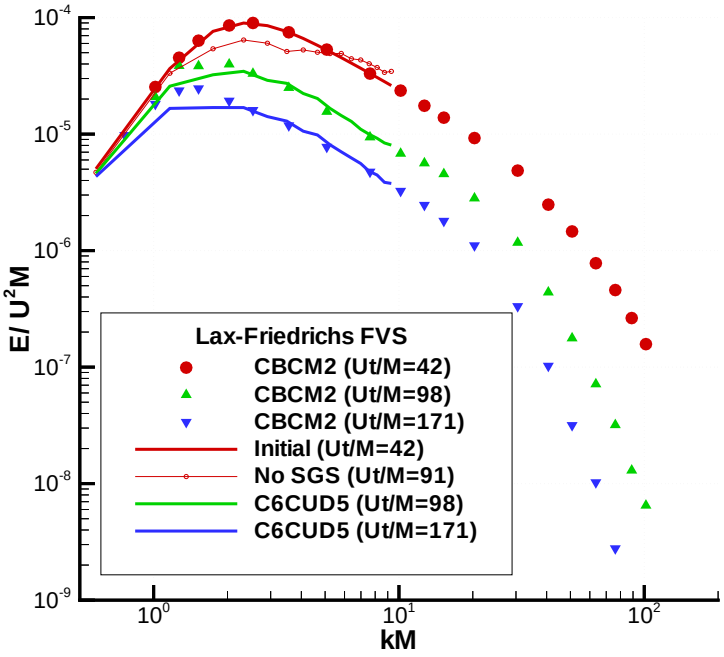

Figure 5.26: Energy Spectrum, 32^3 grid, $IC6 = 9, C_5 = 12$.

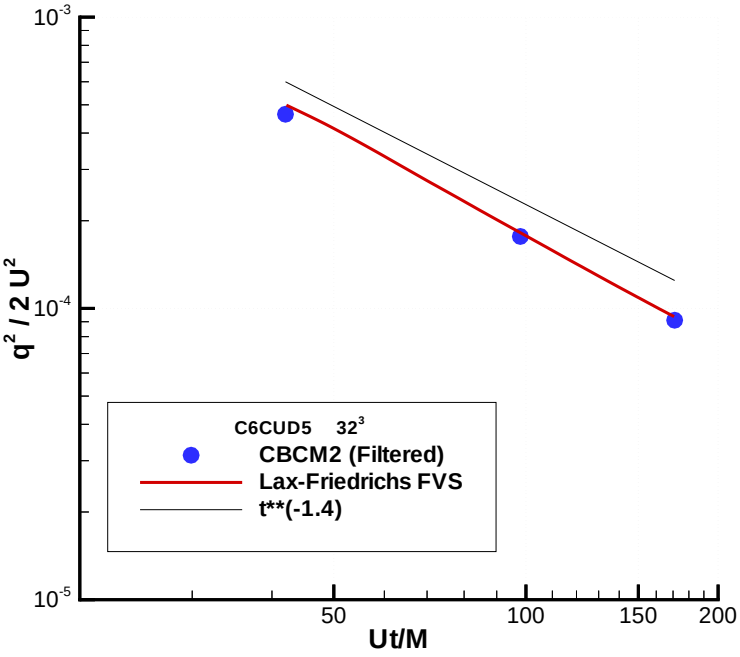

Figure 5.27: Decay of Turbulent Kinetic Energy.

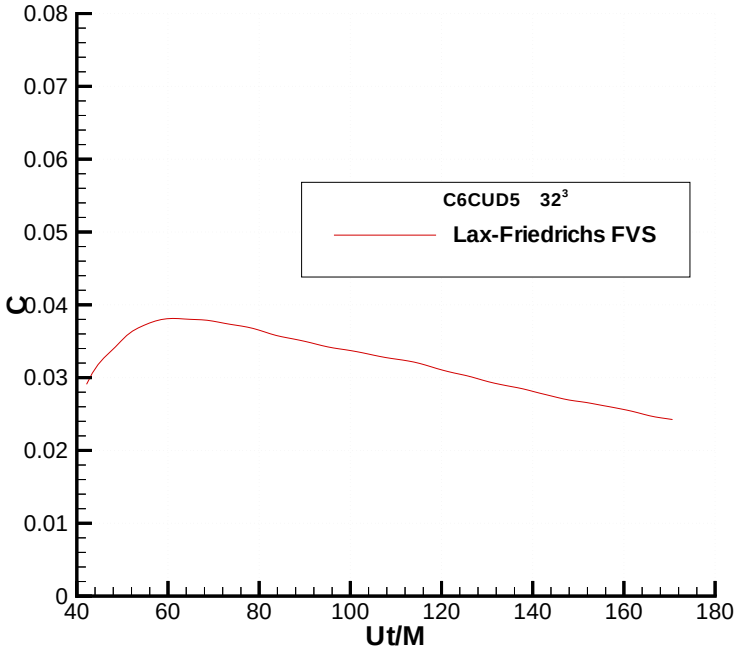

Figure 5.28: Dynamic Model Coefficient.

Chapter 6

Large-Eddy Simulation

6.1 Numerical Model

The CUD-II-5 scheme is used to study the effects of free stream homogeneous turbulence on the flow structure and pressure distribution over a surface-mounted prism. We use Lax-Friedrichs flux vector splitting (FVS) with $C_5 = 0.5$. In one case the prism is placed in a smooth uniform flow, and in another case homogeneous isotropic turbulence with von Karman spectrum is superimposed on the uniform flow at the inflow boundary. The integral length scale is half the prism height, and turbulence intensity at the inflow boundary is 15% of the mean free stream velocity.

The prism height H and the mean free stream velocity U_∞ and temperature T_∞ are used as reference values. The prism has a length/height ratio of 3.425 and span/height ratio of 2.275. The prism is placed on a flat plate ($z = 0$) with its longer side parallel to the free stream velocity. The Reynolds number Re is 30,000 and the Mach number M_∞ is 0.2. In a Cartesian coordinate system, the bounding surfaces of the prism are $x = \pm 1.7125$, $y = \pm 1.1375$, $z = 0$ and $z = 1$. The computational domain extends from the inflow boundary at $x = -10$ to the outflow boundary at $x = 15$. The spanwise boundaries are at $y = \pm 5$. A no-slip wall is assumed at $z = 0$ and free stream boundary at $z = 10$. At the inflow boundary, we specify the velocity and temperature, and extrapolate the pressure from inside the domain.

At the outflow boundary, we extrapolate the transverse velocity components (v and w) and temperature, and determine the pressure and streamwise velocity u using one-dimensional characteristic boundary conditions. The density is obtained from the equation of state. Symmetry conditions are applied at the spanwise planes $y = \pm 5$. On solid walls, no-slip and adiabatic wall conditions are used.

The computational domain including the prism is shown in figure 6.1 with dimensions scaled with the prism height H. The flow field is divided into non-overlapping rectangular domains. A Cartesian grid is generated in each domain in such a way as to ensure the continuity of the grid Jacobian and its derivatives at the interfaces. This continuity is important to achieve high order accuracy. A nonuniform Cartesian grid of $(161 \times 81 \times 101)$ points is used for smooth oncoming flow and a grid of $(181 \times 81 \times 101)$ is used for turbulent incident flow. The minimum step size next to a solid surface is 0.007 in the $x-$direction and 0.01 in the $y-$ and $z-$directions. Figures 6.2 and 6.3 show projections of the gird employed in this study for the smooth flow case in the $xz-$plane and in the $xy-$plane, respectively.

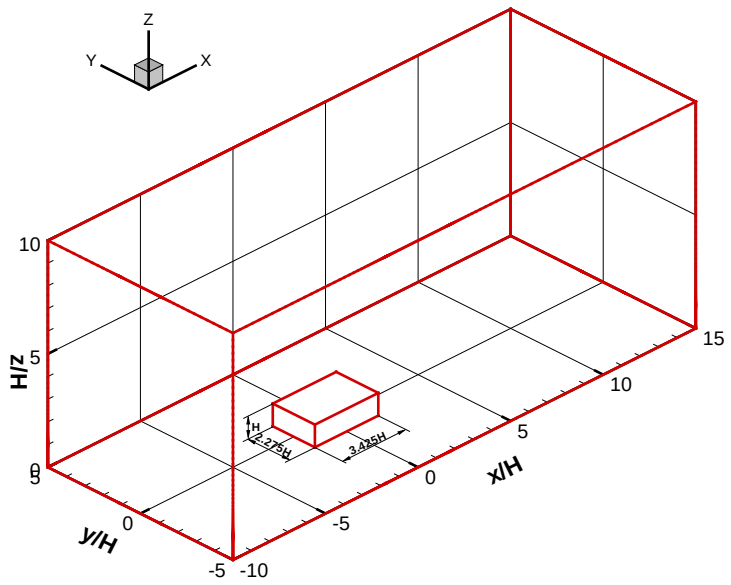

Figure 6.1: Computational domain for surface-mounted prism

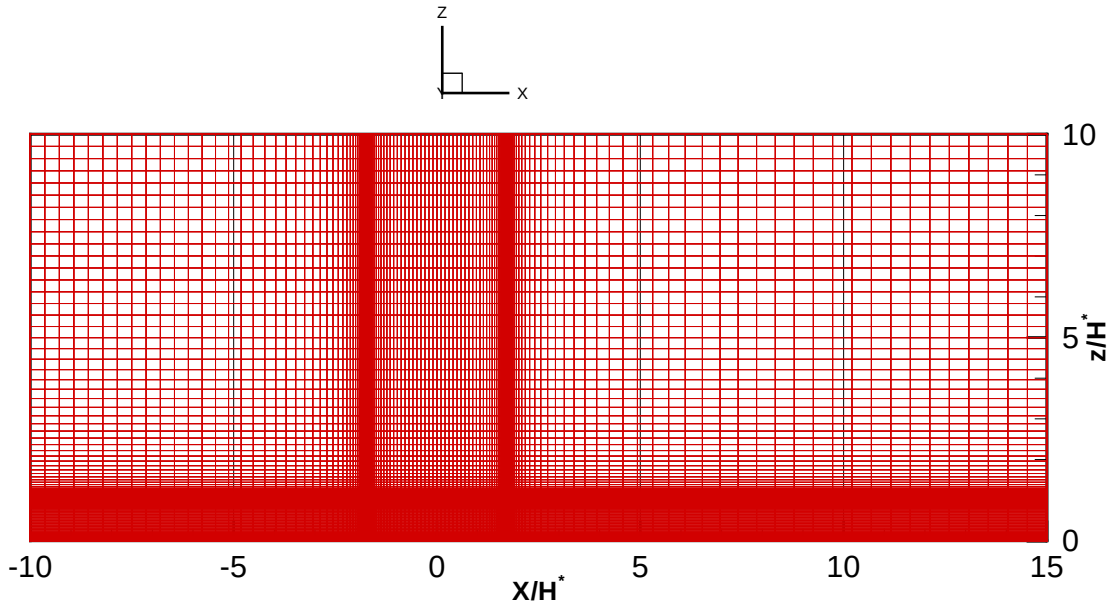

Figure 6.2: Stretched Cartesian grid in the $xz-$plane

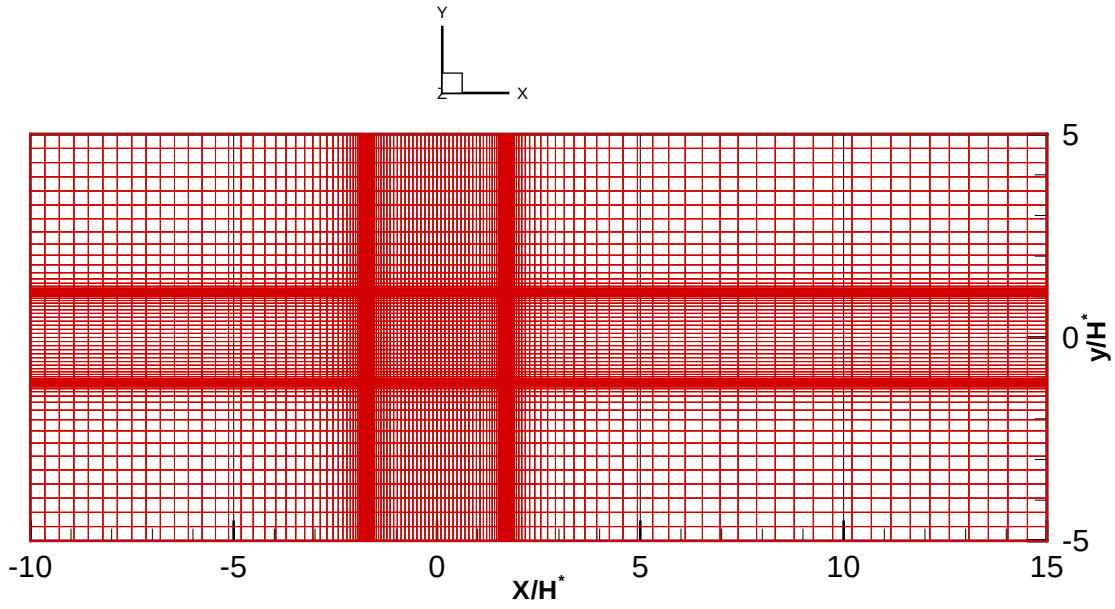

Figure 6.3: Stretched Cartesian grid in the $xy-$plane

6.2 Mean Flow Field

In this section, the mean flow field variables are presented for both the smooth inflow and compared with the homogeneous turbulence inflow case. We present the mean velocity components U, V and W, the mean vorticity $\vec{\Omega}$, and the mean pressure coefficient C_p. These variables are obtained by averaging over time $t = 136$ units of nondimensional time. The resolved turbulent kinetic energy, TKE, and Reynolds stress, $\overline{u'_i u'_j}$, are also presented. Throughout the discussion, we give more attention to the description of the flow in the same planes used in the discussion of the experiments. These planes are the plane of symmetry with respect to the mean flow, i.e. plane of $y = 0$, which we call the center plane. The second plane is the plane located at the edge of the prism, $y = 1.1325$. The third plane is the plane midway between the center plane and the edge plane, which is the plane of $y = 0.567$. It should be noted that the origin of the coordinate system employed in the numerical results data is different from the one used in the description of the experimental results (see figures 6.2 and 6.3). In the following discussion we will denote the homogeneous turbulence inflow case by turbulent inflow case and the case of uniform incident flow by smooth inflow case for simplicity. Limited comparisons between the experimental and the numerical results are presented due to **the large difference in the Reynolds number and characteristics of the incident flows**, turbulence and vorticity characteristics. nevertheless, we will try to establish qualitative and quantitative comparisons between the experimental results and the numerical results where corresponding data are available. Additionally, the definitions of flow reversal, separation and reattachment used in chapter 3 are also employed in this section.

6.2.1 Velocity Field

We first compare LES results and our experimental data. Figures 6.4 and 6.5 show $x - z$ distributions of the the mean velocity components U and W obtained from the experiments, cases I and II, and from the numerical simulations, smooth inflow and turbulent inflow in the center plane on the prism roof. It should be noted that, in figures 6.4 and 6.5, the left

bottom corner, $(x, z) = (0, 1)$, of the figures is at the prism leading edge. The velocities presented in these figures are normalized with the mean free stream velocity in each case. The figures show that the reversed flow velocities in the results of the numerical simulation with smooth inflow are higher than the other three cases. Even after the flow reattaches at $x = 2.3$ in this case, the $U-$velocity component is less than the other three cases until $x = 3$, after that all the four cases show comparable levels of $U-$velocity above the roof. In the mean time, the experimental results show that the velocities in the reversed flow on the roof obtained from case I, where the inflow is dominated by spanwise vorticity, are much less than the other cases from both experiments and numerical simulations. Additionally, case II in the experimental results shows good comparison with the numerical simulation results with homogeneous turbulent inflow, for the $U-$ and $W-$velocity components for $x \geq 0.5$ until the end of the recirculation region, in both cases at $x = 1.75$. Figure 6.6 shows contour lines of zero $U-$velocity in the center plane on the roof of the prism. Recall that this zero $U-$velocity meets the solid wall, the roof surface, at the reattachment point. It is observed in figure 6.6 that the size of the reversed flow region, that is the region enclosed by the roof surface and the zero $U-$velocity contour line, is approximately the same in case II in the experimental results and in the numerical simulation results with homogeneous turbulent inflow. Moreover, the reattachment points in these two cases are almost at the same location at a distance of about 1.75 units downstream of the prism leading edge. It can be seen from figure 6.4 that for $x > 2$, the $U-$velocity levels in the numerical simulation results for smooth inflow case, are considerably higher than the other three cases for $1 < z < 1.4$. This could be attributed to the fact that the flow is very energetic in this case which allows it to gain higher velocities near the wall compared to the other cases.

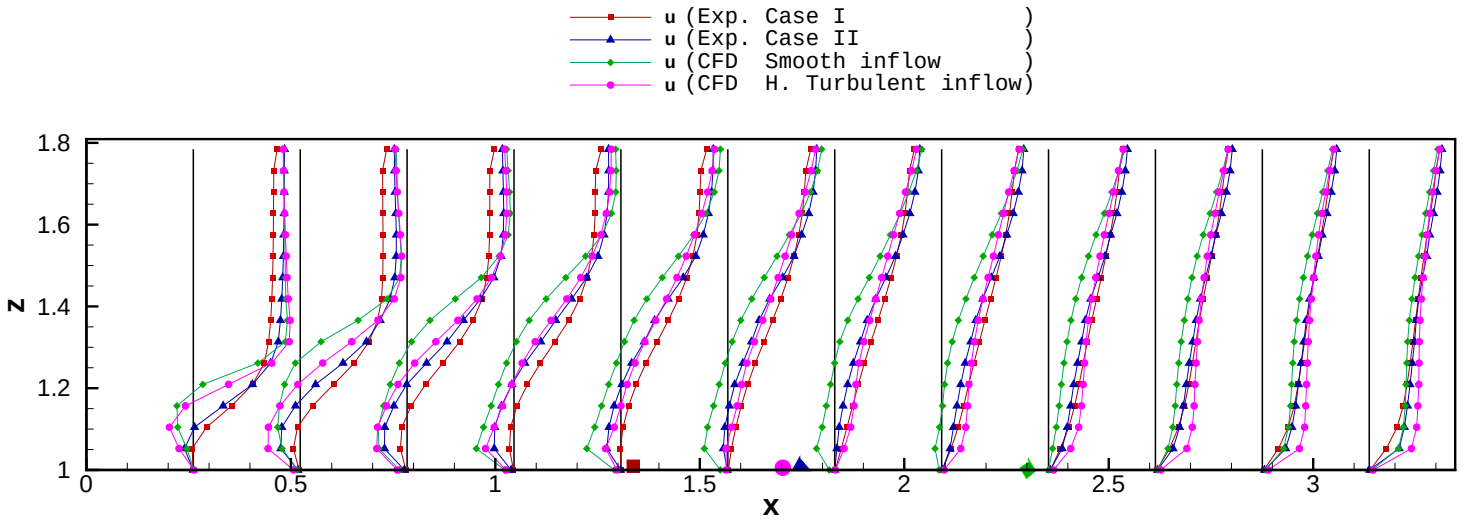

Figure 6.4: Distributions of normalized $U-$velocity component on the roof of the prism at the center plane obtained from experiments and LES

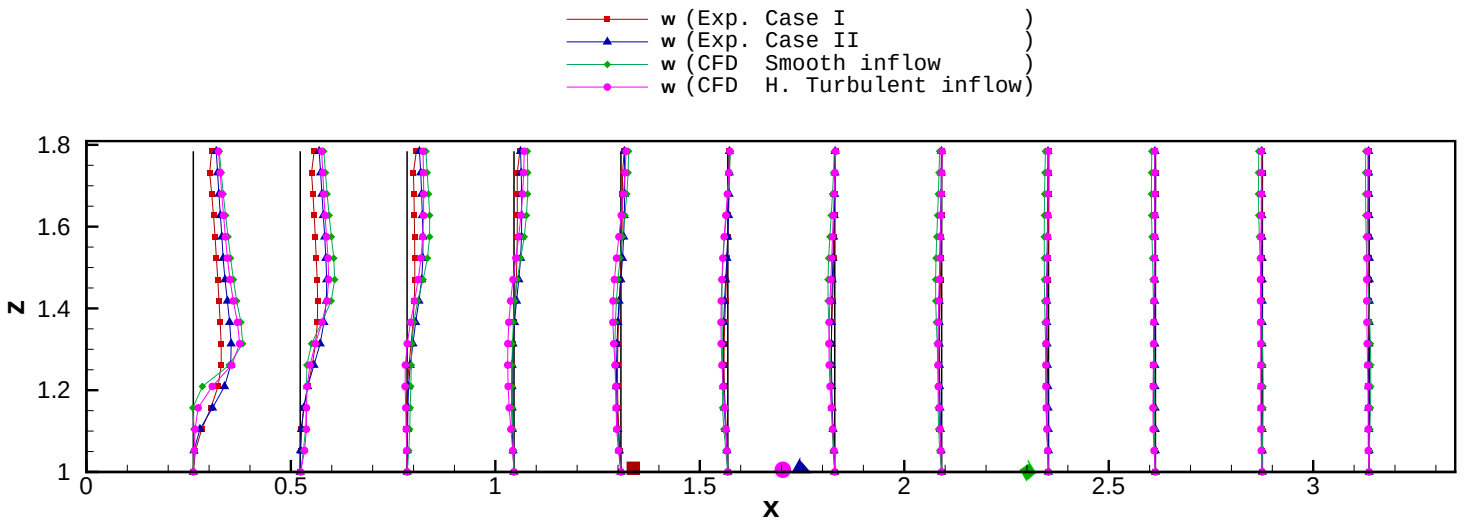

Figure 6.5: Distributions of normalized $W-$velocity component on the roof of the prism at the center plane obtained from experiments and LES

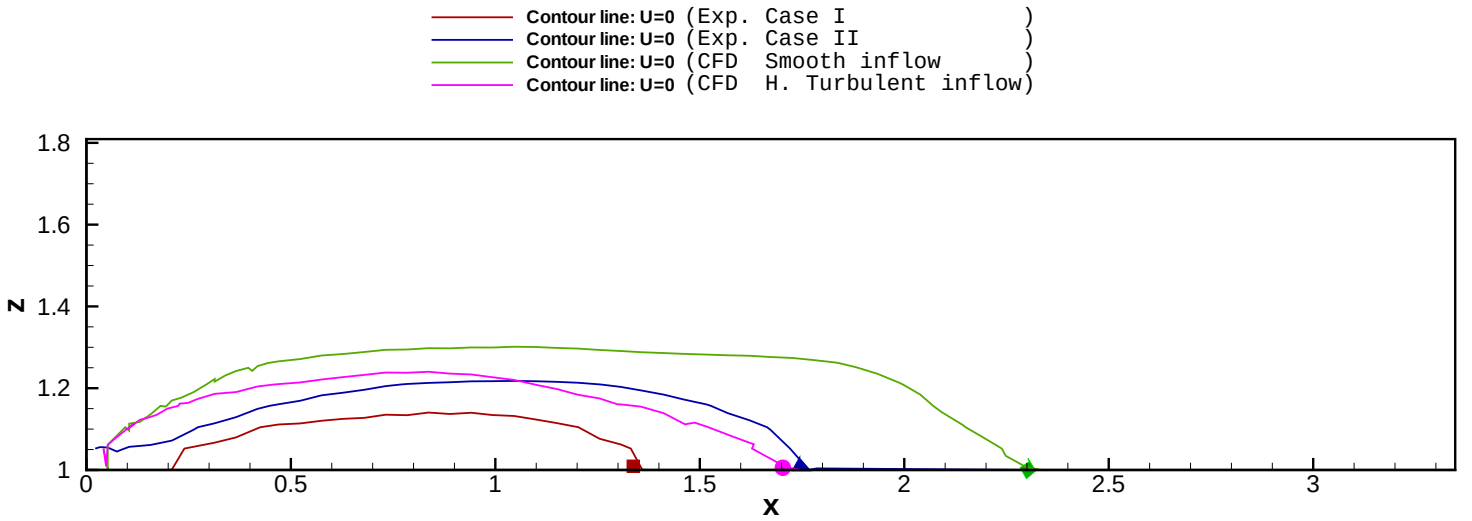

Figure 6.6: Zero $U-$velocity contours on the roof of the prism at the center plane obtained from experiments and LES

Next we present more details about LES results. The mean velocity field is presented in this section mainly through the mean flow streamlines, and mean U, V, and W velocity components. An example of the resolved velocity field is shown in figure 6.7. The figure shows the velocity vectors, for the case of smooth incoming flow, in the center plane with focus on the the domain around the upwind face of the prism. It can be seen that the boundary layer is well resolved by the current gird. The boundary layer is resolved by eleven points of fine grid steps. In the mean time, small eddies, like the secondary corner vortex ahead of the upwind face of the prism, are also well resolved. Flow separation in the incident boundary layer and secondary separation underneath the separating flow on the windward edge of the prism are also well resolved in figure 6.7. Obviously, large flow structures ahead of the prism and on the roof of the prism are well resolved. More details on flow topology is given in figure 6.8 which shows the friction lines on the ground plane. These are streamlines obtained at the plane corresponding to the second grid point in the $z-$direction. It can be seen that the flow is symmetric with respect to the mean flow direction.

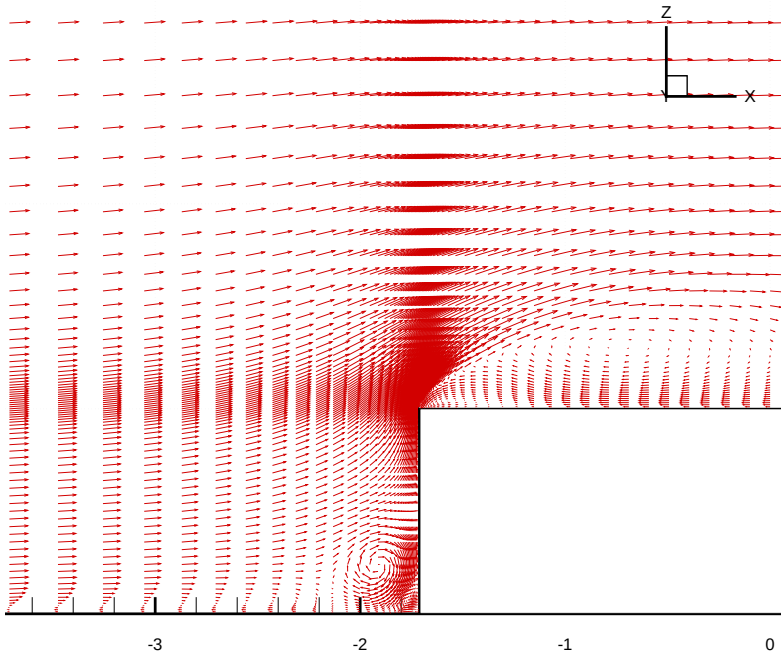

Figure 6.7: Velocity vectors in the center plane in the case of smooth inflow

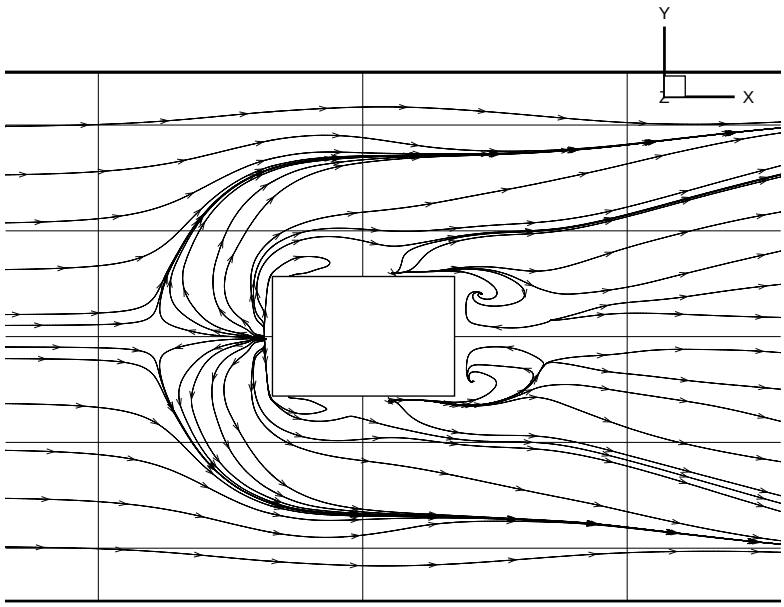

Figure 6.8: Friction lines on the ground in the case of smooth inflow

Figures 6.9 and 6.10 and figures 6.11 and 6.12 show three-dimensional perspective of the streamlines patterns obtained from the experiments and the numerical simulations. It should be noted that only half of the prism is shown in figures 6.9 and 6.10 while the whole prism is shown in figures 6.11 and 6.12. It can be seen that the stagnation points on the upwind face on the prism in the center, quarter and edge planes appear on a line parallel to ground in cases I and II in the experiments and in the case of turbulent inflow in the numerical simulations while they do not seem on the same elevation in the case of smooth inflow. It should be notes that, in the experiments, the resulting stagnation points occur at higher levels, about $z = 0.7$, than in the numerical simulations results where they occur at z about 0.5. This difference can be essentially attributed to the difference in the boundary layer profiles; thicker boundary layers are involved in the experiments than the ones involved in the numerical simulations. The size of the recirculation zone above the roof reduces, as we move from the center plane to the edge plane, in case II in the experiments at a rate comparable to that of the case of homogeneous turbulent inflow. Moreover, patterns of the zero W line in case II in the experiments matches well those of the numerical simulations with turbulent inflow, and more specifically in the bend in this line in the center plane.

From the comparisons of the velocity profiles in the center plane and the streamlines patterns between case II in the experiments and the turbulent inflow case in the numerical simulations, it can be seen that there is very good agreement between the two cases. It should be noted that in case II in the experiments, turbulence is generated by vertical cylinders placed at relatively large enough distance upstream of the prism, about 40 times the prism height. These cylinders generate vortical structures in their wakes with alternating vorticity that is oriented mainly in the $z-$direction. These vortical structures interact with each other as they approach the prism resulting in a rather close environment to the homogeneous turbulence case except in regions very close to the ground where stream wise vortices are expected to develop around the vertical cylinders and thus produce higher turbulence intensities near the ground. The integral length scales in the incident flow in case II in the experiments are the diameters of the cylinders which are about 0.32 and 0.5 the prism height which matches that of the turbulent inflow in the numerical simulations, 0.5 the prism height.

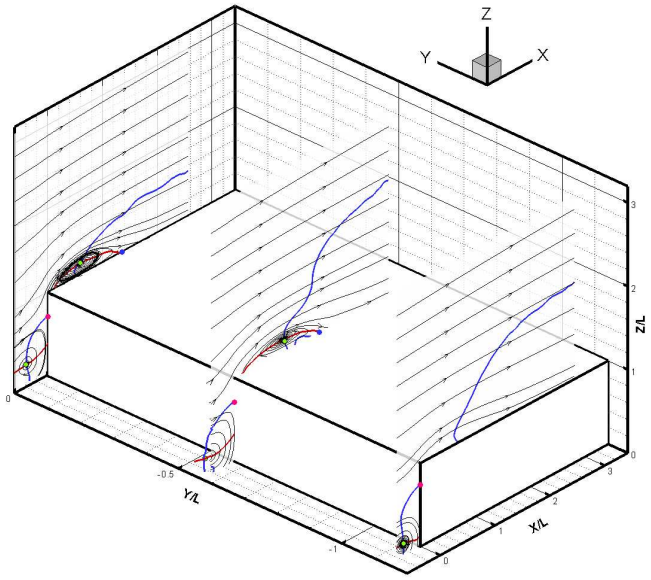

Figure 6.9: Streamlines pattern at the center, quarter and edge planes averaged over 2 seconds. Case I, experiments

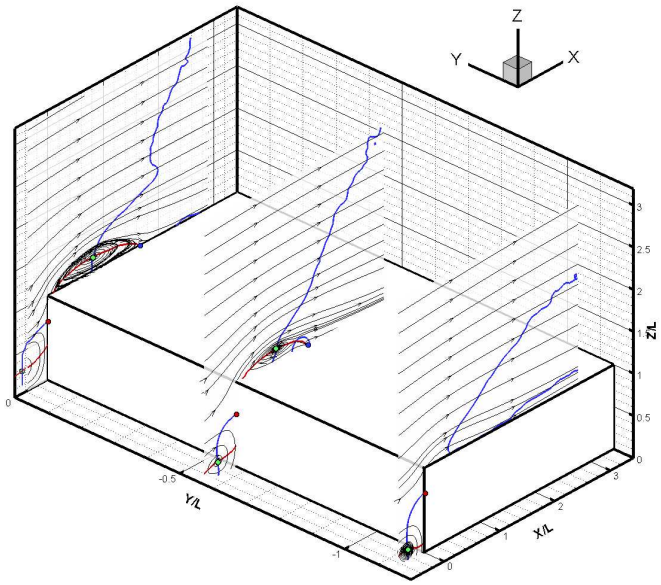

Figure 6.10: Streamlines pattern at the center, quarter and edge planes averaged over 2 seconds. Case II, experiments

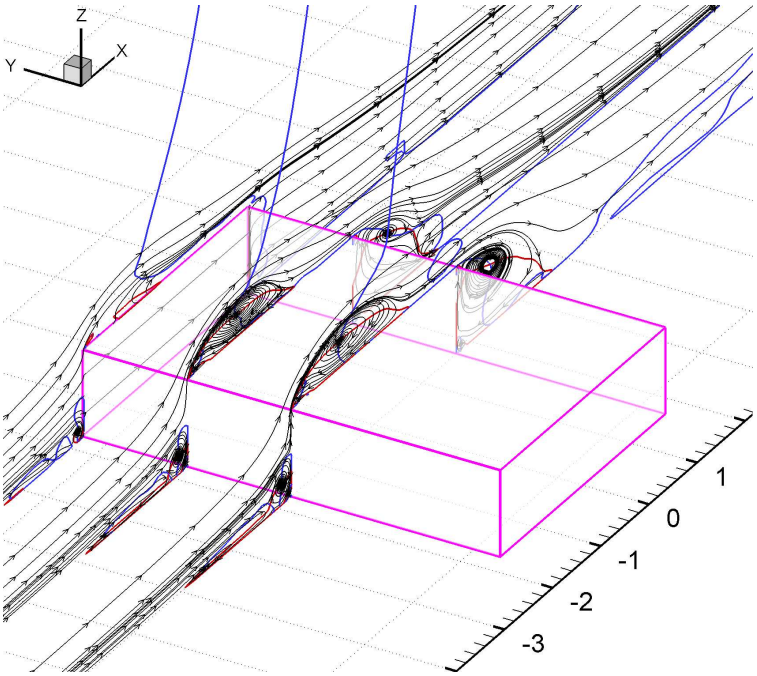

Figure 6.11: Streamlines pattern at the center, quarter and edge planes for the case of smooth inflow, LES

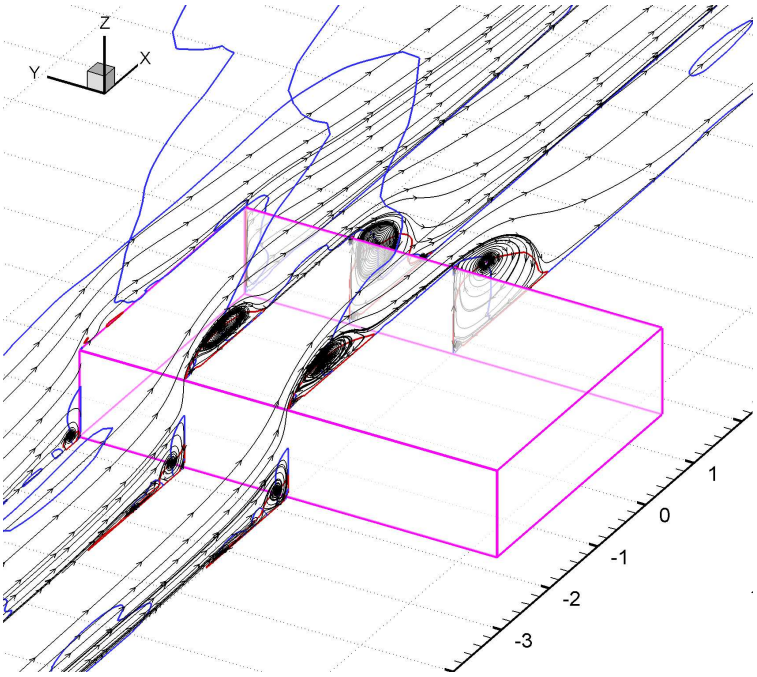

Figure 6.12: Streamlines pattern at the center, quarter and edge planes for the case of turbulent inflow, LES

Figures 6.13 and 6.14 show the streamline patterns in the center plane for the cases of smooth flow and homogeneous turbulence flow. Points where important flow activities and structures are shown on the the two figures.

Figures 6.13 and 6.14 show that in both cases considered, a primary separation of the approaching boundary layer occurs ahead of the prism at $x = -3.95$ in the case of smooth inflow and at $x = -3.5$ in the turbulent inflow case. The approaching flow comes to stagnation at the upwind face of the prism at $z = 0.48$ for the case of smooth inflow and at $z = 0.56$ for the case of turbulent inflow. The incident flow is divided by the stagnation stream line into two parts. The flow above the stagnation streamline moves above the roof of the prism. The flow below the stagnation streamline rolls up in clockwise direction, forming a vortex along the $y-$axis, known in literature as the horseshoe vortex. The center of the vortex is located at $(x, z) = (-1.91, 0.24)$, which corresponds to $0.2H$ from the upwind face along $x-$axis, for the smooth inflow case, and is located at $(x, z) = (-1.95, 0.19)$, or $0.2H$ apart from the upwind face of the prism, for the turbulent inflow case. A secondary eddy, rolling in opposite direction, can be seen at the corner where the forward face of the prism meets the ground. This secondary eddy is of much smaller size than the horseshoe vortex and it appears in the same location in both inflow cases considered. Investigation of the instantaneous flow shows that these vortices are not steady, but they move around their mean positions.

The separating boundary layer flow, upstream of the horseshoe vortex, undergoes a secondary flow reversal at an elevated point above the ground at the interface between the separated boundary layer flow and the horseshoe vortex. A saddle point in the flow field is formed between the horseshoe vortex and the separating boundary layer. That point appears at $0.45H$ and at $0.53H$ upstream of the windward face of the prism for the case of smooth inflow and the case of turbulent inflow, respectively. For both inflow cases, the separated flow near the ground, in the region between the primary separation point and the saddle point, reverses and moves upstream on the ground wall generating a thin recirculation zone ahead of the horseshoe vortex. It can be seen from figures 6.13 and 6.14 that this recirculation zone is thinner in the case of turbulent inflow than in the case of smooth inflow.

The part of the incident flow that moves above the stagnation streamline, in the center plane,

forms a boundary layer on the upwind face of the prism which separates as it moves past the sharp leading edge of the prism. The separating shear layer bends sharply towards the roof as it is convected by the incoming flow which has high momentum in the streamwise direction. The separating flow reattaches further downstream on the roof and forms a large recirculation bubble. The center of the recirculation zone and the reattachment points are respectively $(x, z) = (-0.72, 1.31)$ and at $x = 0.71$ on the roof in the case of smooth inflow, and $(x, z) = (-1.01, 1.24)$ and at $x = 0.05$ on the roof in the case of turbulent inflow. In terms of distance from the leading edge of the prism, the flow reattaches at $2.43H$ for the case of smooth inflow and at $1.76H$ in the case of turbulent inflow. In addition, the cores of the recirculation appear downstream of the leading edge of the prism at $0.99H$ and $0.7H$, respectively. Figures 6.13 and 6.14 clearly show that the size of the separation bubble is larger in the case of smooth inflow than in the case of turbulent inflow.

In the roof separation bubble, the flow in the region below the zero $U-$velocity, i.e. the flow reversal line in the $x-$direction, moves upstream and separates before it reaches the leading edge of the prism and forms another secondary recirculation zone of opposite sign. It should be noted that secondary separation occurs at $0.47H$ and $0.33H$ from the prism leading edge for the smooth inflow case and the turbulent inflow case, respectively.

The reattached flow on the roof of the prism separates again as it leaves the roof and reattaches on the ground downstream the prism at $x = 3.5$ for both incident flow cases. Additionally, a large recirculation zone forms downstream the prism. The center of this recirculation zone is located at $(x, z) = (2.4, 0.69)$ for the case of smooth inflow and at $(x, z) = (2.4, 0.73)$ in the case of turbulent inflow. Clearly, the location of the centers of the this recirculation zone seems to be identical in both inflow cases. In addition to the large structure developing downstream the prism, two small size secondary eddies are also seen attached to the leeward side of the prism in both cases of incident flow. The two eddies roll in opposite sense with respect to $y-$axis. Figures 6.13 and 6.14 show that one of the two small eddies appears just below the trailing edge of the prism while the other one lies on the ground at the corner where the leeward wall of the prism meets the ground.

Figures 6.15 and 6.16 show the mean streamline patterns at the quarter plane over the

surface-mounted prism in the cases of smooth inflow and turbulent inflow, respectively. In both cases, all of the observed flow activities and flow structures in the center plane continue to appear around the same respective locations in the flow domain, yet with some geometric differences. It should be noted that there is only one point on the windward face of the prism that is a stagnation point of the three-dimensional flow, and it appears in the center plane. However, we will continue to see a point which appears as a stagnation point in the other planes that cut the prism parallel to the center plane. However, such a point is a stagnation point only of the cross-stream in the plane.

Figures 6.15, 6.16, 6.17, and 6.18 show the mean streamline patterns at the quarter and the edge planes for both cases of inflow. The intersection of the zero $W-$velocity component with the windward side of the prism represents the point at which the flow has no in-plane motion, however, there could be out-of-plane motion. Therefore, these points do not actually represent stagnation points of the three-dimensional flow, except at the center plane. However, these points and the streamlines associated with them play the same role as the stagnation point and the stagnation line in their respective planes; as they separate the flow domain into two non-interacting regions across the streamline as if these streamlines were slip walls. The points at which these streamlines meet the prism wall will be called zero $W-$component points on the wall.

Figures 6.16 and 6.18 show that the zero $W-$component points, in the case of turbulent inflow, are at the same vertical distance above the ground as the stagnation point in the center plane. On the contrary, figures 6.15 and 6.17 show that the zero W points on the wall in the case of smooth inflow move towards the ground in the quarter plane and move further to the ground at the edge plane.

Figures 6.15, 6.16 show reduction in the size of separation bubble above the roof in both incident flow cases. The center of the recirculation zone above the prism appears in the quarter plane almost at the same location as in the center plane in both of the two cases of incident flow. In the case of smooth inflow, the reattachment point on the roof has a considerable change as compared to the one in the center plane. In this case, the reattachment point is downstream the leading edge of the prism by $2.21H$ in the quarter plane, while this distance is $2.43H$ in the center plane. On the contrary, the reattachment point in the case of

turbulent inflow move slightly from $1.76H$ in the center plane to $1.71H$ in the quarter plane.

Figures 6.15 shows that the location of the reattachment point on the ground and the coordinates of the center of the circulation zone downstream the prism do not change compared to the center plane for the case of smooth inflow. Figures 6.16 shows that the reattachment point comes slightly closer to the prism from $x = 3.5$ in the center plane to $x = 3.42$ in the quarter plane for the case of turbulent inflow, and the center of the circulation zone moves closer to the prism and pushed slightly downward from $(x, z) = (2.4, 0.73)$ in the center plane to $(x, z) = (2.27, 0.64)$ in the quarter plane. Clearly, slight geometric changes are observed to the vortical structure downstream the prism in the quarter plane as compared to the center plane in both cases of incident flow. Nevertheless, there are some physical changes evident in the vicinity of the reattachment point on the ground and these are observed in both cases of incident flow. Figures 6.15 and 6.16 show that streamlines around the point of reattachment on the ground initially assume upstream direction then they reverse direction and move downstream. A saddle point is also predicted in this plane. This saddle point is clearly shown by the intersection of the zero U and zero W velocity components behind the prism at $(x, z) = (2.93, 0.48)$ for the smooth inflow case and at $(x, z) = (2.93, 0.20)$ for the turbulent inflow case.

Figures 6.17 and 6.18 show the streamline patterns in the edge plane in both cases of inflow conditions. Traces of the primary separation of the incident flow boundary layer can still be observed in both cases although it is highly suppressed in the case of turbulent inflow. As mentioned above, the zero $W-$velocity component appears to be pushed down, compared to the center plane and the quarter plane, in the case of smooth inflow; while it maintains its level in the case of turbulent inflow. The horseshoe vortex becomes smaller in size, at the edge, compared to its size at center and quarter planes. In the mean time, the horseshoe vortex comes very close to the ground and to the upwind face of the prism in both inflow cases. The secondary corner vortex on the ground between the horseshoe vortex and the upwind face of the prism, that appears in the center and quarter planes, does no longer appear at the edge. On the roof of the prism, the large recirculation zone is no longer found in the edge plane. Neither the large vortical structure nor the secondary eddies attached

to the leeward side of the prism that appears in the center and quarter planes, are present in the edge plane in both cases. This means that these structures are confined within the recirculation region downstream the prism.

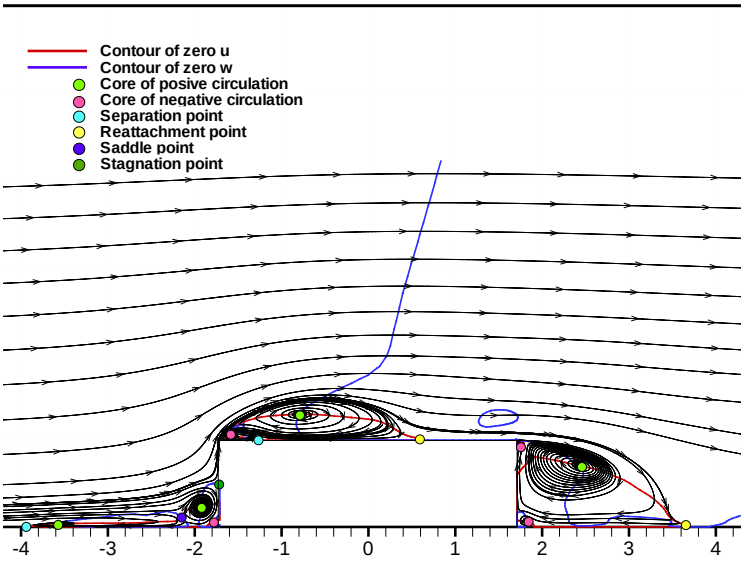

Figure 6.13: Streamlines pattern at the center plane for the case of smooth inflow

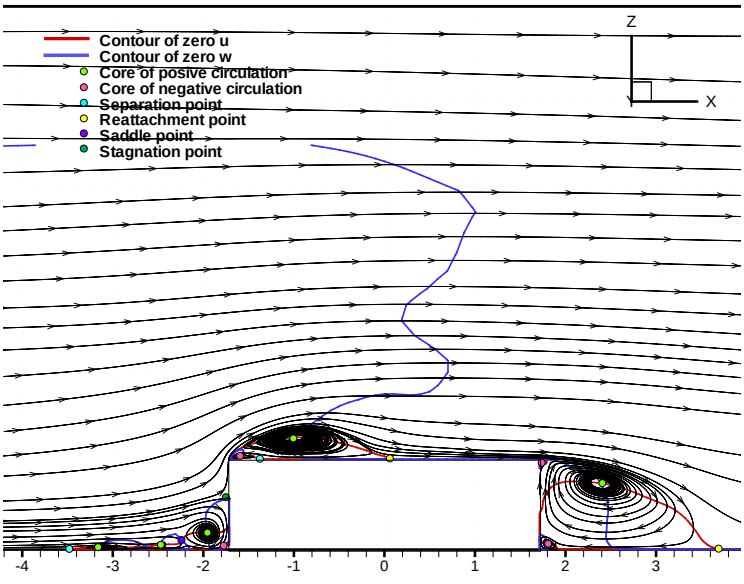

Figure 6.14: Streamlines pattern at the center plane for the case of turbulent inflow

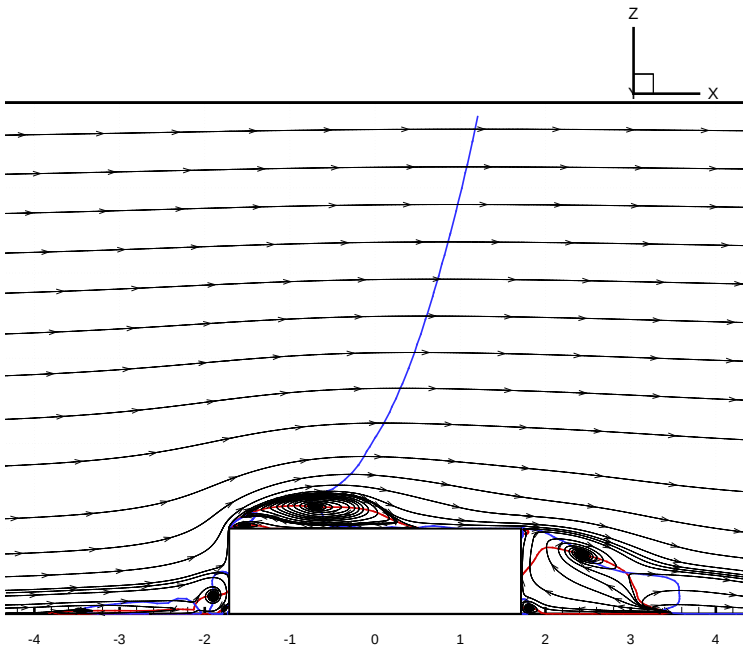

Figure 6.15: Streamlines pattern at the quarter plane for the case of smooth inflow

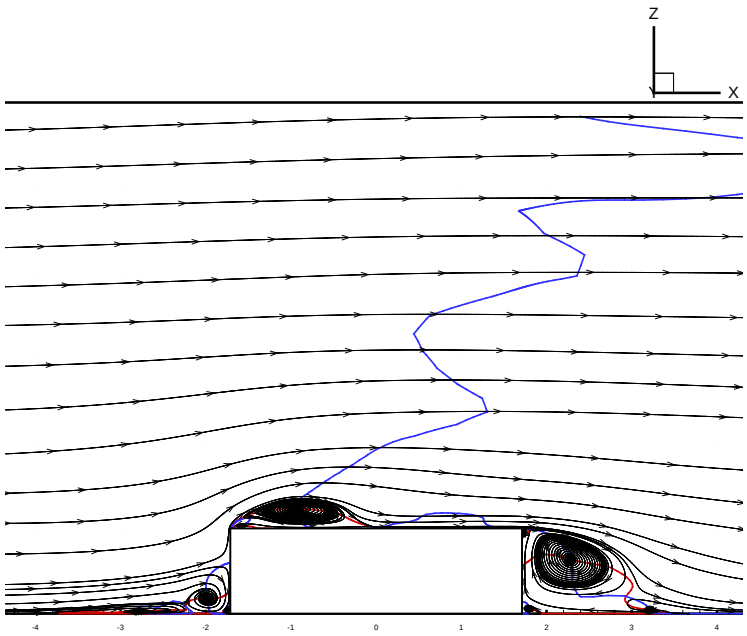

Figure 6.16: Streamlines pattern at the quarter plane for the case of turbulent inflow

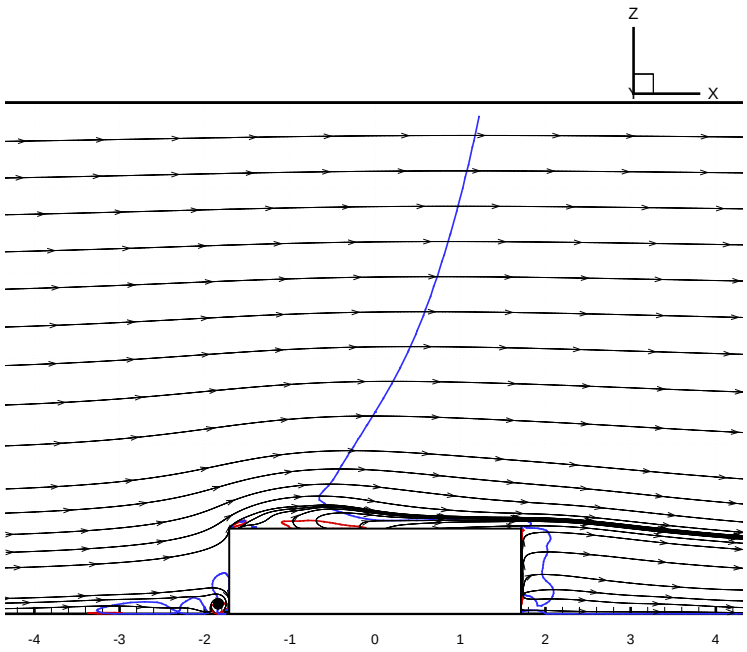

Figure 6.17: Streamlines pattern at the edge plane for the case of smooth inflow

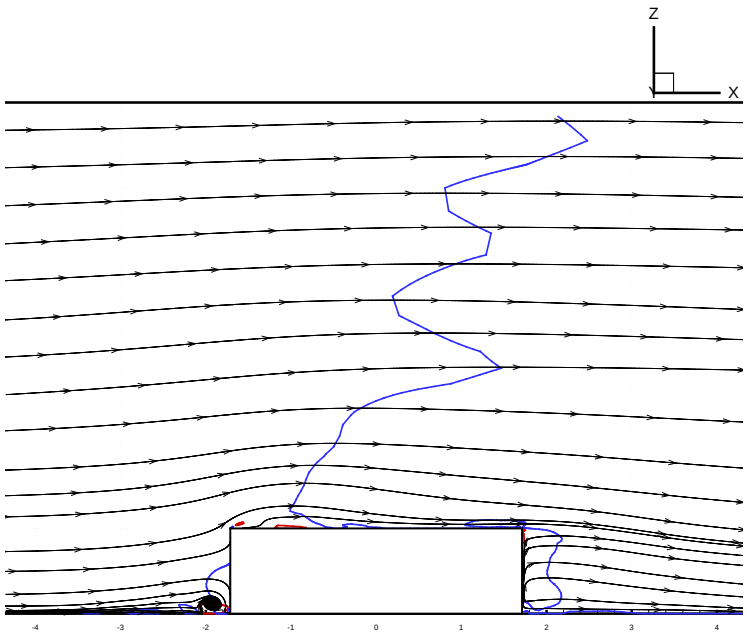

Figure 6.18: Streamlines pattern at the edge plane for the case of turbulent inflow

Figures 6.19 and 6.20 show the locations of the reattachment lines of the roof vortex, the location of the secondary separation line of the reversed flow in the recirculation zone above the roof, the location of the zero $W-$velocity component on the upwind face of the prism, and the location of reattachment of the separated flow on the side walls of the prism for the case of smooth inflow and the case of turbulent flow, respectively. The figures show that the line of zero $W-$component is nearly a horizontal line in the case of turbulent flow while it is a convex line in the case of smooth inflow. These observations agrees with the observations presented earlier in this section using the streamlines pattern figures. The figures also show the trace of the reattachment point on the roof of the prism. The reattachment point has a maximum value at the center plane and maintains this maximum in a zone that extends for about one third of the prism width around the middle plane. The figures clearly show that the flow reattaches closer to the windward edge in the case of turbulent inflow than in the case of smooth inflow. It is also shown that the secondary separation of the reversed flow in the recirculation region above the roof occurs close to the windward edge of the prism in the case of turbulent inflow than in the case of smooth inflow. The area between the secondary separation line and the reattachment line on the roof shows the size of the recirculation zone.

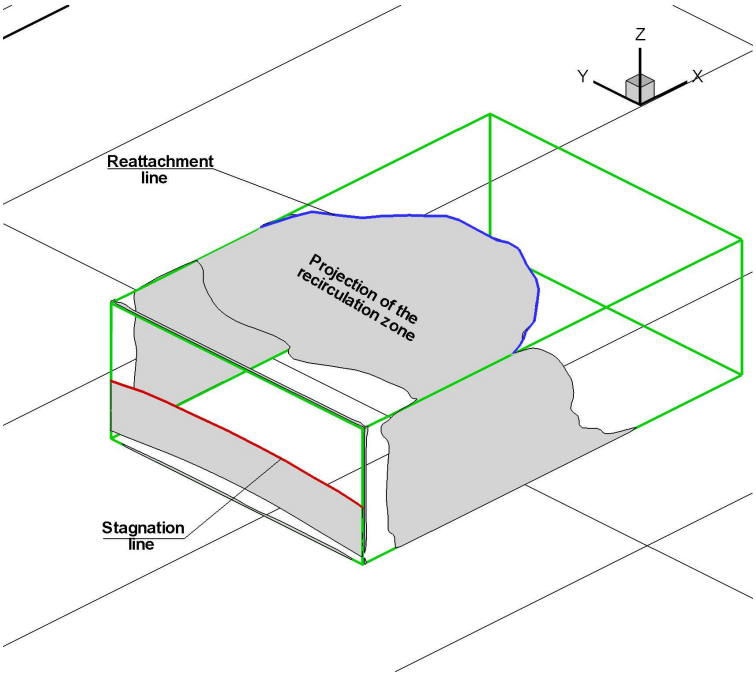

Figure 6.19: Cross-flow stagnation line on the upwind face and reattachment line on the roof of the prism in the case of smooth inflow

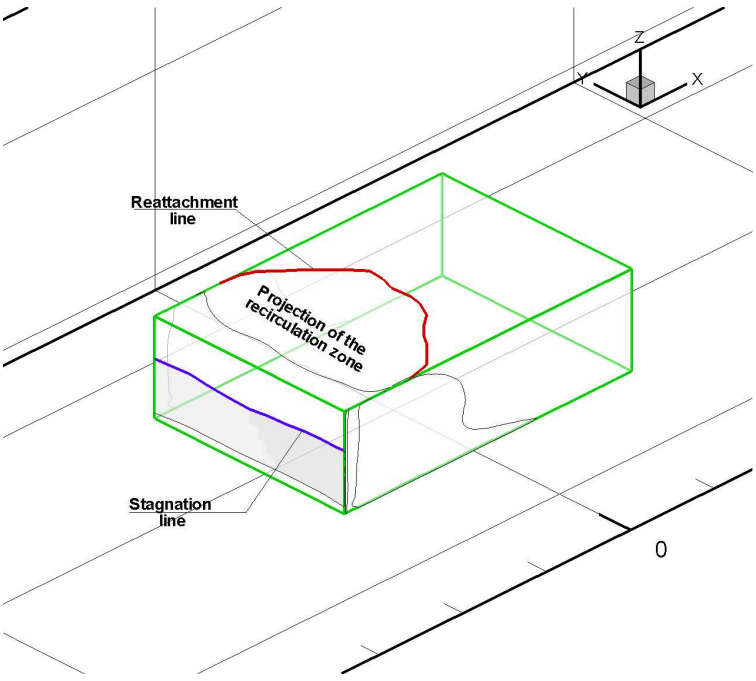

Figure 6.20: Cross-flow stagnation line on the upwind face and reattachment line on the roof of the prism in the case of turbulent inflow

The next set of plots, figures 6.21 through 6.24, show contour maps of mean $U-$velocity component in the center plane, quarter plane and over the edge of the surface-mounted prism for both smooth inflow and turbulent inflow cases. In the plots, the contour maps of absolute values around zero are tiled with white color. Figures 6.21 and 6.22 show that the separating flow over the leading edge of the prism has comparable values of $U-$component in the shear layer in both cases of incident flow. Besides, the maximum observed value of U component in the reversed flow, the flow moving upstream, in the lower region of the recirculation zone over the roof is almost the same in both cases. However, the size of the reversed flow region in the recirculation zone, the region enveloped by the zero U component, above the roof is clearly larger in the case of smooth inflow than in the case of turbulent inflow. This clearly indicates that higher velocity gradient $\frac{\partial U}{\partial z}$ is expected to exist over the roof of the prism in the recirculation bubble in the case of turbulent inflow in comparison to the smooth inflow case. Therefore, higher values of vorticity are expected to develop on the roof of the prism in the case of turbulent inflow. The same trend is further amplified in the quarter plane as shown in figures 6.23 and 6.24. In both inflow cases, the maximum value of reversed $U-$velocity in the center plane and in the separation bubble above the roof is about 0.48. This value increases to about 0.51 at the quarter plane for the case of turbulent inflow while it drops to about 0.38 for the smooth inflow case. Considering the fact that the size of the envelope of the reversed flow reduces in both inflow cases as we move from the center to the quarter plane, and that this reduction is higher in the case of turbulent inflow, we can conclude that the velocity gradient $\frac{\partial U}{\partial z}$ is highly amplified in the vicinity of the quarter plane in the case of turbulent inflow.

We also observe in figures 6.21 through 6.24 that in both inflow cases, the size of the reversed flow region downstream of the leeward side of the prism is almost the same. However, the reversed flow in the center plane in the case of turbulent inflow moves upstream faster than that of the smooth inflow case. The opposite is observed at the quarter plane where the the reversed flow in the turbulent inflow case moves upstream slower than that of the smooth inflow in the respective plane.

Figures 6.27 through 6.32 show contour maps of the $W-$velocity component in the center,

quarter and edge planes for both incident flow cases. Around the leading edge of the prism, the $W-$component is always higher in the case of smooth inflow compared to the turbulent inflow case. In the turbulent inflow case, we observe a slight increase in the $W-$component beginning at as far as $7H$ upstream of the prism in the center plane at $z = 1.33$ (not shown in the domain covered in figure 6.28). This increase in $W-$component in the turbulent inflow case appears also in the quarter and the edge planes, yet it begins much closer to the prism than in the center plane.

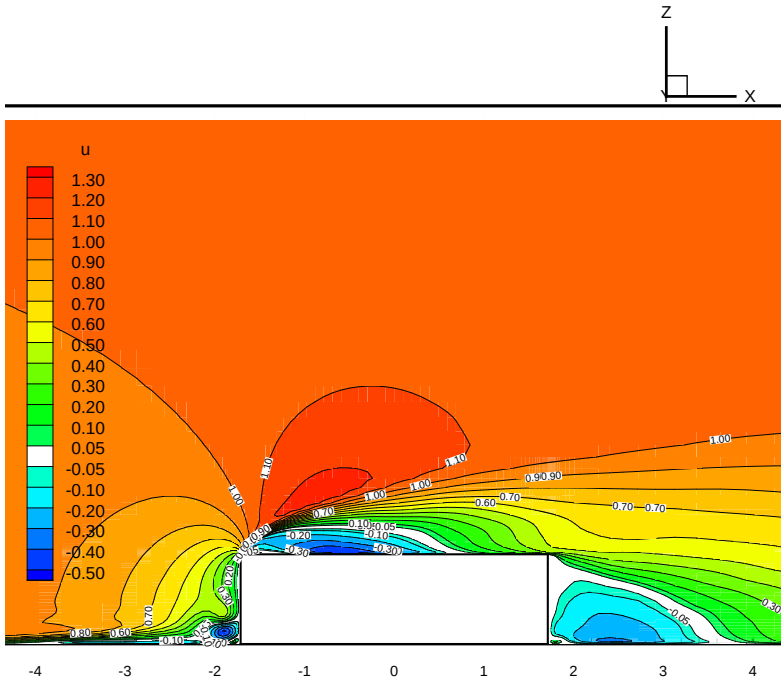

Figure 6.21: Contours of mean $U-$ velocity component at the center plane for the case of smooth inflow

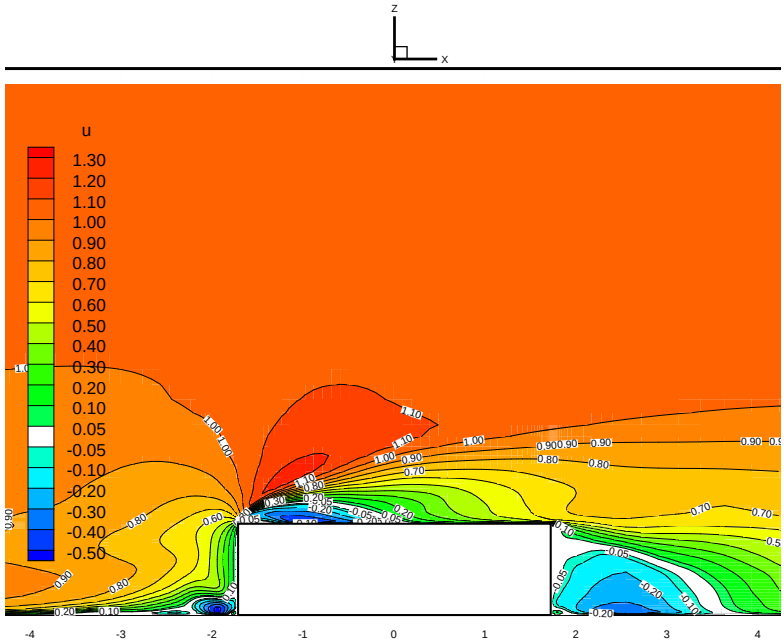

Figure 6.22: Contours of mean $U-$ velocity component at the center plane for the case of turbulent inflow

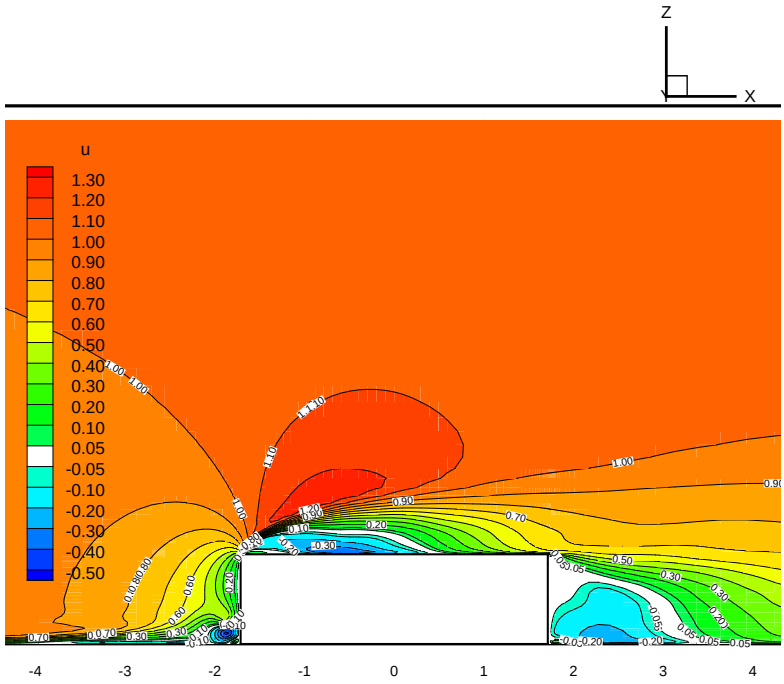

Figure 6.23: Contours of mean $U-$ velocity component at the quarter plane for the case of smooth inflow

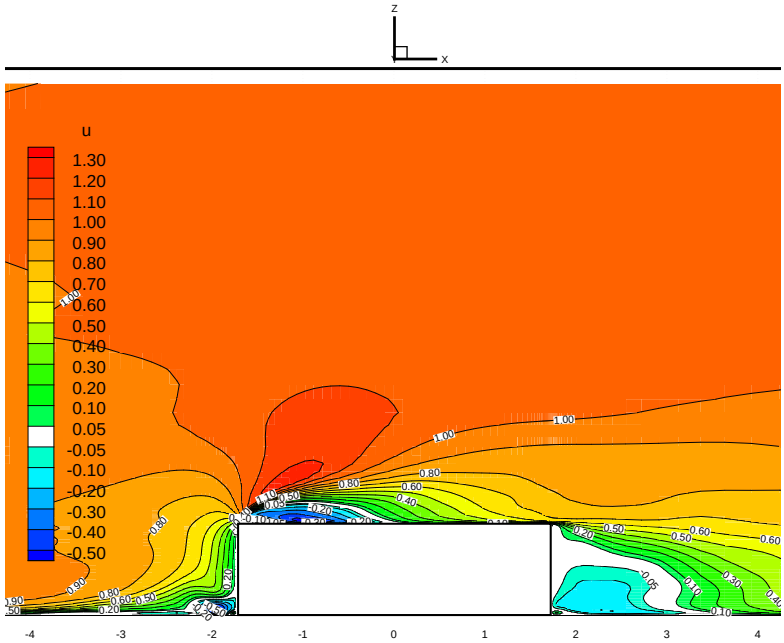

Figure 6.24: Contours of mean $U-$ velocity component at the quarter plane for the case of turbulent inflow

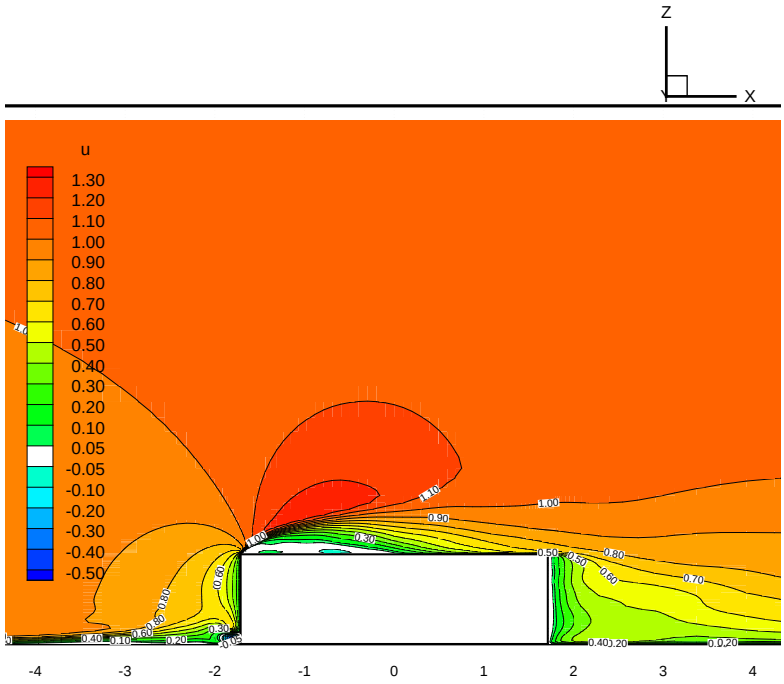

Figure 6.25: Contours of mean $U-$ velocity component at the edge plane for the case of smooth inflow

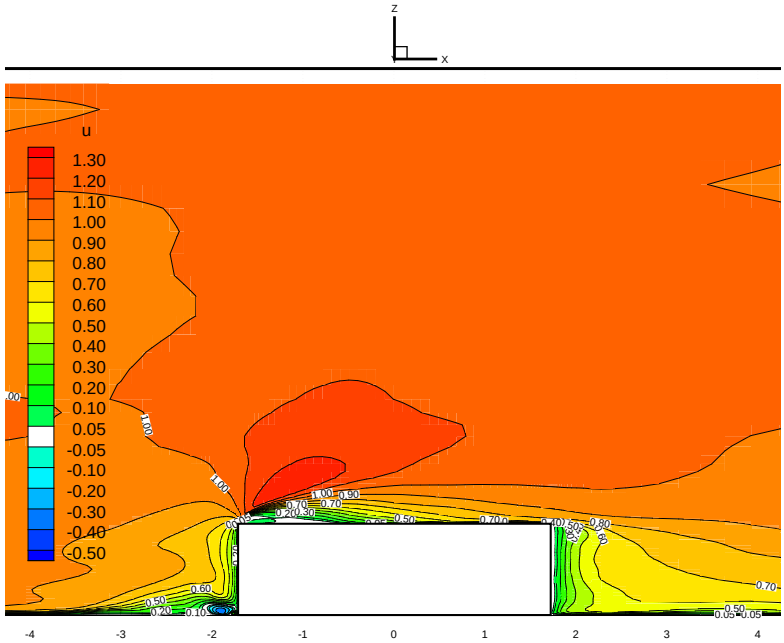

Figure 6.26: Contours of mean $U-$ velocity component at the edge plane for the case of turbulent inflow

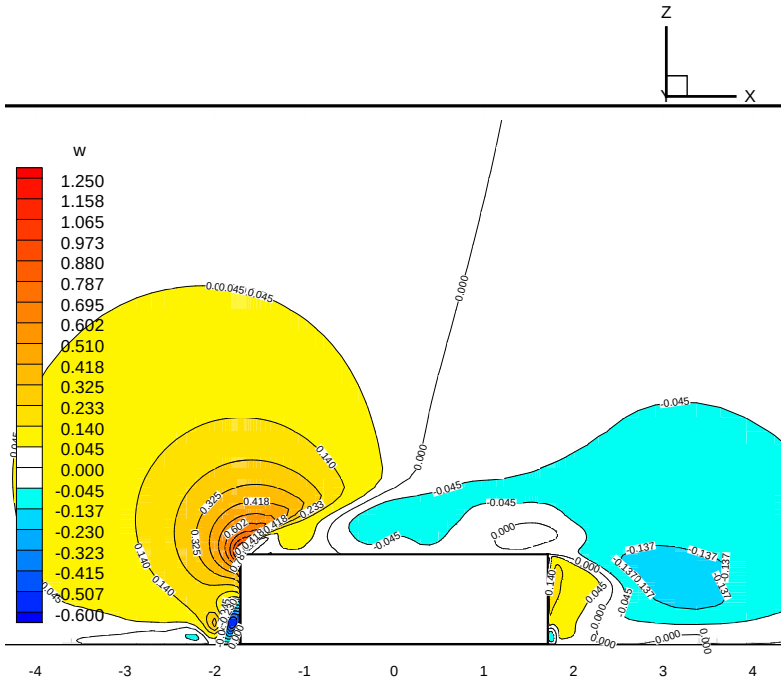

Figure 6.27: Contours of mean $W-$ velocity component at the center plane for the case of smooth inflow

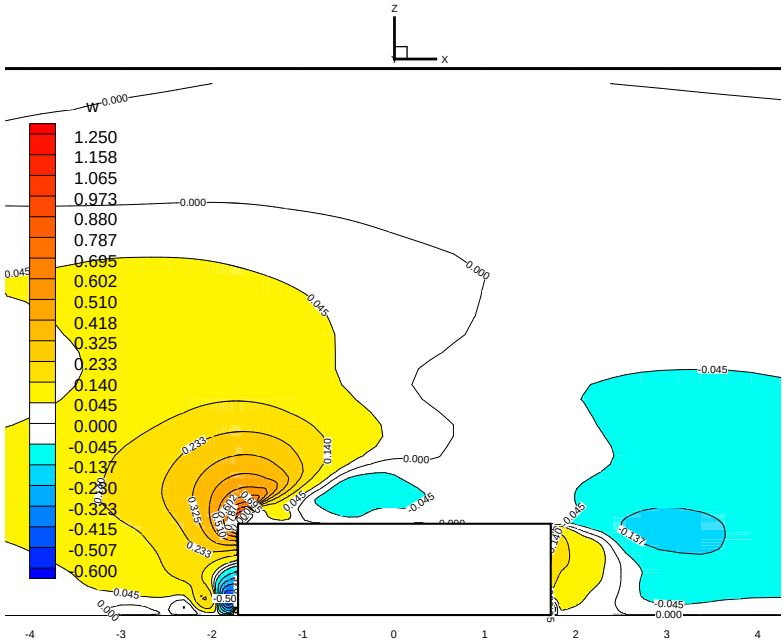

Figure 6.28: Contours of mean $W-$ velocity component at the center plane for the case of turbulent inflow

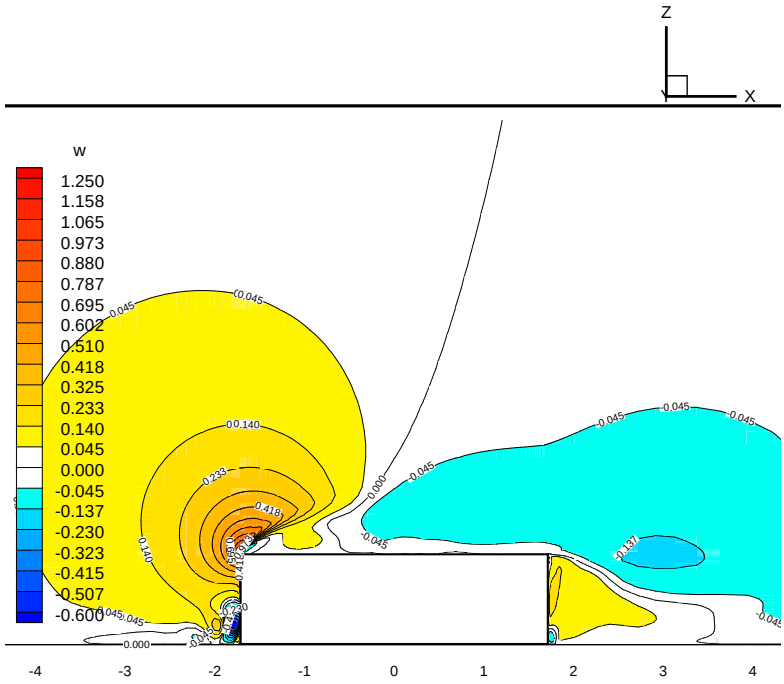

Figure 6.29: Contours of mean $W-$ velocity component at the quarter plane for the case of smooth inflow

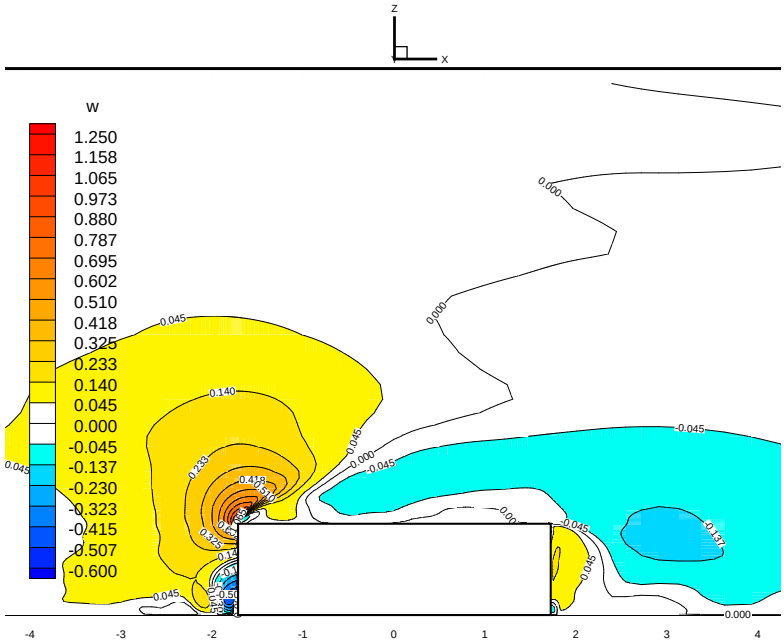

Figure 6.30: Contours of mean $W-$ velocity component at the quarter plane for the case of turbulent inflow

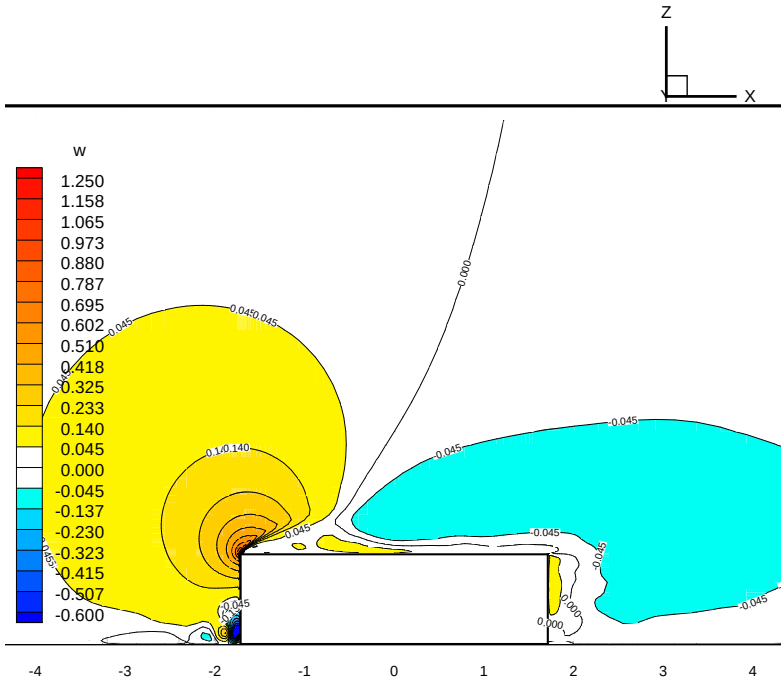

Figure 6.31: Contours of mean $W-$ velocity component at the edge plane for the case of smooth inflow

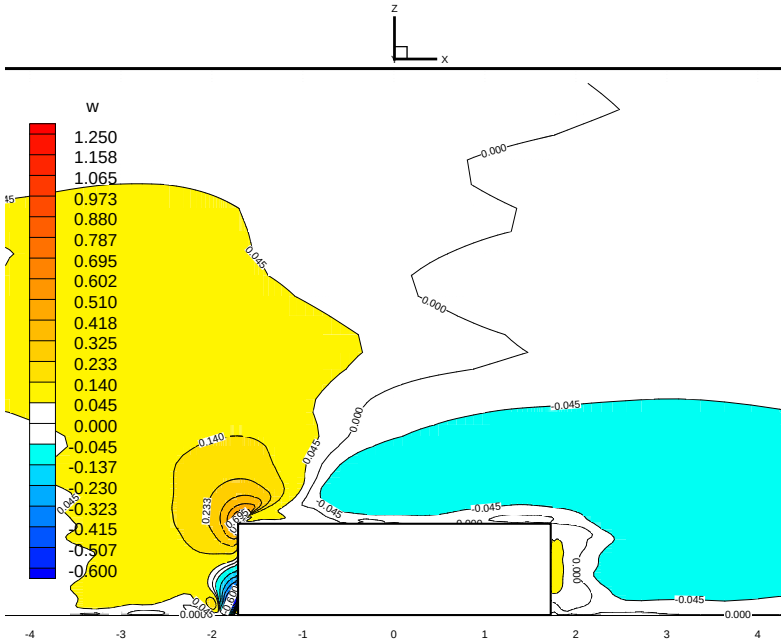

Figure 6.32: Contours of mean $W-$ velocity component at the edge plane for the case of turbulent inflow

The $V-$velocity component in the quarter and edge planes is shown in figures 6.33 to 6.36 for both inflow conditions.The positive values of V represent motion away from the center plane, while the negative values of V represent motion towards the center plane. Upstream of the prism and in the quarter plane, the $V-$component is 0.24 and 0.29 at the center of the horseshoe vortex in the cases of turbulent and smooth inflow, respectively. At the edge plane, the $V-$component reaches 0.75 at the center of the horseshoe vortex in the turbulent inflow while it becomes 0.95 at the center of the horseshoe vortex in the case of smooth inflow. In both incident flow cases, the highest value of $V-$component is observed very close to the upwind face of the prism in the edge plane and it was 1.12 in both inflow cases. Figures 6.33 to 6.36 show that there is lateral cross flow that penetrates underneath the shear layer on the roof of the prism and approaches the center plane form the sides of the prism in the regions downstream the reattachment point. In absolute sense, the peak $V-$velocity of this cross flow is 0.2 at $(x, z) = (-.06, 1.10)$ and 0.18 at $(x, z) = (0.65, 1.09)$ in the cases of turbulent inflow and smooth inflow, respectively. Additionally, at the edge plane, the peak of the $V-$component, in absolute sense, is 0.135 at $(x, z) = (-.05, 1.2)$ for the case of turbulent inflow and 0.175 at $(x, z) = (0.24, 1.15)$ for case of smooth inflow. It can be seen from figures 6.33 and 6.34 that the flow over the prism gains a lateral velocity component in the direction from the center plane to the edge plane as it separates over the the leading edge. On the other hand, as the flow circulates and reverses its direction to move upstream in the lower region of the recirculation bubble above the roof, the flow also moves laterally in the direction from the edge plane towards the center plane.

Figures 6.35 and 6.36 show that in the leeward region of the prism, there is cross flow in the direction from the edge plane towards the center plane. This $V-$component is clearly higher in the case of turbulent inflow than in the case of smooth inflow. Figures 6.33 and 6.34 show that the same observation is seen to continue in the quarter planes with higher velocities in the case of turbulent inflow.

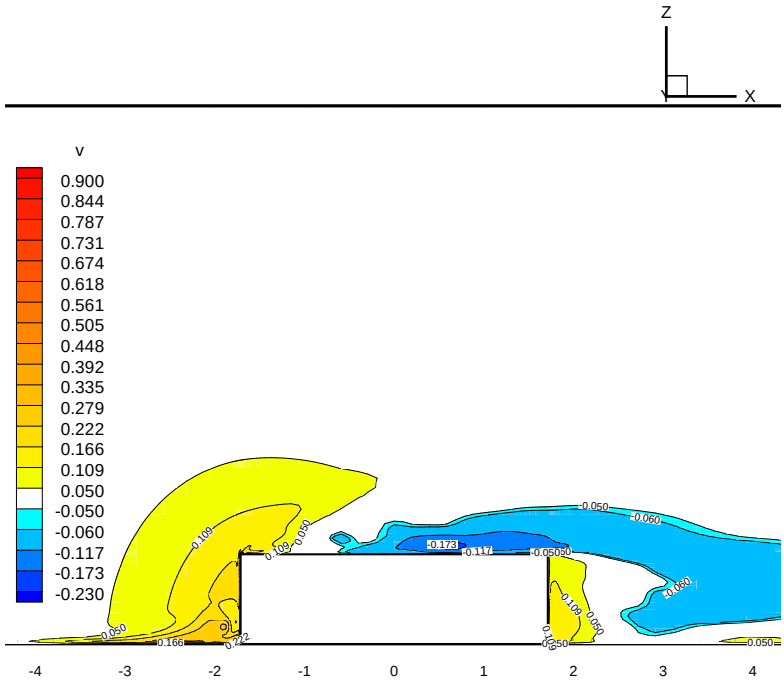

Figure 6.33: Contours of mean $V-$ velocity component at the quarter plane for the case of smooth inflow

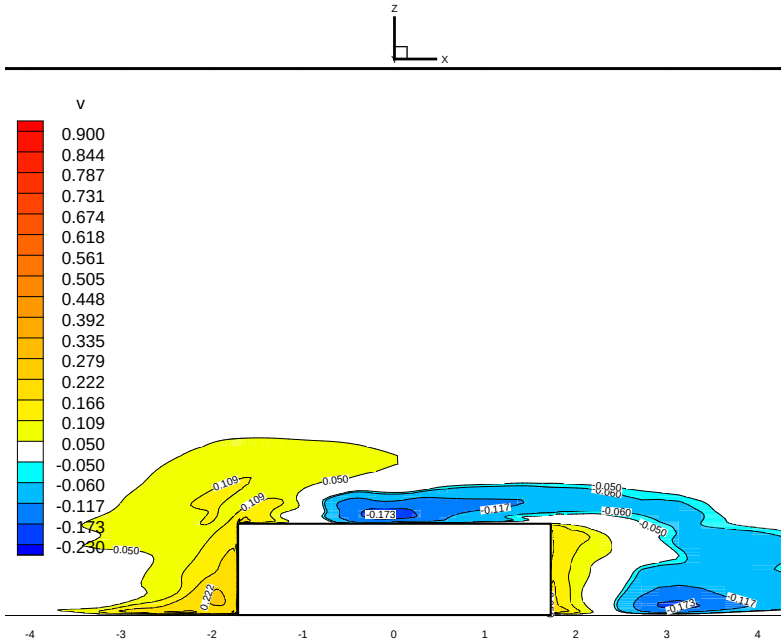

Figure 6.34: Contours of mean $V-$ velocity component at the quarter plane for the case of turbulent inflow

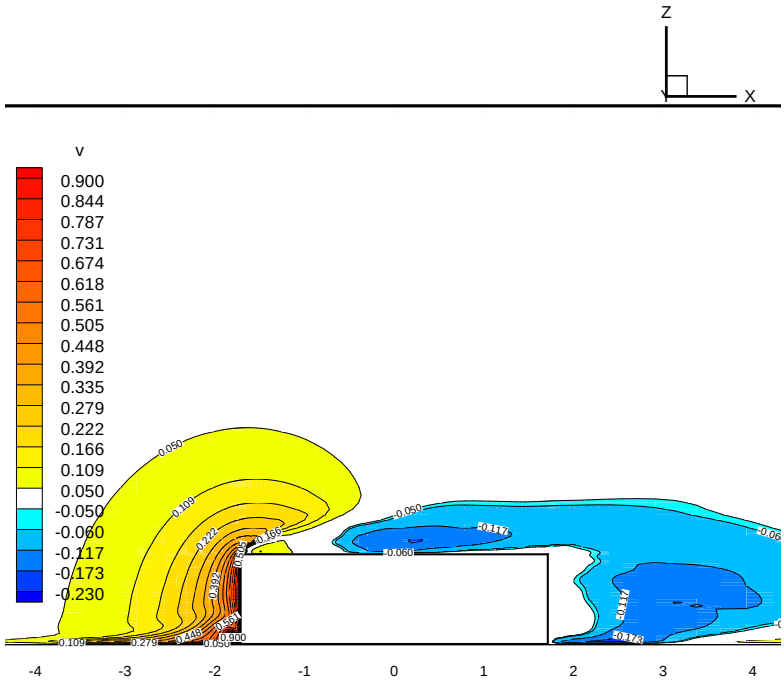

Figure 6.35: Contours of mean $V-$ velocity component at the edge plane for the case of smooth inflow

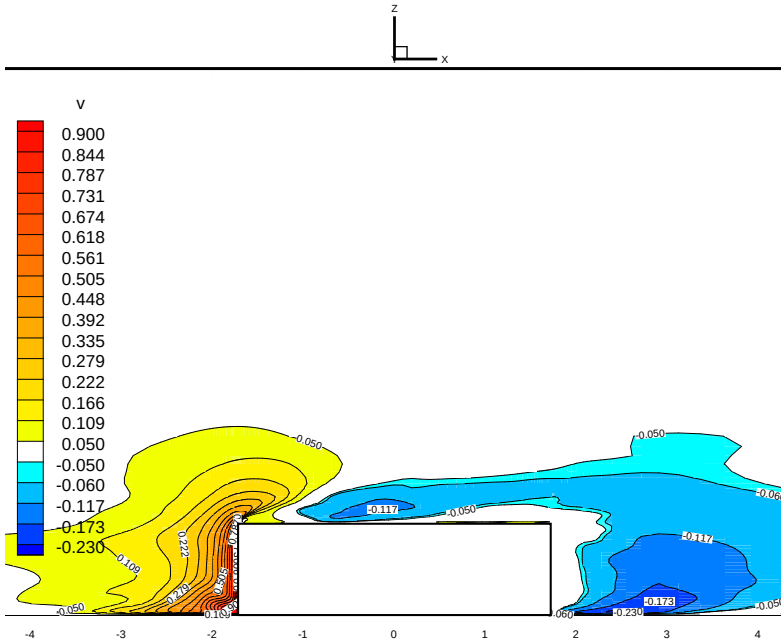

Figure 6.36: Contours of mean $V-$ velocity component at the edge plane for the case of turbulent inflow

6.2.2 Vorticity Field

First, we compare the LES results to our experimental data. The vorticity distributions above the roof of the prism in the center plane is presented in figure 6.37 for both the experimental results cases and the numerical simulation cases. It can be seen for the figure that, for $x > 0.5$, there is a good agreement, in both vorticity levels and locations of peak vorticity, between case II in the experimental results and the numerical simulation results with homogeneous turbulent inflow. In addition, the three cases I and II in the experimental results and the case of turbulent inflow in the numerical simulations all come to a good agreement for regions of $x > 1.6$. The smooth inflow case of the numerical simulations exhibits higher levels of vorticity and also a more elevated shear layer above the roof, outlined by the peak vorticity region, than the other three cases.

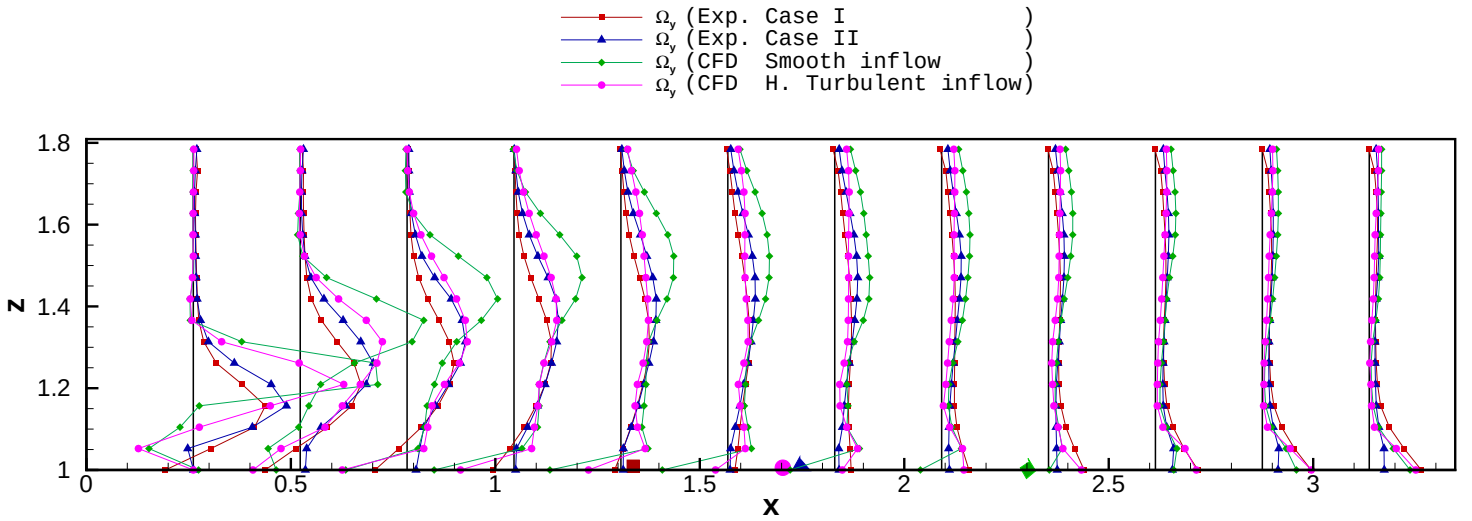

Figure 6.37: Distributions of normalized vorticity Ω_y on the roof of the prism at the center plane obtained from experiments and numerical simulations

Next, we present more details of the LES results. In the following discussion, we present the vorticity field mainly in terms of vorticity magnitude, $\Omega = (\Omega_x^2 + \Omega_y^2 + \Omega_z^2)^{1/2}$, in the center, quarter and edge planes as shown figures 6.38 to 6.43. In both inflow cases, the primary separation region, mentioned in section 6.2.1, exhibits high Ω levels in a thin layer near the ground in all the three planes. It can be seen that the vorticity levels in this region is higher in the center and quarter planes in the smooth inflow case, but lower in the edge plane than in the turbulent inflow case. At the core of the horseshoe vortex, the levels of Ω in the three planes are much higher in the case of smooth inflow than in the case of turbulent inflow. Moreover, the levels of Ω at the core of the horseshoe vortex seem to increase slightly in both inflow cases as we move from the center plane to the edge plane. It can be seen from the figures that in both inflow cases, the regions of high Ω content upstream of the prism are below the stagnation streamline in each plane. Therefore, this high vorticity flow convects with the flow moving around the sides of the prism and it does not flow over the leading edge of the prism.

Figures 6.38 to 6.43 show that the levels of Ω in the separating shear layer on the leading edge of the prism are always higher in the case of smooth inflow than in the turbulent inflow case. The high levels of vorticity extend adjacent to the flow reversal line in $x-$direction, the line of zero U, in the region where the mean $U-$velocity is positive, i.e. above the zero U line. It is clear from the figures that the shear layer in the turbulent inflow case is closer to the roof surface than the shear layer in the smooth inflow case. In addition, relatively higher levels of Ω in the shear layer in the smooth inflow case extend downstream more than in the turbulent inflow case. On the other hand, the reversed flow, in the lower region of the separation bubble above the roof, has higher levels of Ω in the case of turbulent inflow case compared to the smooth inflow case. Moreover, on the roof surface and beyond the reattachment point, the levels of Ω are slightly of higher magnitudes in the case of turbulent inflow case. This can be attributed to the fact that in the turbulent inflow case, the flow reattached after a shorter distance from the leading edge of the prism as compared to the smooth inflow case. The reattached flow in the case of turbulent inflow case is more energetic and thus gains high velocity magnitudes as it convects on the roof.

Figures 6.44 and 6.45 show contours of ω_y at the center plane for both inflow cases. A comparison between the figures show that a thicker positive layer of ω_y appears in the rising boundary layer of the upwind face of the prism in the case of smooth inflow. The figures also show that the positive ω_y in the separating shear layer extends downstream in the case of smooth inflow much more than in the case of turbulent inflow. In additions, the layer of negative ω_y on the roof of the prism at the bottom of the separation bubble, has higher levels, in absolute sense, in the case of turbulent inflow than in the case of smooth inflow. This is expected as presented earlier in section 6.2.1.

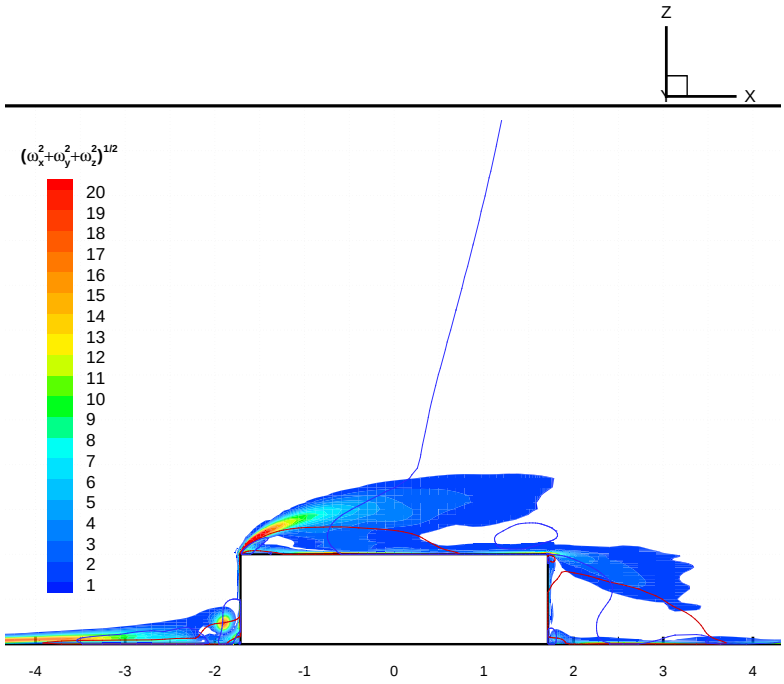

Figure 6.38: Contours of vorticity magnitude at the center plane for the case of smooth inflow

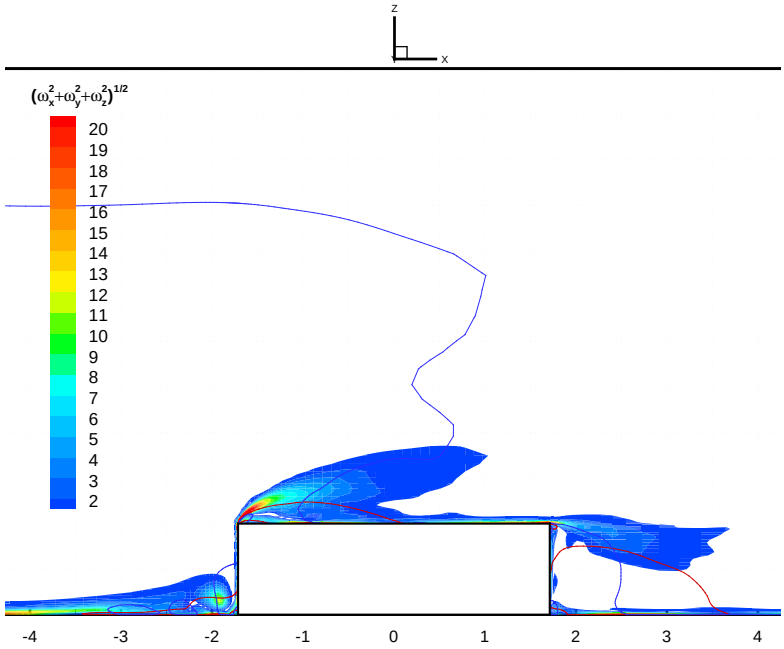

Figure 6.39: Contours of vorticity magnitude at the center plane for the case of turbulent inflow

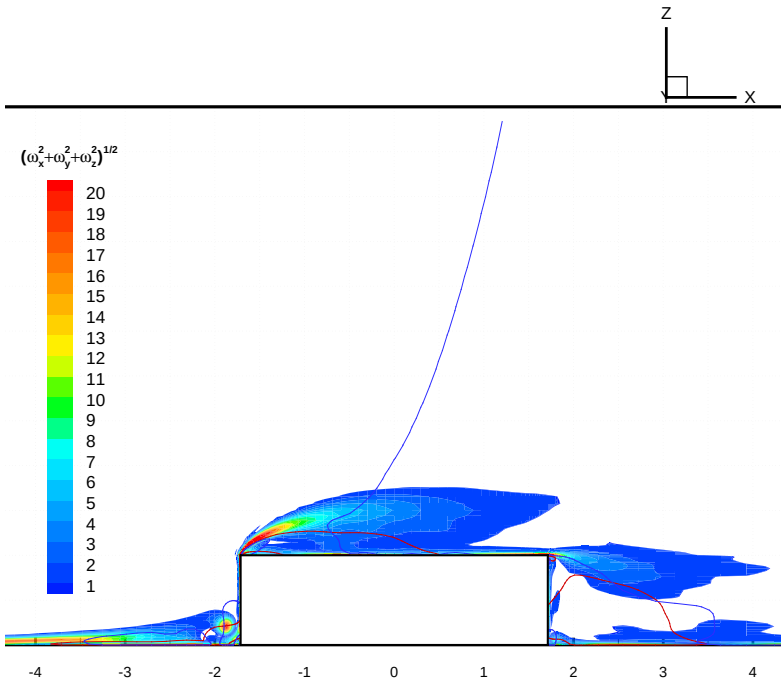

Figure 6.40: Contours of vorticity magnitude at the quarter plane for the case of smooth inflow

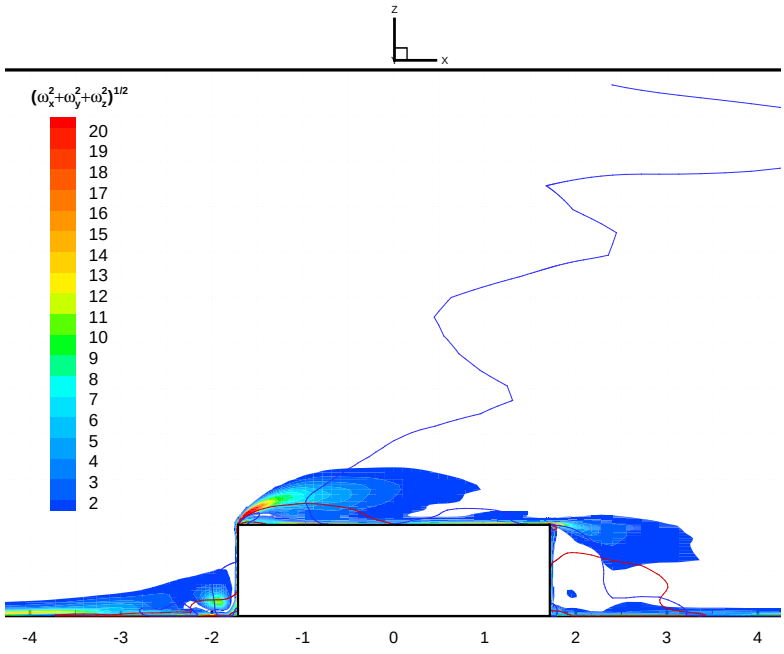

Figure 6.41: Contours of vorticity magnitude at the quarter plane for the case of turbulent inflow

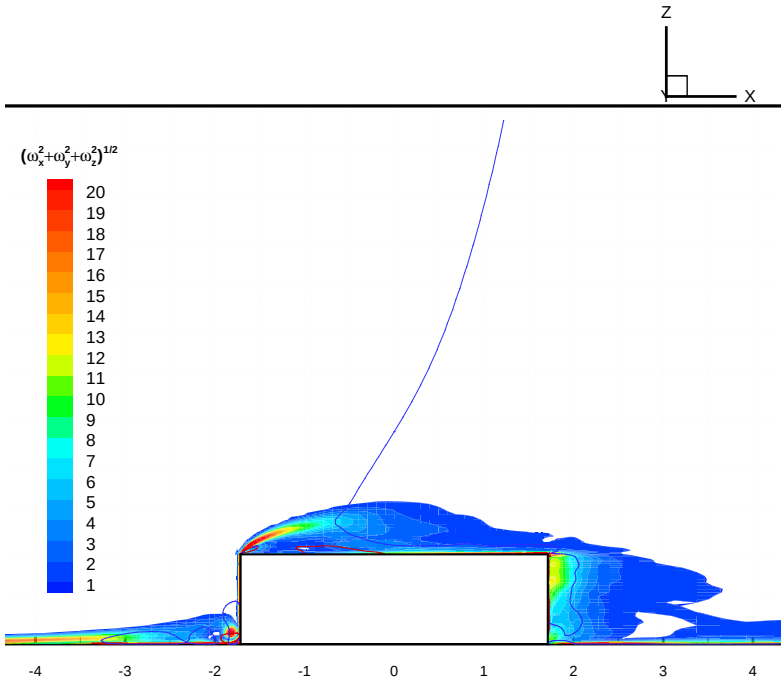

Figure 6.42: Contours of vorticity magnitude at the edge plane for the case of smooth inflow

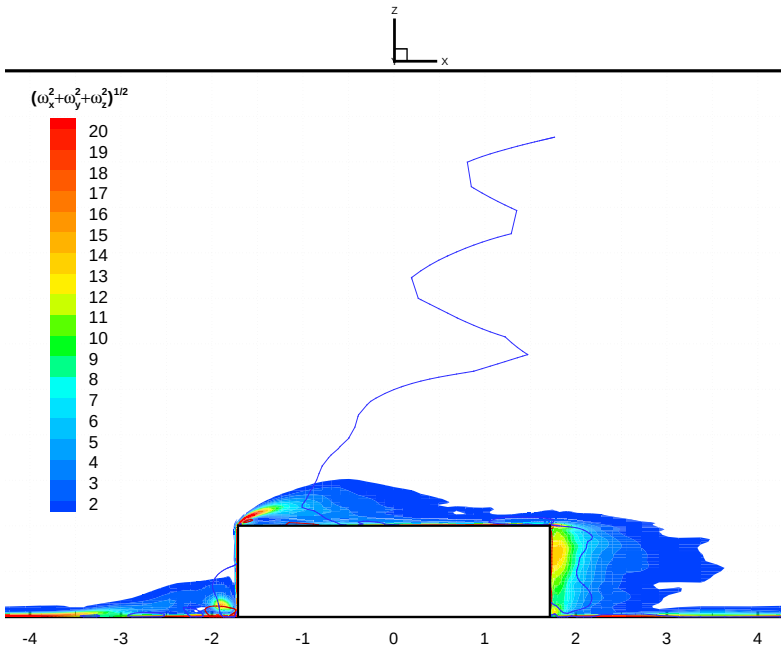

Figure 6.43: Contours of vorticity magnitude at the edge plane for the case of turbulent inflow

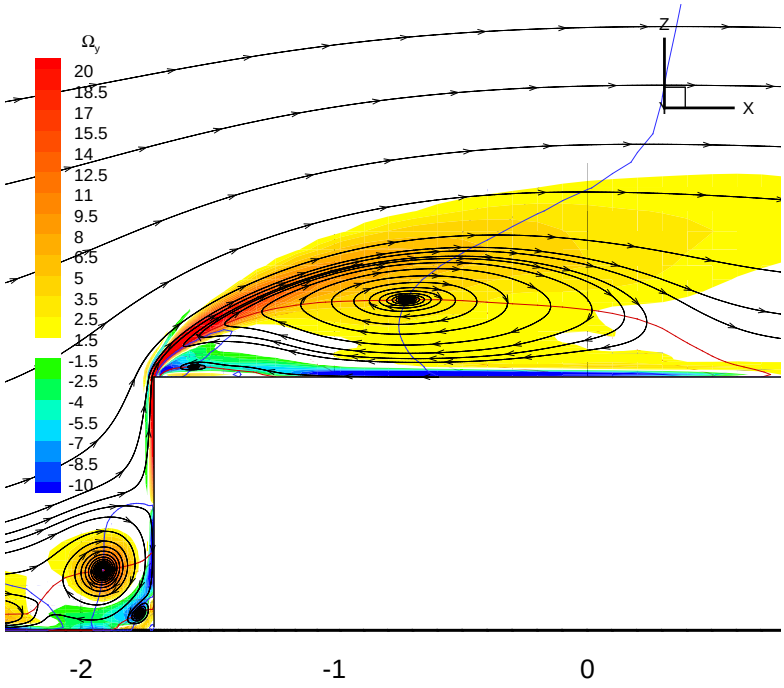

Figure 6.44: Contours of ω_y at the center plane for the case of smooth inflow

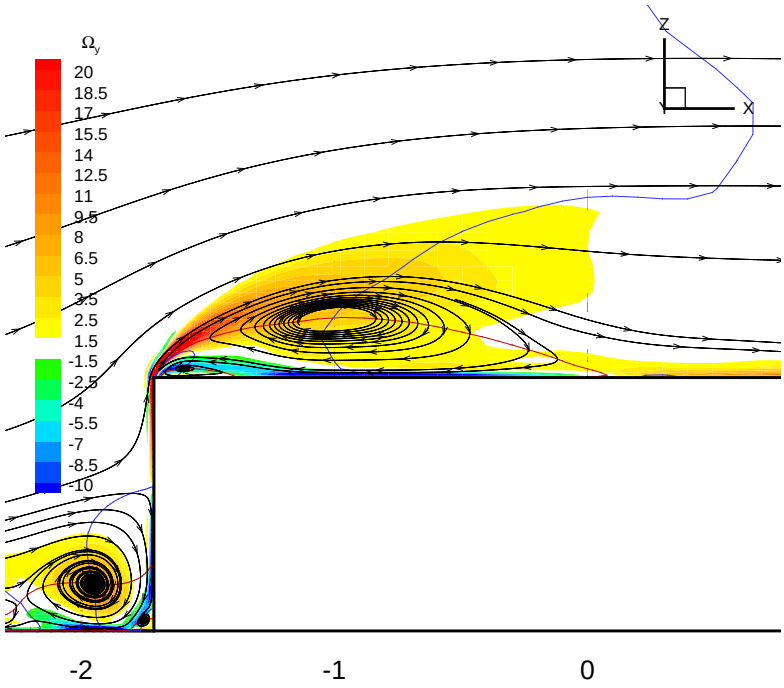

Figure 6.45: Contours of ω_y at the center plane for the case of turbulent inflow

6.2.3 Turbulent Kinetic Energy and Reynolds Stresses

First, we present comparison between LES results and our experimental data. Figures 6.46 through 6.48 show Reynolds stresses,$\overline{u'^2}$,$\overline{w'^2}$, and $\overline{u'w'}$, distributions on the roof in the center plane for the results of both the experiments and the numerical simulations. The turbulence fluctuations from the numerical simulations, which present results of higher Reynolds number inflow with lower boundary layer displacement thickness compared to the experiments, are much higher than those obtained from the experiments especially within the recirculation region. In addition, for $x > 2.3$, the Reynolds stresses, in the case of smooth inflow, become larger than all the other cases including the numerical simulation case with turbulent inflow. It is observed in figure 6.4 that larger velocity gradient $\frac{\partial U}{\partial y}$ developed in the case of smooth inflow was larger than that in the other cases. These high velocity gradients result in highly unstable shear layer as compared to the other cases. With the lack of turbulence in the incident flow together with the high vorticity, figure 6.37, in the shear layer forward flow and the high velocities, figure 6.4, of the reversed flow at the lower region of the recirculation bubble, it is expected that more coherent vortical structures form above the roof of the prism. These large vortical structures result in large scale motion and are expected to develop high flow fluctuations above the roof of the prism.

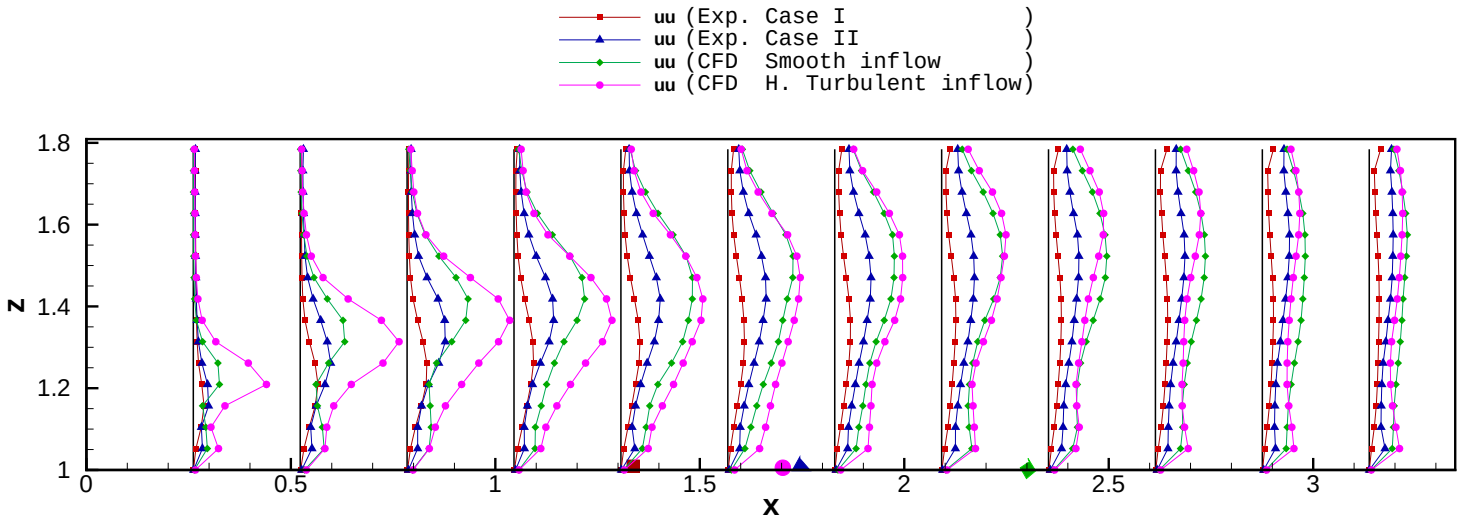

Figure 6.46: Distributions of $\overline{u'^2}$ on the roof of the prism at the center plane obtained from experiments and numerical simulations

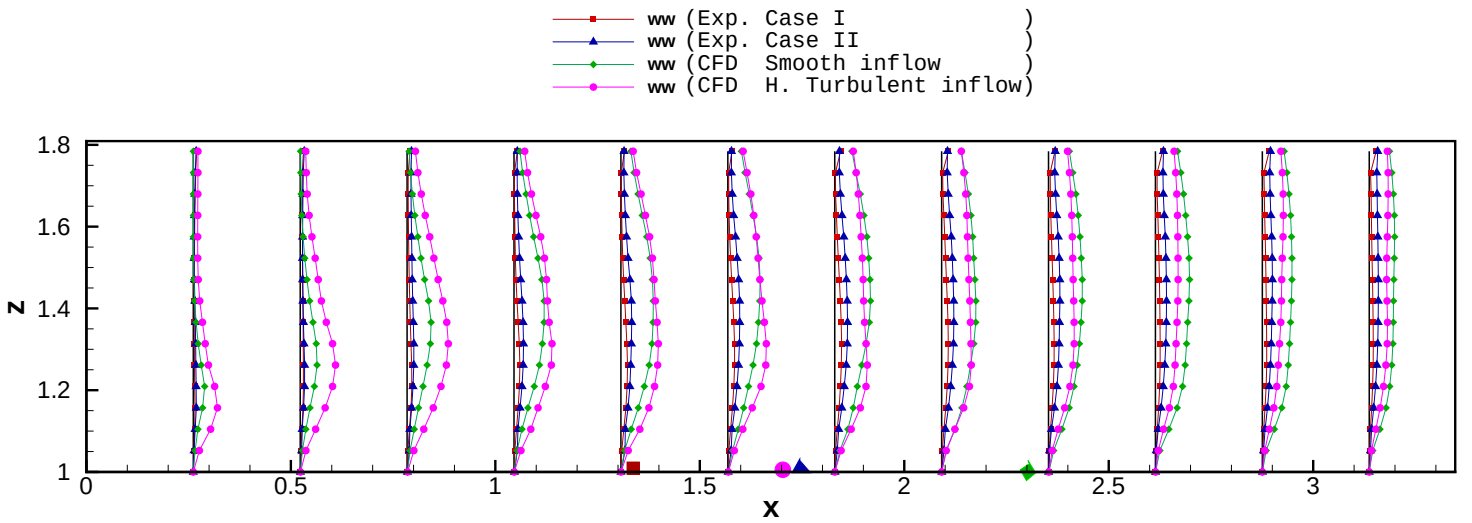

Figure 6.47: Distributions of $\overline{w'^2}$ on the roof of the prism at the center plane obtained from experiments and numerical simulations

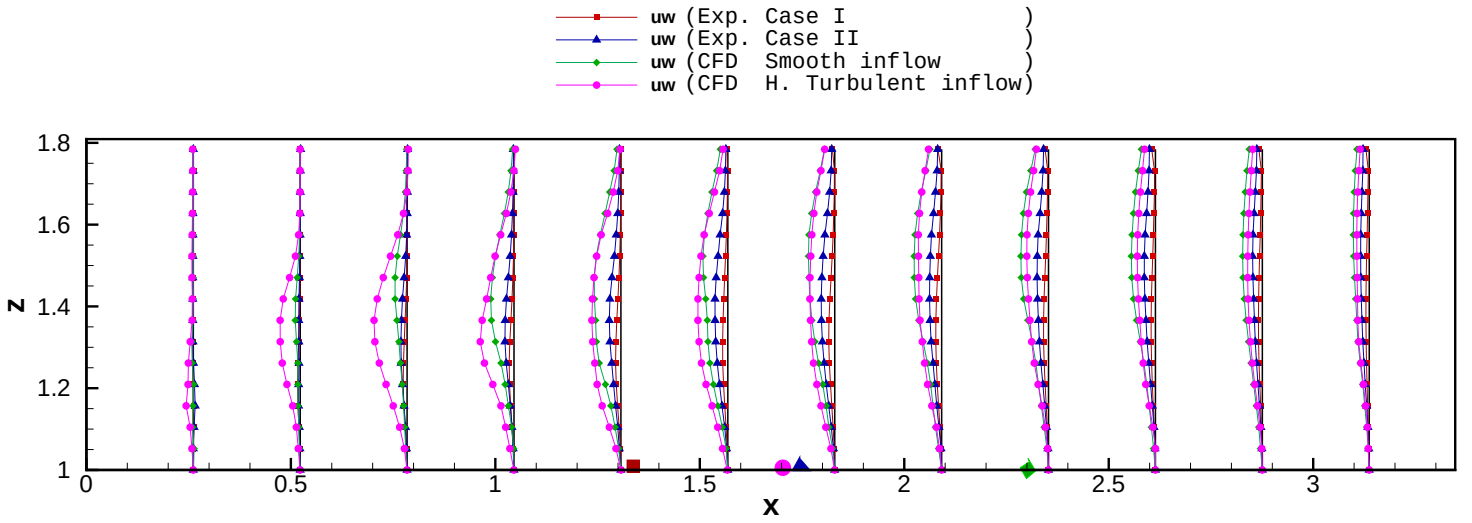

Figure 6.48: Distributions of $\overline{u'w'}$ on the roof of the prism at the center plane obtained from experiments and numerical simulations

Next, we present the turbulent kinetic energy, TKE, of the resolved field and the Reynolds stresses, $\overline{u'w'}$, distributions in both cases of incident inflow. Figures 6.49 and 6.50 show the TKE in the center plane in the cases of smooth inflow and turbulent inflow. Upstream of the prism, there is a region of relatively high levels of TKE at the core of the horseshoe vortex. It is observed from the instantaneous results and the experimental results that the horseshoe vortex is highly oscillating back and forth, and up and down. Therefore, these high levels of TKE are due to the wandering of the horseshoe vortex. Higher levels of TKE are observed in the case of turbulent inflow than in the case of smooth inflow at the core of the horseshoe vortex and above the roof of the prism. In the separating flow above the prism roof, the TKE reaches a peak values of 0.17 at $(x, z) = (-0.38, 1.44)$ and of 0.22 at $(x, z) = (-0.81, 1.35)$ in the cases of smooth and turbulent inflows, respectively. The location of the peak of TKE is approximately above the middle of the separation bubble for each case of incident flow. Figures 6.51 and 6.52 present contour maps of the Reynolds stress $\overline{u'w'}$ in the center plane in the cases of smooth and turbulent inflow, respectively. Higher levels of positive $\overline{u'w'}$ can be seen around the core of the horseshoe vortex in the case of turbulent inflow. In addition, the levels of negative $\overline{u'w'}$ observed in the separation bubble above the roof are of higher magnitudes in the case of turbulent inflow than in the case of smooth inflow.

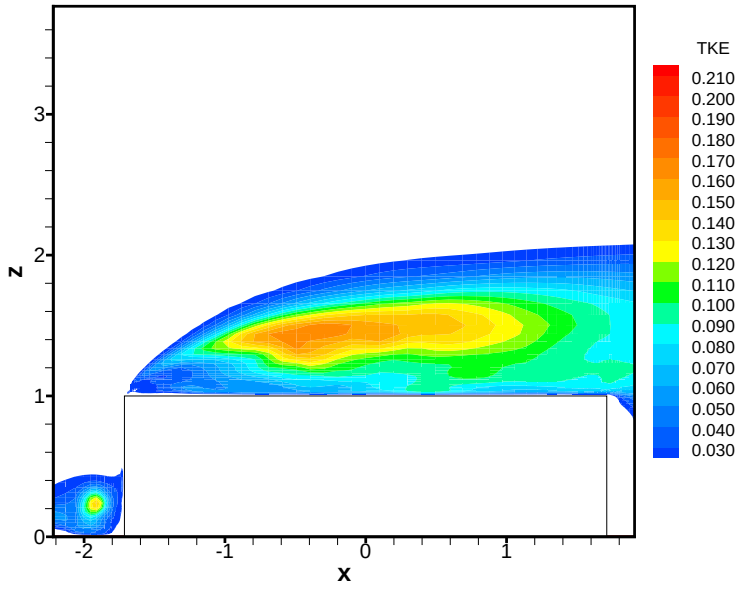

Figure 6.49: Contours of turbulent kinetic energy at the center plane for the case of smooth inflow

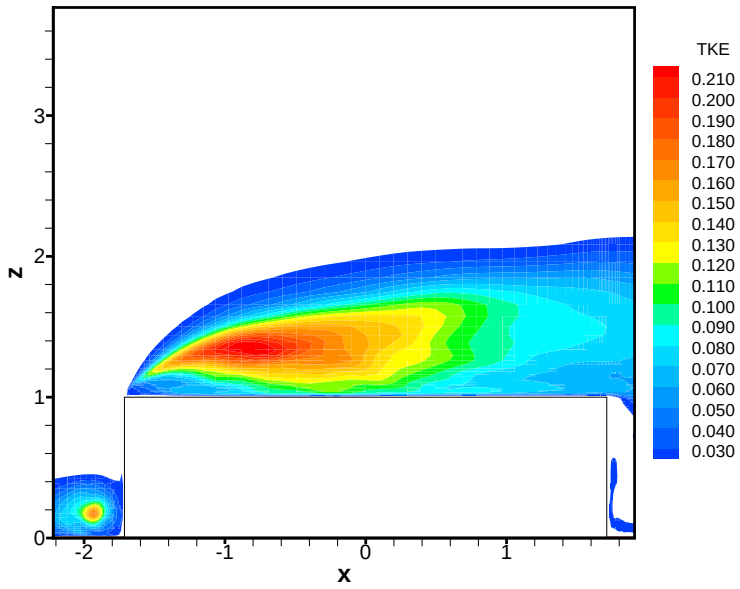

Figure 6.50: Contours of turbulent kinetic energy at the center plane for the case of turbulent inflow

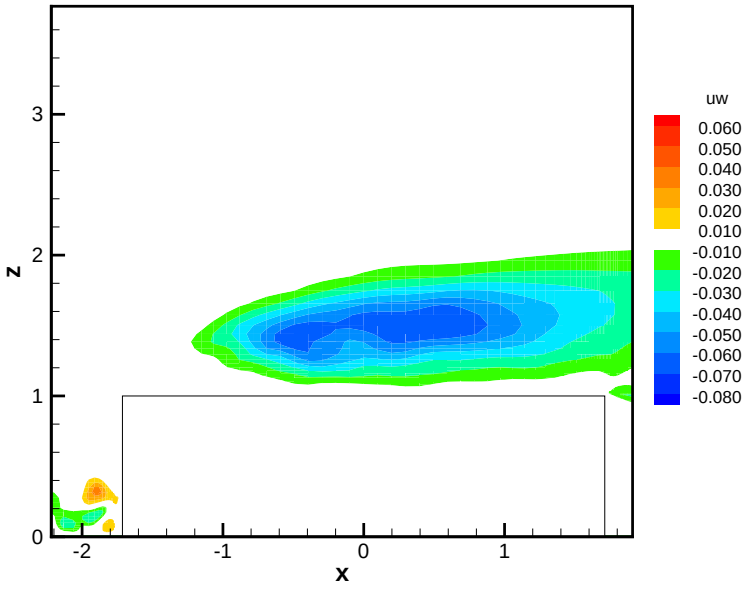

Figure 6.51: Contours of $\overline{u'w'}$ at the center plane for the case of smooth inflow

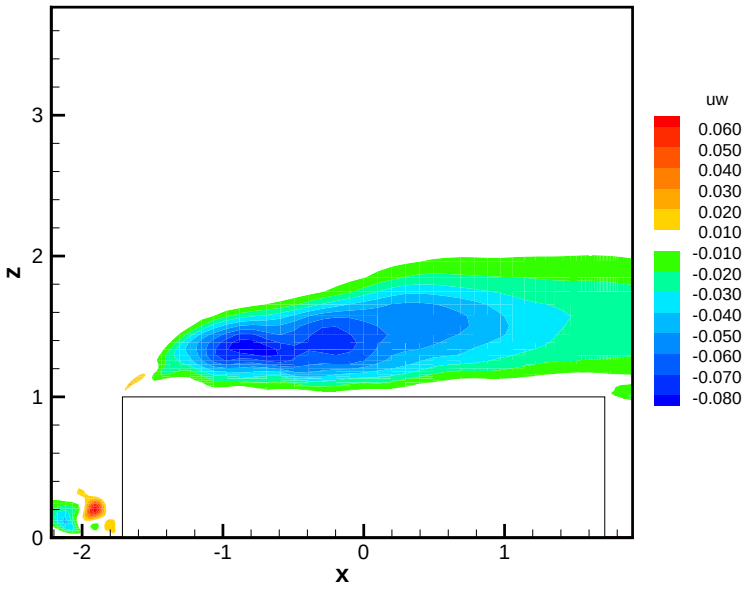

Figure 6.52: Contours of $\overline{u'w'}$ at the center plane for the case of turbulent inflow

6.2.4 Pressure Field

In this section we present LES results for the pressure field around the prism in the center plane and on the prism surface. Figures 6.53 and 6.54 show contour maps of the mean pressure coefficient, C_p, in the center plane in both cases of incident flow. The figures show that the region upstream of the prism exhibits higher pressure values in the case of smooth inflow than the corresponding locations in the turbulent inflow. The difference in C_p between the two cases in this region is about 0.1. We did not expect to see a difference in C_p upstream of the prism. The origin of this difference is not clear to us at this time. It might be caused by non-zero divergence of the inflow turbulence. The inflow turbulence is divergence-free only on a uniform mesh, but the current mesh is non-uniform.

The pressure coefficient at the core of the recirculation bubble above the roof is -1.0 in the case of smooth inflow while it drops to -1.3 in the case of turbulent inflow. On the other hand, the C_p on the roof surface in the center plane is -0.9 and -1.2 in the cases of smooth and turbulent inflow, respectively.

Peak values of $\overline{p'^2}$ are observed in both inflow cases to occur at the location corresponding to the suction peak in the shear layer in each case of incident flow as shown in figures 6.55 and 6.56. The figures also show that the peak value of $\overline{p'^2}$ in the case of turbulent inflow is twice as much as the highest value of $\overline{p'^2}$ in the case of smooth inflow.

Figures 6.57 and 6.58 show contour maps of C_p and surface friction lines on the surface of the prism for both inflow cases. It can be seen that the suction peaks on the roof appear very close to the secondary separation line of the upstream flow in the reversed flow region. It should be noted that the separation line is traced by the cross-stream friction line which form at about $0.7H$ and $0.4H$ downstream the leading edge of the prism for the smooth and turbulent inflow cases, respectively. Additionally, in the vicinity of the quarter plane, there is a suction peak on the roof for both inflow cases and the suction pressure at these locations is higher than that at the the center plane. The appearance of suction peaks at these locations can be attributed to the fact that the center of the roof vortex has an arch-like shape. The vortex center becomes closer to the roof as we move away from the center plane. Moreover,

the vortex maintains its strength along the roof span, yet it is highly stretched very close to the edge plane. Therefore, the highest suction peaks occur where the vortex becomes close to the roof with high strength, which is around the location of the quarter plane. Traces of the vortex centers in the flow field are presented at the end of this chapter. The figures also show that the suction peak pressures on the side walls occur near the bottom and at the location of the separation line on the side wall. In both inflow cases, the suction peak on the side wall is higher, in absolute sense, than the suction peaks on the roof.

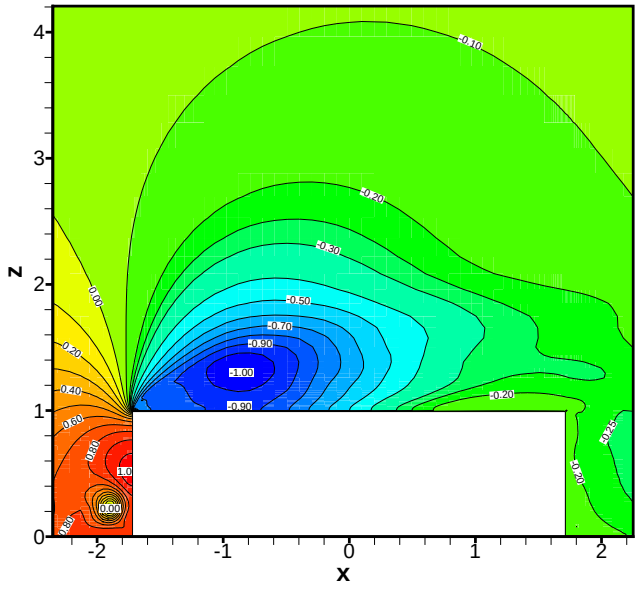

Figure 6.53: Contours of mean pressure coefficient at the center plane for the case of smooth inflow

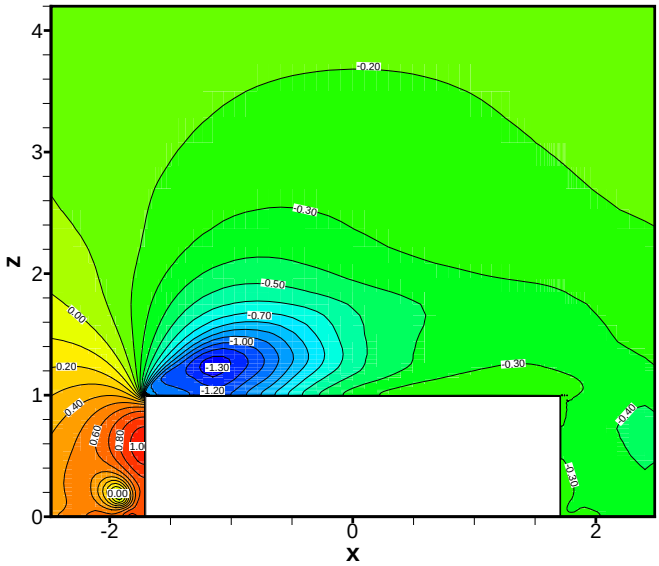

Figure 6.54: Contours of pressure fluctuations at the center plane for the case of turbulent inflow

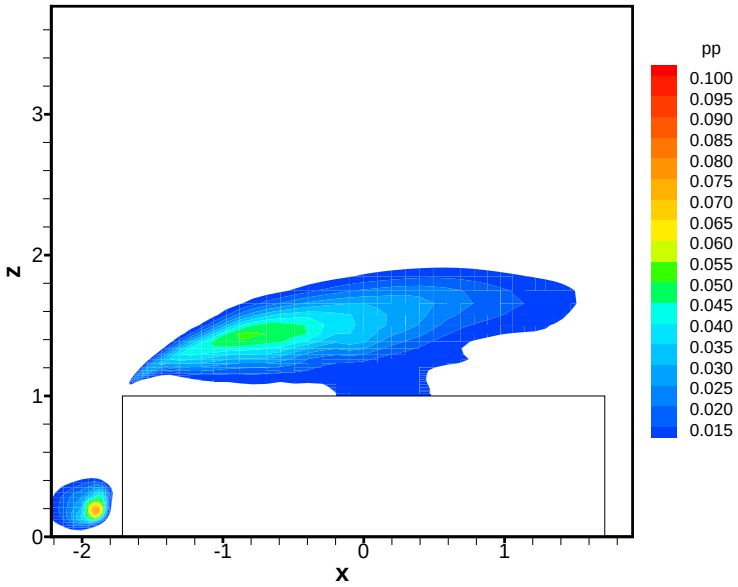

Figure 6.55: Contours of $\overline{p'^2}$ at the center plane for the case of smooth inflow

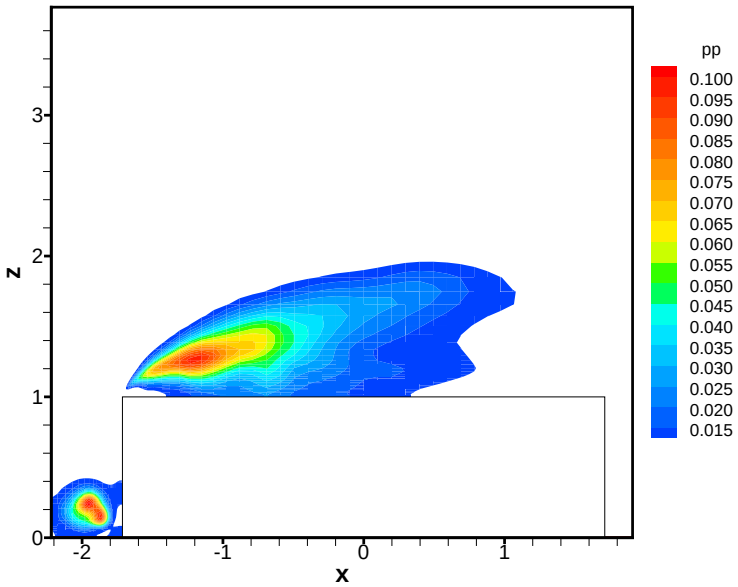

Figure 6.56: Contours of $\overline{p'^2}$ at the center plane for the case of turbulent inflow

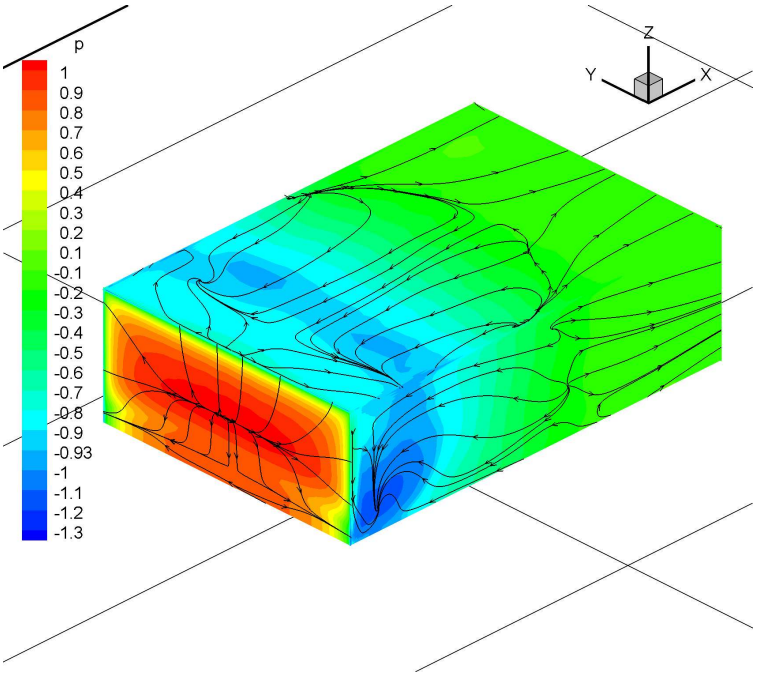

Figure 6.57: Contours of mean surface pressure coefficient for the case of smooth inflow

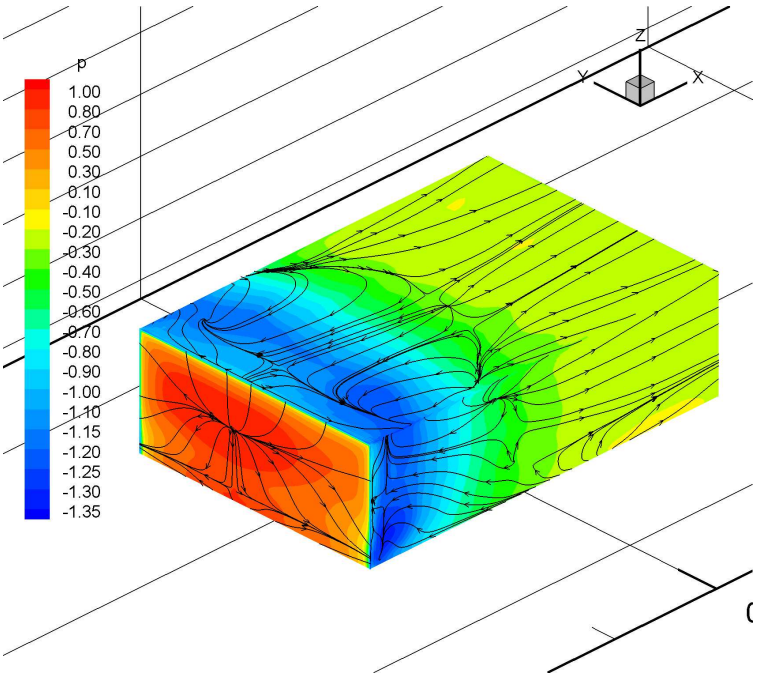

Figure 6.58: Contours of mean surface pressure coefficient for the case of turbulent inflow

6.2.5 Mean Flow Structures

A description of the mean flow topology of the flow around surface-mounted prism is given in this section. Figures 6.59 and 6.60 show three-dimensional presentation of the flow field over surface mounted prism for the smooth inflow and the turbulent inflow cases, respectively. The figures show slices of the flow domain with the streamlines in the plane shown superimposed on contour maps of vorticity magnitude Ω. Ground friction lines are also shown in the two figures.

Upstream of the prism, the convected flow below the cross-stream stagnation streamlines, reaches the the prism upwind face and thus is forced to turn down towards the ground. Part of this flow rolls resulting in a horseshoe vortex upstream of the prism. Another portion of this flow moves closer to the ground and generates a wall jet flowing upstream. This wall jet penetrates underneath the incoming boundary layer causing it to separate early upstream in what we defined, in section 6.2.1, as primary separation. Since, these two opposite flows carry opposite vorticity to one another, they finally roll resulting in a thin eddy upstream of the prism. This thin vortex continue to roll as the flow turns around the prism. As this separated flow reattaches to the prism sides and to the ground downstream of the prism, this vortex continue to appear downstream. On the other hand, the horseshoe vortex turns around the sides of the prism and stretches downstream. Moreover, fluid particles, that are convected with the reattached flow on the roof and the sides of the prism, roll downstream of the prism and form a large vortex that has both of its ends attached to the ground downstream of the prism. This vortex is clearly shown to be symmetric across the center plane. This vortex is known in literature as the portal vortex.

The development of this complex flow field has been speculated by many researchers, yet we believe that accurate picture of the whole flow field has not yet been presented especially for the development of the primary separation region and the horseshoe vortex. Figures 6.61 and 6.62 present traces of the vorticity magnitude along the core of the horseshoe vortex in the $xy-$ planes that crosses the vortex. The figures show that the high vorticity magnitude, at the core of the horseshoe vortex upstream of the prism, diffuses after the vortex axis

bends in the downstream direction. The levels of vorticity magnitude indicate that the vortex continues to appear downstream, yet it becomes very week. In addition, the vortex formed by the primary separation of the boundary layer also appears downstream along the sides of the prism. This eddy is much weaker in the case of turbulent inflow.

Although the two frontal eddies, the primary separation vortex and the horseshoe vortex, continue to exist to the sides of the prism and further downstream, it should be noted that these two structures become very weak and less coherent as they stretch downstream. The swirling streamlines in the sections normal to the incident flow in figures 6.59 and 6.60 affirm that these eddies survive downstream. However, these swirling streamlines exaggerate the actual strength of the vortex motion because these streamlines are drawn in plane sections where the out-of-plane component is not presented. Figures 6.63 and 6.64 present three-dimensional stream traces of the mean flow showing the development of the primary separation flow and the horseshoe vortex in the case of smooth inflow. The figures confirm the aforementioned observation that these eddies undergo slight swirling motion as they stretch downstream in the direction of the incident flow. Additionally, figures 6.64 show that the horseshoe vortex flow spreads laterally at the reattachment lines on the sides of the prism, as it moves around the recirculation regions on the sides, then it convects downstream in a rather parallel orientation to the incident flow. in addition, figures 6.59 and 6.60 show that both frontal eddies have high vorticity levels as they roll upstream of the prism. However, as they bend around the prism, high vorticity levels appear only in a thin layer above the ground. This indicates that the recirculation of the flow in the in cross-flow planes is very weak.

Figure 6.65 presents three-dimensional stream traces of the mean flow that shows the flow around the sides of the prism as it penetrates underneath the separating shear layer, on the roof, for the smooth inflow case. This observation was introduced earlier in in the presentation of $V-$velocity component in section 6.2.1. It can be seen from the figure that fluid particles penetrate below the shear layer and recirculate in the separation bubble before they eventually escape the recirculation zone and convect downstream. Figure 6.66 shows the development of the portal vortex in the leeward side of the prism.

Figures 6.67 through 6.74 show a three-dimensional perspective and its projections in the coordinate directions of the traces of the cores of the dominant vortices in the mean flow over surface mounted prism in both turbulent and smooth inflow cases. These vortices are extracted by the data analysis software. Figures 6.67 and 6.69 show that the roof vortex is bent to an M-shape in the top view in the case of smooth inflow. To check the validity of the software and to verify this observation, vortex cores are extracted from the intersection of the zero U and zero W velocity components on the roof at the center plane and at the plane of $y = -0.29$. The traces of the vortex cores at these two planes are shown in figure 6.75 to match loci of the vortex core shown in figure 6.63.

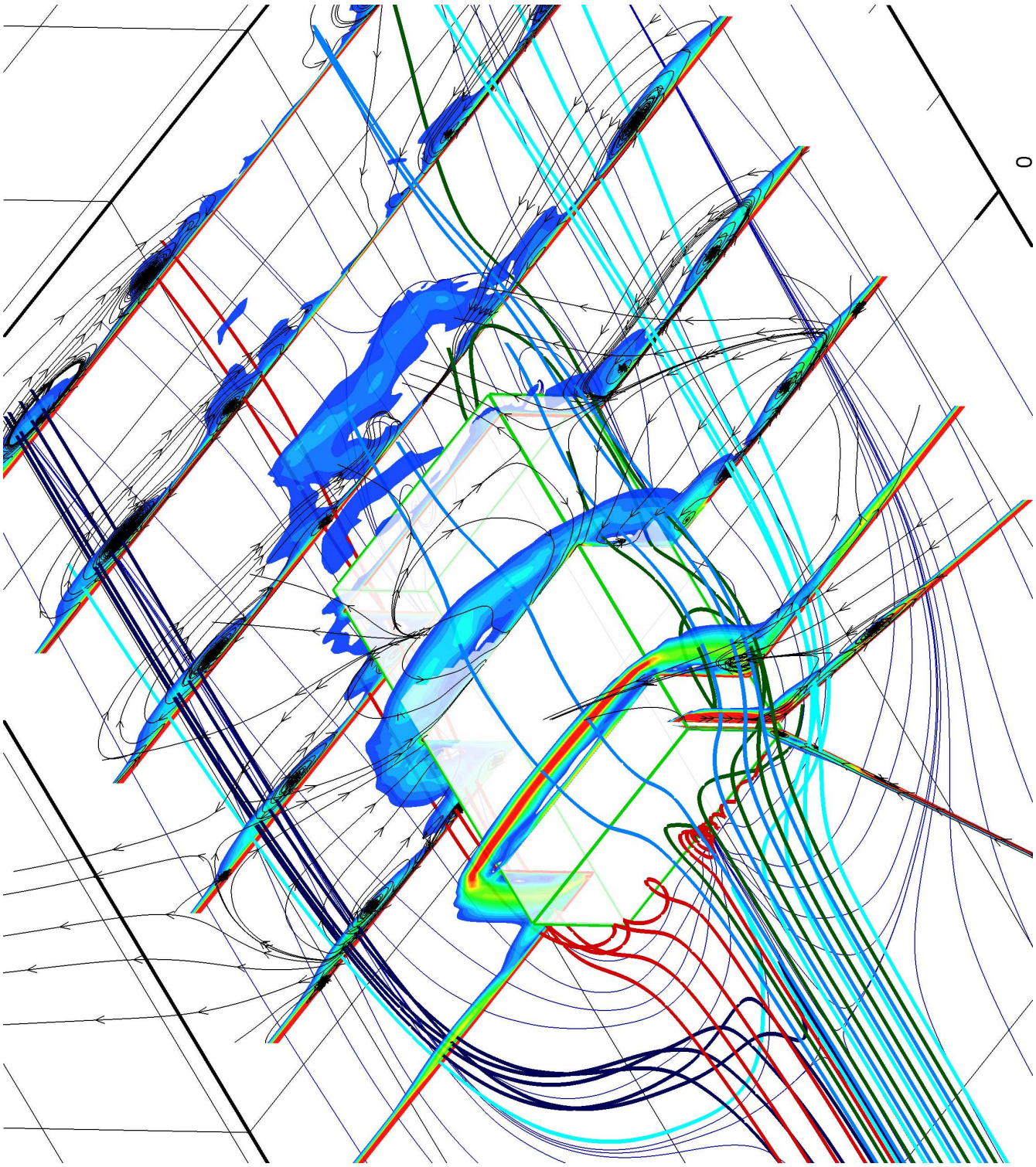

Figure 6.59: Sections with contours of vorticity magnitude and streamlines for the case of smooth incident flow

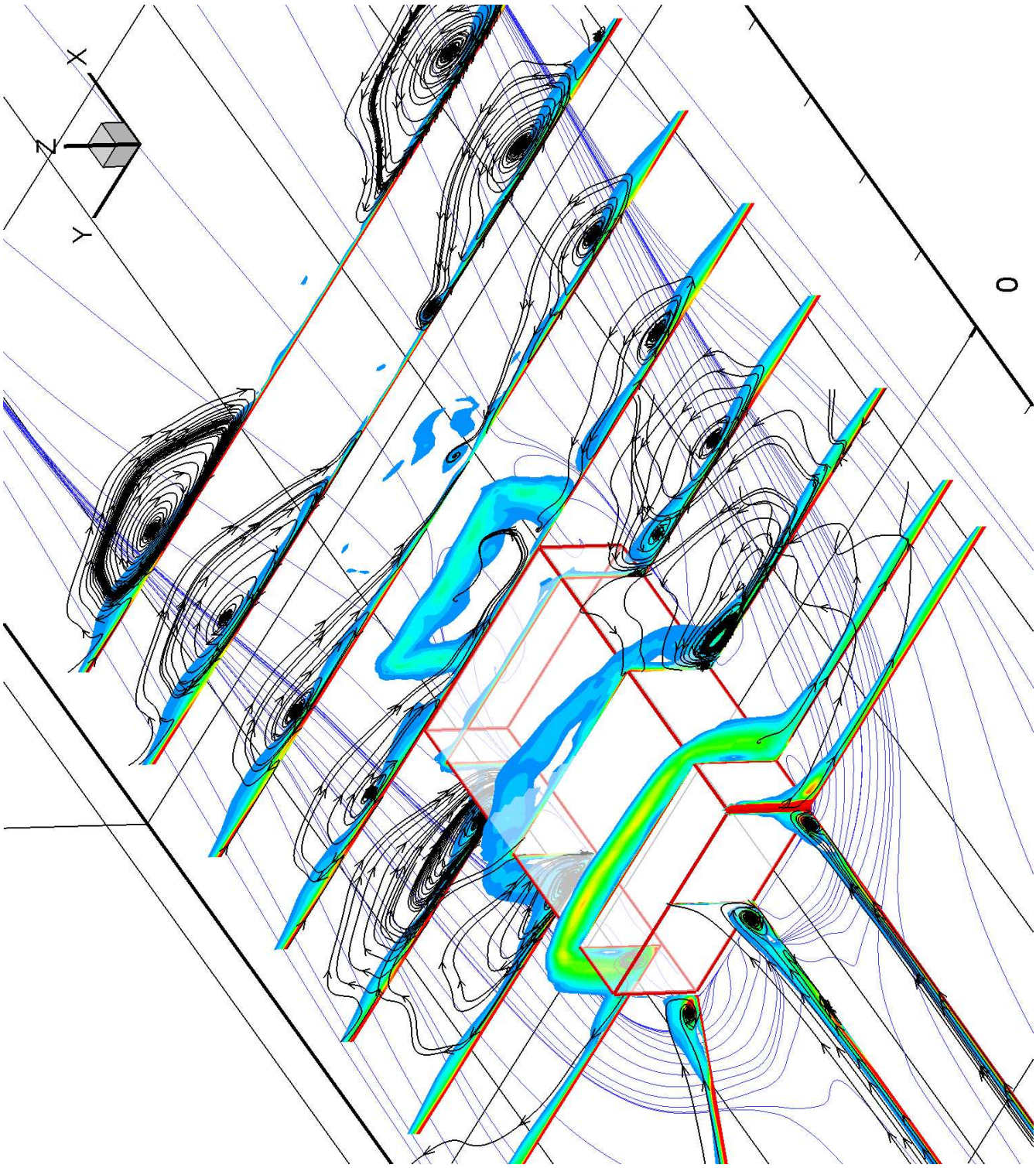

Figure 6.60: Sections with contours of vorticity magnitude and streamlines for the case of turbulent incident flow

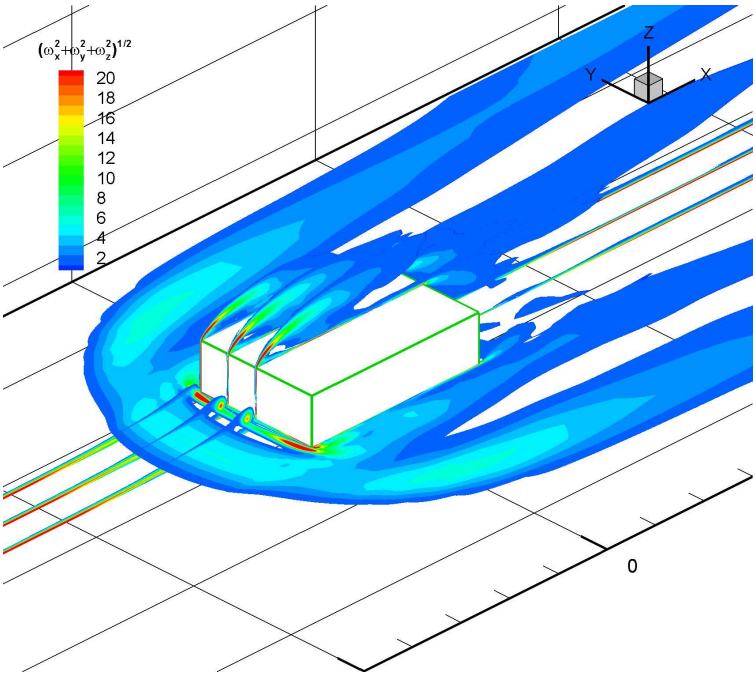

Figure 6.61: Vorticity magnitude at the center, quarter, and the edge planes and at the plane $z = 0.12$ for the case of smooth incident flow

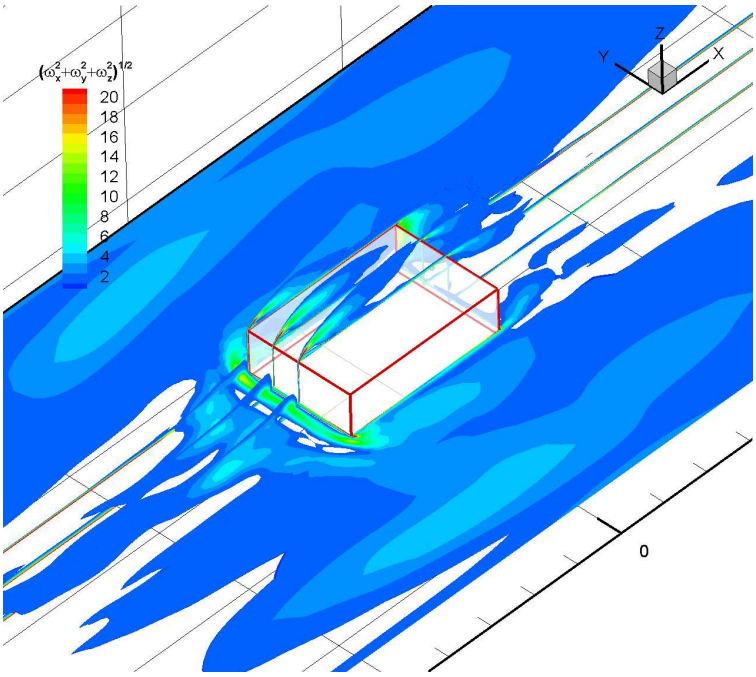

Figure 6.62: Vorticity magnitude at the center, quarter, and the edge planes and at the plane $z = 0.12$ for the case of turbulent incident flow

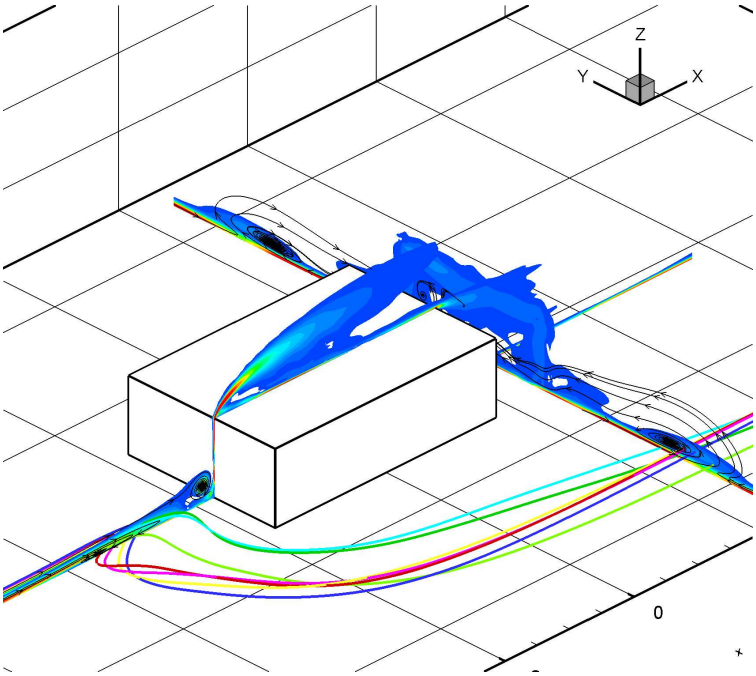

Figure 6.63: Three-dimensional stream traces of the mean flow showing the development of the primary separation flow for the smooth inflow case

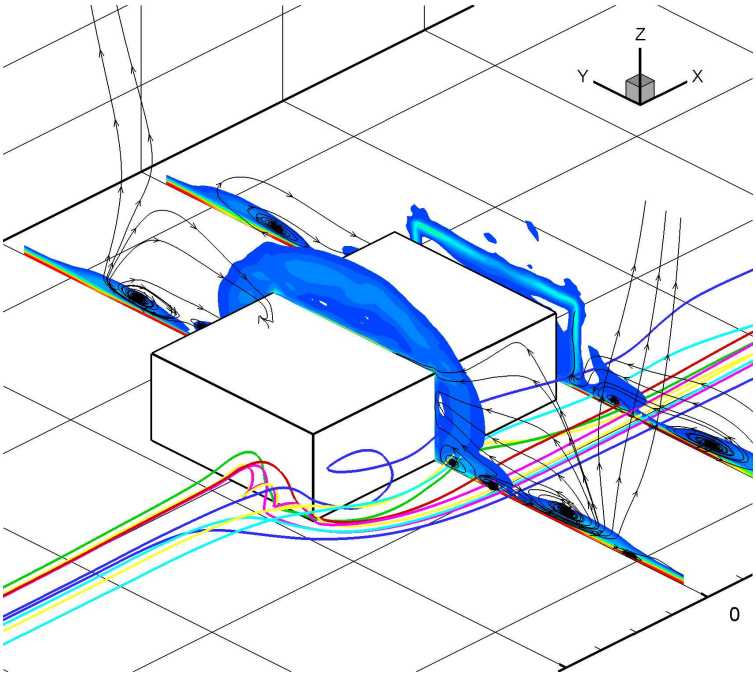

Figure 6.64: Three-dimensional stream traces of the mean flow showing the development of the horseshoe vortex flow for the smooth inflow case

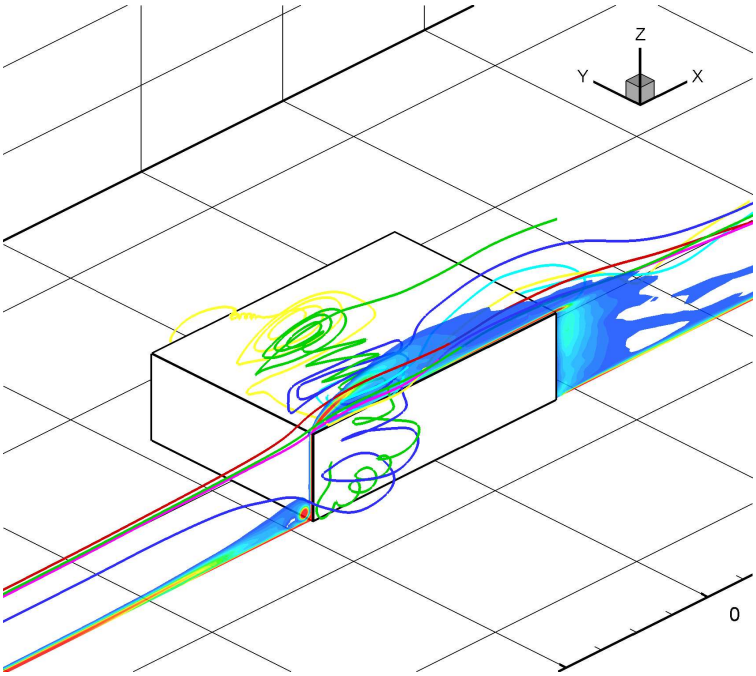

Figure 6.65: Three-dimensional stream traces of the mean flow showing the side flow around the prism penetrates on the roof for the smooth inflow case

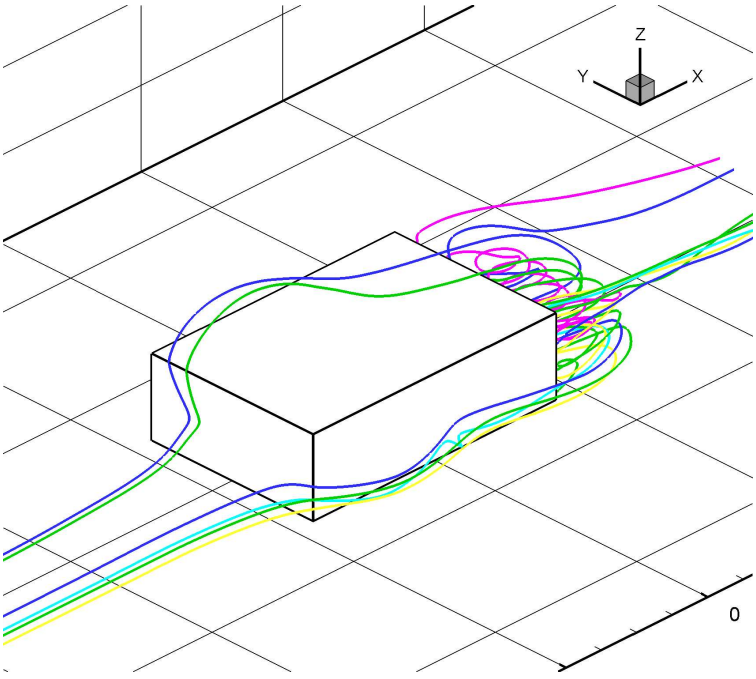

Figure 6.66: Three-dimensional stream traces of the mean flow showing the development of the portal vortex in the leeward side of the prism for the smooth inflow case

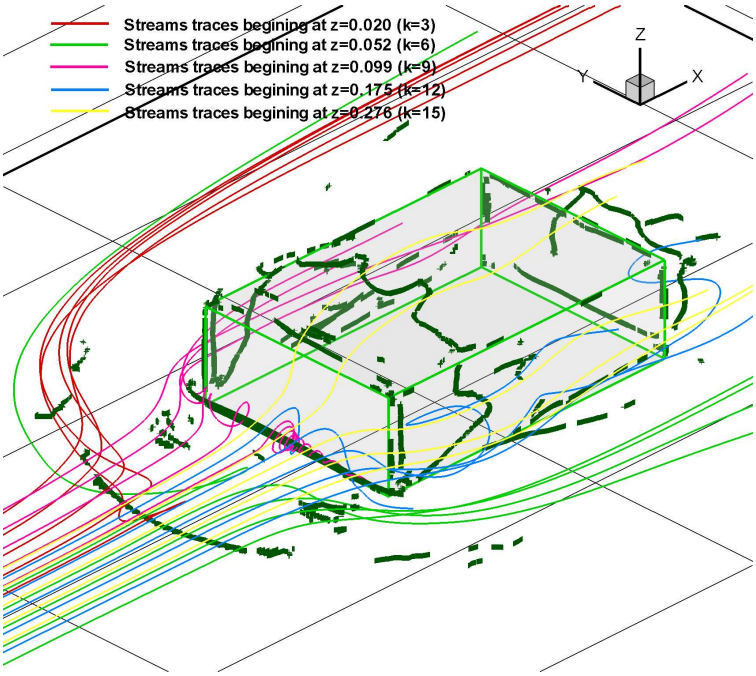

Figure 6.67: Traces of vortex cores in the mean flow field in the case of smooth incident flow

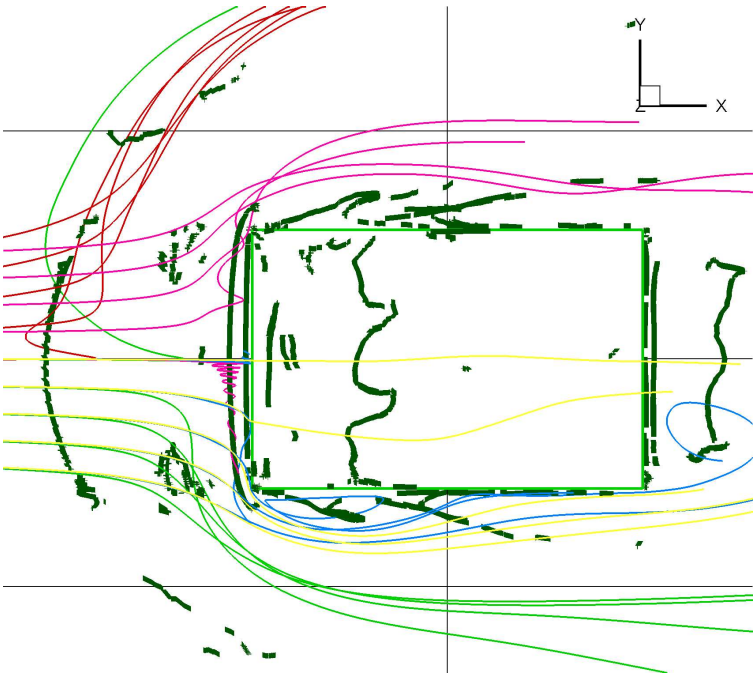

Figure 6.68: Top view of the traces of vortex cores in the mean flow field in the case of smooth incident flow

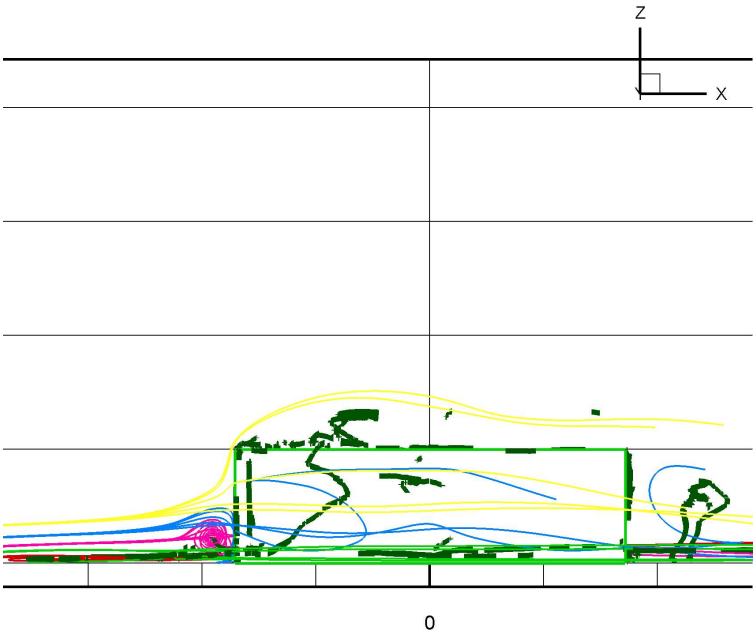

Figure 6.69: Side view of the traces of vortex cores in the mean flow field in the case of smooth incident flow

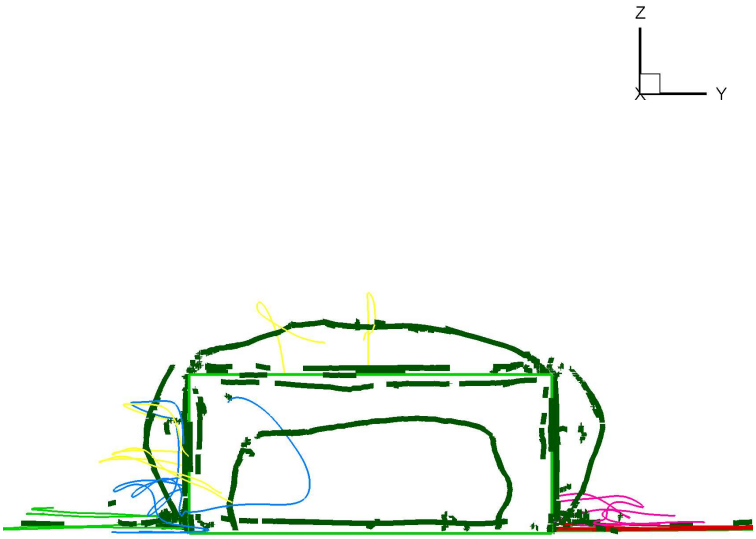

Figure 6.70: Rear view of the traces of vortex cores in the mean flow field in the case of smooth incident flow

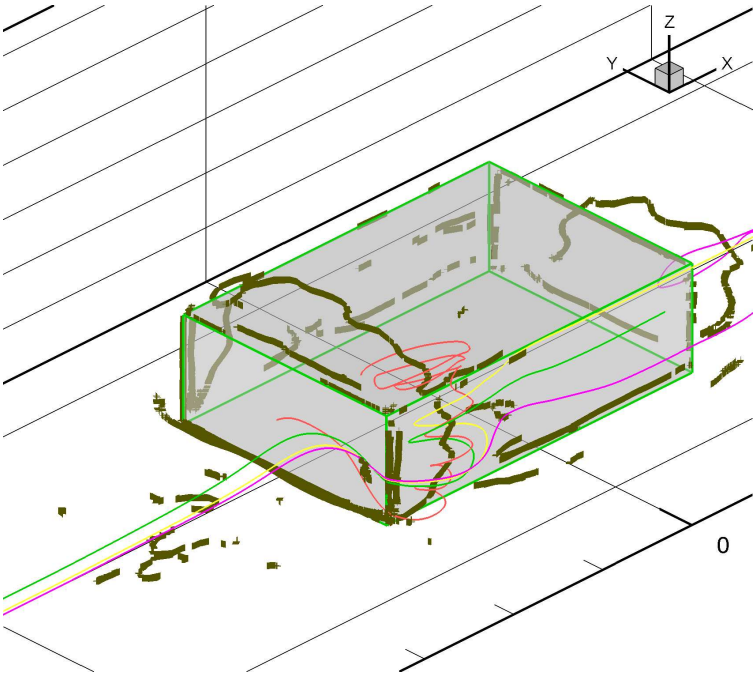

Figure 6.71: Traces of vortex cores in the mean flow field in the case of turbulent incident flow

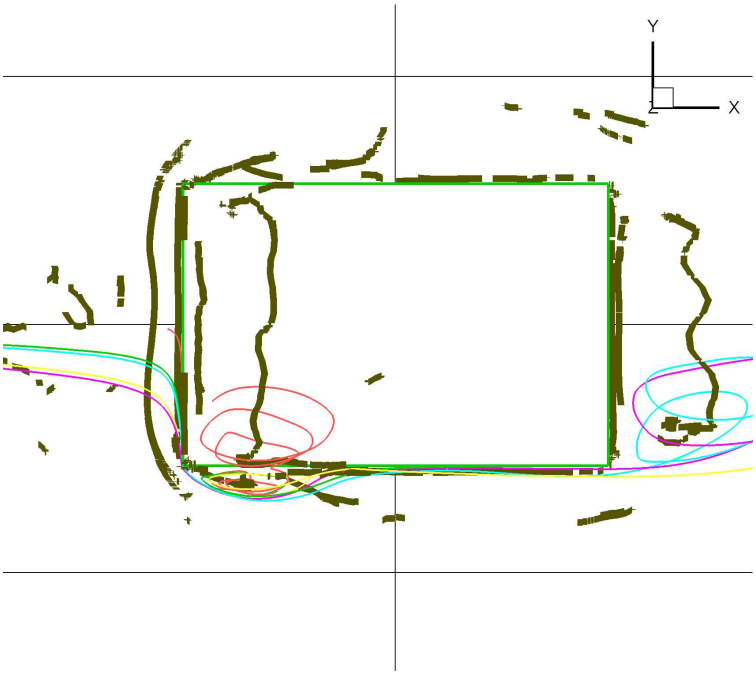

Figure 6.72: Top view of the traces of vortex cores in the mean flow field in the case of turbulent incident flow

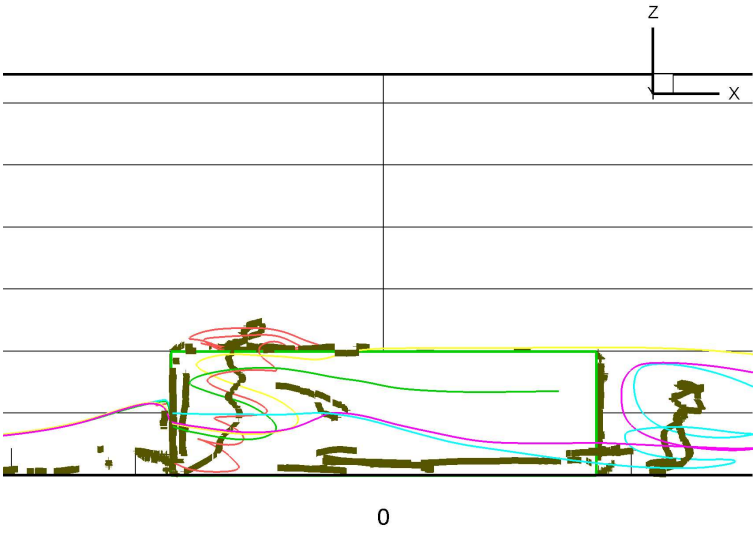

Figure 6.73: Side view of the traces of vortex cores in the mean flow field in the case of turbulent incident flow

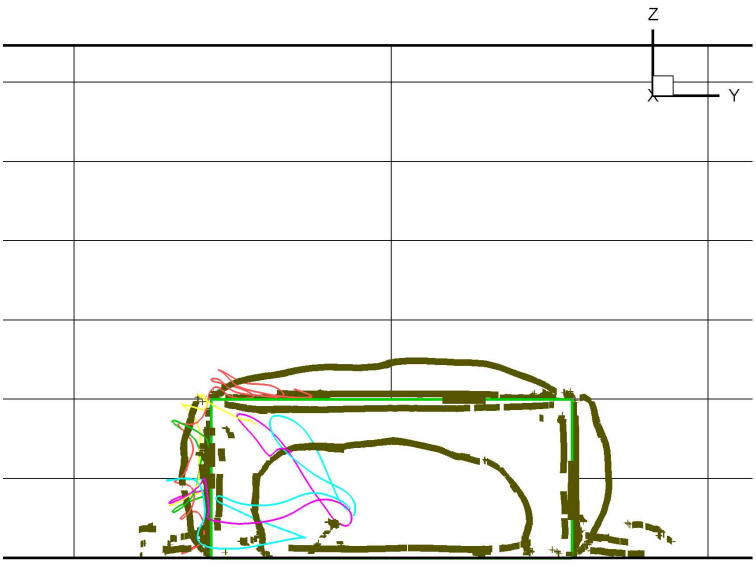

Figure 6.74: Rear view of the traces of vortex cores in the mean flow field in the case of turbulent incident flow

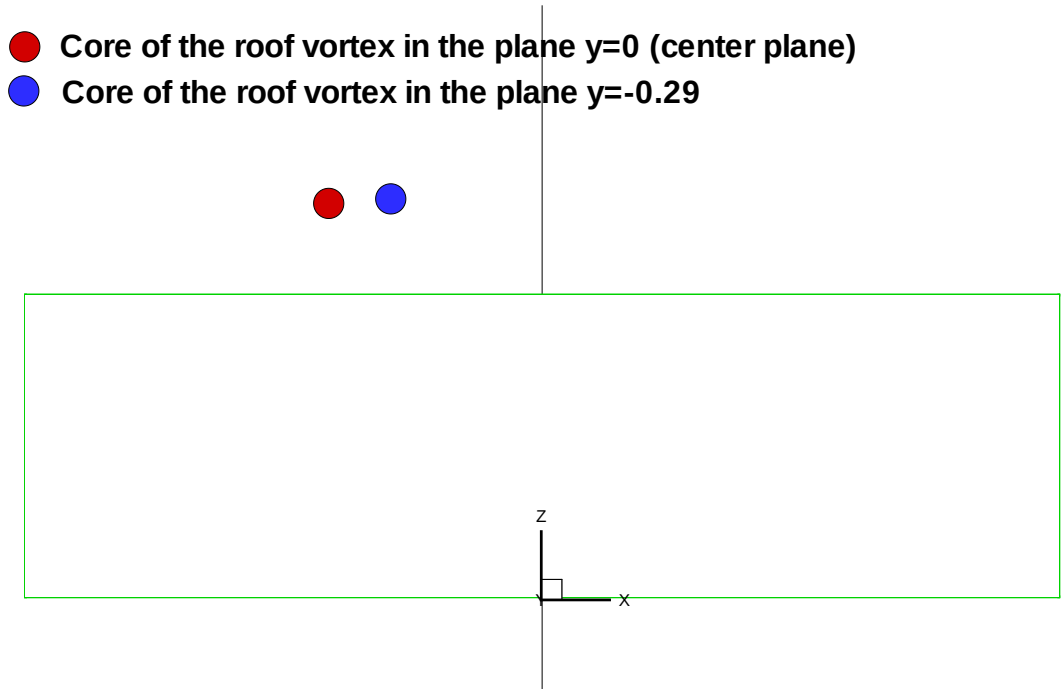

Figure 6.75: Locations of the roof vortex core at the planes $y = 0$ and $y = -0.29$

Chapter 7

Conclusions

In this work, experimental and numerical investigations of the flow field over a surface-mounted prism are conducted. In particular, the issue of the effect of free stream turbulence is addressed. The experimental studies involve particle image velocimetry of the flow field under two cases of incident flow conditions. In one case, turbulence is introduced by a surface roughness element. In the second case, it is introduced by a set of vertically-placed cylinders. The results clearly show that the mean flow separation, reattachment and parameters such as mean velocity, rms, Reynolds stresses and turbulent kinetic energy are affected by the turbulence characteristics of the incident flow. The results show also a common interaction mechanism between the flow field and the solid surface. Positive vorticity sheds from the leading edge to form a shear layer. This vorticity starts to accumulate and strengthens over certain parts of the layer. The strengthening of the vorticity causes the generation of opposite sign (negative) vorticity at the solid wall, i.e. the roof of the prism. The interaction of the two vorticity regions leads to pulling the negative vorticity into the flow and cutting the shear layer into two parts. One part sheds and the other part rolls towards the roof of the prism. The results also show that, in the case where a floor roughness element was introduced and the turbulence in the incident flow consisted mostly of spanwise vorticity and affected the incoming boundary layer, there was additional interaction between the incident turbulence and the shear layer. More specifically, the negative vorticity in the incident turbulence cuts

off the positive vorticity of the shear layer and causes shedding as well as turning of the positive vorticity towards the roof of the prism.

In the numerical investigations, large eddy simulation of the flow field under two different conditions, namely smooth and isotropic homogeneous turbulent inflow, are carried out. In these simulations, higher order schemes were introduced, fine-tuned for dissipation and efficiency and validated. Based on validation studies, a new procedure, that we denote by $C6CUD5$ and that combines a compact sixth-order scheme with a compact upwind difference fifth-order scheme is recommended for performing large eddy simulations of complex flows.

The results presented include new physical aspects of the of flow field. These aspects include the development of the primary separation flow ahead of the upwind face of the prism, the development of the horseshoe vortex flow, the penetration of the side flow around the building to underneath the separating shear layer on the leading edge, the secondary separation of the reversed flow on the roof, and finally the locations of the suction peaks on the roof and the sides of the prism with respect to the secondary separation lines. The effects of the incident flow homogeneous turbulence are determined by pointing out the differences in the flow topologies between the two incident flow cases.

In the LES results, the highest suction levels on the roof are found to occur very close to the secondary separation line. The peaks of such high suction levels occur between the edge and the plane of symmetry close to the edge of the prism. In addition, the suction peak pressures on the side walls occur near the bottom and at the location of the separation line on the side wall. In both cases of incident flow, the suction peaks on the side walls are higher, in absolute sense, than the suction peaks on the roof. Explanations of such pressure distribution of the surface of the prism are presented.

Bibliography

[1] Shakeel Ahmed, Krishen Kumar, *Effect of geometry on wind pressure on low-rise hip roof buildings*, J. Wind Eng. Ind. Aerodyn.90 (2002) 755-779.

[2] Architectural Institute of Japan, *Numerical prediction of wind loading on buildings and structures*, Technical report, March, 1998.

[3] P.W. Bearman, T. Morel, *Effect of free stream turbulence on the flow around bluff bodies*, Proc. Aerospace Sci., Vol 20, pp 97-123, 1983.

[4] S. Becker, H. Lienhart, F. Durst, *Flow around three-dimensional obstacles in boundary layers*, J. Wind Eng. Ind. Aerodyn.90 (2002) 265-279.

[5] Carati, D., Jansen, K., Lund, T., "A family of dynamic models for large-eddy simulation", in *Annual Research Briefs, Center for Turbulence Research*, NASA Ames/Stanford University, 1995.

[6] Carpenter, M. H., C. A. Kennedy, C. A., "Fourth-Order, 2N-Storage Runge-Kutta Schemes," ICASE, NASA Langley Research Center, NASA TM 109112, 1994.

[7] I.P. Castro, A.G. Robins *The flow around a surface mounted cube in uniform and turbulent streams*, J. Fluid Mech. 79 (2) (1977) 307-335.

[8] Ian P. Castro, Ian R. Cowan, Alan G. Robins, *Simulation of flow and dispersion around buildings*, J. Aerospace Eng., Vol. 12, No. 4, 1999.

[9] Comte-Bellot, G., Corrsin, S., "Simple Eulerian time correlation of full- and narrow-band velocity signals in grid-generated isotropic turbulence," JFM, Vol. 48, part 2, pp. 273-337, 1971.

[10] Durbin, P. A., Reif, B. A. P., *Statistical Theory and Modeling for Turbulent Flows*, Wiley, New York, 2001.

[11] C. Dyrbye and S. Hansen, 1997, *Wind Loads on Structures*, John Wiley & Sons, England.

[12] J. Ehrhard, N. Moussiopoulos, *On a new nonlinear turbulence model for simulating flows around building-shaped structures*, J. Wind Eng. Indust Aerody. 88(2000)91-99.

[13] J.C.H. Fung, *Shear flow turbulence structure and its lagrangian statistics*, Fluid Dynmaics Research. 17 (1996) 147-180.

[14] Germano, M., Piomelli, U., Moin, P. and Cabot, W. H.", "A Dynamic Subgrid-scale Eddy Viscosity Model," Physics of Fluids, Vol. 3, No. 7, pp. 1760-1765, 1991.

[15] M.R. Hajj, H.W. Tieleman, L.Tian, *Wind tunnel simulation time variations of turbulence and effects on pressure on surface-mounted prisms*, J. Wind Eng. Ind. Aerodyn.88 (2000) 197-212.

[16] Jianming He, Charles C.S. Song, *A numerical study of wind flow around the TTU building and the roof corner vortex*, J. Wind Eng. Indust Aerody. 67&68 (1997) 547-558.

[17] H.R. Hillier, N.J. Cherry, *The effects of stream turbulence on separation bubbles*, J. Wind Eng. Indust Appl. 8 (1981) 49-58.

[18] Hinze, J.O., 1975. *Turbulence*, 2nd ed.,McGraw-Hill,N.Y.

[19] R.P. Hoxey, A.M. Reynolds, G.M. Richardson, A.P. Robertson, *Observation of Reynolds number sensitivity in the separated flow region on a bluff body*, J. Wind Eng. Indust Aerody. 73 (1998) 231-249.

[20] M.C. Jischke, B.D. Light *Laboratory simulation of tornadic wind loads on a rectangualr model structure*, J. Wind Eng. Ind. Aerodyn. 13 (1983) 371-382.

[21] Jordan, S., and Ragab, S. A. (1996). *A large-eddy simulation of the shear-driven cavity flow using dynamic modeling*, Int. J. CFD, Vol. 6, pp. 321-335.

[22] Sung-Eun Kim, Ferit Boysan, *Application of CFD to environmental flows*, J. Wind Eng. Indust Aerody. 81 (1999) 145-158.

[23] M. Kiya, K. Sasaki. *Structure of a turbulent separation bubble*, J. of Fluid Mech. 137 (1983) 83-113.

[24] K. Kondo, S. Murakami, A. Mochida, *Generation of velocity fluctuations for inflow boundary conditions for LES*, J. Wind Eng. Ind. Aerodyn.67&68 (1997) 51-64.

[25] S. Krajnovic , L Davidson, *Large-eddy simulation of flow around a surface mounted cube using dynamic one-equation subgrid model*, The First Intl. Symp. On Turbulence and Shear Flow Phenomena (1999) pp. 741-746.

[26] Krajnovic, S., and Davidson, L. (2001). *Large-Eddy Simulation of the Flow Around a Three-Dimensional Bluff Body*, AIAA Paper 2001-0432.

[27] Kyung Chun Kim, Ho Seong Ji, and Seung Hak Seong. *Flow structure around 3-D rectangular prism in a turbulent bounday layer*, J. Wind Eng. Indust Aerody. 91 (2003) 653-669.

[28] D. Lakehal, W. Rodi, *Calculation of the flow past a surface-mounted cube with two-layer turbulence models*, J. Wind Eng. Indust Aerody. 67&68 (1997) 65-78.

[29] Sangsan Lee, Sanjiva K. Lele, Parviz Moin, *Simulation of spatially evolving turbulence and the application of Taylor's hypothesis in compressible flow*, Phys. Fluids, 4 (7) (1992) 1521-1530.

[30] Sangsan Lee, *Unstready aerodynamic force prediction on a square cylinder using k-epslon turbulence models*, J. Wind Eng. Indust Aerody. 67&68 (1997) 79-90.

[31] Sungsu Lee, Bogusz Bienkiewicz, *Large-eddy simulation of wind effects on bluff bodies using finite element method*, J. Wind Eng. Indust Aerody. 67&68 (1997) 601-609.

[32] Lele, S. K., "Compact Finite Difference Schemes With Spectral-Like Resolution," JCP, Vol. 103, pp. 16-42, 1992.

[33] C.W. letchford, R. marwood, *On the influence of v and w component turbulence on roof pressure bneath conical vortices*, J. Wind Eng. Indust Aerody. 69-71 (1997) 567-577.

[34] T. Lund, X. Wu, K. Squires *Generation of turbulent inflow data for spatially-developing bounday layer simulations*, J. Comp. Physics 140, 233-258, 1998.

[35] Jakob Mann, *Wind field simulation*,Prob. Eng. Mech. Vol. 13, No. 4 (1998) 269-282.

[36] Martín, M. P., Piomelli, U., and Candler, G. V., "Subgrid-Scale Models for Compressible Large-Eddy Simulations," TCFD, Vol. 13, pp. 361-376, 2000.

[37] R. Martinuzzi, C. Tropea *The flow around surface-mounted, prismatic obstacles placed in a fully developed channel flow*, J. Fluid Eng. Vol. 115 (1993) 85-92.

[38] S. Murakami, S. Ilzuka, *CDF analysis of turbulent flow past square cylinder using dynamic LES*, J. of Fluids Structures (1999) 13,1097-1112.

[39] S. Murakami, S. Ilzuka, *Wind Engineering Report*, Japan (1998).

[40] K. Nozawa, T. Tamura, *Large eddy simulation of the flow around a low-rise building immersed in a rough-wall turbulent boundary layer*, J. Wind Eng. Ind. Aerodyn.90 (2002) 1151-1162.

[41] Siva Parameswaran, Ramesh Andra, Richard Sun, Mark Gleason, *A critical study on the influence of the far field boundary conditions on the pressure distribution around a bluff body*, J. Wind Eng. Indust Aerody. 67&68 (1997) 117-127.

[42] Park, N., Yoo, J. Y., and Choi, H., "Discretization errors in large eddy simulation: on the suitability of centered and upwind-biased compact difference schemes," Paper in press, JCP, 2004.

[43] Ragab, S. A., Sheen, S., Sreedhar, M. (1992). *An investigation of finite-difference methods for large-eddy simulation of a mixing layer*, AIAA Paper 92-0554.

[44] Ragab, S. A., and S. Sheen, S., "Large Eddy Simulation of Mixing Layers," in *Large Eddy Simulation of Complex Engineering and Geophysical Flows*, eds. Galprin, B., and Orszag, S., Cambridge University Press, pp. 255-285, 1993.

[45] Ragab Ragab, S. A., "Numerical Simulation of Turbulence" in *Handbook of Fluid Dynamics and Fluid Machinery*, Volume 2 , Eds. Schetz, J. A. and Fuhs, A. E., John Wiley & Sons, pp. 1506-1527, 1996.

[46] G.N.V. Rao, *Extrapolation of wind tunnel model results to full scale, Proc. Intl Symp. on Experimental Determination of Wind Loads on Civil Eng. Structures*, Dec. 5-7, 1990, New Delhi.

[47] S. Reichrath, T.W. Davies, *Computational fluid dynamics simulations and validation of the pressure distribution on the roof o a commercial multi-span Venlo-type glasshouse*, J. Wind Eng. Indust Aerody. 90(2002) 139-149.

[48] P.J. Richards, R.P. Hoxey, and L.J. Short, *Anisotropic turbulence in the atmospheric surface layer*, J. Wind Eng. Indust Aerody. 69-71 (1997) 903-913.

[49] P.J. Richards, R.P. Hoxey, L.J. Short, *Wind pressure on a 6m cube*, J. Wind Eng. Indust Aerody. 89(2001) 1553-1564.

[50] P. Saathoff, W.H. Melbourne, *Effect of turbulence on streamwise pressure measured on a square-section cylinder*, J. Wind Eng. Ind. Aerodyn.79 (1999) 61-78.

[51] Sagaut, P., and Lê, T. H., "LES-DNS : The Aeronautical and Defence Point of View," in *New Tools in Turbulence Modelling*, , eds. Métas, O., and Ferziger, J., Springer-Verlag, pp. 183-197, 1997.

[52] H. Lübcke, St. Schmidt, T. Rung, F.Thiele, *Comparison of LES and RANS in bluff-body flows*, J. Wind Eng. Indust Aerody. 89 (2001) 1471-1485.

[53] R. Panneer Selvam, *Computation of pressure on Texas Tech building using large eddy simulation*, J. Wind Eng. Indust Aerody. 67&68 (1997) 647-657.

[54] Kishan B. Shah, Joel H. Ferziger, *A fluid mechanics view of wind engineering: large eddy simulation of flow past a cubic obstacle*, J. Wind Eng. Indust Aerody. 67&68 (1997) 211-224.

[55] Shu, C. (2001), *High Order Finite Difference and Finite Volume WENO Schemes and Discontinuous Galerkin Methods for CFD*, ICASE Report No. 2001-11.

[56] Roger L. Simpson, *Junction flows*, Annu. Rev. Fluid Mech. (2001) 33:415-43.

[57] Smagorinsky, J. , *General circulation experiments with the primitive equations. I. The basic experiment*, Monthly Weather Review , vol. 91 , no.3, pp. 99-164, 1963.

[58] J.M.M. Sousa, *Turbulent flow around a surface-mounted obstacle using 2D-3C DPIV*, Exper. Fluids 33 (2002) 854-862.

[59] C.N. Sun, E.G. Burdette, R.O. Banett *Theoritical tornado vortex model for nuclear plant design*, Nuclear Eng. and Design 44 (1977) 407-411.

[60] T. Tamura, T. Miyagi *The effect of turbulence on aerodynamic forces on a square cylinder with various corner shapes*, J. Wind Eng. Ind. Aerodyn. 83 (1999) 135-145.

[61] W. Tieleman, T.A. Reinhold, M.R. Hajj, *Importance of turbulence for the prediction of surface pressures on low-rise structures*, J. Wind Eng. Ind. Aerodyn.79 (1999) 61-78.

[62] H.W. Tieleman, *Universality of velocity spectra*, J. Wind Eng. Ind. Aerodyn. 56 (1995) 55-69.

[63] H.W. Tieleman, M.R. Hajj, T.A. Reinhold, *Wind tunnel simulation requirements to assess wind loads on low-rise buildings*, J. Wind Eng. Ind. Aerodyn. 74-76 (1998) 675-685.

[64] Hoong Thiam Toh, Large Eddy Simulation of Supersonic Twin-Jet Impingement Using a Fifth-Order WENO Scheme, Ph.D. dissertation, Virginia Polytechnic Institute and State University, 2003.

[65] Tolstykh, A. I. (1994). *High Accuracy Non-Centered Compact Difference Schemes For Fluid Dynamics Applications*, World Scientific, New Jersey.

[66] Tolstykh, A. I., and Lipavskii, M. V., "On performance of methods with third- and fifth-order compact upwind differencing," J. Computational Physics, Vol. 140, pp. 205-232, 1998.

[67] M. Tutar, G. Oguz, *large eddy simulation of wind flow around parallel buildings with varying configurations*, Fluid Dynamics Research 31 (2002) 289-315.

[68] Visbal, M. R., and Rizzetta, D. P., "Large-eddy simulation on curvilinear grids using compact differencing and filtering schemes," JFE, Vol. 124, pp. 836-847, 2002.

[69] Wilson, R. V., A.O. Demuren, A. O., and M. Carpenter, M., "Higher-Order Compact Schemes for Numerical Simulation of Incompressible Flows," ICASE,NASA Langley Research Center, ICASE Report No. 98-13, Hampton, VA, 1998.

[70] C.N. Sun, E.G. Burdette, R.O. Banett *Differential pressures on building walls during tornados*, Nuclear Eng. and Design 41 (1977) 53-57.

[71] Da-hai Yu, Ashan Kareem, *Numerical simulation of flow around rectangular prism*, J. Wind Eng. Indust Aerody. 67&68 (1997) 195-208.

[72] Zhang, W., Chen, Q., "A new filtered dynamic subgrid-scale model for large eddy simulation of indoor airflow," Proceedings of Building Simulation '99, Kyoto, Japan, 1999.

Vita

Yasser Mohamed El-Okda was born in Morcombe, England in 1972. He finished his secondary school education in his hometown, Mit Ghamr, Egypt. He earned his Bachelor degree from the Mechanical Power Engineering Department, Zagazig University in 1994. Upon his graduation, he joined EMIDC Co. for drilling mud production, Alexandria, Egypt, as a maintenance engineer. He moved on to work as a service engineer with Baker Oil Tool for oil well completion and work-over, regional office, Cairo, Egypt. At Baker Oil Tools, he earned a remarkable experience and spent a very interesting period of his life. He visited many of the land and offshore drilling rigs, oil production platforms, and even giant tankers all over the Egyptian deserts and seas. He joined Zagazig University in 1995 and worked there as a research/teaching assistant. He joined the Department of Engineering Science and Mechanics in 1999. In May 2002, he earned a Master's degree in Engineering Mechanics from Virginia Polytechnic Institute and State University.